



**FREQUENCY DIVERSE ARRAY RADAR:
SIGNAL CHARACTERIZATION AND
MEASUREMENT ACCURACY**

THESIS

Steven Brady, Flight Lieutenant, RAAF
AFIT/GE/ENG/10-04

**DEPARTMENT OF THE AIR FORCE
AIR UNIVERSITY**

AIR FORCE INSTITUTE OF TECHNOLOGY

Wright-Patterson Air Force Base, Ohio

APPROVED FOR PUBLIC RELEASE; DISTRIBUTION UNLIMITED.

The views expressed in this document are those of the author(s) and do not reflect the official policy or position of the United States Air Force, Department of Defense, United States Government, the corresponding agencies of any other government, NATO, or any other defense organization.

AFIT/GE/ENG/10-04

FREQUENCY DIVERSE ARRAY RADAR:
SIGNAL CHARACTERIZATION AND MEASUREMENT ACCURACY

THESIS

Presented to the Faculty
Department of Electrical and Computer Engineering
Graduate School of Engineering and Management
Air Force Institute of Technology
Air University
Air Education and Training Command
in Partial Fulfillment of the Requirements for the
Degree of Master of Science in Electrical Engineering

Steven Brady, BaEng (hons)
Flight Lieutenant, RAAF

25 March 2010

APPROVED FOR PUBLIC RELEASE; DISTRIBUTION UNLIMITED.

FREQUENCY DIVERSE ARRAY RADAR:
SIGNAL CHARACTERIZATION AND MEASUREMENT ACCURACY

Steven Brady, BaEng (hons)
Flight Lieutenant, RAAF

Approved:

//signed//

March 2010

Michael A. Saville (Chairman)

Date

//signed//

March 2010

Richard K. Martin (Member)

Date

//signed//

March 2010

Mark E. Oxley (Member)

Date

Abstract

Radar systems provide an important remote sensing capability, and are crucial to the layered sensing vision; a concept of operation that aims to apply the right number of the right types of sensors, in the right places, at the right times for superior battle space situational awareness. The layered sensing vision poses a range of technical challenges, including radar, that are yet to be addressed. To address the radar-specific design challenges, the research community responded with waveform diversity; a relatively new field of study which aims reduce the cost of remote sensing while improving performance. Early work suggests that the frequency diverse array radar may be able to perform several remote sensing missions simultaneously without sacrificing performance.

With few techniques available for modeling and characterizing the frequency diverse array, this research aims to specify, validate and characterize a waveform diverse signal model that can be used to model a variety of traditional and contemporary radar configurations, including frequency diverse array radars. To meet the aim of the research, a generalized radar array signal model is specified. A representative hardware system is built to generate the arbitrary radar signals, then the measured and simulated signals are compared to validate the model.

Using the generalized model, expressions for the average transmit signal power, angular resolution, and the ambiguity function are also derived. The range, velocity and direction-of-arrival measurement accuracies for a set of signal configurations are evaluated to determine whether the configuration improves fundamental measurement accuracy.

Acknowledgements

I wish to thank the Royal Australian and United States Air Forces for the unique opportunity to study at the Air Force Institute of Technology. My entire family has enjoyed the expatriate experience and we'll return to Australia with many cherished memories. We appreciate how fortunate we are and we will never forget our new friends.

The people who have made a positive impact to our life in the US are too many to mention individually. However, I'd like to acknowledge the following groups. The students, for enriching my educational experience and being great mates. The many professors, from who I have learnt so much and for who I may have caused some consternation. The support staff, who are always there to help out. The Australians in Dayton, for fully supporting us and creating a home-away-from-home. And, the staff at the Australian embassy, who take excellent care of all Australians serving in the US.

A few key individuals played a large role in shaping the AFIT experience. Maj. Saville, thank you for being such a great educator, mentor and role-model. I appreciate all that you have done for me. Dr. Oxley and Dr. Martin, thank you for agreeing to be on my committee and reviewing my work. I consider myself privileged to have you both on my team. Mrs. Robb, thank you for working tirelessly on behalf of the international community at AFIT. You help the international students bridge the cultural gaps so that we can concentrate on completing our assignments.

Finally, I extend my deepest gratitude to my family. To my beautiful wife and daughter, you both have showed extreme patience and compassion while I struggle through odd hours and bizarre routines. Thank you both for your unwavering faith in my abilities and for appreciating the value of my work – without that support I would not accomplish even a fraction of what I do. To my family, who decided to

make the journey half-way around the world to be with me at the graduation, thank you for thinking I'm worth the time and expense.

Steven Brady

Table of Contents

	Page
Abstract	iv
Acknowledgements	v
Table of Contents	vii
List of Figures	xi
List of Tables	xv
List of Symbols	xvi
List of Abbreviations	xix
 I. Introduction	 1
1.1 Research Motivation	1
1.2 Problem Description	5
1.3 Research Hypothesis and Scope	7
1.4 Thesis Overview	10
 II. Background	 12
2.1 Chapter Overview	12
2.2 Layered Sensing, Waveform Diversity and Frequency Diverse Arrays	 12
2.3 Constant Frequency Array Theory	17
2.3.1 Geometry	18
2.3.2 Signal Model	23
2.3.3 Array Factor	27
2.3.4 Pattern Synthesis and the Fourier Transform	31
2.3.5 Field Characteristics	35
2.3.6 Receivers	37
2.4 Ambiguity Function	39
2.5 Orthogonal Frequency Division Multiplexing	48
2.6 Frequency Diverse Array with Linear Frequency Progression	 52
2.6.1 Additional Geometry	53
2.6.2 Signal Model	56
2.6.3 Field Pattern	57
2.6.4 Array Factor	59
2.6.5 Received Signal and Receiver Models	60
2.6.6 Synthetic Aperture Radar Application Study	64
2.6.7 Recommended FDA Research	66
2.7 Chapter Summary	67

	Page
III. Research Methodology	69
3.1 Chapter Overview	69
3.2 Limitations to Scope and Assumptions	70
3.3 Transmit Signal Characterization	71
3.4 Received Signal Processing	72
3.5 Comparisons	73
3.6 Chapter Summary	73
IV. Transmit Signal Model and Analysis	75
4.1 Chapter Overview	75
4.2 Transmit Signal Geometry	75
4.3 Transmit Signal	76
4.4 Transmit Field	80
4.5 Transmit Field Characteristics	82
4.5.1 Average Power	82
4.5.2 Angular Difference	84
4.6 Spectral Analysis	89
4.7 Experimental Field Model Validation	92
4.8 Chapter Summary	95
V. Received Signal and Analysis	99
5.1 Chapter Overview	99
5.2 Geometry	99
5.3 Received Signal	102
5.4 Doppler Approximation Comparison	104
5.5 Receiver Processing	108
5.6 Ambiguity Function	112
5.7 Received Signal Model Validation	117
5.8 Chapter Summary	119
VI. FDA Design Examples	120
6.1 Chapter Overview	120
6.2 LFP-FDA Examples	120
6.2.1 Transmit Array Inter-element Spacing	122
6.2.2 Sub-Carrier Separation	124
6.2.3 Chirped Waveforms	126
6.2.4 Phase Coding with $M = 4$	127
6.2.5 Combining a Signal and Its Complement	130
6.3 Waveform Diverse Array	135
6.4 Chapter Summary	139

	Page
VII. Conclusions	141
7.1 Research Summary	141
7.2 Suggestions for Future Research	144
7.2.1 Waveform Optimization	144
7.2.2 Receiver Design and Optimal Array Processing	145
7.2.3 High Fidelity Simulation	146
7.2.4 Planar and Distributed Aperture Geometries	147
7.2.5 Joint Radar and Communications Waveforms	147
A. Derivations	149
1.1 Far-field Approximation	149
1.2 Average Transmit Power	151
1.3 Signal Difference	155
1.4 Spectral Analysis Development	158
B. Experimental Configuration	165
2.1 Overview	165
2.2 System Block Diagram	166
2.3 Primary Instruments	167
2.3.1 Oscilloscope	168
2.3.2 Arbitrary Waveform Generator	169
2.3.3 Real-time Spectrum Analyzer	169
2.4 Circuit Configuration	169
2.4.1 Component List	171
2.4.2 Pre-conditioning Circuit	172
2.4.3 Transmitter Stage	173
2.4.4 Antenna Characteristics	174
2.4.5 Receiver Processing	175
2.5 Results	178
2.5.1 Field Measurements	179
2.5.2 Target Measurements and Receiver Processing	190
2.6 Summary	194
C. Fourier Transforms: Properties, Transform Pairs and Application to Optics	196
3.1 One Dimension Fourier Transforms	196
3.1.1 Temporal Signals	196
3.1.2 Spatial Signals	197
3.1.3 Amplitude and Phase Spectra	200
3.1.4 Discrete Fourier Transform	200

	Page
3.2 Two Dimension Fourier Transform	201
3.2.1 Transform in Rectangular Coordinates	202
3.2.2 Transform in Polar Coordinates	203
3.3 Fourier Optics	204
3.3.1 Diffraction Pattern and the Fourier Transform	206
3.3.2 Optical Array Theorem	208
Bibliography	210
Vita	214

List of Figures

Figure		Page
1.1.	Layered Sensing Topology.	2
1.2.	JORN's Primary Radar Sites.	4
2.1.	Chapter 2's Relation to the Research.	13
2.2.	Layered Sensing Model.....	14
2.3.	Radar Coordinate System and Linear Array Geometry.	20
2.4.	Transmit Configuration: CFA.....	24
2.5.	CFA Array Factors.	29
2.6.	Signal Field Pattern: CFA.....	32
2.7.	General Array Processor.	36
2.8.	AF Principal Planes.	40
2.9.	AF Principal Planes and Axes: CFA.	46
2.10.	Phase Coded OFDM Signals.....	50
2.11.	Signal Field Pattern: OFDM.	52
2.12.	SAR Global Coordinates and Reconstruction Grid.	54
2.13.	Analytical Spotlight SAR Geometry.	55
2.14.	Transmit Configuration: LFP-FDA.	56
2.15.	Signal Field Pattern: LFP-FDA.....	58
2.16.	Signal Field Pattern Comparison: CFA, LFP-FDA and OFDM.	58
2.17.	Transmit-Receive Configurations: LFP-FDA for STAP and SAR.....	61
2.18.	Apparent Collection Geometry.	62
3.1.	Research Overview Diagram.	70

Figure	Page
4.1.	Transmit Configuration: Generalized FDA. 76
4.2.	Time-Frequency Coded Transmit Signal. 76
4.3.	Signal Field Pattern: Randomly Weighted FDA. 81
4.4.	Average Transmit Signal Power: LFP-FDA. 84
4.5.	Average Transmit Signal Power: Randomly Weighted FDA. 85
4.6.	Signal Difference Comparison: CFA and LFP-FDA, $u_0 = 0$ 88
4.7.	Signal Difference Comparison: CFA and LFP-FDA, $u_0 = 0.5$ 89
4.8.	Signal Field Pattern and Spectra Comparison: CFA, LFP-FDA and OFDM. 92
4.9.	Experimental Field Measurement Configuration: Simplified Diagram. 93
4.10.	Comparison of Measured (DSB-SC) and Simulated (DSB-SC) Field Data: <i>OFDM4</i> and <i>OFDM1</i> 96
4.11.	Transmit Signal Characteristics: Randomly Weighted FDA. 97
5.1.	Generalized FDA Transmitter-Receiver. 101
5.2.	Doppler Model Comparison. 107
5.3.	FDA Receiver Processor. 108
5.4.	AF Principal Planes and Axes: LFP-FDA. 115
5.5.	AF Principal Planes and Axes: Random-weighted FDA. 116
5.6.	Target Measurement Configuration: Simplified Diagram. 118
5.7.	Comparison of Measured (DSB-SC) and Simulated (DSB-SC) Received Signal Data: <i>OFDM4</i> and <i>OFDM1</i> 118

Figure	Page
6.1. Transmit Signal Characteristics: LFP-FDA, $\Delta_{\hat{y},t} = \lambda_{min}$	122
6.2. AF Principal Planes and Axes: LFP-FDA, $\Delta_{\hat{y},t} = \lambda_{min}$	123
6.3. Transmit Signal Characteristics: LFP-FDA, $B = 8$	125
6.4. AF Principal Planes and Axes: LFP-FDA, $B = 8$	126
6.5. AF Principal Planes and Axes: LFP-FDA, LFM.	127
6.6. AF Principal Planes and Axes: LFP-FDA, $M = 4$ Barker Code.	128
6.7. AF Principal Planes and Axes: LFP-FDA, $M = 4$ Hadamard Code.	130
6.8. AF Principal Planes and Axes: LFP-FDA, $ \chi^{(+)}(\Delta\tau, v_t, u_t, \Delta u) $	132
6.9. AF Principal Planes and Axes: LFP-FDA, $ \chi^{(\times)}(\Delta\tau, v_t, u_t, \Delta u) $	135
6.10. Transmit Signal Characteristics: Waveform Diverse Signal.	136
6.11. AF Principal Planes and Axes: Waveform Diverse Configuration.	137
A.1. Average Transmit Power Comparison: CFA and FDA.	155
B.1. Experimental Configuration Block Diagram.	166
B.2. Experimental Circuit Diagram.	170
B.3. Instrument Connection Diagram.	171
B.4. Pre-Condition Circuit and Signals.	173
B.5. Antenna Dimensions.	174
B.6. Pyramidal Horn Beam Pattern.	175
B.7. Waveform Record.	176
B.8. Digital Receiver Processing Block Diagram.	177

Figure	Page
B.9.	Field Sampling Configuration. 179
B.10.	Comparison of Measured and Simulated Data: CFA Signal. 181
B.11.	Comparison of Measured (DSB-SC) and Simulated (SSB-SC) Data: <i>Barker2</i> and <i>Hadamard2</i> Signals. 182
B.12.	Comparison of Measured (DSB-SC) and Simulated (SSB-SC) Data: <i>Hadamard2</i> and <i>Hadamard1</i> 182
B.13.	Comparison of Measured (DSB-SC) and Simulated (SSB-SC) Data: <i>OFDM4</i> and <i>LFM3</i> 186
B.14.	Illustration of a Baseband Signal Spectrum. 186
B.15.	Illustration of the Spectra for DSB-SC and SSB-SC Signals. 187
B.16.	Comparison of Measured (DSB-SC) and Simulated (DSB-SC) Data: <i>OFDM4</i> and <i>LFM3</i> 188
B.17.	DSB-SC and SSB-SC Comparison: LFM Signal. 189
B.18.	Comparison of Measured (SSB-SC) and Simulated (SSB-SC) Data: <i>OFDM4</i> and <i>LFM3</i> 190
B.19.	Target Measurement Configuration. 191
B.20.	Comparison of Measured (DSB-SC) and Simulated (DSB-SC) Data: <i>LFM4</i> with Targets. 192
B.21.	Comparison of Measured (DSB-SC) and Simulated (DSB-SC) Data: <i>OFDM4</i> and <i>LFM1</i> with Targets. 192
B.22.	Comparison of Measured (DSB-SC) and Simulated (DSB-SC) Data: <i>OFDM4</i> and <i>OFDM1</i> with Targets. 193
B.23.	Measured Data: Adding Two Signals and Their Complements. 194
C.1.	Rectangular Aperture Geometry. 204
C.2.	Optical Array Geometry. 208

List of Tables

Table		Page
2.1.	CFA Simulation Parameters	31
2.2.	OFDM Simulation Parameters	49
2.3.	FDA Simulation Parameters	57
4.1.	Signal Measurement Parameters: Single-Chip Signals	94
6.1.	Comparison Simulation Parameters	121
6.2.	Summary of Results.	140
B.1.	Circuit Components.	172
B.2.	Antenna Dimensions.	174
B.3.	Signal Measurement Parameters: Binary, Phase Coded Signals	180
B.4.	Signal Parameters: Binary, Phase Coded Signals	181
B.5.	Signal Measurement Parameters: Single-Chip Signals	183
B.6.	Signal Parameters: Single Chip, Single Frequency Signals	184
B.7.	Signal Parameters: Single Chip, OFDM Signals	184
B.8.	Signal Parameters: Single Chip, LFM Signals	185
C.1.	1D Fourier Transform Properties	198
C.2.	1D Fourier Transform Pairs	198
C.3.	2D Fourier Transform Properties	202

List of Symbols

Symbol		Page
$\bar{\mathbf{r}}$	Displacement Vector	18
r	Range	19
θ	Azimuth Angle	19
ψ	Elevation Angle	19
$\hat{\mathbf{k}}$	Direction Vector	19
c_0	Speed of Light	20
f	Frequency (Hertz)	20
λ	Wavelength.....	20
k	Wavenumber	20
ω	Frequency (radians per second)	20
$\bar{\mathbf{k}}$	Wave Vector	21
P	Number of Array Transmit Elements.....	21
$\Delta d_{\hat{y},t}$	Transmit ULA Inter-element Spacing	21
p	Transmit Element Index	21
$\bar{\mathbf{d}}$	Array Element Displacement.....	21
L	Aperture Length	22
Q	Number of Array Receiver Elements	22
q	Receive Element Index	23
\tilde{a}_p	Complex Signal Weight	23
A_p	Signal Amplitude	24
φ_p	Signal Phase.....	24
$\hat{b}(t)$	Chip Envelope	24

Symbol		Page
T_c	Chip Duration	24
K_{tx}	One-way Propagation, Signal Amplitude, Scale Factor	24
τ	Propagation Delay	25
$\tilde{\mathbf{a}}$	Vector of Complex Signal Weights	26
$\tilde{\mathbf{w}}_{tx}$	Transmit Array Manifold Vector	26
u	Sine of the Azimuth Angle	26
$D_P(\cdot)$	Modified Dirichlet Kernel	28
ξ	Normalized Azimuth Angle Parameter	33
$r(t)$	Received Signal	37
$x(t)$	Demodulated Received Signal	37
$\tilde{\mathbf{x}}(t)$	Vector of Demodulated Received Signals	37
$h(t)$	Impulse Response	37
$y(t)$	Processed Signal	37
ν	Doppler Frequency (rad/s)	40
v_t	Target Velocity Relative to the Radar	41
BW_s	Signal Bandwidth	41
α	Doppler Scale Factor	42
T_s	Total Pulse Duration	42
$\bar{\mathbf{r}}_t$	Target Displacement	43
$\bar{\mathbf{v}}_t$	Target Velocity	43
Ξ_t	Set of Target Parameters.	43
$\tilde{n}(t)$	Signal Noise After Quadrature Demodulation	44
$\tilde{s}_p(t)$	Complex Baseband Representation of Transmit Signal	44

Symbol		Page
δ_τ	AF Mainlobe Width in Delay	47
δ_ν	AF Mainlobe Width in Doppler	47
δ_u	AF Mainlobe Width in Angle	47
B	Total Number of Sub-carriers	48
Δf	Differential Frequency Offset	48
M	Number of Temporal Chips in a Pulse	48
L_s	Synthetic Aperture Length	54
$\bar{\mathbf{R}}(t)$	SAR Platform Position	54
N	Number of Pulses in a CPI	77
T_p	Pulse Repetition Interval	77
f_p	Pulse Repetition Frequency	77
ϑ	Chirp Rate	78
BW_ϑ	Chirp Bandwidth	78
$\tilde{\Upsilon}$	Set of Signal Parameters	78
\bar{y}	Transform Domain Corresponding to u	90
$\Delta d_{\hat{y},r}$	Receive ULA Inter-element Spacing	99
ρ	Radial dimension in the Fourier transform domain.	203
ϕ	Azimuth angle in the Fourier transform domain	203
$\mathcal{H}_k\{\cdot\}$	Hankel Function of order k	203
$J_k(\cdot)$	k th-order Bessel function of the first kind	203

List of Abbreviations

Abbreviation		Page
IW	Irregular Warfare	1
ISR	Intelligence, Surveillance and Reconnaissance	1
SAR	Synthetic Aperture Radar	3
GMTI	Ground Moving Target Indication	3
STAP	Space-Time Adaptive Processing	3
MIMO	Multiple-Input, Multiple-Output	3
FD	Frequency Diversity	3
FDA	Frequency Diverse Array	3
RF	Radio Frequency	3
US	United States	3
JORN	Jindalee Operational Radar Network	3
SNR	Signal-to-Noise Ratio	5
CFA	Constant Frequency Array	7
AF	Ambiguity Function	9
CEM	Computational Electromagnetic	16
DOA	Direction-of-Arrival	18
RSC	Radar Spherical Coordinates	18
LOS	Line-of-Sight	19
ULA	Uniform Linear Array	21
DFT	Discrete Fourier Transform	33
FNBW	First-Null Beamwidth	35
HPBW	Half-Power Beamwidth	35

Abbreviation		Page
TBP	Time-Bandwidth Product	49
LFP-FDA	Linear Frequency Progression, Frequency Diverse Array	52
CBA	Convolution Backprojection Algorithm	56
PSF	Point Spread Function	65
CPI	Coherent Processing Interval	76
PRI	Pulse Repetition Interval	77
PRF	Pulse Repetition Frequency	77
LFM	Linear Frequency Modulation	78
DSB-SC	Double Sideband - Suppressed Carrier	92
SSB-SC	Single Sideband - Suppressed Carrier	92
RCS	Radar Cross Section	101
PSL	Peak Sidelobe Level	115
VISA	Virtual Instrument Software Architecture	167
RFE	Receiver Front End	175
FIR	Finite Impulse Response	177

FREQUENCY DIVERSE ARRAY RADAR:
SIGNAL CHARACTERIZATION AND MEASUREMENT ACCURACY

I. Introduction

1.1 Research Motivation

The emergence of Irregular Warfare (IW) in addition to conventional warfare has changed how modern militaries strategically prepare for future conflicts. IW is defined in [44] as “a violent struggle among state and non-state actors for legitimacy and influence over the relevant populations.” Those who employ IW tactics favor indirect approaches, can potentially incorporate conventional tactics, and, aim to erode their adversary’s power, influence and will. The modern war is intelligence-intensive and fusion of intelligence from different sources is required to provide timely, accurate and relevant information to all command levels [44] through interoperability of Intelligence, Surveillance and Reconnaissance (ISR) capabilities [45]. Current, monolithic ISR systems were designed to provide superiority in conventional warfare but lack the persistence and flexibility required for IW threats – layered sensing is one approach that may address this problem.

Tailored integration of ISR capabilities is characterized by layered sensing and the concept is illustrated in Fig. 1.1 from an Air Force perspective. Layered sensing is a vision for future ISR capabilities [10] that may provide decision makers with the necessary information to maintain situational awareness in an IW scenario. A challenging layered sensing requirement is that it should be [10] “robust, agile and adaptable by incorporating automatic sensing into ISR networks that allow the networks to reflex-

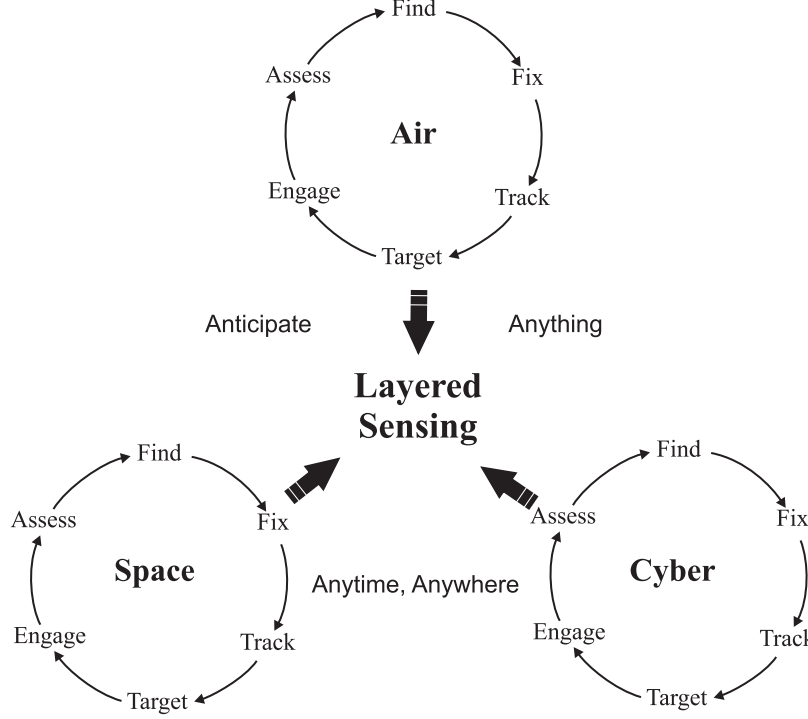


Figure 1.1. Layered Sensing Topology. Layered sensing integrates air, space and cyber-space ISR capabilities. Adapted from [37].

ively optimize themselves based on changes to the sensing environment.” The primary goal is surveillance superiority through persistence, using existing monolithic ISR capabilities supplemented with smaller, low-cost sensors; and is expected to achieve greater ISR superiority than investing in more powerful and more advanced monolithic ISR platforms. The requirement encourages a cross-disciplinary and imaginative approach to ISR capability development. However, there are currently few solutions to the myriad of technical challenges posed by modern ISR needs.

One project aiming to address a subset of technical challenges posed by layered sensing is the Sensors-as-Robots project. The problem description [3] states the USAF’s science and technology vision is to to “anticipate, find, fix, track, target, engage and assess anything, anytime, anywhere”. The project aims to deploy constellations of low-cost, autonomous sensors to collect and process data. Then, using advanced signal processing techniques and knowledge-based algorithms the Sensors-

as-Robots proposes to improve ISR performance with respect to inter-sensor interference rejection, target detection, identification and tracking. Waveform diversity is described in [3] as an important radar signal and system design approach that potentially enables both Sensors-as-Robots and layered sensing scenarios. Recent research is quoted as having incorporated transmit waveform adaptivity for multi-mode, multi-mission applications such simultaneous Synthetic Aperture Radar (SAR) and Ground Moving Target Indication (GMTI) through Space-Time Adaptive Processing (STAP). Two potential benefits of waveform diversity are the ability to employ a single asset to perform simultaneous ISR missions using monolithic platforms; and the ability to provide the persistent surveillance using the low-cost autonomous sensors.

Waveform diversity generalizes radar system signal design by leveraging spatial, temporal, polarization and frequency diversity. Waveform diverse system design and analysis presents a high-order multi-dimensional problem. Currently popular waveform diversity topics include Multiple-Input, Multiple-Output (MIMO) systems with Frequency Diversity (FD), Frequency Diverse Array (FDA) and Radio Frequency (RF) tomography [3]. Exploiting higher signal dimensionality is a logical step toward developing more advanced radar signal schemes for use in layered sensing, and an important key to improving existing ISR capabilities.

ISR capability is not only of interest to the United States (US). For example, one component of Australia’s strategic vision for ISR capability development [2] is to improve regional situational awareness by advancing methods that integrate information collected by currently fielded sensor systems. Long-range surveillance capabilities are key in protecting Australia’s northern approaches and radar surveillance systems play a critical role. One example of an Australian radar system that could be considered a MIMO system is the Jindalee Operational Radar Network (JORN). The network is a large and sophisticated radar system based on high frequency over-the-

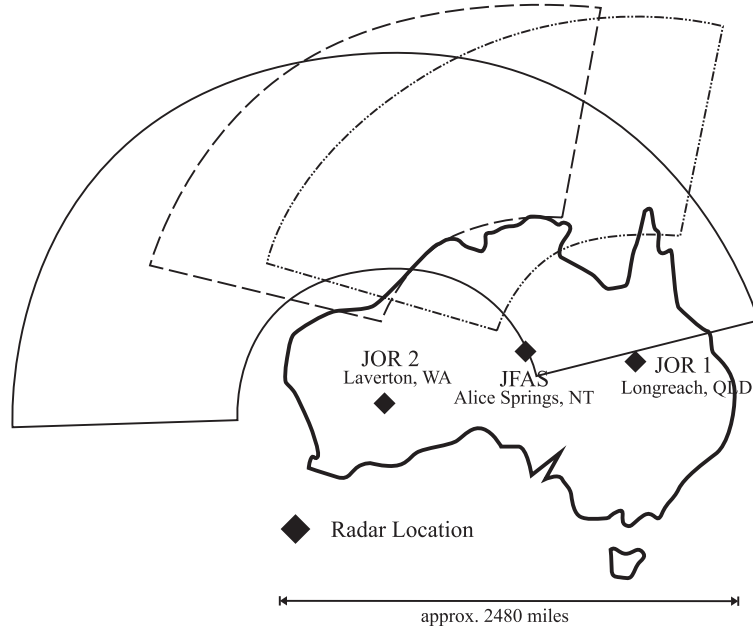


Figure 1.2. JORN's primary radar sites. Adapted from [12].

horizon radar technology consisting of two primary sites shown as JOR1 and JOR2 in Fig. 1.2. The JFAS site is a research radar that can be switched into the JORN network as required. The JORN design consists of a receiver array over 3km long and the high-band transmit array has 28 elements fed by 20kW solid state amplifiers. The system is supported by numerous ionospheric sounding sites located around Australia to measure the atmospheric propagation channel. The network has an operational range between 1000km and 3000km [12].

Given future remote sensing requirements, the level of global interest, and despite the imagination, creativity and best efforts of ISR technology developers, layered sensing remains elusive. The impending technical challenges span most scientific fields and include sensor fusion, inter-platform communications and networking, information management, command and control, countermeasures, sensor technology and signal processing [10]. Maturing waveform diverse technology will be an important contribution to the realization of layered sensing systems. The frequency aspect of waveform diverse signal design research has received comparatively little attention in

the contemporary literature. The goal of this study is to examine waveform diversity using the FDA framework.

1.2 Problem Description

Waveform diverse radar system design requirements can be derived from the layered sensing framework discussed in the previous section. For example, the requirement that sensor systems should be inter-operable, implies that after combining the diverse set of data the resulting information is “better” in some respect than using a single sensor system. It is proposed that in radar signal design, “better” is improved target detection, target parameter estimation or image quality. Methods to coherently combine signals collected by a single sensor are well established in the literature.

Coherent signal integration has been a cornerstone of radar signal processing to improve target detection and target parameter estimation. The underlying principle is to improve performance by increasing the Signal-to-Noise Ratio (SNR). Specific coherent pulse integration techniques all rely on some manner of coherent signal addition and examples are readily found in the phased-array, STAP, SAR, FDA and MIMO signal processing literature. Current research is addressing how to coherently combine data collected by disparate systems to either detect targets and estimate their parameters, or to perform imaging. However, a major challenge is how to design and analyze multi-dimensional, waveform diverse systems.

Waveform diversity can improve radar functional performance either by optimizing the set of transmitted signals and/or by applying advances in radar signal processing to the received signals. Transmit signal optimization requires that the system’s performance is well defined in terms of the signal’s temporal, spectral, polarization and spatial signal characteristics. The fundamental spatial-temporal-spectral signal properties need to be understood in order to develop sophisticated waveform design

and signal processing techniques that can leverage the diversity.

Researchers are currently addressing highly diverse signal and system characterization in the literature but the specialty is far from mature. To persist with the traditional analytic approaches to radar design, which are primarily based on geometric analysis, will require restriction of the system's degrees-of-freedom to manage the increased analytic complexity. Such constraints are not conducive to studying waveform diversity. Recently reported FDA research uses a configuration that is constrained spatially, temporally and spectrally, with no polarization diversity. Without measured or experimental data, the constraints were necessary to derive the analytic models.

Constrained FDAs have been used to show improved performance in theoretical SAR [16] and GMTI [7] application studies, but more recently the analytic signal model has been verified both experimentally and by using high fidelity electromagnetic modeling. It is believed that several constraints that were imposed in previous FDA studies can now be relaxed so that arbitrary waveforms can be used with the FDA signal model.

There is significant scope to extend either the SAR or the GMTI applications using the constrained FDA signal model; however, the scope's limits will rapidly be reached because of the model constraints. Alternately, the effort to search for optimal, generalized FDA configurations (frequency allocation, number of transmitters and receivers, spatial distribution of sensors, waveform coding) without system optimization would be a pot-luck process. There is adequate justification to continue researching waveform diversity using the FDA; however, it is prudent to first consider a generalized model and associated analytic techniques to guide future efforts.

1.3 Research Hypothesis and Scope

This research aims to both characterize the FDA signal model, and address whether the generalized FDA improves fundamental measurement accuracy. The research is important, because when frequency diversity is applied to the array's signal model, traditional array analysis and design techniques become extremely difficult to use, if not completely ineffective. As a result, there are currently few techniques available to analyze FDA radar performance, and the only approach to designing these radar systems is through trial-and-error.

A generalized FDA model is specified that can model amplitude, phase, frequency and chirp-coded signals. Each array element is capable of transmitting a unique baseband signal, but all baseband signals transmitted from the array are modulated by a common local oscillator signal. The signal reflected from a target is collected and processed by all receiver elements. This is distinct from previous FDA research, which assumes that different local oscillators feed each of the transmit elements, and only a subset of the received signals are used in subsequent processing. A two channel radar system capable of transmitting and receiving the arbitrary waveforms is built, and data collected using the hardware system is used to validate the simulated transmit and receive signals.

Constant Frequency Array (CFA) theory characterizes an array's transmit waveform by the peak transmit power and the array factor. The array factor is a spatial signal characterization that describes how the transmit signal's power is spatially distributed, the width of the mainlobe, and the height of the sidelobes. The mainlobe width is closely related to the array's angular resolution. Previous FDA research derives an approximate, closed-form expression for the FDA's spatial-temporal transmit signal, which is called the array factor. It is claimed that the expression completely characterizes the transmit waveform, however, there are two deficiencies in the char-

acterization. First, the array factor is only derived for a FDA with linear frequency progression, which is a special case of the generalized FDA signal. Second, characteristics embodied by the array factor are not considered in the previous research, such as the transmit power's spatial distribution and angular resolution. Because of the incomplete characterization, it is difficult to compare the FDA's performance to other configurations.

An array factor can be used to approximately describe a highly constrained FDA, however, constraining the FDA to facilitate analysis limits the design choices. Instead, it is proposed that the transmit signal characteristics described by the array factor, such as the angular resolution and spatial power variation, are better characterized using the fundamental equations for average power and angular resolution. Using the generalized signal model in the fundamental equations, general expressions for the average power and angular resolution are derived. When the expressions are simplified for the case of a CFA, the expressions are shown to match the CFA theory.

Analyzing the FDA's transmit signal in space and time may not be the best approach for FDA analysis, because the FDA model represents a space-time-frequency coded signal. Instead of approaching the analysis using methods such as the array factor, a two-dimension Fourier transform is developed which relates a linear array's space-frequency coding to the transmitted signal field pattern. The transform is applied to the expression for the generalized FDA transmit signal field, and the resulting spectrum clearly shows the array's size and the signal's bandwidth limits.

It seems that a focus of previous FDA research is directed to the transmit signal. However, any benefit of the space-time-frequency coding will be realized in the radar receiver and subsequent signal processing. The SAR and STAP applications used different receiver designs, for example, the SAR application used a single antenna to collect the scattered signal and did not use a matched filter receiver prior to

forming the SAR image. In contrast, the STAP application collected the signals using all of the array elements and match filtered the signals, but the design assumes that each element is responsive only to the frequency it transmits. Even though both applications reported performance improvements, they fail to make use all the information contained in the received signal.

To develop a foundation from which to explore more advanced receiver designs, a matched filter structured is considered for processing the set of received FDA signals scattered from an ideal point target. The structure is based on an array of receivers collecting the entire received signal, each received signal is matched filtered, and the outputs from the set of receivers are combined. An expression for the receiver's Ambiguity Function (AF) is derived, which predicts the receiver's output when the filter structure is imperfectly matched to the target parameters. The width of the AF's mainlobe is the standard metric used to characterize a signal's range, angle and velocity measurement accuracy.

Finally, several FDA designs are evaluated using the AF to determine whether the space-time-frequency coding improves fundamental measurement accuracy. The SAR application study showed that cross-range resolution can be improved using an FDA configuration which suggests that the FDA should improve angular resolution. The AF for each linear array design is evaluated numerically, and the mainlobe widths are compared to a CFA with similar array size and bandwidth. It is shown that the fundamental measurement accuracy using standard processing is limited by the array size and signal bandwidth. However, it is shown that by exploiting the space-time-frequency coding there may be methods to suppress range and angle ambiguous sidelobes.

1.4 Thesis Overview

The research is reported over several chapters, each attempting to focus on a different perspective of FDA signal design and analysis. Chapter II reviews theory that was important to the study's development. The review serves three primary purposes, the first is to establish the notation and methods that will be used in subsequent analysis, the second is to justify the validity of the approaches used in this study based on work that the community considers authoritative, and the third is to serve as a primer for future FDA researchers studying SAR applications. Chapter III attempts to connect the literature review in Chapter II to the work developed in subsequent chapters and outlines the methodology applied to the study.

Chapter IV considers a generalized waveform diverse signal model and develops techniques that may be useful to characterize the transmit signal. Spectral analysis based on CFA and Fourier Optics theory is developed for the transmit signal's field which complements the geometrically-based analysis. Next, Chapter V considers the signal collected at a receiver array and examines approximations to the Doppler scaling. The generic matched filter receiver is used to process the set of received signals and the receiver's performance is characterized using the AF. The AF's development follows the approach in the MIMO literature, but modified to incorporate the frequency diversity.

In Chapter VI, the constrained FDA's performance is examined by varying the key parameters and observing the result. The experiment aims to determine whether the FDA's measurement performance is fundamentally limited by aperture size and signal bandwidth. Methods to combine a signal with its spatial complement are presented, one of which is based upon the cross-range resolution improvement technique in the FDA SAR application. Finally, the FDA's parameters are diversified to examine whether randomizing the signal improves either the range or angle measurement

performance. Finally, the research is concluded in Chapter VII with an analysis of the work's results and suggestions for future research.

II. Background

2.1 Chapter Overview

This chapter aims to distill the fundamental theory that provides the foundation to this study. The reviewed material is a balance between traditional array theory and contemporary radar research that influences the research and Fig. 2.1 illustrates how the material supports the research objective. It is assumed the reader is familiar with elementary radar system and signal design concepts covered in texts such as [33] and [42].

The potential benefits of layered sensing and waveform diversity are discussed in this chapter, further justifying why FDA is an important application to study. The review of CFA theory summarizes several techniques and fundamental results that are useful to this study. The traditional AF is then reviewed along with the wideband, Doppler scaled signal model and its narrowband approximation. The ambiguity function was recently extended by the MIMO community to include angular measurement performance and its development is summarized. A brief discussion of Orthogonal Frequency Division Multiplexing (OFDM) follows to highlight its performance characteristics and its similarity to both the CFA and the FDA signal structure. Finally, the FDA research is summarized with particular attention to the SAR application study and suggestions for further research.

2.2 Layered Sensing, Waveform Diversity and Frequency Diverse Arrays

Layered sensing was introduced in Chapter I, now consider the simplified layered sensing scenario presented in Fig. 2.2, where a set of sensors operate in a theater to track a target. Each transmitter is able to transmit a temporally and spectrally diverse set of waveforms and each receiver is able to receive and interpret all signals

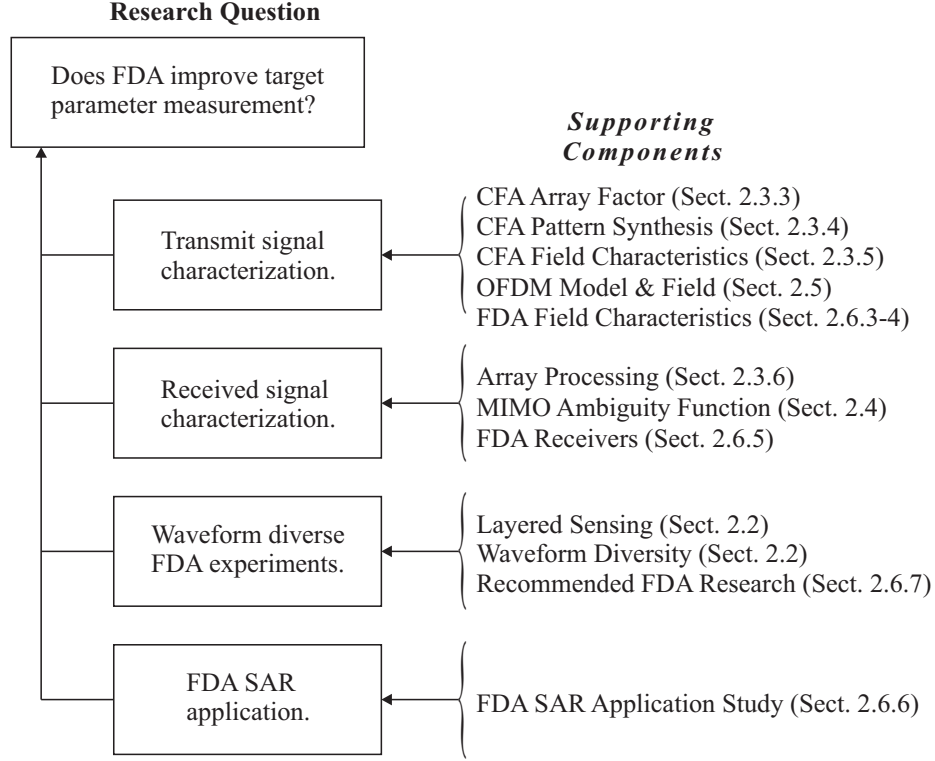


Figure 2.1. Chapter 2’s relation to the research. The research objectives are composed of several components, and each component is partially supported by prior research.

that were transmitted. As the environment and target location changes over time, the sensors adapt their configuration autonomously to maximize the benefit of waveform diversity.

Some sensors may be configured to only transmit, for example a communications transmitter, a non-cooperative source, or a natural source. Some sensors may be configured to only receive, for example a passive electro-optic sensor system or a passive-bistatic receiver such as the system described in [13]. Examples of sensors that both transmit and receive may be representative of more conventional, monolithic sensor platforms. Signals collected by the receivers may be partially processed into data at the receiver; and then, the data may be transformed into information at a processing center. In the future this type of ISR scenario may be realized under the layered sensing paradigm.

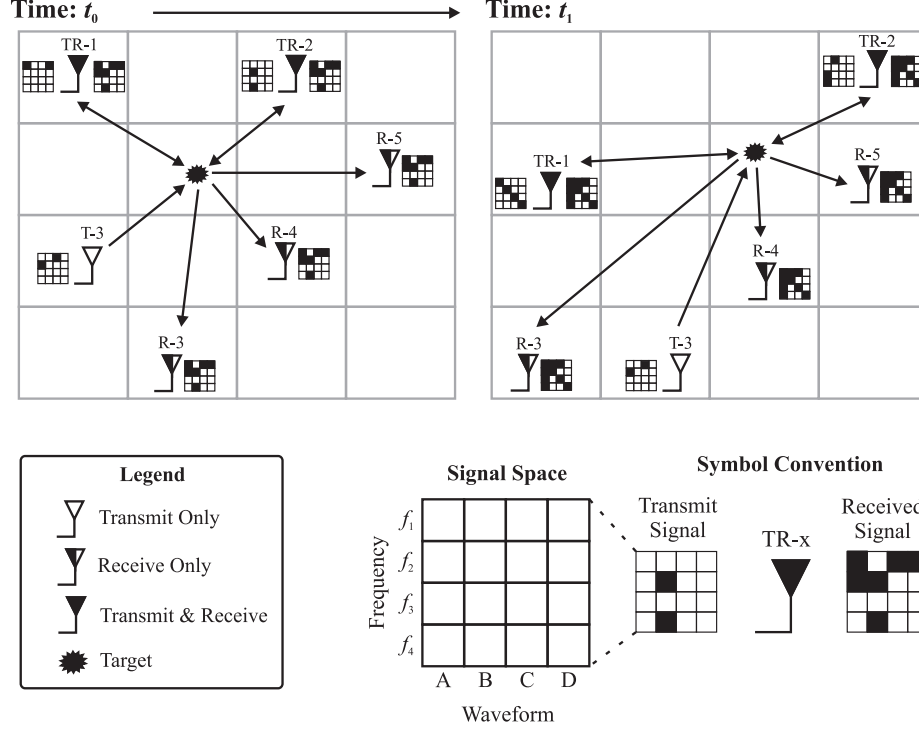


Figure 2.2. Layered sensing model. The diagram depicts a layered sensing scenario where sensor and target configuration change over time. The symbols representing the sensor configuration, defined in the lower portion of the diagram, will be used in diagrams that follow.

It is difficult to imagine the full spectrum of future scenarios; or to envision how layered sensing can be applied to problems that don't currently have a solution. However, some potential scenarios are summarized in [49]. The vision for future surveillance systems includes concepts such as autonomous sensor systems, advanced inter-system communications and sensors that automatically avoid inter-sensor interference. There are many fields being studied that may advance layered sensing such as knowledge-aided processing, programming language and model development, artificial intelligence, communication protocols, computer architectures, software development, and waveform diversity [49]. Advances across all of the aforementioned application areas are required to enable the layered sensing vision.

Waveform diversity will play an important part in the layered sensing model [49]. Waveform diversity was recently given a definition in [1] as “adaptivity of the radar

waveform to dynamically optimize the radar performance for the particular scenario and task”; the definition continues by suggesting that the waveform adaptivity can be performed across the following domains: antenna radiation pattern (spatial domain), time domain, frequency domain, coding domain and polarization domain.

Considering the temporal, spectral, polarization and spatial aspects individually, waveform diversity does not present anything new [48] because most current radar systems use one or more diversity dimensions. The difference in the current interpretation is that contemporary waveform diversity challenges system designers to create novel, high-performance systems by combining as many dimensions as possible into a single design. This adds significant complexity because each dimension added to the radar problem adds one or more extra dimensions to the problem’s solution space.

The FDA framework was chosen for this study after considering the current waveform diversity literature, such as the MIMO radar framework. It seemed that FDA offered insight into spectrally and temporally diverse system design and analysis using constrained spatial diversity. Applying the FDA to problems such as SAR imaging generalizes the constrained array processing to include distributed aperture processing. Therefore, FDA includes most of the dimensions included in the waveform diversity definition except polarization diversity.

FDA is not the only framework used to study this type of problem. There is also similar work occurring in parallel in the MIMO community such as the frequency diverse MIMO (FD-MIMO) research recently reported in [50], [51], and to a certain extent, in [11]. However when this study began, MIMO-related research was dominated by statistical MIMO, which in contrast, is a significantly different approach to traditional radar design.

The original MIMO radar concept was to apply the MIMO communications methods to the radar problem [18]. The general MIMO concept is to determine the

transmit-target-receive path, out of a set of possible transmitter/receiver combinations, yielding the most gain. The highest gain path or channel is selected to transmit the majority of power. A slightly different formulation of MIMO radar, found in statistical MIMO radar, seems to focus on two objectives. The first is to design waveforms that, on average, approximate a beam-pattern design by designing signal parameters in an optimal sense. The second objective is to design signals that maximize the cross-correlation between signals returned by the same target [34] in order to maximize estimation and detection in an optimal sense. Both MIMO perspectives have inspired much research activity along with many claims of superior performance over existing technology.

The claims of MIMO radar’s superior performance are based primarily on theoretical analysis neglecting many real-world effects. An extremely pragmatic comparison of some MIMO radar claims compared to accepted CFA performance was recently presented in [14]. The presentation discusses several areas in which the theoretical MIMO performance may not be reflected in a real system along with several examples where performance may be degraded by using MIMO waveforms. This is not to say MIMO radar will not work in practice at all, merely that in some cases, there seems to be a lack of physical evidence supporting the theoretically-based claims of superiority.

In comparison to the MIMO research, the FDA claims have been more modest because a different methodology has been applied to the early research of conceptual FDA systems. Emphasis has been placed on verifying the field patterns through Computational Electromagnetic (CEM) models and experimentation in addition to application studies. These studies, in addition to continuing research, gradually build the evidence required to answer whether FDA will be useful to the waveform diversity field or to future layered sensing engagements.

The original intent of FDA was consistent with generalized waveform diversity with constrained spatial diversity [5; 6]. It was claimed that an array using multiple diversity dimensions could perform simultaneous missions such as SAR and moving target indication (MTI) despite significantly different signal requirements. Support for this claim, and others, is slowly emerging but they have not been entirely satisfied in the literature.

Despite the original intent, the prevailing FDA research focus is limited to arrays with linear frequency progression (LFP-FDA) along the array using an orthogonal frequency configuration [8; 17; 28; 29; 39; 41]. The benefit of applying the LFP-FDA to SAR and STAP individually was shown in [16] and [8] respectively.

The LFP-FDA signal constraints allowed the transmit signal field pattern to be described by a closed-form equation using geometric analysis from the CFA theory. Lacking either CEM modeling or experimental results, the analysis allowed researchers to verify the expected LFP-FDA behavior under ideal conditions. Since the initial studies, the signal model and the analytic results have been supported by both CEM modeling [16; 28] and experimental results [4]. It is appropriate to now move beyond LFP-FDA and consider more generalized FDA configurations. LFP-FDA research will be summarized later in Section 2.6; the review of CFA theory is presented next.

2.3 Constant Frequency Array Theory

A background to CFA theory is provided here for several reasons. First, methods applied to CFA analysis have been extended LFP-FDA analysis in past research with varying success. It is important to understand CFA theory along with the assumptions and limitations.

Second, CFA could be considered mature – the sheer volume of reference material is testament to the important role it plays in modern radar systems. In contrast to

the more conceptual MIMO and FDA systems, a review of CFA theory provides a good indication of where further work is required in each of the conceptual systems.

Finally, CFA theory offers insight into array design that may be useful for this study. A prime example is the design of the array's complex weights by taking the Fourier transform of the array factor. While this technique is but one of many in CFA theory [9], a similar idea may have great utility in FDA analysis, and possibly FDA design.

In the following review, the geometric and signal models are presented. Simplifications to the signal model are made by using common radar assumptions and approximations. Following the approximations, the signal gives rise to a far-field distribution whose equation is separable in range and angle. The angular component is often called the array factor and its relationship to the element spacing is examined. There are several techniques to design the element weights (amplitude and phase) in order to approximate a desired beam, but the Fourier transform technique is presented and provides a reference for later work.

Once the signal is transmitted, it may reflect from a target and some scattered energy may reach a receiver array. The receiver array can be used to localize a received signal's Direction-of-Arrival (DOA) by filtering and adding the set of received signals. The general linear processor is presented from which the phased array processor (or digital beamformer) is derived.

2.3.1 Geometry

This study uses the geometric model developed in [16] and the relation between the cartesian coordinates and the Radar Spherical Coordinates (RSC) is shown in Fig. 3(a). Geometric vectors are denoted by lowercase, bold font symbols with a bar, and the associated unit vectors distinguished by a hat. The displacement, $\bar{\mathbf{r}}$, of an

arbitrary point in space from the phase reference is:

$$\bar{\mathbf{r}}_0 = \hat{\mathbf{x}}x_0 + \hat{\mathbf{y}}y_0 + \hat{\mathbf{z}}z_0.$$

The displacement can also be represented in the RSC system. The range, r , is the magnitude of the vector and for $\bar{\mathbf{r}}_0$ the range is

$$\begin{aligned} r_0 &= |\bar{\mathbf{r}}_0| \\ &= \sqrt{x_0^2 + y_0^2 + z_0^2}. \end{aligned} \tag{2.1}$$

The azimuth angle, θ , and elevation angle, ψ , to $\bar{\mathbf{r}}_0$ are

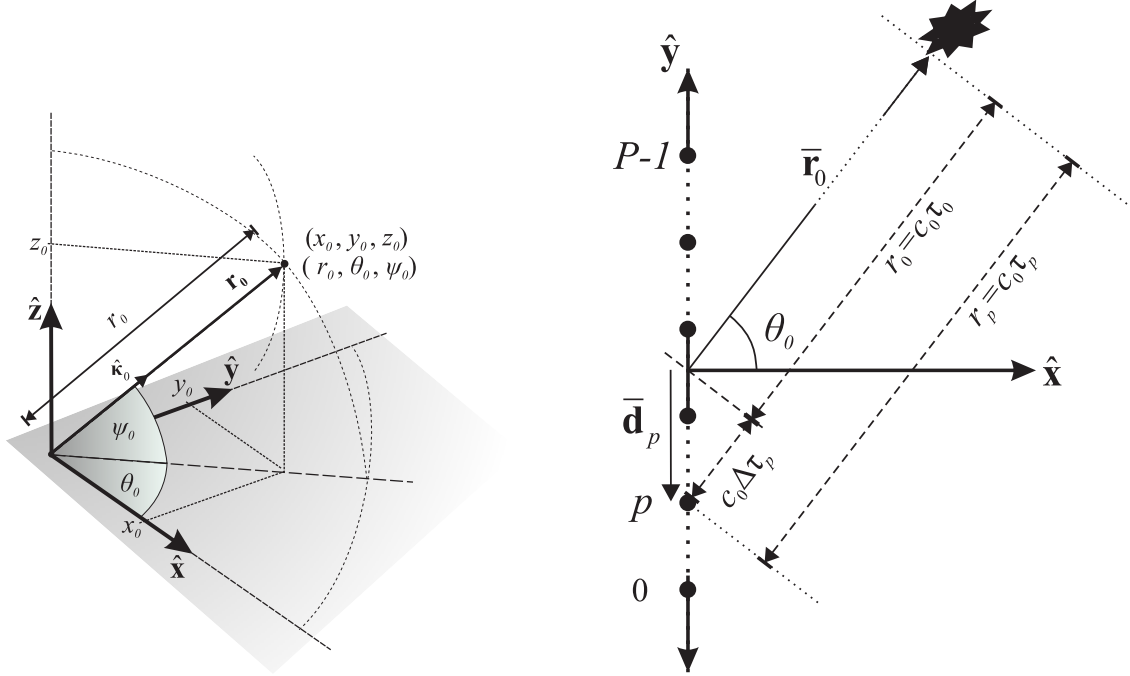
$$\begin{aligned} \theta_0 &= \tan^{-1} \frac{y_0}{x_0} \\ \psi_0 &= \tan^{-1} \frac{z_0}{\sqrt{x_0^2 + y_0^2}}. \end{aligned} \tag{2.2}$$

The Line-of-Sight (LOS) unit vector, $\hat{\boldsymbol{\kappa}}$, collinear with $\bar{\mathbf{r}}_0$ is

$$\begin{aligned} \hat{\boldsymbol{\kappa}}_0(\theta_0, \psi_0) &= \frac{\bar{\mathbf{r}}_0}{\sqrt{x_0^2 + y_0^2 + z_0^2}} \\ &= \hat{\mathbf{x}}\kappa_x(\theta_0, \psi_0) + \hat{\mathbf{y}}\kappa_y(\theta_0, \psi_0) + \hat{\mathbf{z}}\kappa_z(\theta_0, \psi_0), \end{aligned} \tag{2.3}$$

where

$$\begin{aligned} \kappa_x(\theta_0, \psi_0) &= \cos \psi_0 \cos \theta_0 \\ \kappa_y(\theta_0, \psi_0) &= \cos \psi_0 \sin \theta_0 \\ \kappa_z(\theta_0, \psi_0) &= \sin \psi_0. \end{aligned} \tag{2.4}$$



(a) The diagram shows both the standard cartesian coordinates and the radar coordinate including unit vectors.

(b) The diagram illustrates the linear array geometry. The P sensors are arranged along the \hat{y} axis and the phase reference is the array's geometric center. The displacement of the p th sensor is $\bar{\mathbf{d}}_p$. The target's displacement from the phase center is $\bar{\mathbf{r}}_0$ and from the p th sensor is $\bar{\mathbf{r}}_p$.

Figure 2.3. Radar coordinate system and linear array geometry.

The direction vector $\hat{\kappa}_0(\theta_0, \psi_0)$ is a function of the angular coordinates, however, the arguments will not be written unless required for clarity.

A signal transmitted from a sensor located at the origin of the coordinate system will propagate as a spherical, time-harmonic wave at the speed of light, c_0 . Frequency, f , and wavelength, λ , are related through $c_0 = f\lambda$; while the wavenumber, k , is related to frequency and wavelength through $k = \frac{2\pi f}{c_0} = \frac{2\pi}{\lambda}$. For notational convenience, the frequency can also be represented as ω radians per second where $\omega = 2\pi f$. The radar's transmit frequency, associated wavelength and wavenumber are denoted using f_0 (or ω_0), λ_0 and k_0 respectively. Wave propagation at the speed of light is an ideal assumption, but is appropriate in most radar scenarios where the signal is transmitted

through the atmosphere.

A sensor modeled as an ideal point source will produce a wave that is spherically symmetric such that $k_0^2 = k_{x,0}^2 + k_{y,0}^2 + k_{z,0}^2$. The wavevector, $\bar{\mathbf{k}}$, is collinear with $\bar{\mathbf{r}}_0$ in isotropic media and

$$\begin{aligned}\bar{\mathbf{k}}_0 &= k_0(\hat{\mathbf{x}}\kappa_x + \hat{\mathbf{y}}\kappa_y + \hat{\mathbf{z}}\kappa_z) \\ &= k_0\hat{\boldsymbol{\kappa}}_0.\end{aligned}\tag{2.5}$$

Allowing the direction vector $\hat{\boldsymbol{\kappa}}_0$ to vary over all θ and ψ will map out the entire unit sphere. However for a single coordinate θ_0 and ψ_0 , the wavevector $\bar{\mathbf{k}}_0$ represents an infinite plane wave, with wavenumber, k_0 , propagating in the direction of $\hat{\boldsymbol{\kappa}}_0$. Representing the spherical wave using an infinite collection of plane waves is sometimes referred to as a plane wave decomposition [47] because the spherical wave is decomposed by a set of plane wave basis functions [27].

Consider the constant frequency, Uniform Linear Array (ULA) with geometry in Fig. 3(b). The array consists of P ideal elements on the \hat{y} axis with equal inter-element separation $\Delta d_{\hat{y},t}$ and is symmetric about the origin. The sensors are indexed by $p \in [0, \dots, P-1]$. The p th sensor's displacement, $\bar{\mathbf{d}}$, from the phase reference is

$$\begin{aligned}\bar{\mathbf{d}}_p &= \hat{\mathbf{y}}d_p \\ &= \hat{\mathbf{y}}\left(p - \frac{P-1}{2}\right)\Delta d_{\hat{y},t}, \quad 0 \leq p \leq P-1.\end{aligned}\tag{2.6}$$

The displacement to $\bar{\mathbf{r}}_0$ from the p th sensor is

$$\bar{\mathbf{r}}_p = \bar{\mathbf{r}}_0 - \bar{\mathbf{d}}_p.\tag{2.7}$$

Using the far-field approximation (see Appendix A), the distance $|\bar{\mathbf{r}}_p|$ is approximated

by

$$|\bar{\mathbf{r}}_p| \simeq r_0 - \bar{\mathbf{d}}_p \cdot \hat{\boldsymbol{\kappa}}_0. \quad (2.8)$$

In the CFA literature, an array is considered to be a sampled approximation to a continuous aperture which has a length, L , of [47]

$$L_P = P\Delta d_{\hat{y},t}. \quad (2.9)$$

Note that the length of the continuous aperture is longer than the distance between the end elements of the array by an additional factor of $\Delta d_{\hat{y},t}$.

For an array with a maximum dimension L_p , the far-field approximation is appropriate providing the following conditions are met [35]

$$r_0 > 10L_p, \quad \{\text{Amplitude Condition}\}, \quad (2.10)$$

and

$$r_0 > \frac{2L_p^2}{\lambda_0}, \quad \{\text{Phase Condition}\}. \quad (2.11)$$

The approximation enables the CFA signal's range component and the angular component to be separated and greatly simplifies the analysis.

Next consider the ULA receiver array's geometry. It is centered about the phase reference; however, it may have a different number of elements and possibly different inter-element spacing. Let Q be the total number of elements in the receiver array where the elements are indexed by $q \in \{0, \dots, Q-1\}$ with equal inter-sensor spacing

$\Delta d_{\hat{y},r}$. The q th receive element is located at

$$\bar{\mathbf{d}}_q = \hat{\mathbf{y}} d_q \quad (2.12)$$

$$= \hat{\mathbf{y}} \left(q - \frac{Q-1}{2} \right) \Delta d_{\hat{y},r}. \quad (2.13)$$

Similarly, the displacement to $\bar{\mathbf{r}}_0$ from $\bar{\mathbf{d}}_q$ is

$$\bar{\mathbf{r}}_q = \bar{\mathbf{r}}_0 - \bar{\mathbf{d}}_q, \quad (2.14)$$

and using the far-field approximation the distance is

$$|\bar{\mathbf{r}}_q| \simeq r_0 - \bar{\mathbf{d}}_q \cdot \hat{\boldsymbol{\kappa}}_0. \quad (2.15)$$

For a linear array with ideal elements placed along the \hat{y} -axis, the transmitted field is symmetric about the \hat{y} -axis. Analysis of the field on any plane containing the \hat{y} -axis is sufficient to describe the field in all planes containing the \hat{y} -axis [9]. For the analysis that follows, the $\hat{z} = 0$ plane is implied unless stated otherwise.

2.3.2 Signal Model

Figure 2.4 illustrates the CFA transmit configuration using the symbols introduced in Section 2.2. The CFA transmits a single tone, narrowband signal $s_0(t)$ modulated by a set of complex weights \tilde{a}_p . The signal transmitted by the p th element is

$$\begin{aligned} s_p(t) &= \tilde{a}_p s_0(t) \\ &= \tilde{a}_p \hat{b}(t) \exp(j\omega_0 t) \end{aligned} \quad (2.16)$$

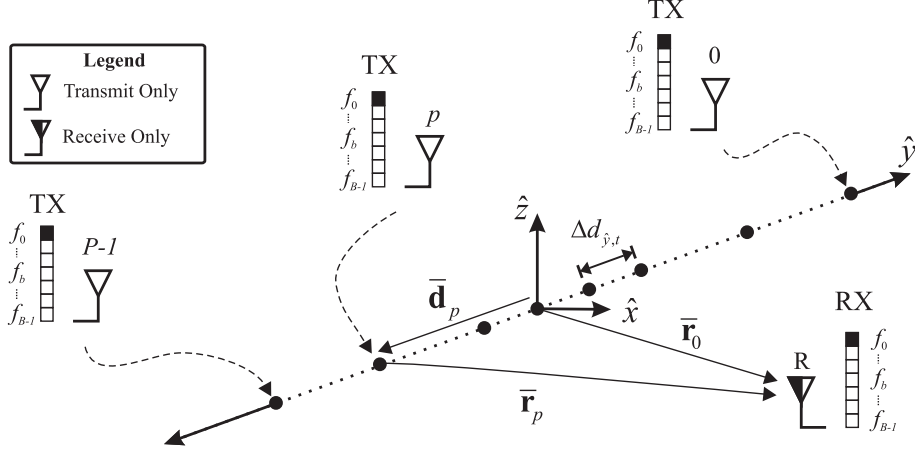


Figure 2.4. Transmit configuration: CFA. The diagram indicates the array's element locations and the signals applied to the elements. The transmit signal model represents the signal collected by a receiver located at $\bar{\mathbf{r}}_0$.

where the p th signal's complex weight has amplitude A_p , phase φ_p

$$\tilde{a}_p = A_p \exp(j\varphi_p), \quad (2.17)$$

and a unit amplitude pulse envelope $\hat{b}(t)$, with duration T_c seconds, given by

$$\hat{b}(t) = \begin{cases} 1, & 0 \leq t \leq T_c \\ 0, & \text{otherwise.} \end{cases} \quad (2.18)$$

Assuming ideal transmission, the signal that would be received by an ideal antenna located at $\bar{\mathbf{r}}_0$ is proportional to

$$\begin{aligned} s(t, \bar{\mathbf{r}}_0) &= K_{tx} \sum_{p=0}^{P-1} s_p(t - \tau_p) \\ &= K_{tx} \sum_{p=0}^{P-1} \tilde{a}_p \hat{b}(t - \tau_p) \exp[j(\omega_0 t - \omega_0 \tau_p)]. \end{aligned} \quad (2.19)$$

Where K_{tx} accounts for the amplitude scaling due to one-way propagation predicted by the Friis transmission equation. The scaling is not important to the study and it

is assumed $K_{tx} = 1$ for convenience. The p th signal's delay, τ , is

$$\tau_p = \frac{|\bar{\mathbf{r}}_0 - \bar{\mathbf{d}}_p|}{c_0}, \quad (2.20)$$

and applying the far-field approximation Eq. (2.20) is

$$\begin{aligned} \tau_p &\simeq \frac{r_0}{c_0} + \frac{\bar{\mathbf{d}}_p \cdot \hat{\boldsymbol{\kappa}}_0}{c_0} \\ &\simeq \tau_0 + \Delta\tau_p. \end{aligned} \quad (2.21)$$

The first component, τ_0 , is the propagation delay from the phase reference to $\bar{\mathbf{r}}_0$, and the second component, $\Delta\tau_p$, is the propagation time from $\bar{\mathbf{d}}_p$ to the phase reference in the direction of $\hat{\boldsymbol{\kappa}}_0$. The geometric interpretation of these symbols are indicated in Fig. 3(b).

Substituting Eq. (2.21) into Eq. (2.19) yields

$$s(t, \bar{\mathbf{r}}_0) = \sum_{p=0}^{P-1} \tilde{a}_p \hat{b}(t - \tau_0 - \Delta\tau_p) \exp[j\omega_0(t - \tau_0 - \Delta\tau_p)]. \quad (2.22)$$

To factor Eq. (2.22) into the familiar phased array form, the narrowband array approximation is applied. The narrowband approximation assumes that $T_c \gg \Delta\tau_p \quad \forall p$ leading to

$$\hat{b}(t - \tau_0 - \Delta\tau_p) \simeq \hat{b}(t - \tau_0). \quad (2.23)$$

Applying the approximation to Eq. (2.22), and factoring out the common signal element, the signal becomes separable in the range-time dimension and the azimuth

angle dimension

$$\begin{aligned}
s(t, \bar{\mathbf{r}}_0) &= b(t - \tau_0) \exp(j\omega_0 t - jk_0 r_0) \sum_{p=0}^{P-1} \tilde{a}_p \exp(jk_0 d_p \sin \theta_0) \\
&= s_0(t - \tau_0) \sum_{p=1}^P \tilde{a}_p \exp(jk_0 d_p \sin \theta_0).
\end{aligned} \tag{2.24}$$

It can also be convenient to represent Eq. (2.24) using signal vector notation [47]. The use of the manifold vector appears frequently in the literature because it allows the operations in Eq. (2.24) to be represented compactly. The signal becomes

$$s(t, \bar{\mathbf{r}}_0) = s_0(t - \tau_0) \tilde{\mathbf{a}}^T \tilde{\mathbf{w}}_{tx}(u), \tag{2.25}$$

where $(\cdot)^T$ is the transpose operation, and bold font letters with a tilde distinguish signal vectors from geometric vectors. The vector $\tilde{\mathbf{a}}$ is the set of signal weights

$$\tilde{\mathbf{a}} = [\tilde{a}_0, \dots, \tilde{a}_p, \dots, \tilde{a}_{P-1}]^T, \tag{2.26}$$

the vector $\tilde{\mathbf{w}}_{tx}$ is referred to as the array's manifold vector [47]

$$\begin{aligned}
\tilde{\mathbf{w}}_{tx}(u) &= [\tilde{w}_0, \dots, \tilde{w}_p, \dots, \tilde{w}_{P-1}]^T \\
&= [\exp(jk_0 d_0 u), \dots, \exp(jk_0 d_p u), \dots, \exp(jk_0 d_{P-1} u)]^T,
\end{aligned} \tag{2.27}$$

and $u = \sin \theta_0$. Representing $\sin \theta_0$ by u linearizes the azimuth angle dimension and representing a signal with a functional dependence on u is called the u -space representation [47]. The domain $-1 \leq u \leq 1$ is called the visible region because it is the only region of u -space that maps to real values of θ . The region is a one-to-one mapping to $\theta_0 \in \{-\frac{\pi}{2}, \frac{\pi}{2}\}$.

The amplitude of the array's far-field signal distribution has a constant range en-

velope for a given angle and the amplitude varies with azimuth angle. This motivates the use of the array factor to describe the distribution which is discussed next.

2.3.3 Array Factor

The theory related to the CFA's array factor is well known and can be found in many array-related texts. There are several reasons that an overview is provided in this section. First, there are several array concepts discussed in subsequent sections that require a basic understanding of the array factor and the review provides a reference for the subsequent material. Second, there are implementation considerations which impact CFA design that are directly related to the array factor such as grating lobes. Finally, the array factor arises in discussion of the CFA's performance measures such as transmit power and beamwidth (both on transmit and receive). An analytic array factor has been derived for the FDA with linear frequency progression, but an analytic array factor will not be possible for most generalized FDA configurations. Other methods of describing the FDA's performance will be required; however, the methods will be related to the array factor theory.

The array factor allows a simple representation of the transmitted CFA far-field signal distribution in azimuth angle which is independent of range. The functional behavior depends primarily on the array weights $\tilde{\mathbf{a}}$, the operating frequency and the element locations inherent in the manifold vector $\tilde{\mathbf{w}}_{tx}(u)$. The element weights and locations can also be designed to approximate a desired field distribution [9] and two design methods are discussed later.

The summation term in Eq. (2.24) is called the array factor [9] which is defined for the transmitter as

$$\text{AF}_P(u) \triangleq \sum_{p=0}^{P-1} \tilde{a}_p \exp(jk_0 d_p u). \quad (2.28)$$

For constant frequency ULAs the array factor is only a function of azimuth angle because the range component is constant for any angle. In the simplest case, the array transmits the same signal from each element, such that $\tilde{a}_p = 1$, and the elements are uniformly distributed along the $\hat{\mathbf{y}}$ -axis symmetric about the origin. Using the partial geometric sum formula [25]

$$\sum_{l=0}^n a^l = \frac{1 - a^{n+1}}{1 - a}, \quad a \neq 1, \quad (2.29)$$

it is straightforward to show that Eq. (2.28) is

$$\begin{aligned} \text{AF}_P(u) &= \frac{\sin\left(\frac{P}{2}k_0\Delta d_{\hat{\mathbf{y}},t}u\right)}{\sin\left(\frac{1}{2}k_0\Delta d_{\hat{\mathbf{y}},t}u\right)} \\ &= PD_P(k_0\Delta d_{\hat{\mathbf{y}},t}u), \end{aligned} \quad (2.30)$$

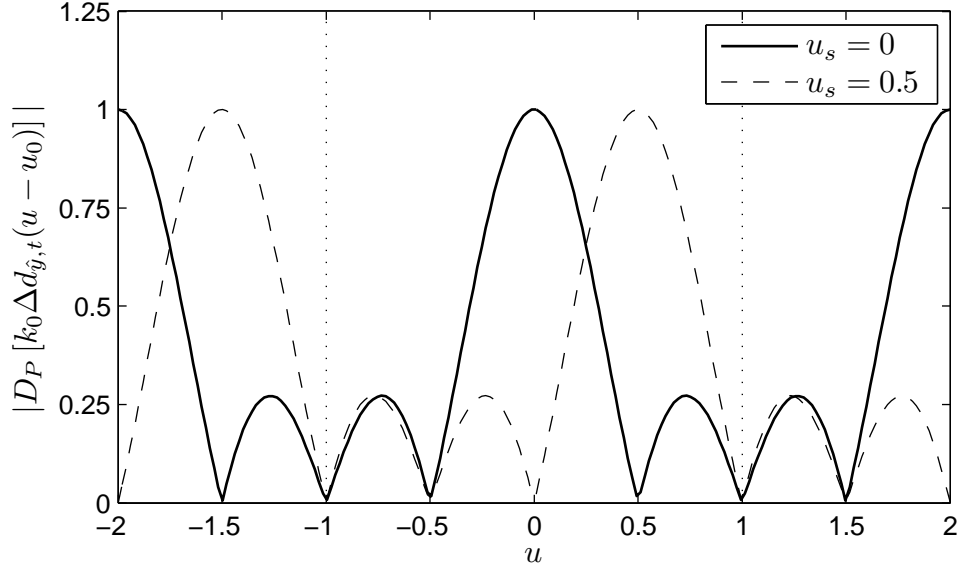
where $D_P(\cdot)$ is a form of the Dirichlet kernel [15]. The kernel arises in discrete time-frequency analysis, in which slightly different notation is used, but here the modified function is defined as

$$D_P(x) \triangleq \frac{\sin\left(\frac{P}{2}x\right)}{P \sin\left(\frac{1}{2}x\right)}. \quad (2.31)$$

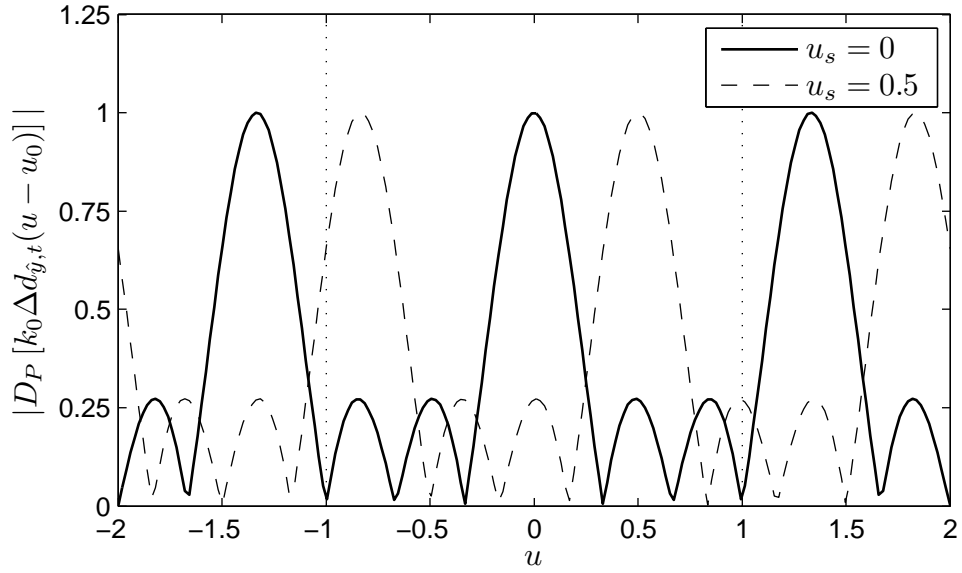
For arbitrary configurations, either Eq. (2.28) is used directly or the vector representation can be used to calculate the array factor over u

$$\text{AF}_P(u) = \tilde{\mathbf{w}}_{tx}(u)^T \tilde{\mathbf{a}}. \quad (2.32)$$

An important feature of the CFA is the ability to steer the beam to desired squint angles which focuses energy along the line-of-sight (LOS). This beam is steered by applying a linear phase progression across the array's weights \tilde{a}_p such that for a squint



(a) The CFA array factor in u -space for $P = 4$ and $\Delta d_{\hat{y},t} = \frac{\lambda_0}{2}$ with a mainlobe directed broadside (solid line). When the array is directed to $u_s = 0.5$ (dashed line) there is still a single mainlobe in the visible region.



(b) The CFA array factor in u -space for $P = 4$ and $\Delta d_{\hat{y},t} = \frac{3\lambda_0}{4}$ with a single mainlobe directed broadside (solid line). When the array is directed to $u_s = 0.5$ (dashed line) there are two mainlobes in the visible region.

Figure 2.5. CFA array factors. The CFA array factor for equal sensor spacing and constant, unit amplitude.

angle $u_s = \sin \theta_s$ the element weights are

$$\tilde{a}_p = \exp(-jk_0 d_p u_s). \quad (2.33)$$

The linear phase progression causes the array factor to shift by u_s in u -space. Examples of the array factor for $\tilde{a}_p = 1$, for two different element spacings and for a shift of $u_s = 0.5$ are shown in Fig. 2.5.

In Fig. 5(a) the element spacing is $\Delta d_{\hat{y},t} = \lambda_0/2$, and within the visible region there is a single main lobe. For this spacing, the array can be squinted to any angle with only a single primary lobe in the visible region. This element spacing is the upper limit to prevent grating lobes.

Grating lobes are multiple main lobes in the array factor, have equal amplitude to the mainlobe and are typically undesirable. When the separation is $\lambda_0/2 < \Delta d_{\hat{y},t} < \lambda_0$ grating lobes will not occur when the array is directed broadside (i.e. $\theta = 0$). However, when the array is squinted away from broadside, grating lobes can appear depending on both element spacing and squint angle. This case is shown in Fig. 5(b) where the spacing is $\Delta d_{\hat{y},t} = 3\lambda_0/4$ and the array is squinted to $\theta_s = 30^\circ$. Finally, when the inter-element separation is $\Delta d_{\hat{y},t} > \lambda_0$ the field pattern has grating lobes regardless of the squint angle.

The array factor predicts the CFA signal's far-field, angular amplitude distribution for an array consisting of ideal transmitters but in practice real antennas are used in the array. To model an array of identical, practical antenna elements the field pattern for the practical antennas can be multiplied to the array factor [9]. This is referred to as pattern multiplication and it is a simple method to approximate a practical CFA's field pattern.

The field pattern for the parameters in Table 2.1 is shown in Fig. 2.6. In Fig. 6(a) the field is shown on the (\hat{x}, \hat{y}) plane after the wave has propagated for $\tau_0 = 20\text{ns}$. This

Table 2.1. CFA simulation parameters. The CFA simulation parameters used to generate the signal field plots in Fig. 2.6.

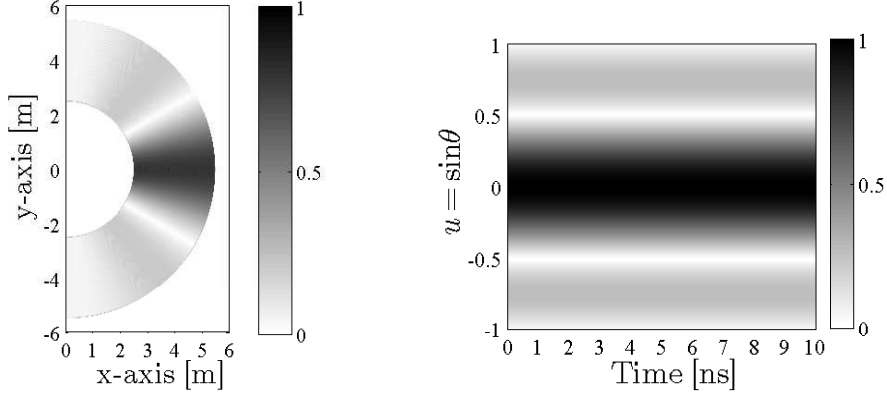
Parameter	Value
Transmitters P	4
Frequency f_0	10GHz
Bandwidth BW_s	100MHz
Transmitter spacing $\Delta d_{\hat{y},t}$	$\lambda_0/2$
Chips M	1
Pulses N	1
Chip duration T_c	10ns

view of the field is expensive to calculate, especially for longer signals with high ω_0 and τ_0 because of the sampling required to satisfactorily represent the signal. Alternately, the field can be represented in $t - u$ or (r, u) space as shown in Fig. 6(b). Under the far-field assumption, with no amplitude scaling, this representation is invariant of the time or range at which the field is observed.

Note the CFA field pattern is constant in time (or range) for a given angle. The field pattern has a primary lobe centered on $u = 0$, two sidelobes located at $u = \pm 0.75$ and nulls at $u = \pm 0.5, \pm 1$. The array's weights and the array factor are related through a Fourier transform. The Fourier transform relationship can be used to design the array's element weights to approximate a desired far-field amplitude distribution which is discussed next.

2.3.4 Pattern Synthesis and the Fourier Transform

The relationship between the array factor and the element weights has been long recognized as a Fourier transform relationship. There are several methods to de-



(a) CFA field pattern in the (\hat{x}, \hat{y}) plane at $t_0 = 20\text{ns}$. Note the beam along $\theta_0 = 0$ and the nulls at $\theta_0 = \pm 30^\circ$ and $\theta_0 = \pm 90^\circ$. (b) The field pattern in Fig. 6(a) plotted on the (t, u) plane with $\tau_0 = 0$. Plotting in the (t, u) plane is analogous with plotting (r, u) .

Figure 2.6. Signal field pattern: CFA. The CFA signal field plots on the (\hat{x}, \hat{y}) and (t, u) planes simulated using the parameters in Table 2.1.

sign the weights [9; 47] such as various pattern synthesis techniques based on the z-transform and the Fourier series or Fourier transform methods. The Fourier series and Fourier transform methods will be useful for later discussion of FDA pattern analysis.

The Fourier series method to find the array element weights from a desired far-field distribution from [9] is considered first. For P odd, p 's indexing and the array locations are modified such that

$$-\frac{P-1}{2} \leq p \leq \frac{P-1}{2} \quad (2.34)$$

$$d_p = p\Delta d_{\hat{y},t} \quad (2.35)$$

To ensure that the array factor is periodic over 2π , the inter-element spacing must

be $\Delta d_{\hat{y},t} = \lambda_0/2$. The desired array factor for a ULA with non-uniform weights is

$$\widehat{\text{AF}}_P(\xi) = \sum_{p=-\frac{P-1}{2}}^{\frac{P-1}{2}} \tilde{a}_p \exp(jp\xi), \quad (2.36)$$

where

$$\xi = k_0 \Delta d_{\hat{y},t} \sin \theta, \quad -\pi \leq \xi \leq \pi. \quad (2.37)$$

It is common to see the parameter ξ in the array processing literature because it simplifies the notation in some problems. The Fourier series expansion of $\widehat{\text{AF}}_P(\xi)$, evaluated at index values p , results in the element weights approximating $\widehat{\text{AF}}_P(\xi)$

$$\tilde{a}_p = \frac{1}{2\pi} \int_{-\pi}^{\pi} \widehat{\text{AF}}_P(\xi) \exp(-jp\xi) d\xi, \quad -\frac{P-1}{2} \leq p \leq \frac{P-1}{2}. \quad (2.38)$$

In this case the element index p plays the role of a frequency in the transform. The same design method is called the Least Squares Error Pattern synthesis in [47] because this method approximates the desired pattern in the least squares sense. The primary drawback with the Fourier series method is that to satisfy the periodicity requirement the element spacing must be $\Delta d_{\hat{y},t} = \lambda_0/2$. Otherwise, the technique becomes more complicated requiring the use of fill-in functions [9]. Alternately, a Discrete Fourier Transform (DFT) based method is developed in [47] which overcomes some of the limitations.

The DFT method overcomes the periodicity requirement, however, it still assumes a ULA configuration. The method is derived from the z -transform method of array factor synthesis and by using the DFT it is possible to use the original element

indexing and spacing

$$p \in [0, 1, \dots, P-1], \quad (2.39)$$

and ξ is discretized into P samples with sample spacing

$$\Delta\xi = \frac{2\pi}{P}, \quad (2.40)$$

such that

$$\xi_k = \left(k - \frac{P-1}{2}\right) \Delta\xi, \quad k = 0, 1, \dots, P-1. \quad (2.41)$$

The desired array factor $\widehat{\text{AF}}_P(\xi)$ is sampled such that

$$\text{AF}_P(k) = \widehat{\text{AF}}_P^*(\xi_k) \exp \left[-j\xi_k \left(\frac{P-1}{2} \right) \right], \quad (2.42)$$

where $(\cdot)^*$ is the complex conjugate. Next, the weights are modified so that

$$\tilde{b}_p = \tilde{a}_p \exp \left[jp\pi \left(\frac{P-1}{P} \right) \right] \quad (2.43)$$

which is a consequence of the z -transform mapping to the DFT domain. Finally, the following DFT pair relates the element weights (through \tilde{b}_p) and the desired array factor [47]

$$\widehat{\text{AF}}_P(k) = \sum_{p=0}^{P-1} \tilde{b}_p \exp \left(-jkp \frac{2\pi}{P} \right) \quad (2.44)$$

$$\tilde{b}_p = \frac{1}{P} \sum_{k=0}^{P-1} \widehat{\text{AF}}_P(k) \exp \left(jkp \frac{2\pi}{P} \right). \quad (2.45)$$

Knowing $\text{AF}_P(k)$, allows \tilde{b}_p and \tilde{a}_p to be found. Once \tilde{a}_p is found, it is possible to determine $\text{AF}_P(\xi)$. The array factor is completely determined by pattern samples with $\Delta\xi = 2\pi/P$ spacing [47].

The primary concept from this section is that the array weights and the resulting signal field pattern are related through a Fourier transform. This is also similar to optics where an aperture and its diffraction pattern are related through a Fourier transform. The assumption in both the radar and optics applications is that the signal is monochromatic. The relationship for colored signals is less clear and will be addressed in later chapters.

2.3.5 Field Characteristics

For a CFA signal, the array factor predicts the signal's far-field amplitude as a function of angle and is closely related to the signal's radiated field pattern. Alternatively, field pattern could be described using the power pattern which is the square of the field pattern, and measures the average power radiated by the field. Both the array factor and power pattern assume that the signal amplitude is constant along any time/range cut, and are examples of a radiation pattern [9].

The CFA signal's far-field amplitude is described using the array factor and can be characterized by a First-Null Beamwidth (FNBW), with respect to u , of

$$\text{FNBW}_u = 2 \frac{2\pi}{Pk_0 \Delta d_{y,t}}. \quad (2.46)$$

The FNBW is a straightforward calculation using Eq. (2.30) and can be used to approximate the Half-Power Beamwidth (HPBW) [9]

$$\text{HPBW} \simeq \frac{\text{FNBW}}{2}. \quad (2.47)$$

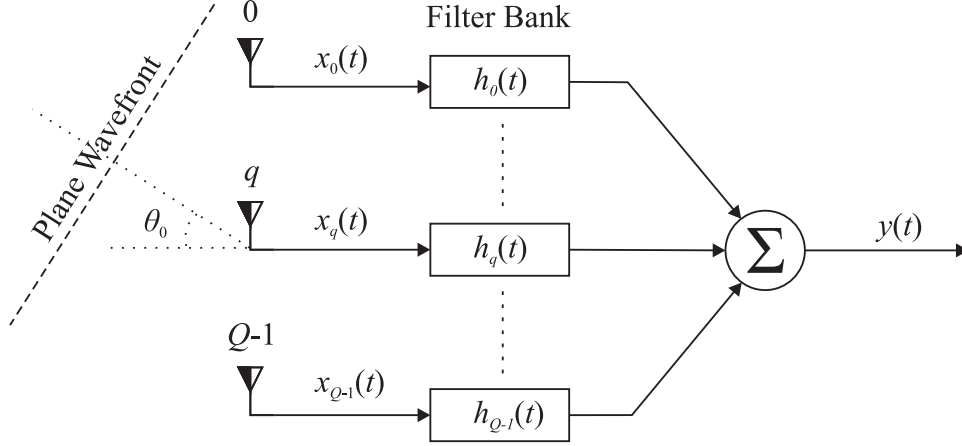


Figure 2.7. General Array Processor.

The HPBW is an adequate measure of the array's angular resolution δ_u or δ_θ [9; 46] but is more accurately a measure of the far-field diffraction. Angular resolution is defined as the minimum angular separation between two targets before they can be resolved as distinct targets.

The CFA's average transmit power follows easily from the transmit signal equation

$$\begin{aligned}
 P_{ave}\{s(t, \bar{\mathbf{r}}_0)\} &= \frac{1}{T_c} \int_{t_0}^{t_0+T_c} s(t, \bar{\mathbf{r}}_0) s^*(t, \bar{\mathbf{r}}_0) dt \\
 &= P^2 |D_P(k_0 \Delta d_{\hat{y}, t} u)|^2.
 \end{aligned} \tag{2.48}$$

If the signal's amplitude is constant in range, then the power pattern is the square of the array factor. In general, care should be taken when defining the power pattern, especially if the signal's amplitude is not constant in range. If the radiation pattern is not constant in range, then the average power must be calculated using Eq. (2.48) and this point is revisited with respect to the FDA.

2.3.6 Receivers

Using the array structure it is possible to spatially filter incoming waveforms. The generalized linear beamformer is shown in Fig. 2.7. The signal arriving from θ_0 is assumed to be a plane wave, $r(t)$, impinging upon a Q element linear array. The quadrature demodulated signal, $x(t)$, at the q th element is

$$x_q(t, \theta_0) = x(t - \Delta\tau_q) \quad (2.49)$$

where $\Delta\tau_q$ is a differential signal delay compared to the phase reference. The set of received signals, $\tilde{\mathbf{x}}(t)$, is

$$\begin{aligned} \tilde{\mathbf{x}}(t) &= [x_0(t), \dots, x_q(t), \dots, x_{Q-1}(t)]^T \\ &= [x(t - \Delta\tau_0), \dots, x(t - \Delta\tau_q), \dots, x(t - \Delta\tau_{Q-1})]^T. \end{aligned} \quad (2.50)$$

Each signal is processed using a filter with impulse response $h(t)$ and the collection of impulse responses is

$$\tilde{\mathbf{h}}(t) = [h_0(t), \dots, h_q(t), \dots, h_{Q-1}(t)]^T. \quad (2.51)$$

In general, the output of a beamformer with linear processing, $y(t)$, has a temporal representation

$$y(t) = \sum_{q=0}^{Q-1} \int_{-\infty}^{\infty} x_q(\eta) h_q(t - \eta) d\eta, \quad (2.52)$$

with a compact frequency-domain representation

$$\tilde{\mathbf{Y}}(\omega) = \tilde{\mathbf{H}}^T(\omega) \tilde{\mathbf{X}}(\omega). \quad (2.53)$$

where $\tilde{\mathbf{H}}(\omega)$ and $\tilde{\mathbf{X}}(\omega)$ contain the set of Fourier transformed impulse responses and signals [47]. This representation is purposely generalized, and from this representation the usual beamformers can be derived. The delay-and-sum beamformer implements filters that delay the signals so they align in time and the method is described next.

The delay-and-sum beamformer filters the set of received signals using a bank of filters with impulse responses

$$h_q(t) = \delta(t + \Delta\tau_q), \quad (2.54)$$

which aligns the signals in time so they add constructively. A constant initial time offset can be applied to all impulse responses so the filters are causal. The delay-and-sum beamformer can also be implemented in the frequency domain by applying a linear phase function to the received signal spectra

$$Y(\omega) = \sum_{q=0}^{Q-1} X_q(\omega) \exp(j\omega\Delta\tau_q). \quad (2.55)$$

The delay-and-sum beamformer is useful when the signals do not satisfy the narrowband approximation and can be implemented in a wide variety of receivers. The delay filter bank may be used in applications such as SAR to align disparate signals to a common reference point. This type of filtering is more accurate than the phased array processing discussed next.

If the received signals have sufficiently narrow bandwidths then it is possible to approximate the delay-and-sum beamformer by sampling the linear phase functions at ω_0 so the filters become multiplicative constants. The delay-and-sum beamformer

becomes the phased array, or narrowband, beamformer

$$y(t) = \sum_{q=0}^{Q-1} x_q(t) \exp(j\omega_0 \Delta\tau_q). \quad (2.56)$$

The individual differential delays $\Delta\tau_q$ are found using the geometry in Fig. 3(b). For a ULA with inter-element spacing $\Delta d_{\hat{y},r}$ the delays are given by

$$\Delta\tau_q = k_0 \Delta d_{\hat{y},r} u \left(q - \frac{Q-1}{2} \right). \quad (2.57)$$

The phased array processor provides greater computational savings and can be applied to a signal that has been matched filtered and sampled at the range bin locations. However, the waveform must be monochromatic with a sufficiently narrow bandwidth. Phased array processing is also called digital beamforming because the pattern resulting when the receiver scans through all values of θ is analogous to the transmit field pattern for the same frequency, element spacing and weights. Therefore, it is possible to forego a more complete discussion of digital beamforming and its beampattern.

It is not clear which form of array processing is best for processing the generalized FDA signal because the topic has not been subjected to thorough examination. The frequency-domain beamforming, also described in [47], may be more suitable for STAP applications but is not summarized here.

2.4 Ambiguity Function

In the classical array literature [9; 47] the array factor's HPBW was found to adequately quantify the array's DOA measurement accuracy and is closely related to the angular resolution [46]. In MIMO radar, and waveform diversity, this definition is problematic because the field pattern cannot always be described using an array

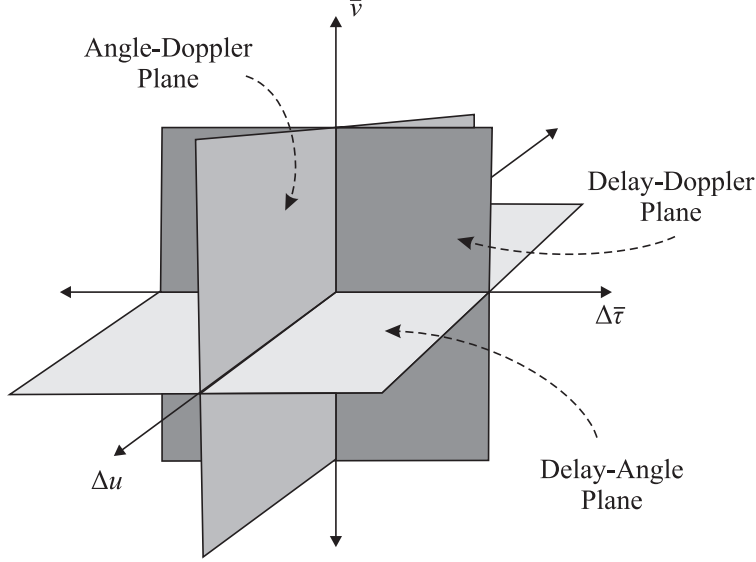


Figure 2.8. AF principal planes. The diagram illustrates the principal planes of the delay-Doppler-angle ambiguity function.

factor. Relatively recent work in MIMO radar systems extended the AF to include DOA measurement accuracy because the array factor is not an adequate descriptor in generalized waveform diverse models.

The AF is a correlative time-frequency representation because the on-axis delay and Doppler profiles are equal to the autocorrelation of the function in the time and frequency domains respectively. It is also closely related to the signal's Wigner distribution [36]. Woodward's AF is a three dimensional function depicting the receiver's range and velocity measurement accuracy for a particular transmit signal [1]. A monostatic, narrowband radar signal's ambiguity function is [33]

$$|\chi(\Delta\tau, \nu)| = \left| \int_{-\infty}^{\infty} x(t) \hat{x}^*(t + \Delta\tau) \exp(j\nu t) dt \right|, \quad (2.58)$$

where $\hat{x}(t)$ is the filter matched to the expected signal $x(t)$, $\Delta\tau$ represents a temporal mismatch between the filter and the signal, and ν is the Doppler frequency shift in radians per second.

Equation (2.58) is based on the narrowband approximation to the Doppler scaled signal. In the narrowband approximation a target's velocity is measured as rate-of-change in the range over successive pulses. It can be shown that the impact of the Doppler amounts to a frequency shift observed over successive pulses where

$$\begin{aligned}\nu &\approx 2\pi(f_r - f_0) \\ &\approx -2k_0 v_t,\end{aligned}\tag{2.59}$$

where v_t is the component of the target's velocity in the direction from the radar to the target, f_r is the received frequency and f_0 is the transmitted frequency. A common heuristic used to determine whether a signal is narrowband is whether the signal bandwidth BW_s satisfies $\text{BW}_s < f_0/10$. It is also suggested in [33], that $\text{BW}_s < 4f_0/10$ is a reasonable bound for a wide range of signals. The validity of the narrowband Doppler approximation needs to be re-evaluated when the Doppler scaling is observed in a single pulse of the received signal. If the signal does not satisfy the narrowband assumption the wideband Doppler model must be used.

Doppler scaling is potentially observed within a single pulse in three cases. The first is when the signal's bandwidth exceeds the heuristics discussed (i.e. a wideband signal). The second is when v_t is very large. The third is when the signal's duration is such that the frequency shift is observed in a single pulse. The second case can be discounted in many cases because the platform or target speed is typically small relative to the velocity of propagation. The first and third cases could impact the FDA signal and have been studied in relation to OFDM [38].

In the relativistic, or wideband, Doppler model the received signal is a scaled

replica of the transmit signal

$$x(t) = \sqrt{\alpha} s [\alpha(t - 2\tau_0)], \quad (2.60)$$

where τ_0 accounts for the two-way propagation delay and where the scale factor, α , is

$$\alpha = \frac{c_0 - v_t}{c_0 + v_t}. \quad (2.61)$$

The scale factor can be approximated in a pulsed signal providing the resulting frequency shift cannot be observed within the pulse. This leads to an additional condition for the narrowband Doppler approximation, relating the signal's time-bandwidth-product to the target's relative velocity [38]

$$\frac{2|v_t|}{c_0 + v_t} \ll \frac{1}{\text{BW}_s T_s}, \quad (2.62)$$

where T_s is the signal's total pulse duration. In relation to an OFDM signal, the narrowband approximation to the Doppler scaling has a region of validity that is bound by the relation between the bandwidth, duration, number of sub-carriers and maximum target velocity [19]. This bound is also likely to apply to the FDA signal model.

The next question is how to measure angular resolution when the signal's field cannot be described using an array factor. This question was addressed by the MIMO community, and, the solution is to extend the ambiguity function to account for angular performance.

Ambiguity functions for MIMO arrays were developed in [11; 40] amongst several other references. However, the background and development in [40] seems much

more complete and comprehensive than the others. The results are summarized here because the FDA ambiguity function will be developed using a similar approach.

The development in [40] begins with the wideband signal model and ambiguity function which, following a sequence of simplifications, the narrowband array version of the MIMO ambiguity function is derived. These assumptions have been discussed throughout the summary provided to this point and are recapped here for ease of reference.

First, it is assumed that the narrowband approximation to the Doppler scaling can be made because the target relative velocity is relative small. This assumption allows the Doppler scale factor to be treated as a frequency shift. Second, the sensors are close to each other such that the individual sensor LOS are approximately identical and the largest bistatic angle between any two array sensors and a target is small (e.g. $< 5^\circ$ [40]). The small bistatic angle approximation permits separability of the manifold vector in terms of a transmit and a receive manifold vector. Third, the targets of interest are in the array's far-field. This allows separability of the equation into range and angle components when the signal's propagation delay is approximated using the far-field assumption (such as in Section 2.3.1). Finally, it is assumed that the signals are sufficiently narrowband (i.e. their durations are relatively long) that the propagation time across the array is negligible. This assumption allows the envelope of the waveform to be described using a single, simple pulse shape function.

To summarize the development in [40] some additional definitions are required. First the development uses a point target model where the target's position is $\bar{\mathbf{r}}_t$ with a constant velocity vector $\bar{\mathbf{v}}_t$. The target's position and velocity vectors are annotated using the parameter set, Ξ_t , where $\Xi_t = (\bar{\mathbf{r}}_t, \bar{\mathbf{v}}_t)$. The radar receiver tests for a target with estimated parameters $\hat{\Xi}_t = (\bar{\mathbf{r}}_{t,est}, \bar{\mathbf{v}}_{t,est})$. After quadrature demodulation, the general, wideband received MIMO signal at the q th receiver due to a target with

parameter Ξ_t is

$$x_q(t, \Xi_t) = \sum_{p=0}^{P-1} K_{p,q} \sqrt{\alpha_{p,q}(\Xi_t)} \tilde{s}_p \{ \alpha_{p,q}(\Xi_t) [t - \tau_{p,q}(\Xi_t)] \} \\ \times \exp \{ -j [\omega_0 + \nu_{p,q}(\Xi_t)] \tau_{p,q}(\Xi_t) \} \exp [j \nu_{p,q}(\Xi_t) t] + \tilde{n}_q(t), \quad (2.63)$$

where $K_{p,q}$ represents the bistatic target reflectivity and the amplitude scaling due to the range equation parameters; $\tilde{n}(t)$ is the complex noise waveform at the output of the demodulator; $\tilde{s}_p(t)$ represents the complex, baseband representation of the p th transmit signal; $\alpha_{p,q}(\Xi_t)$ is the relativistic Doppler scale factor resulting from the constant target velocity, and $\nu_{p,q}(\Xi_t)$ is the frequency shift resulting from the scaling evaluated at ω_0 ,

$$\nu_{p,q}(\Xi_t) = k_0 \left[\frac{d}{dt} (|\bar{\mathbf{r}}_p(t)| + |\bar{\mathbf{r}}_q(t)|) \right], \quad (2.64)$$

and the propagation time from the p th transmitter, to the target, to the q th receiver is

$$\tau_{p,q}(\Xi_t) = \frac{|\bar{\mathbf{r}}_{p,t}|}{c_0} + \frac{|\bar{\mathbf{r}}_{q,t}|}{c_0} \\ = \frac{|\bar{\mathbf{r}}_t - \bar{\mathbf{r}}_p|}{c_0} + \frac{|\bar{\mathbf{r}}_t - \bar{\mathbf{r}}_q|}{c_0}. \quad (2.65)$$

Note that $\nu_{p,q}(\Xi_t)$ and $\tau_{p,q}(\Xi_t)$ represent the Doppler frequency offset and propagation delay respectively for any bistatic angle between the transmitter, the target and the receiver.

The signal is processed using a bank of filters matched to each of the transmitted waveforms and the estimated target parameters. The output of the filter matched to

the \hat{p} th transmit signal and to a target with parameters $\hat{\Xi}_t$ at the q th receiver is

$$\begin{aligned}
y_{q,\hat{p}}(\Xi_t, \hat{\Xi}_t) &= \sum_{p=0}^{P-1} K_{p,q} \left(\sqrt{\alpha_{p,q}(\Xi_t)} \sqrt{\alpha_{\hat{p},q}(\hat{\Xi}_t)} \right) \\
&\times \int_{-\infty}^{\infty} \tilde{s}_p \{ \alpha_{p,q}(\Xi_t) [t - \tau_{p,q}(\Xi_t)] \} \tilde{s}_{\hat{p}}^* \{ \alpha_{\hat{p},q}(\hat{\Xi}_t) [t - \tau_{\hat{p},q}(\hat{\Xi}_t)] \} \\
&\times \exp \{ -j [\omega_0 + \nu_{p,q}(\Xi_t)] \tau_{p,q}(\Xi_t) \} \exp \left\{ j \left[\omega_0 + \nu_{\hat{p},q}(\hat{\Xi}_t) \right] \tau_{\hat{p},q}(\hat{\Xi}_t) \right\} \\
&\times \exp [j \nu_{p,q}(\Xi_t) t] \exp \left[-j \nu_{\hat{p},q}(\hat{\Xi}_t) t \right] dt + \tilde{n}_{q,\hat{p}}(t), \tag{2.66}
\end{aligned}$$

Each of the integral terms can be viewed as an element from a $P \times P$ covariance matrix $\mathbf{R}(\Xi_t, \hat{\Xi}_t, q)$ [40].

It can be shown using the set of assumptions summarized earlier that the temporal and spatial terms become separable. Factoring the spatial terms from the matched filter integral, each term in the covariance matrix reduces to a narrowband cross ambiguity function between the received signal component with index p and the matched filter component with index \hat{p} . The new, narrowband covariance function $\mathbf{R}(\Delta\tau, \Delta\nu)$ is independent of the receiver index q . The variables $\Delta\tau$ and $\Delta\nu$ are the time and Doppler mismatches respectively. Neglecting target reflectivity and noise, it is shown in [40] that the wideband MIMO AF can be expressed as

$$|\chi(\Xi, \hat{\Xi}_t)|^2 = \left| \tilde{\mathbf{w}}_{tx}^H(\Xi_t) \mathbf{R}(\Delta\tau, \Delta\nu, q) \tilde{\mathbf{w}}_{tx}(\hat{\Xi}_t) \tilde{\mathbf{w}}_{rx}^H(\Xi_t) \tilde{\mathbf{w}}_{rx}(\hat{\Xi}_t) \right|^2. \tag{2.67}$$

The manifold vectors follow the same definition as before but with a frequency shift due to the Doppler

$$\begin{aligned}
\tilde{\mathbf{w}}_{tx}(\Xi_t) &= [\exp[j(\omega_0 + \nu) \bar{\mathbf{d}}_1 \cdot \hat{\boldsymbol{\kappa}}(\theta, \psi)/c_0], \dots, \\
&\exp[j(\omega_0 + \nu) \bar{\mathbf{d}}_2 \cdot \hat{\boldsymbol{\kappa}}(\theta, \psi)/c_0], \dots, \\
&\exp[j(\omega_0 + \nu) \bar{\mathbf{d}}_{P-1} \cdot \hat{\boldsymbol{\kappa}}(\theta, \psi)/c_0]]^T, \tag{2.68}
\end{aligned}$$

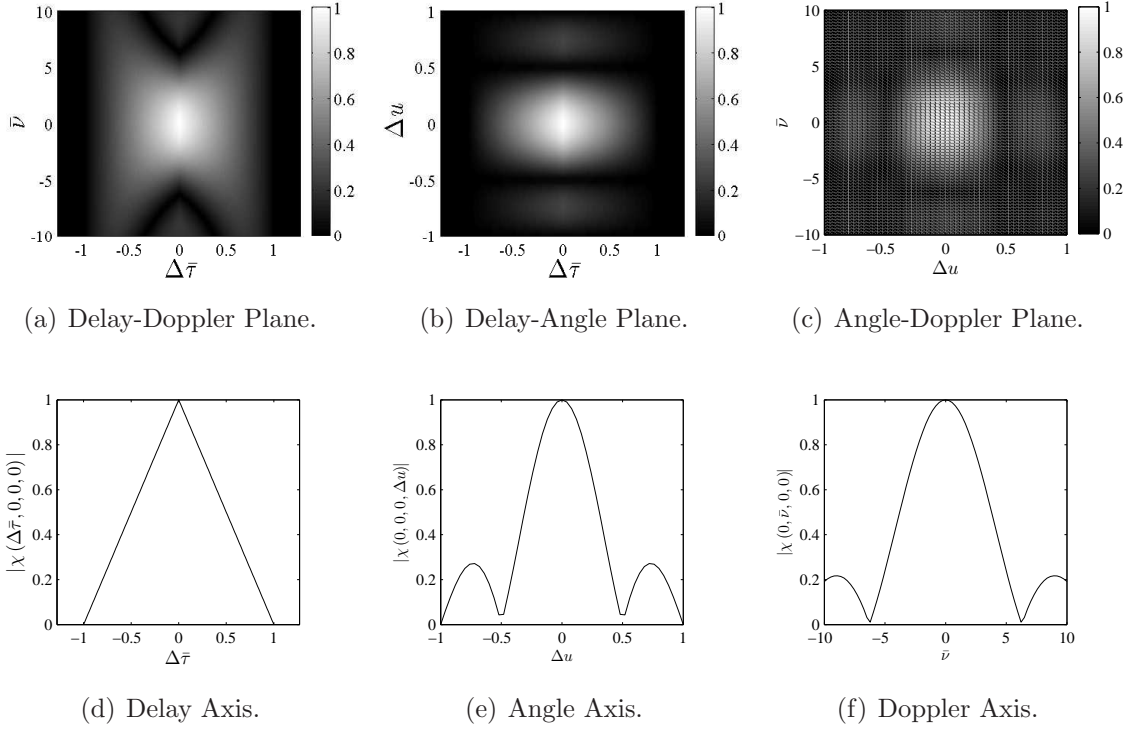


Figure 2.9. AF principal planes and axes: CFA. Note that the delay and Doppler axes are normalized.

and $\tilde{\mathbf{w}}_{rx}(\boldsymbol{\Xi}_t)$ has the same form except that $\bar{\mathbf{d}}_q$ replaces $\bar{\mathbf{d}}_p$ in Eq. (2.68).

Equation (2.67) shows that the narrowband MIMO AF is the sum of self- and cross-correlation functions weighted by the transmit and receive manifold vectors. The receiver manifold vector, through the $\tilde{\mathbf{w}}_{rx}^H(\boldsymbol{\Xi}_t)\tilde{\mathbf{w}}_{rx}(\hat{\boldsymbol{\Xi}}_t)$ term, has little to no impact on the MIMO AF except to scale the result by the digitally beamformed pattern where factors such as grating lobes may result in ambiguities in the angular dimension [11].

Figure 2.9 shows the AF principal planes and axes for the CFA with signal parameters in Table 2.1 for a target at $u_t = 0$ with varying relative delay and velocity mismatches between the signal and the matched filter. To explain the AF plot consider that the target parameters are expressed in polar coordinates $\boldsymbol{\Xi}_t = (r_t, u_t, v_t)$. This example evaluates a single receiver matched to a target with parameters $\hat{\boldsymbol{\Xi}}_t =$

$(r_t + \Delta r, u_t + \Delta u, 0)$ while the signal input to the receiver is due to a target with parameters $\Xi_t = (r_t, 0, v_t)$. The AF can then be expressed in terms of a differential delay, $\Delta\tau = 2\Delta r/c_0$, and differential azimuth angle parameter Δu and a Doppler frequency evaluated at ω_0 .

Note that the delay and Doppler axes in Fig. 2.9 have been normalized, while the angular parameter u is dimensionless. The delay axis is normalized by the inverse of the signal's bandwidth, $\Delta\bar{\tau} = \Delta\tau\text{BW}_s$, while the Doppler axis is normalized by the signal bandwidth, $\bar{\nu} = \nu/\text{BW}_s$. Although the angular parameter is dimensionless, it is sometimes normalized by the array's inter-element spacing, and in Section 2.3.4 the variable xi is introduced as a normalized angular parameter. The angular parameter u has not been normalized here because it is intended that later comparisons will maintain the array's size and number of elements. However, should one wish to normalize the angular parameter the normalized parameter, ξ , would be suitable for comparing different array geometries with different operating frequencies.

Using the AF principal axes the AF's mainlobe width along each of the axes can be determined. The definition used previously for the CFA's FNBW and HPBW can be applied to mainlobe measurements. Let the mainlobe width along any of the axes be defined as half the distance between the mainlobe's first nulls. For the CFA's AF shown in Fig. 2.9, the mainlobe's width along the normalized delay axis, δ_τ , is $\delta_u = 1$. The mainlobe's width along the normalized Doppler axis, δ_ν , is $\delta_\nu = 6.22$; and along the angle axis, δ_u , is $\delta_u = 0.5$. The width of the mainlobe along each of the axes is closely related to the signal and receiver's resolution in each of the dimensions.

Before the FDA research is summarized it will be useful to examine OFDM theory. The majority of OFDM radar research has considered single transmitter systems with limited work in MIMO. The results are analogous to a FDA signal with zero inter-element spacing; and it is likely that OFDM and FDA theory are not mutually

exclusive.

2.5 Orthogonal Frequency Division Multiplexing

OFDM signal theory is discussed here because the signal structure is similar to that used in FDA. The primary reference is [33] in which the author calls the OFDM signal a multi-carrier, phase coded signal (MCPC) – these signals are referred to as OFDM signals here. OFDM has been considered for a variety of radar applications such as range-Doppler processing [43], compressive sensing [32], high resolution radar [31], and combined radar-communication modes [23; 22]. It is not unreasonable to consider that FDA may also prove beneficial in similar applications.

Consider the general multiplexing concept. Multiplexing is a method to package information so that it can be decoded accurately by a receiver [36]. Simple methods include sending information at different times (time multiplexing) or at completely different carrier frequencies with mutually exclusive spectra (frequency multiplexing). In OFDM, the transmitted signals use uniformly spaced, mutually orthogonal sub-carrier frequencies with overlapping spectra to transmit multiple temporal signals simultaneously.

The transmit signal is a sequence of arbitrarily amplitude and phase coded basis signals, modulated in parallel using B sub-carriers separated by a constant frequency offset Δf and for orthogonal sub-carriers $\Delta f = T_c^{-1}$. A single, baseband pulse containing M chips is

$$s(t) = \sum_{b=0}^{B-1} \sum_{m=0}^{M-1} \tilde{a}_{b,m} \hat{b}(t - mT_c) \exp(j2\pi b\Delta ft). \quad (2.69)$$

Within a pulse there are BM complex symbols $\tilde{a}_{b,m} = A_{b,m} \exp(j\varphi_{b,m})$ modulating the B sub-carriers. The signal's bandwidth is $\text{BW}_s = B\Delta f$ and its Time-Bandwidth

Table 2.2. OFDM simulation parameters.

Parameter	Value
Transmitters P	1
Frequency f_0	10GHz
Bandwidth BW_s	400MHz
Sub-carriers B	4
Sub-carrier separation Δf	100MHz
Chips M	1
Pulses N	1
Chip duration T_c	10ns
Amplitudes E_b and $A_{b,m}$	1
Zero phase (Fig. 10(a)) φ_b	0
Linear phase offset (Fig. 10(b)) φ_b	$\pi f_b T_c$
Newman phase (Fig. 10(c)) φ_b	$\pi \frac{(b-1)^2}{B}$
Narahashi-Nojima phase (Fig. 10(d)) φ_b	$\pi \frac{(b-1)(b-2)}{B-1}$

Product (TBP) is BM .

According to [33], when B is large, and the complex weights are randomized, the ambiguity function approaches the desirable thumbtack shape. For the randomly weighted OFDM, the AF has delay and Doppler mainlobe widths of $\delta_\tau = \frac{1}{B\Delta f}$ and $\delta_\nu = \frac{\Delta f}{M}$ respectively with an average side lobe level relative to the mainlobe of $\frac{1}{MB}$. Both δ_τ and δ_ν are closely related to the waveform's delay and Doppler resolution respectively [33].

This may lead one to think that the delay or Doppler resolutions could be decreased arbitrarily by increasing B or M . For a fixed bandwidth BW_s , increasing B decreases Δf and increases T_c . Depending on the increase in T_c , the narrowband

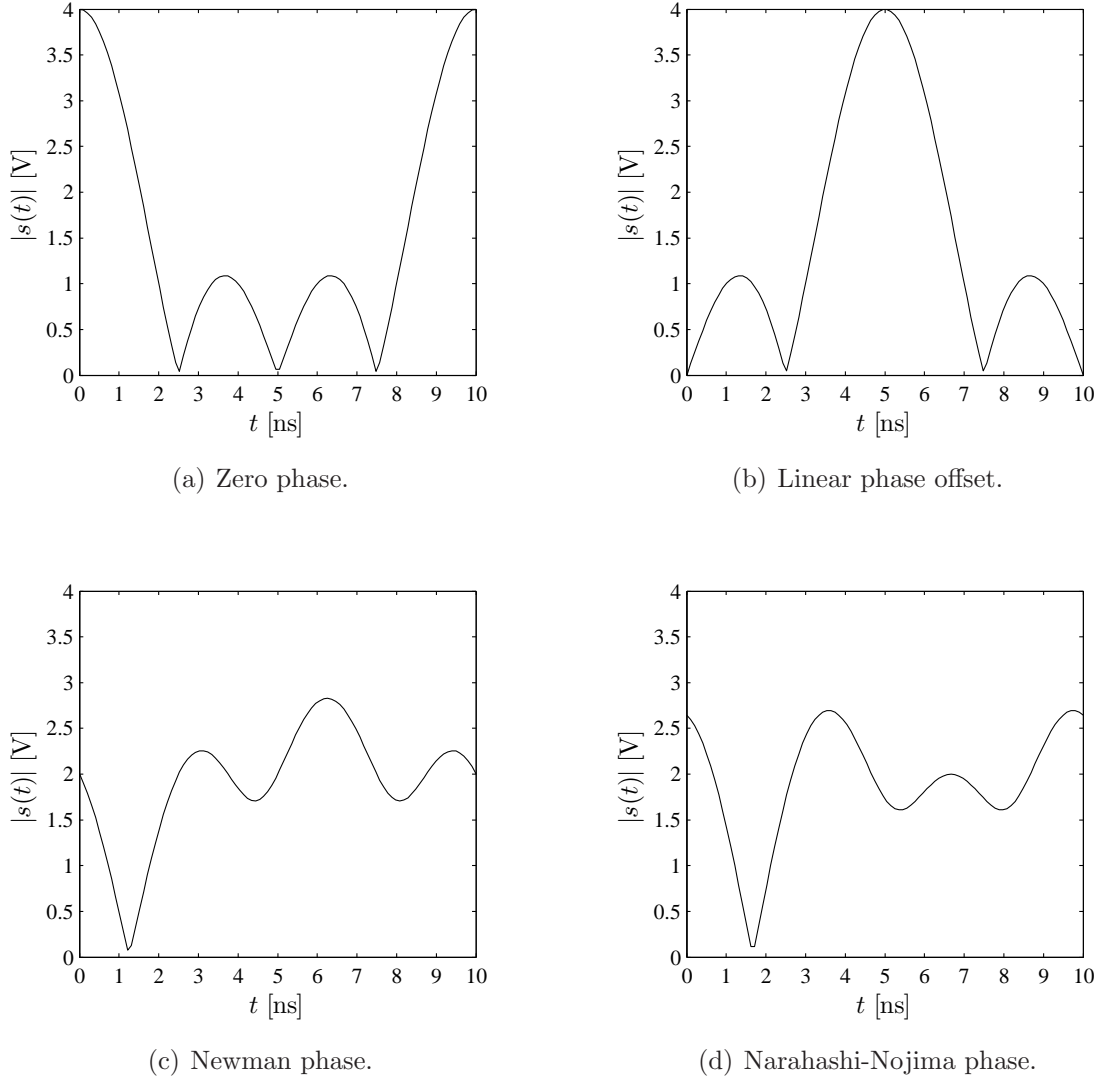


Figure 2.10. Phase Coded OFDM Signals. Phase coded OFDM signals simulated using the parameters in Table 2.2.

approximation to the Doppler model used in the ambiguity function [33] may become invalid. Increasing M , the number of chips, may impact the maximum pulse repetition frequency and the maximum observable Doppler. The design involves trade-offs that must be carefully evaluated given the radar's function.

OFDM has potential as a radar signal, but suffers from one main weakness – it lacks a constant modulus, baseband envelope. A constant modulus signal allows the

radar's high power amplifier to operate efficiently in the saturation region. When a signal with a non-constant envelope is transmitted, the amplifier must operate in the linear region to represent the signal accurately. To illustrate OFDM signals with non-constant envelopes Fig. 2.10 shows several OFDM signals which were modeled using the parameters in Table 2.2.

In terms of the power amplifier, the waveforms have poorest performance with either zero phase or linear phase shown in Fig. 10(a) and Fig. 10(b) respectively. In both cases, the peak instantaneous power is $\max\{P(t)\} = (\sum |w_b|)^2 = B^2$, while the average power is only $P_{ave} = \sum |w_b|^2 = B$ [33].

The ratio of the peak instantaneous envelope power to the mean envelope power is called the peak-to-mean envelope power ratio (PMEPR) [33]. The PMEPR approximates the peak-to-average power ratio (PAPR), but can be easier to use in optimization algorithms. Compared to a constant envelope signal the losses in the power amplifier due to a non-constant envelope amounts to $10 \log_{10}(\text{PMEPR})$ [33]. The FDA transmit configuration overcomes this problem, but in the receivers the PMPER may result in similar losses compared to a constant envelope signal in the receiver amplifier. This may be a cause for concern in some applications.

Because of the systemic impact of PAPR in OFDM a variety of methods have been developed to code the signal's transmit phases to reduce the PAPR. Two phase coding methods to reduce the PAPR, the Newman and Narahashi-Nojima methods, are summarized in [33]. Figures 10(c) and 10(d) show the waveforms generated using the two methods and the phase relationships are provided in Table 2.2. It is clear that each envelope's peak is significantly reduced and the envelopes are closer to being constant than either of Fig. 10(a) or 10(b).

Figure 2.11 shows the field pattern for the OFDM signal with the linear phase offset. It is usually unnecessary to plot the field pattern for a single ideal transmitter

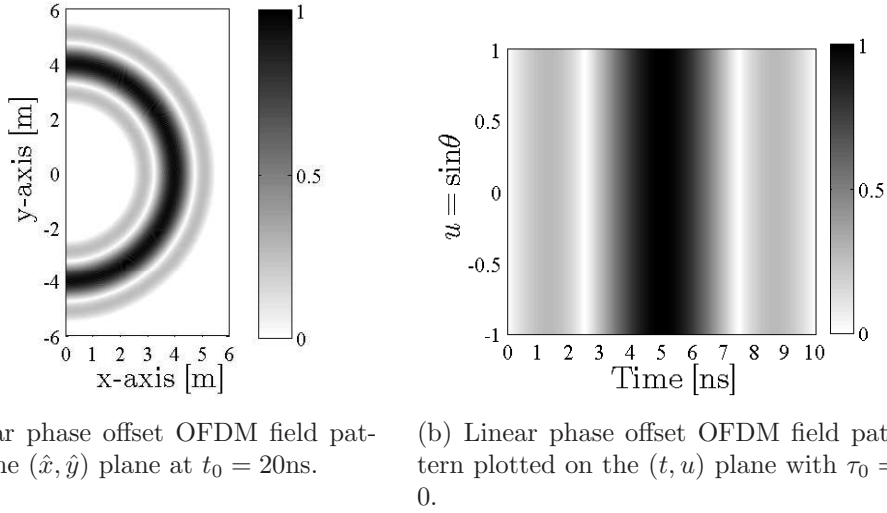


Figure 2.11. Signal field pattern: OFDM. Linear phase offset OFDM signal field pattern for the parameters in Table 2.2.

because the field is characterized solely by the range cut. For this study, it is interesting to observe the duality between OFDM signal field pattern in Fig. 2.11 and the CFA signal field pattern with similar parameters in Fig. 2.6. They are related to each other by a 90° rotation in the (t, u) plane about $u = 0$, $t = 5\text{ns}$. Comparing Equations (2.28) and (2.69) reveal the CFA's array factor equation and the baseband OFDM signal are mathematically similar. It is straightforward to show that for a CFA with $\lambda_0/2$ element spacing, the harmonic terms in Eq. (2.28) are mutually orthogonal. It is not surprising that there is a strong relationship between the two field pattern plots.

2.6 Frequency Diverse Array with Linear Frequency Progression

A primary Linear Frequency Progression, Frequency Diverse Array (LFP-FDA) research focus has been to characterize the apparent “range-dependent beam” with “automatic beam scanning”. A novel application has been designed to exploit this feature to simplify receiver processing [16]. The approach and results are summarized,

but will not be used in this study because it restricts the configurations that can be considered.

In this section, current literature relating to FDA design and analysis is reviewed; however, there are relatively few published FDA studies. First, the LFP-FDA geometric and signal models are presented. There is an increasing body of evidence that suggests the signal models presented in previous FDA research are in good agreement with both CEM models and measured data [28; 29; 16]. This is important because signal models will be used exclusively in this study, supported by limited measured data.

Second, the analytic approach to characterizing the FDA signal's far-field amplitude distribution is summarized because it is a possible reason why the LFP-FDA attracted so much attention but is also why it is difficult to work with analytically. The difficulty in analyzing the far-field amplitude distribution motivates the work in Chapter IV to understand the underlying principals required to analyze the FDA signal and then exploit the diversity offered by the FDA configuration.

Finally, the LFP-FDA SAR case study in [16] is summarized. The technique used in [16] to process the waveforms will not be used in this research; however, there are several results and observations resulting from the work in [16] that pose interesting research questions that could be studied in the future.

2.6.1 Additional Geometry

First, additional geometry is required to summarize the work in [16]. Consider the global geometry in 12(a), illustrating the array's location and the target scene center with reference to an arbitrary reference.

The airborne platform traverses a path $l \in [-\frac{L_S}{2}, \frac{L_S}{2}]$ defining a synthetic aperture

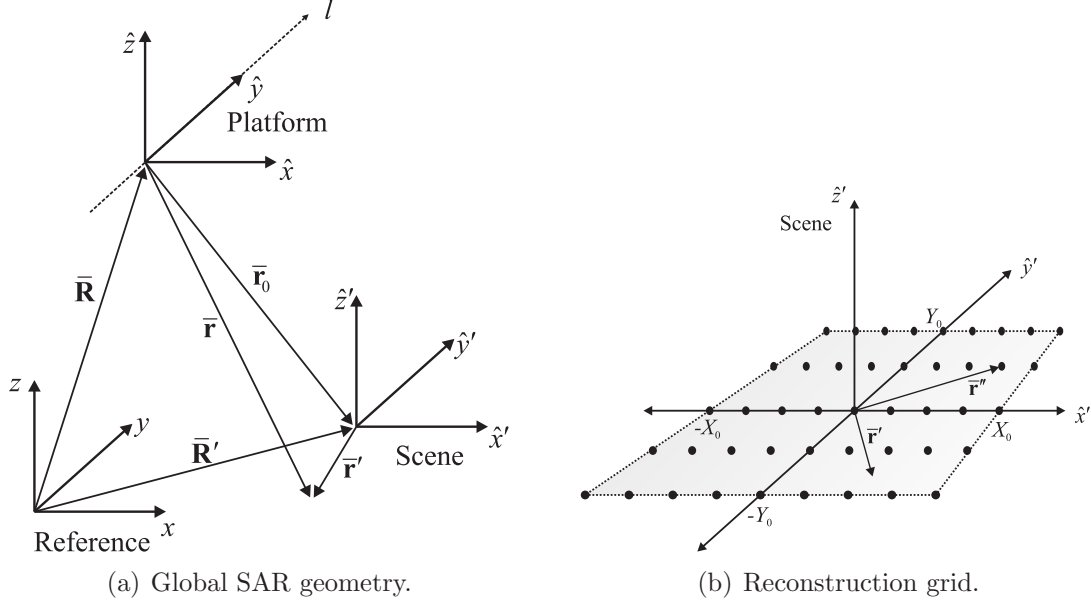


Figure 2.12. SAR global coordinates and reconstruction grid.

L_s where the platform position is

$$\bar{\mathbf{R}}(t) = \hat{\mathbf{x}}R_x(t) + \hat{\mathbf{y}}R_y(t) + \hat{\mathbf{z}}R_z(t). \quad (2.70)$$

The linear array elements are centered at $\bar{\mathbf{R}}(t)$ with $\hat{\mathbf{y}}$ aligned to the flight path shown in Fig. 2.14. The p th sensor's location, with $p \in [0, 1, \dots, P-1]$, is

$$\bar{\mathbf{d}}_p = -\hat{\mathbf{y}}p\Delta d_{\hat{\mathbf{y}},t}, \quad (2.71)$$

where $\Delta d_{\hat{\mathbf{y}},t}$ is uniform inter-element spacing as before.

The platform images a stationary scene whose center from the global reference is

$$\bar{\mathbf{R}}' = \hat{\mathbf{x}}X_c + \hat{\mathbf{y}}Y_c + \hat{\mathbf{z}}Z_c. \quad (2.72)$$

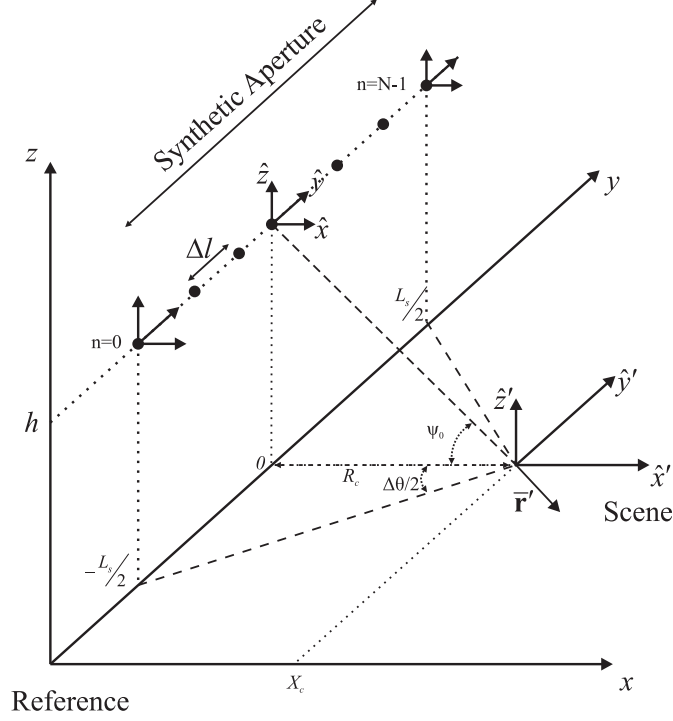


Figure 2.13. Analytical spotlight SAR geometry.

The displacement to an arbitrary point in the scene from the scene center is

$$\bar{\mathbf{r}}' = \hat{\mathbf{x}}x' + \hat{\mathbf{y}}y' + \hat{\mathbf{z}}z'. \quad (2.73)$$

The scene is bound using a rectangular volume $x', y', z' \in V$ such that $x' \in [-X_0, X_0]$, $y' \in [-Y_0, Y_0]$ and $z' \in [0, Z_0]$. The line-of-sight (LOS) vector from radar to the scene center is $\bar{\mathbf{r}}_0(t) = \bar{\mathbf{R}}' - \bar{\mathbf{R}}(t)$ with range, azimuth angle and elevation angle

$$r_0(t) = \{[X_c - R_x(t)]^2 + [Y_c - R_y(t)]^2 + [Z_c - R_z(t)]^2\}^{\frac{1}{2}}, \quad (2.74)$$

$$\theta_0(t) = \tan^{-1} \left[\frac{Y_c - R_y(t)}{X_c - R_x(t)} \right], \quad (2.75)$$

$$\psi_0(t) = \sin^{-1} \left[\frac{Z_c - R_z(t)}{r_0(t)} \right]. \quad (2.76)$$

The unit vector along $\bar{\mathbf{r}}_0$ is $\hat{\mathbf{r}}_0$ defined in Section 2.3.1. The displacement to an

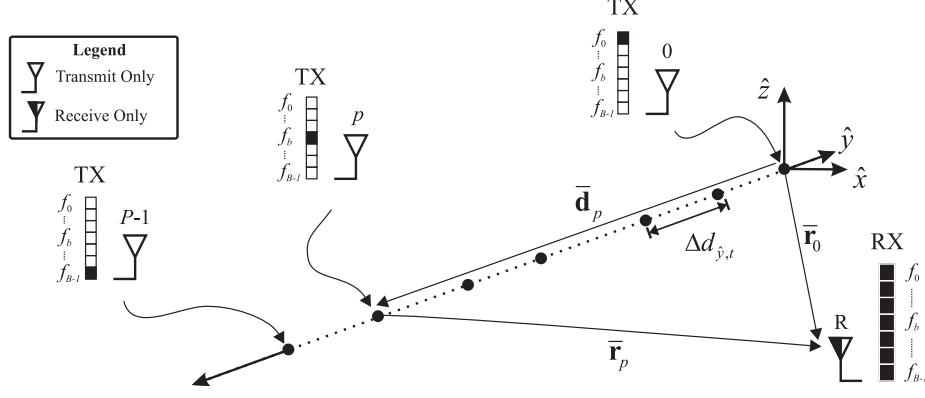


Figure 2.14. Transmit configuration: LFP-FDA. In previous FDA research, the FDA transmits identical signals from the P sensors, but use different frequencies at each sensor. In the LFP-FDA configuration, an incremental frequency is applied to the transmit signal along the array dimension.

arbitrary point in the scene, $\bar{\mathbf{r}}'$, from the array's phase center is $\bar{\mathbf{r}} = \bar{\mathbf{r}}_0 + \bar{\mathbf{r}}'$. The SAR image is produced using the Convolution Backprojection Algorithm (CBA). The CBA uses N pulses received over l to reconstruct the scene on a two dimensional grid on the $\hat{x}'\text{-}\hat{y}'$ plane centered at $\bar{\mathbf{R}}'$. The image is reconstructed at individual points located on the grid shown in Fig. 12(b), where

$$\bar{\mathbf{r}}'' = \hat{\mathbf{x}}x'' + \hat{\mathbf{y}}y''. \quad (2.77)$$

The grid is also bound by the volume, V , such that $x'' \in [-X_0, X_0]$ and $y'' \in [-Y_0, Y_0]$.

2.6.2 Signal Model

The LFP-FDA was extensively studied in [16] for several configurations including a planar array. Part of this work is summarized, adapted to the notation used here, and simplified to focus on the ULA result. Fig. 2.14 shows the transmitter geometry and configuration used in [16] for positive frequency progression. The FDA has a linear array geometry oriented along the \hat{y} -axis, with $\Delta d_{\hat{y},p} = \frac{\lambda_c}{2}$, and frequency progression $f_p = f_0 + p\Delta f$. The wavelength of the center-band frequency $f_c = f_0 + \frac{P-1}{2}\Delta f$ is λ_c .

Table 2.3. FDA simulation parameters.

Parameter	Value
Transmitters P	4
Frequency f_0	10GHz
Bandwidth BW_s	400MHz
Sub-carrier separation Δf	100MHz
Transmitter spacing $\Delta d_{\hat{y},t}$	$\lambda_{min}/2$
Chips M	1
Pulses N	1
Chip duration T_c	10ns
Phases $\varphi_{p,m,n}$	$\pi f_p T_c$
Amplitudes $A_{p,m,n}$	1

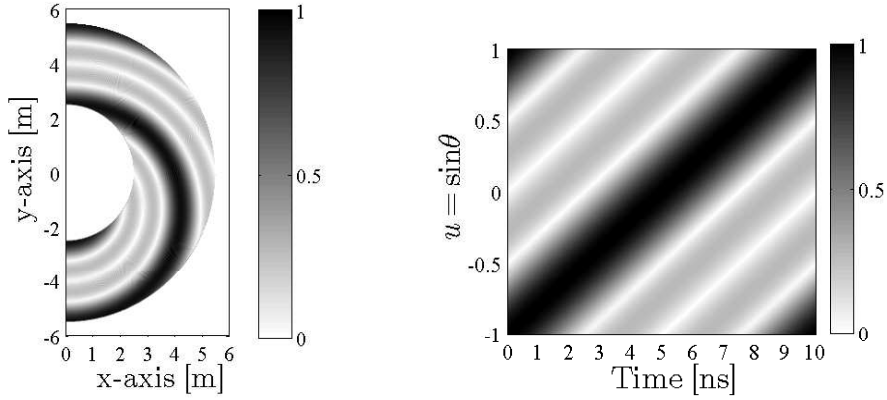
The transmit signal at an arbitrary point relative to the radar is

$$s(t, \bar{\mathbf{r}}_0, \bar{\mathbf{r}}') = \sum_{p=0}^{P-1} \exp[j\omega_p(t - \tau_0)] \exp(j\bar{\mathbf{k}}_p \cdot \bar{\mathbf{d}}_p) \exp(-j\bar{\mathbf{k}}_p \cdot \bar{\mathbf{r}}'), \quad (2.78)$$

where $\bar{\mathbf{k}}_p = k_p \hat{\mathbf{r}}_0$ is the wavevector of the p th signal. Note that Eq. (2.78) does not have any phase coding on the initial phases, however to obtain the signal field patterns in Fig. 2.15 a linear phase offset is required. When a phase is referred to in the following, the component signals in Eq. (2.78) are prefixed by a complex weight $\tilde{a}_p = \exp(-j\omega_p T_c/2)$.

2.6.3 Field Pattern

Fig. 2.15 shows the LFP-FDA field pattern of Eq. (2.78) for the parameters in Table 2.3. The waveform is not constant in either time (range) or azimuth angle



(a) FDA field pattern on the (\hat{x}, \hat{y}) plane at $t_0 = 20\text{ns}$ for the parameters in Table 2.3. (b) FDA field pattern in Fig. 6(a) plotted on the (t, u) plane with $\tau_0 = 0$.

Figure 2.15. Signal field pattern: LFP-FDA. The LFP-FDA field patterns simulated using the parameters in Table 2.3.

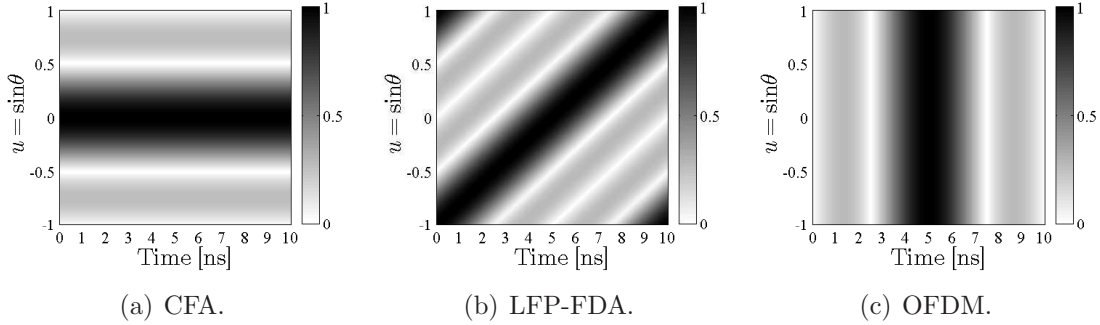


Figure 2.16. Signal field pattern comparison: CFA, LFP-FDA and OFDM. While the OFDM and CFA signal fields seem to be related through a 90° rotation on the (t, u) plane, the LFP-FDA's signal field appears to be a vertically sheared version of the CFA's signal field or a horizontally sheared version of the OFDM's signal field.

and has a peak that runs diagonally through (t, u) space. This feature caused FDA to be coined with the descriptions “range-dependent beamforming” and “automatic angular scanning”. While the location of the field pattern’s peak varies with both angle and time/range it is arguable whether this a beam in the typical usage of the word. If this definition for a beam is appropriate, then the OFDM signal also has a range dependent beam. The location of the field’s peak corresponds to times and angles where the transmitted signals are in-phase.

Comparing the field patterns for the CFA, the OFDM signal and the FDA in Fig. 2.16 reveals an interesting relationship. Compared to the CFA far-field amplitude pattern, the LFP-FDA is a vertically sheared version; and compared to the OFDM far-field amplitude pattern it is a horizontally sheared version. Applying the linear frequency progression along the array is a spatial analog to the stepped-frequency approximation to a linear frequency modulated signal.

2.6.4 Array Factor

An analytic solution for the general LFP-FDA field pattern is provided in [16]. To develop an analytic solution it is necessary to restrict the FDA parameters so that

$$P^2 \Delta k \Delta d_{\hat{y},p} \kappa_y < \pm \frac{\pi}{4}, \quad (2.79)$$

where $\Delta k = \Delta \omega / c_0$ is the differential wavenumber. The restriction permits the transmit signal to be simplified to

$$s(t, \bar{\mathbf{r}}_0, \bar{\mathbf{r}}') = g(t, \bar{\mathbf{r}}_0, \bar{\mathbf{r}}') \text{AF}_P(t, \bar{\mathbf{r}}_0, \bar{\mathbf{r}}'), \quad (2.80)$$

where the signal components associated with ω_0 are factored into

$$g(t, \bar{\mathbf{r}}_0, \bar{\mathbf{r}}') = \exp[j\omega_0(t - \tau_0)] \exp(-j\bar{\mathbf{k}}_0 \cdot \bar{\mathbf{r}}'), \quad (2.81)$$

and the remaining spatial signal components are grouped into a two dimensional array factor

$$\text{AF}_P(t, \bar{\mathbf{r}}_0, \bar{\mathbf{r}}') = \sum_{p=0}^{P-1} \exp[jp\Theta_P(t, \bar{\mathbf{r}}_0, \bar{\mathbf{r}}')], \quad (2.82)$$

where

$$\Theta_P(t, \bar{\mathbf{r}}_0, \bar{\mathbf{r}}') = \Delta\omega(t - \tau_0) - k_0\Delta d_{\hat{\mathbf{y}},p}\kappa_y - \Delta k\hat{\boldsymbol{\kappa}}_0 \cdot \bar{\mathbf{r}}'. \quad (2.83)$$

If the signals are transmitted with the same amplitude and initial phase, Eq. (2.82) can be simplified further to

$$\text{AF}_P(t, \bar{\mathbf{r}}_0, \bar{\mathbf{r}}') = \exp \left[j \left(\frac{P-1}{2} \right) \Theta_P(t, \bar{\mathbf{r}}_0, \bar{\mathbf{r}}') \right] D_P[\Theta_P(t, \bar{\mathbf{r}}_0, \bar{\mathbf{r}}')], \quad (2.84)$$

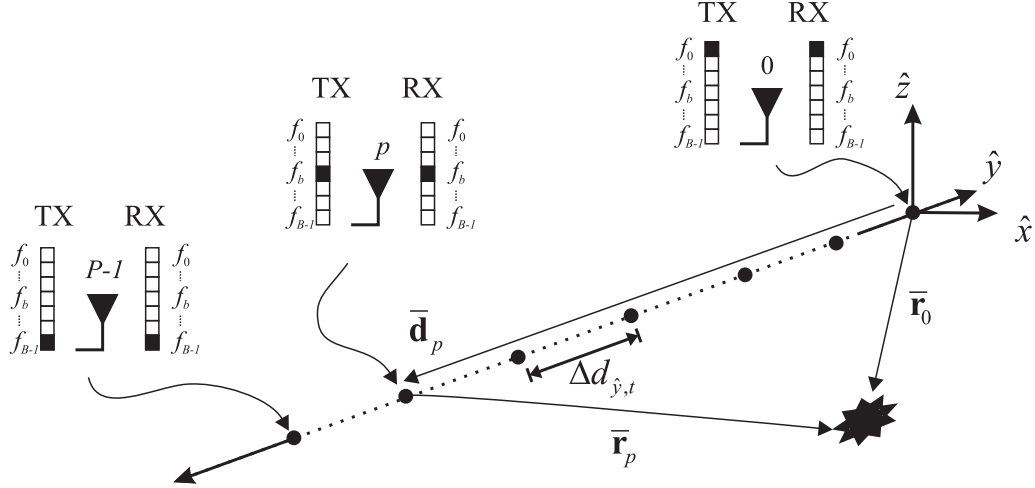
where the Dirichlet kernel $D_P[\Theta_P(t, \bar{\mathbf{r}}_0, \bar{\mathbf{r}}')]$ is the same as defined in Eq. (2.31).

The analytic expression for the LFP-FDA was shown to be in good agreement with electromagnetic models using ideal point sources [16] and was verified experimentally and reported in [4].

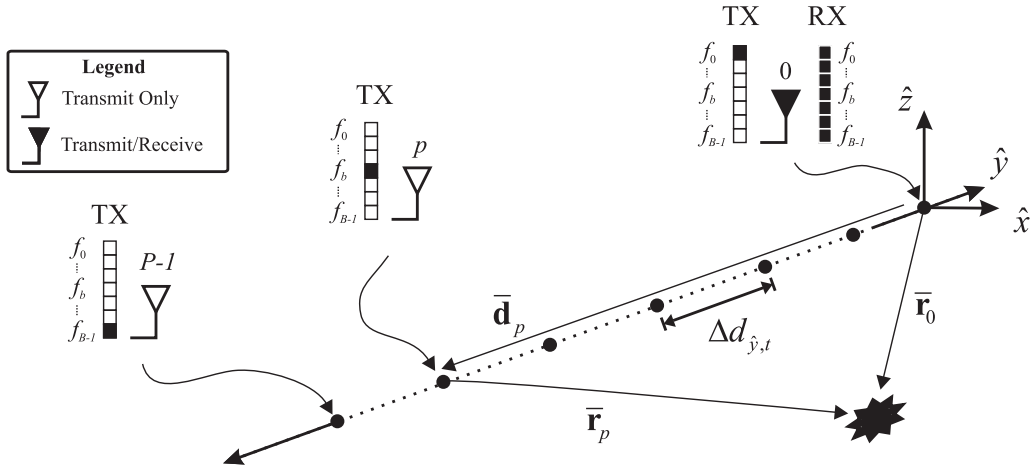
2.6.5 Received Signal and Receiver Models

Two receivers have been studied in relation to LFP-FDA and the transmitter-receiver configurations are shown in Fig. 2.17. The first receiver was used in [7] and is shown in Fig. 17(a). It is assumed that the signals do not have overlapping spectrums and that each array element is receptive only to the frequency it transmitted. A vectorized STAP model was developed for the transmitted and the received signal using the space-time snapshot [30]. If each array element can only receive signals within its transmit bandwidth, there's limited opportunity to study generalized FDA using this model.

The second receiver model is shown in Fig. 17(b) and was used in [16]. The configuration does not use any processing across the array; instead, it was recognized that the transmitted LFP-FDA far-field amplitude has a similar envelope to a matched filtered LFM signal. A single quadrature demodulated received signal is used directly



(a) The FDA transmit-receive configuration used in the GMTI study [7]. Note that each sensor receives only the frequency that it transmits. The configuration represents P independent radar systems.



(b) The FDA transmit-receive configuration used in the SAR study [16]. Note that all sensors transmit using separate frequencies and only a single sensor receives the multi-frequency signal.

Figure 2.17. Transmit-receive configurations: LFP-FDA for STAP and SAR.

in a modified CBA to perform SAR image reconstruction. The CBA is functionally similar to regular array processing except it is performed across the synthetic aperture.

The transmitted signal model in Section 2.6.2 accounted for the signal at the target's position $\bar{\mathbf{r}}'$. The model for the received signal assumes that only the reference element at $\bar{\mathbf{R}}(t)$ collects the reflected signals. With either zero initial phase or a linear

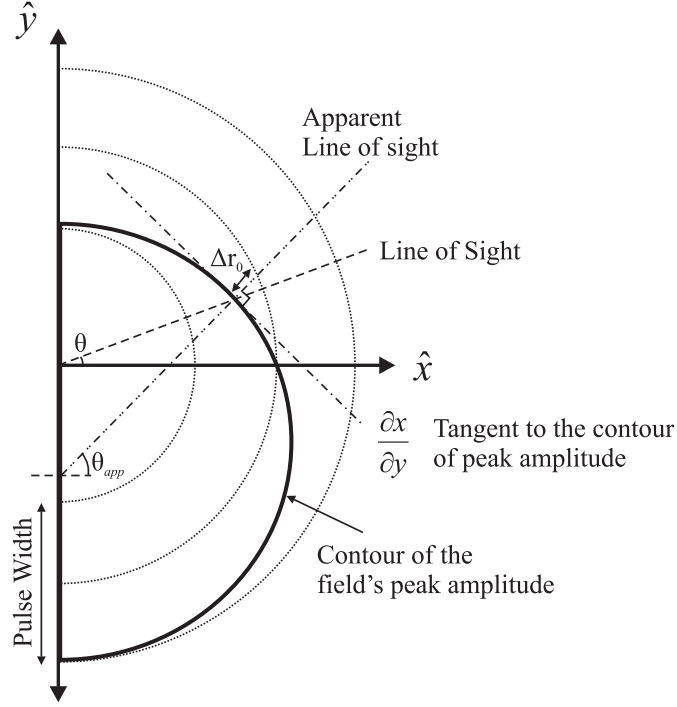


Figure 2.18. Apparent collection geometry. Geometry for the apparent collection locations shown for a positive frequency progression. For positive azimuth angles the peak lags the center of the wave making a target along the LOS appearing further from the radar, and the plane wave appears to have originated at an apparent azimuth angle.

phase progression across the elements, the resulting waveform has a single main lobe in range.

The signal received at the reference element, $p = q = 0$, from a target at $\bar{\mathbf{r}}'$, with reflectivity $\rho_{\bar{\mathbf{r}}'}$, is

$$r_q(t, \bar{\mathbf{r}}', \bar{\mathbf{r}}_0) = \rho_{\bar{\mathbf{r}}'} \exp[j\omega_c(t - 2\tau_0)] \exp(-j2\bar{\mathbf{k}}_c \cdot \bar{\mathbf{r}}') \\ \times \exp\left[-j\left(\frac{P-1}{2}\right)k_0\Delta d_{\hat{y},t}\kappa_y\right] D_P[\Theta_Q(t, \bar{\mathbf{r}}', \bar{\mathbf{r}}_0)], \quad (2.85)$$

where the argument of the Dirichlet kernel is

$$\Theta_Q(t, \bar{\mathbf{r}}', \bar{\mathbf{r}}_0) = \Delta\omega(t - 2\tau_0) - k_0\Delta d_{\hat{y},p}\kappa_y - 2\Delta k \hat{\mathbf{k}}_0 \cdot \bar{\mathbf{r}}'. \quad (2.86)$$

It was of interest in [16] to locate the signal's peak amplitude within the overall pulse for use in the modified BPA. Solving

$$\frac{1}{2}\Theta_Q(t, \mathbf{r}', \mathbf{r}_0) = 0, \quad (2.87)$$

in terms of t yields the round-trip time of the envelope's peak to a target at \mathbf{r}' (referred to as the apparent round-trip time) of

$$t_{app} = 2\tau_0 + \frac{2\hat{\mathbf{\kappa}}_0 \cdot \mathbf{r}'}{c} + \frac{\Delta d_{\hat{y},t}\kappa_y}{\lambda_0\Delta f}. \quad (2.88)$$

In addition to the apparent time, it is possible to find an apparent azimuth angle. For any angle, a line tangential to the contour of peak field amplitude is not parallel with the line normal to the wavevector. This is illustrated in Fig. 2.18. As a result it appears that the non-uniform plane wave propagated as a uniform plane wave with an apparent angle θ_{app} . The apparent angle is found by calculating the gradient to the field's contour of peak amplitude in the x - y plane and projecting its normal back to the \hat{y} -axis.

To find the apparent azimuth angle, Eq. (2.88) is converted to a function of range. The resulting equation is implicitly differentiated in terms of x and y on the $x - y$ plane to find the tangent to the contour at an arbitrary point

$$\frac{\partial x}{\partial y} = -\frac{(y - R_y) + \frac{\Delta d_{\hat{y},t}f_0}{\Delta f}(1 + \kappa_y^2)}{(x - R_x) + \frac{\Delta d_{\hat{y},t}f_0}{\Delta f}(\kappa_x\kappa_y)}. \quad (2.89)$$

Evaluating (2.89) at the scene center, $y = Y_c$ and $x = X_c$, and taking the inverse

tangent provides the apparent azimuth angle of the plane wave

$$\theta_{app} = -\tan^{-1} \left[\frac{(Y_c - R_y) + \frac{\Delta d_{\hat{y},t} f_0}{\Delta f} (1 + \kappa_y^2)}{(X_c - R_x) + \frac{\Delta d_{\hat{y},t} f_0}{\Delta f} (\kappa_x \kappa_y)} \right]. \quad (2.90)$$

The apparent azimuth angle and apparent time can be used to create a set of apparent collection locations and to modify the BPA.

2.6.6 Synthetic Aperture Radar Application Study

In the modified BPA, it was found that if $\Delta f > 0$ was applied for $R_y \in [-\frac{L_s}{2}, 0)$ and $\Delta f < 0$ for $R_y \in [0, \frac{L_s}{2}]$ that the apparent collection locations form a wider aperture from which to perform the BPA. First, the differential time in Eq. (2.88) is used to modify the range

$$\begin{aligned} r_{app} &= r_0 + \Delta r_0 \\ &= r_0 + \frac{\Delta d_{\hat{y},t} \kappa_y}{\Delta f}. \end{aligned} \quad (2.91)$$

For each of the actual collection locations, apparent collection locations are calculated using Eq. (2.90) and Eq. (2.91)

$$\begin{aligned} R_{x,app} &= X_c - r_{app} \kappa_x (\psi_0, \theta_{app}), \\ R_{y,app} &= Y_c - r_{app} \kappa_y (\psi_0, \theta_{app}), \\ R_{z,app} &= Z_c - r_{app} \kappa_z (\psi_0, \theta_{app}). \end{aligned} \quad (2.92)$$

Defining a new line-of-sight unit vector allows the remaining apparent geometry vectors to be written

$$\begin{aligned}
\hat{\mathbf{\kappa}}_{app} &= \hat{\mathbf{x}}\kappa_x(\psi_0, \theta_{app}) + \hat{\mathbf{y}}\kappa_y(\psi_0, \theta_{app}) + \hat{\mathbf{z}}\kappa_z(\psi_0, \theta_{app}), \\
\bar{\mathbf{r}}_{app} &= r_{app} \hat{\mathbf{\kappa}}_{app}, \\
\bar{\mathbf{k}}_{app} &= k_c \hat{\mathbf{\kappa}}_{app}, \\
\bar{\mathbf{R}}_{app} &= \hat{\mathbf{x}}R_{xapp} + \hat{\mathbf{y}}R_{yapp} + \hat{\mathbf{z}}R_{zapp}.
\end{aligned} \tag{2.93}$$

The received signal's phase needs to be corrected because the collection locations have been modified. The phase component

$$\exp[j\omega_c(t - 2\tau_0)] \exp\left[-j\left(\frac{P-1}{2}\right)k_0\Delta d_{\hat{\mathbf{y}},t}\kappa_y\right], \tag{2.94}$$

is calculated from the geometry and is removed by the receiver. The first phase correction accounts the change in apparent range and

$$\exp\left(-j\omega_c\frac{\Delta d_{\hat{\mathbf{y}},t}\kappa_y}{\lambda_0\Delta f}\right), \tag{2.95}$$

corrects the phase corresponding to the range adjustment. The second correction

$$\exp[-j2\bar{\mathbf{r}}' \cdot (\bar{\mathbf{k}}_{app} - \bar{\mathbf{k}}_c)], \tag{2.96}$$

accounts for the change in the wave vector and should be applied for all grid points in the image for each collection location. However, in [16] this is left uncorrected, and in extreme cases the phase error causes the image to defocus away from the scene's center.

The Point Spread Function (PSF) was derived in [16] for the cross range axis. For

an ideal point target at $\bar{\mathbf{r}}'$ with reflectivity $\rho_{\bar{\mathbf{r}}'}$ the cross-range PSF for the LFP-FDA simplifies to

$$\text{PSF}_{cr} = \rho_{\bar{\mathbf{r}}'} \int_{\theta_{app}} d\theta_{app} \exp \left[-j2k_c \left(y' - y'' \frac{\theta_{app}}{\theta_0} \kappa_y \right) \right]. \quad (2.97)$$

Although not explicitly shown here, the PSF is a function of L_s and, and with all other parameters fixed, Δf [16].

Although the FDA was shown to improve cross-range resolution in [16], there are several limitations to the approach. First, the scene size is small compared to the area potentially illuminated by the FDA. Second, the configuration is sensitive to many non-ideal conditions in a practical system such as phase noise and timing errors. These conditions may cause the field pattern to lose its well-defined shape and the PSF performance would decrease.

The technique of reversing the frequency progression half-way through the collection was beneficial to cross-range resolution performance for a point target at the scene center. It would be difficult to conclude that the technique would offer improvement for all locations in an extended scene; however, similar techniques may have some benefit in either SAR or general array processing. Next recommendations for future research offered by previous FDA researchers are reviewed.

2.6.7 Recommended FDA Research

The first recommendation, from [4], is to study waveform diversity using the FDA framework. Specifically, the author suggests the configuration can be extended to use chirp-diversity, phase coded signals, amplitude weighted signals, and stepped-frequency or Costas coded signals. The second recommendation in the same study, is to investigate non-uniform element spacing similar to the “wavelength array” already considered in [39]. The third recommendation is to investigate a configuration that

allows simultaneous SAR and GMTI.

The fourth recommendation, from [16], is to investigate different array configurations to gain more directivity from the array, which is also being considered in MIMO [20]. The final recommendation is to use a full-scene simulation tool to study FDAs performance at imaging extended scenes.

None of the aforementioned recommendations are the focus of the study. However, apart from the recommendation for simultaneous GMTI-SAR waveform configurations, the remaining recommendations will be examined to varying degrees. As stated in Chapter I, a waveform diversity study without optimization would be a hit-and-miss approach, and an expected outcome of this study is to provide a solid analytic foundation for future waveform diversity research using the FDA configuration.

2.7 Chapter Summary

This chapter reviewed important literature pertaining to this FDA study. First, the layered sensing and waveform diversity concepts introduced in Chapter I were expanded and discussed in terms of other approaches to the same challenge. A contrast was made between between the MIMO and the FDA approaches.

Second, a brief review of CFA theory was presented. The review introduced key concepts such as array design using the DFT, the array factor, performance measures and basic receiver processing. In comparison, the FDA literature lacks a suite of mature analytic techniques to analyze and design FDA configurations.

Third, the ambiguity function was introduced as a measure of a signal's range and Doppler measurement performance. The narrowband versus wideband Doppler models were discussed in terms of the OFDM signal along with the bounds of the narrowband model's validity. Ambiguity functions have been developed by the MIMO

community to address a configuration's angular measurement accuracy. The same concept will be extended to the FDA configuration.

Fourth, the OFDM signal and model was summarized. The OFDM model is also being considered for a variety of radar applications. However, the OFDM signal used in a single transmitter potentially suffers from poor PAPR, and methods to improve the PAPR through phase coding was discussed. The OFDM field pattern was shown to be a rotated version of the CFA pattern when plotted on the (t, u) plane. The results concerning the OFDM signal performance and PAPR reduction techniques are likely to be valid when discussing the received FDA signal.

Finally, LFP-FDA work presented in [16] was summarized. The key features of the summary was that the FDA signal model is similar to the OFDM signal model and the LFP-FDA field pattern was similar to a skewed version of either the CFA or OFDM field pattern. It would be interesting to explore the relationship further. An interesting approach to process the LFP-FDA returns into a SAR image was reviewed. Although the technique will not be explored further in this study, the results provide useful insight. Recommendations made in previous research suggest that generalizing the FDA signal model to allow waveform diversity would be a significant contribution to the field. In Chapter III, the research methodology applied to this study is explained.

III. Research Methodology

3.1 Chapter Overview

The aim of this chapter is to bridge the background theory with the new work that is developed in this research. Chapter II reviewed literature that is relevant to this study. The topics included CFA design, performance characterization and receiver processing; the ambiguity function and the narrowband and wideband Doppler models; OFDM signal model and performance issues; and finally, recent FDA theory developed to support a SAR application study. Fig. 2.1 pictorially represented how each of those topics relate to the research objective. The new work developed to help address the research objective are represented in Fig. 3.1.

There are several aspects that were not considered in previous FDA work such as generalized transmit signal characterization; signal power; angular resolution; delay and Doppler ambiguity performance; and generalized signal design. Furthermore, FDA analysis using standard geometric and monochromatic techniques was difficult, and required a constrained configuration.

The broad objective of this study is to examine waveform diversity using the FDA configuration. To both support the conclusions, and to provide a fair comparison with competing technology, several fundamental areas will be examined using a generalized signal model. The methods applied to investigate the generalized FDA are discussed in more detail in subsequent sections. However, in brief, the methodology focusses on an analytic signal-level model, numerical analysis using the signal-level model, and representative measurements using the radar instrumentation laboratory.

First, the transmit signal performance is characterized in terms of transmit power and angular difference. A spectral analysis method will be developed to help understand the underlying signal structure. Second, the Doppler scaled received signal is

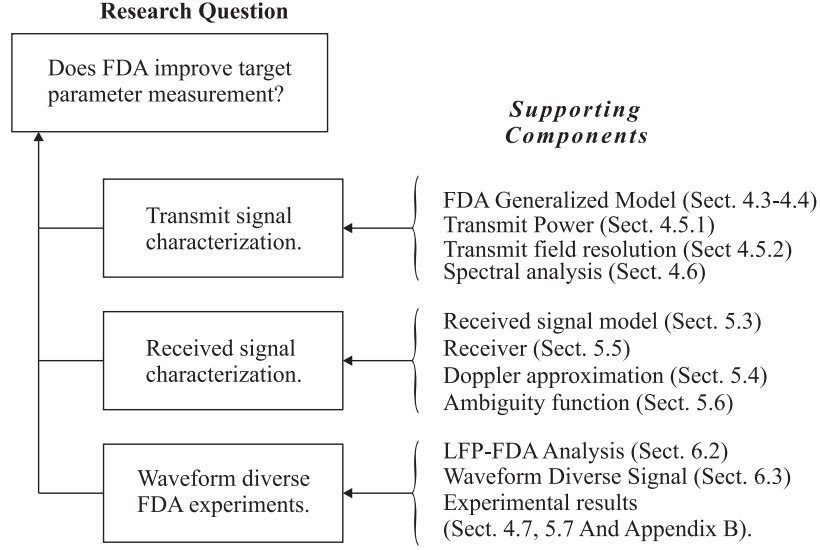


Figure 3.1. Research overview diagram.

approximated and processed using a generic matched filter receiver. The receiver's measurement accuracy is characterized by an AF. The AF is used to compare the fundamental LFP-FDA measurement accuracy to the CFA. A method to coherently combine a signal and its complement is presented. Finally, a performance results for an FDA using full diversity is compared to the LFP-FDA.

3.2 Limitations to Scope and Assumptions

Before discussing what will be covered by this study, it is worth discussing the limitations of this study. First, the signal model is idealized and the results generated may represent the best-case performance. Real performance depends on a variety of practical issues such as hardware quality and electromagnetic effects. Second, while the spectral relationship between the field pattern and the element signals is well established in CFA theory, the method proposed in this study is different from the methods in the current literature. The method's validity and acceptance is a risk to the research. Third, some FDA configurations may not be achievable due to system complexity and cost. Where possible, theoretical performance will be compared to

measured data providing some indication of a configuration's realizability. Fourth, the focus of the research will be to characterize the transmit waveform and propose a suitable receiver. Only a cursory examination of waveform diverse signal performance and SAR will be performed, primarily to test the field characterization techniques and performance of the receiver processing. Finally, a discussion on parameter estimation should include deleterious noise and clutter, and is not complete without characterizing the signal in terms of statistical performance. Statistical performance is not considered here and it will limit any claims of improved parameter estimation.

3.3 Transmit Signal Characterization

Previous FDA research developed an array factor that describes the LFP-FDA field pattern and has verified the field pattern using CEM modeling and experimental results. However, there are other properties of the transmit signal that have not been characterized. Using the generalized FDA signal model the signal field's average transmitted power will be determined allowing the power pattern [9] to be established. This should allow a fair comparison between the FDA and CFA in terms of transmit power. It is not expected that the expression will reduce to a simple, closed-form solution and the power will be assessed numerically.

It doesn't make sense to call the difference between the transmit signal at two different angles *angular resolution* because the resolution is a performance characteristic of the receiver. However, if the transmit signal is received by a single antenna located at the origin the signals arriving from different directions can be distinguished providing the energy difference between the signal and a matched filter is large. It is using this interpretation, and following the angular resolution work in [46], that a *pseudo-beam* is defined for the FDA's transmit signal. The pseudo-beam should provide a similar measurement to the CFA array factor's FNBW to described how the

transmit array's spatial diversity impacts spatial resolution. Similar to the average signal power, it is not expected that the signal difference will result in a closed-form solution.

Finally, a spectral analysis technique will be developed to analyze the FDA. The method will be similar to the DFT method used in CFA pattern synthesis, and the Fourier optics approach to relate an aperture and the diffraction pattern. This may improve insight into FDA design and analysis once consideration moves beyond the LFP-FDA configuration. There is an inherent risk that without due care in justifying the technique that it may not be accepted.

Where possible, experimental data will be used to support the analytic results. An unfortunate limitation is that the experimental set-up is limited to two channels. However, in the lab the constant modulus requirement should not be a problem and multiple signals can be multiplexed onto each of the transmitters.

By characterizing the transmit signal, it should be possible to compare the FDA transmit signal performance to existing technology such as CFA. The analysis should provide insight on how the FDA could be designed to provide improved performance in future research.

3.4 Received Signal Processing

The signal received from an ideal point target is modeled at the receiver where the approximation to the Doppler scaling is an important consideration. An intermediate approximation to the Doppler scaling is considered for the signal model where Doppler shifts are evaluated for each sub-carrier frequency. The intermediate approximation is compared to the narrowband approximation to verify that it more accurately represents the Doppler scaling for the multi-carrier signal.

Once the signal is collected by a receiver array the it is processed using a set of

filters matched to both the signal and estimated target parameters. The AF for the FDA receiver is based on the approach to AF design summarized in Chapter II. The AF is subsequently used to compare FDA configurations and performance.

Similar to the transmit signal characterization, limited experimentation will be used to test the receiver's delay and angular measurement accuracy. Two limitations to the practical receiver experiments is that the signal's duration is limited due to the relatively small lab space and the impact of Doppler cannot be measured.

Developing a standard processing method and signal measurement tool will allow different configurations to be compared. It will then be possible to use the insight gained through the spectral analysis and ambiguity performance to design waveforms for future studies.

3.5 Comparisons

Using the methods developed in Chapters IV and V the performance of the LFP-FDA configuration will be compared to the CFA to determine whether there is any fundamental performance improvement. The impact of altering the LFP-FDA's sub-carrier and inter-element spacing is examined. The LFP-FDA will be then used to examine whether the method of increasing SAR cross-range resolution by adding a signal and its complement has greater applicability in FDA array theory. A multiplicative combining method will also be examined. Finally, full diversity will be applied to the FDA to evaluate the resulting performance.

3.6 Chapter Summary

The activities supporting the research goals were presented in this chapter. The bulk of the work involves developing the fundamental signal-level analysis of the transmitted and received, generalized FDA signal. Several techniques for characterizing

the CFA, OFDM and FDA configurations were summarized in Chapter II providing the background to this study, and Chapter III summarized how these techniques will be extended to the generalized FDA. In the following chapters the generalized FDA transmit and receive configurations and performance are explored in more detail.

IV. Transmit Signal Model and Analysis

4.1 Chapter Overview

In CFA theory there are several features of the transmitted far-field amplitude that are considered important to characterize a transmit configuration such as the transmit power, the array factor and the beamwidth. Additionally, a variety of techniques exist for designing a CFA's complex weights to achieve a desired array factor. In comparison, generalized FDA analysis is currently devoid of these measures. The aim of this chapter is to characterize the configuration's average transmit power, its pseudo-beamwidth (for lack of a better term), and a spectral method to decompose and understand the field's characteristics.

4.2 Transmit Signal Geometry

This study primarily uses the geometric framework developed in [16]. This was introduced by the CFA summary in Section 2.3.1 and was extended by the FDA summary in Section 2.6.1 to include a SAR collection geometry. There was a difference between the two sections in terms of array element locations.

In this study the array is centered such that the phase reference corresponds to the array's geometric center regardless whether it coincides with an element. The displacement to the p th transmitter from the phase center is

$$\bar{\mathbf{d}}_p = \hat{\mathbf{y}}d_p, \quad (4.1)$$

and for a ULA

$$\bar{\mathbf{d}}_p = \hat{\mathbf{y}}\Delta d_{\hat{\mathbf{y}},t} \left(p - \frac{P-1}{2} \right). \quad (4.2)$$

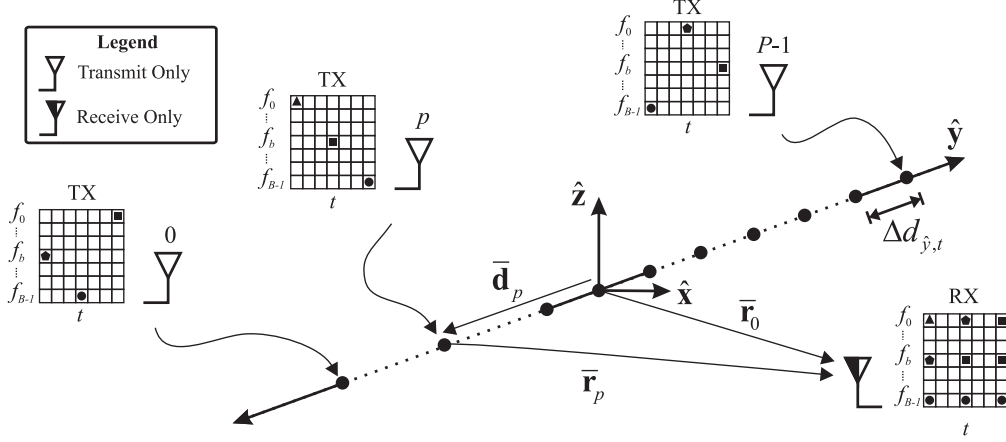


Figure 4.1. Transmit configuration: generalized FDA. The generalized FDA configuration provides the ability to transmit time, frequency, amplitude, phase and chirp coded signals from each the array's elements.

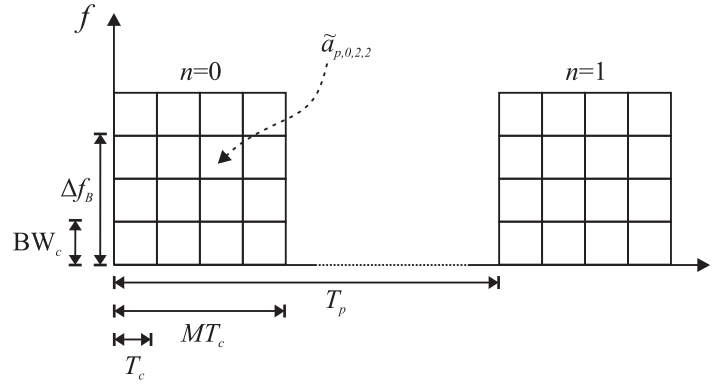


Figure 4.2. Time-frequency coded transmit signal. Schematic of the generalized transmit signal shown for $M = B = 4$ and $N = 2$.

where $\Delta d_{\hat{y},t}$ is the inter-element spacing. Centering the array around the phase reference reduces the extra phase terms that manifest in other geometries.

4.3 Transmit Signal

The arbitrary signal model allows a wide range of signal and spatial configurations at the expense of simplicity. Most modeling elements and approximations to the transmit signal were discussed previously in the relevant sections of Chapter II. Consider a generalized radar signal as a weighted sum of a set of time and frequency shifted elementary signals. The p th transmitter's Coherent Processing Interval (CPI)

and signal is

$$\begin{aligned}
s_p(t) &= \exp(j\omega_0 t) \sum_{b=0}^{B-1} \sum_{m=0}^{M-1} \sum_{n=0}^{N-1} \tilde{a}_{p,b,m,n} s_b(t - mT_c - nT_p) \\
&= \exp(j\omega_0 t) \sum_{b=0}^{B-1} \sum_{m=0}^{M-1} \sum_{n=0}^{N-1} \tilde{a}_{p,b,m,n} \hat{b}(t - mT_c - nT_p) \\
&\quad \times \exp[j\Delta\omega_b(t - mT_c - nT_p)].
\end{aligned} \tag{4.3}$$

The difference between this signal model and the previous FDA signal models is subtle but the implication has significant consequence on the hardware design. The previous FDA models were based on an array where each element has an independent oscillator operating at a unique frequency, transmitting a pulsed waveform. The independent oscillators will cause coherency difficulties in the receiver processing stage. Equation (4.3) represents a set of arbitrary baseband signals modulated by a single, local oscillator. This allows a degree of coherency across the array and allows the returns received by every element in the array to be combined more easily by the processor.

A schematic of the signal model $s_p(t)$ for $M = B = 4$ and $N = 2$ is shown in Fig. 4.2. Starting at the overall waveform level and then narrowing the focus, the CPI consists of N pulses that are transmitted with a constant Pulse Repetition Interval (PRI) T_p seconds with an associated Pulse Repetition Frequency (PRF) f_p Hertz, where $f_p = T_p^{-1}$. Within each PRI's pulse, there are up to M temporal chips each with duration T_c and satisfying $MT_c \ll T_p$. For each temporal chip index m , the transmitter can transmit up to B spectral chips using one of the B sub-carriers with baseband frequency $\Delta\omega_b = 2\pi\Delta f_b$. Each temporal-spectral chip is modulated by a complex weight

$$\tilde{a}_{p,b,m,n} = A_{p,b,m,n} \exp(j\varphi_{p,b,m,n}), \tag{4.4}$$

and the pulse shaping function, $\hat{b}(t)$, was defined in Eq. (2.18), Chapter II. The complex weight's amplitude is limited to $A_{p,b,m,n} \in [0, A_{max}]$ where A_{max} is the largest allowable amplitude. Similarly, the weight's phase will satisfy $\varphi_{p,b,m,n} \in [0, 2\pi)$.

The differential frequency term for each temporal-spectral chip,

$$\exp [j\Delta\omega_b (t - mT_c - nT_p)],$$

begins with zero phase. This is unlike the previous FDA work that assumed uncoupled, free-running oscillators. Adding quadratic phase to Eq. (4.4) allows Linear Frequency Modulation (LFM) to be modeled to study chirp diversity. Inclusive of the quadratic phase component, the model becomes

$$\begin{aligned} s_p(t) = & \sum_{b=0}^{B-1} \sum_{m=0}^{M-1} \sum_{n=0}^{N-1} \tilde{a}_{p,b,m,n} \hat{b}(t - mT_c - nT_p) \\ & \times \exp(j\omega_0 t) \exp[j\Delta\omega_b (t - mT_c - nT_p)] \\ & \times \exp[j\pi\vartheta_{p,b,m,n} (t - mT_c - nT_p)^2], \end{aligned} \quad (4.5)$$

where the chirp rate, ϑ , is

$$\vartheta_{p,b,m,n} = \pm \frac{\text{BW}_\vartheta}{T_c}, \quad (4.6)$$

and BW_ϑ is the bandwidth spanned by the chirp. The set of signal parameters can be collected in a set $\tilde{\Upsilon}$ defined as

$$\tilde{\Upsilon}_{p,b,m,n} \triangleq (A_{p,b,m,n}, \varphi_{p,b,m,n}, \vartheta_{p,b,m,n}). \quad (4.7)$$

In the following development, Eq. (4.3) will be used almost exclusively and Eq. (6.6) is provided as a reference for later chapters.

The minimum, maximum and center baseband frequencies are

$$\begin{aligned}
\Delta\omega_{min} &= \Delta\omega_0 \\
\Delta\omega_{max} &= \Delta\omega_B \\
\Delta\omega_c &= \frac{\Delta\omega_B - \Delta\omega_0}{2}.
\end{aligned} \tag{4.8}$$

The RF frequencies are similarly defined

$$\begin{aligned}
\omega_{min} &= \omega_0 + \Delta\omega_0 \\
\omega_{max} &= \omega_0 + \Delta\omega_B \\
\omega_c &= \omega_0 + \Delta\omega_c,
\end{aligned} \tag{4.9}$$

with associated wavelengths

$$\begin{aligned}
\lambda_{min} &= \frac{2\pi c_0}{\omega_{max}} \\
\lambda_{max} &= \frac{2\pi c_0}{\omega_{min}} \\
\lambda_c &= \frac{2\pi c_0}{\omega_c},
\end{aligned} \tag{4.10}$$

and wavenumbers

$$\begin{aligned}
k_{min} &= \frac{\omega_{min}}{c_0} = k_0 + \Delta k_{min} \\
k_{max} &= \frac{\omega_{max}}{c_0} = k_0 + \Delta k_{max} \\
k_c &= \frac{\omega_c}{c_0} = k_0 + \Delta k_c.
\end{aligned} \tag{4.11}$$

A single time-frequency chip occupies a baseband bandwidth $\text{BW}_c = T_c^{-1}$ and the

bandwidth spanned by the set of sub-carriers is

$$\text{BW}_s = \text{BW}_c + \frac{\Delta\omega_{max} - \Delta\omega_{min}}{2\pi}. \quad (4.12)$$

There is no assumption that the frequencies are regularly spaced or that they are orthogonal to each other. However, the set of overlapping and orthogonal sub-carriers is useful for analysis in which case $\Delta f_b = b\Delta f = bT_c^{-1}$ for $b \in [0 \dots B-1]$.

The constraints limiting true generality are that each chip shares a common pulse duration T_c and a common PRI T_p . The constraints are suitable for analysis and can easily be relaxed for numerical analysis or experimentation. Despite the constraints on Eq. (4.3), it is possible to represent a diverse set of waveforms transmitted by P transmitters, including CFA, OFDM, and LFP-FDA. For example, Fig. 2.16 in Chapter II illustrates signal field patterns for CFA, OFDM and LFP-FDA configurations. The CFA signal field pattern is specified by setting $M = N = B = 1$ and the OFDM signal field pattern is specified by setting $N = P = 1$ with orthogonal frequencies $\Delta\omega_b = b2\pi T_c^{-1}$. The LFP-FDA signal field pattern is specified by setting $B = P$, $M = N = 1$, with orthogonal frequencies $\Delta\omega_b = b2\pi T_c^{-1}$ and weights

$$\tilde{\Upsilon}_{p,b,m,n} = \begin{cases} (1, b\pi, 0), & p = b \\ 0, & \text{otherwise.} \end{cases} \quad (4.13)$$

4.4 Transmit Field

Given a set of signals $s_p(t)$ transmitted from ideal antenna elements configured as a linear array, the signal at a point $\bar{\mathbf{r}}_0$ is

$$s(t, \bar{\mathbf{r}}_0) = \sum_{p=0}^{P-1} K_p s_p(t - \tau_p). \quad (4.14)$$

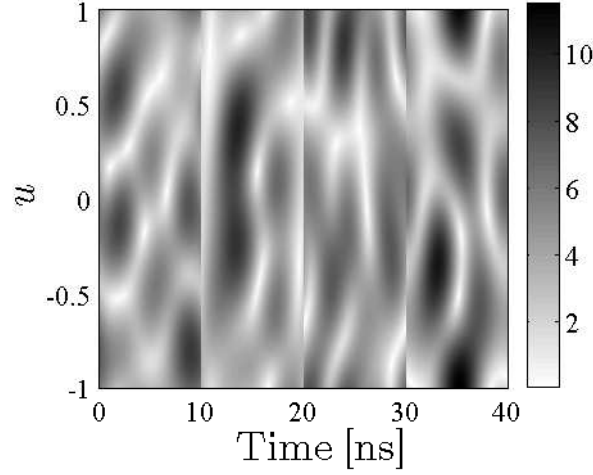


Figure 4.3. Signal field pattern: randomly weighted FDA. Signal field pattern plot with $P = B = 4$, $M = 2$ and $N = 1$ where the $\tilde{a}_{p,b,m,n}$ are circularly Gaussian random variables.

Applying both the far-field and narrowband approximations to the generic signal in Eq. (4.3) the scalar transmit field at $\bar{\mathbf{r}}_0$ is proportional to

$$s(t, \bar{\mathbf{r}}_0) = K_{tx} \sum_{p=0}^{P-1} \sum_{b=0}^{B-1} \sum_{m=0}^{M-1} \sum_{n=0}^{N-1} \tilde{a}_{p,b,m,n} \hat{b}(t - \tau_0 - mT_c - nT_p) \exp[j\omega_0(t - \tau_0 + \Delta\tau_p)] \\ \times \exp[j\Delta\omega_b(t - \tau_0 + \Delta\tau_p - mT_c - nT_p)]. \quad (4.15)$$

The development focusses on the signal properties and not propagation it is possible to consider that $K_{tx} = 1$ without loss of generality.

Consider the signal field shown in Fig. 4.3 generated using Eq. (4.15) with $\tau_0 = 0$, $P = B = 4$, $M = 2$, $N = 1$, $T_c = 10\text{ns}$, $\Delta f_b = bT_c^{-1}$ and the complex weights are unit variance, circular Gaussian random variables. Apart from the question whether the field is physically realizable, it is impossible to derive a closed-form expression to describe the field's amplitude or array factor. It is also difficult to compare the performance of this signal to either the CFA or the LFP-FDA in terms of delay, Doppler or angular resolution; transmit beamwidth; or transmit power. Such generalized signal's and their fields motivates developing techniques to compare different configurations.

4.5 Transmit Field Characteristics

Section 2.3 reviewed several transmit field properties that are useful in CFA analysis such as the transmit power and the beamwidth. The LFP-FDA's instantaneous power has a peak that is dependent on both angle and range, however, the average power may be a more useful characteristic to compare the FDA's performance to other configurations. The transmit field's beamwidth is more difficult to envision because the LFP-FDA transmit pattern does not have a beam in the typical sense. However, it is possible to define a pseudo-beamwidth that characterizes the difference between the field's signals along two different angles. This may be useful in discussions comparing how much angular resolution is due to the transmit waveform as opposed to the receiver array.

4.5.1 Average Power

The average power of a signal $s(t, \bar{\mathbf{r}}_0)$ with duration T collected by an ideal receiver is proportional to

$$P_{ave}\{s(t, \bar{\mathbf{r}}_0)\} \triangleq \frac{1}{T} \int_{\tau_0}^{\tau_0+T} s(t, \bar{\mathbf{r}}_0) s^*(t, \bar{\mathbf{r}}_0) dt. \quad (4.16)$$

The average power considered next, neglects the period of time that the radar does not transmit. To determine the true average power over a CPI the power needs to be averaged over the CPI's duration.

Substituting Eq. (4.15) into Eq. (4.16) and simplifying the result (see Appendix A) gives the collected signal's average power

$$P_{ave}\{s(t, \bar{\mathbf{r}}_0)\} = \frac{1}{MN} \sum_{p=0}^{P-1} \sum_{p'=0}^{P-1} \sum_{b=0}^{B-1} \sum_{b'=0}^{B-1} \sum_{n=0}^{N-1} \sum_{m=0}^{M-1} \tilde{a}_{p,b,m,n} \tilde{a}_{p',b',m,n}^* \exp[j(\omega_b \Delta \tau_p - \omega_{b'} \Delta \tau_{p'})] \\ \times \exp[j(\Delta \omega_b - \Delta \omega_{b'}) \frac{T_c}{2}] \text{sinc}[(\Delta \omega_b - \Delta \omega_{b'}) \frac{T_c}{2}], \quad (4.17)$$

where the un-normalized sinc function is

$$\text{sinc}(x) \triangleq \frac{\sin x}{x}. \quad (4.18)$$

The signal was integrated over time, corresponding to range, and the resulting average signal power is a function of angle. When $B = 1$ Eq. (4.17) simplifies to Eq. (2.48) in Chapter II for the CFA signal's average transmit power.

Next, considering the LFP-FDA with model parameters in Section 4.3, it follows that Eq. (4.17) simplifies to

$$\begin{aligned} P_{ave}\{s(t, \bar{\mathbf{r}}_0)\} &= \sum_{p=0}^{P-1} \sum_{p'=0}^{P-1} \exp[j(\omega_p \Delta \tau_p - \omega_{p'} \Delta \tau_{p'})] \\ &\quad \times \text{sinc}\left[(\Delta \omega_p - \Delta \omega_{p'}) \frac{T_c}{2}\right]. \end{aligned} \quad (4.19)$$

For signal's with orthogonal sub-carriers, the argument of the sinc function is

$$(\Delta \omega_p - \Delta \omega_{p'}) \frac{T_c}{2} = \pi(p - p'), \quad (4.20)$$

and

$$\text{sinc}[\pi(p - p')] = \begin{cases} 1, & \text{for } p = p' \\ 0, & \text{otherwise.} \end{cases} \quad (4.21)$$

Finally, the average LFP-FDA transmit power is

$$P_{ave}\{s(t, \bar{\mathbf{r}}_0)\} = P. \quad (4.22)$$

Compared to the CFA transmit power discussed in Section 2.3.5, LFP-FDA's average power is constant in azimuth angle and is independent of the array factor that was

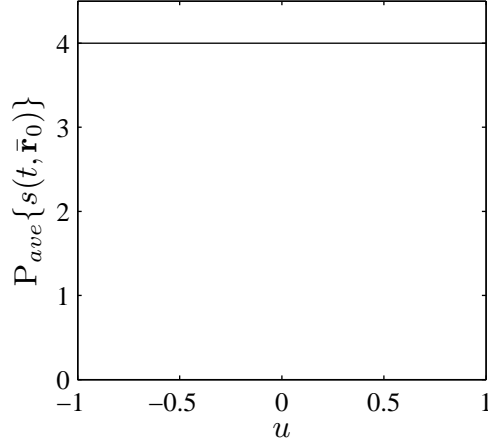


Figure 4.4. Average transmit signal power: LFP-FDA. The average power in the LFP-FDA signal's field for the FDA with configuration in Table 2.3. The average power is proportional to the number of transmitters P .

developed in [16]. As a result, the LFP-FDA field is not directive in the same sense that the CFA power pattern is directive. Equation (4.22) can only be determined analytically in several special cases and will generally be evaluated numerically.

Figure 4.4 shows the average power for the LFP-FDA numerically using Eq. (4.16) and the parameters in Table 2.3. The resulting function is in good agreement with the analytic result in Eq. (4.22).

The average power pattern shown in Fig. 4.5 was calculated for the field pattern produced by the randomly weighted FDA shown in Fig. 4.3. The power is no longer constant in azimuth angle because more than one element transmits a given frequency in a given time period. The average power pattern would be difficult to predict from the signal's field pattern.

4.5.2 Angular Difference

In Chapter II it was shown that a CFA concentrates the transmitted power in a main beam, and reduces power transmitted in the other directions. In terms of the

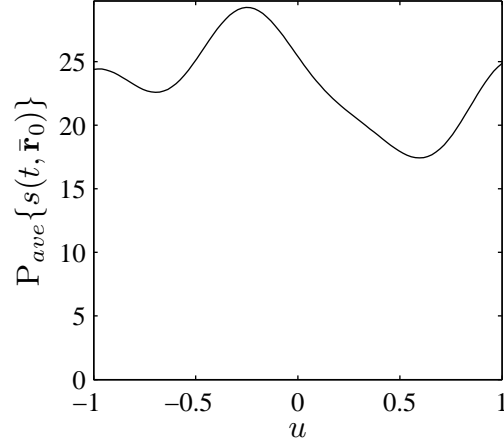


Figure 4.5. Average transmit signal power: randomly weighted FDA. The average power calculation for the FDA with random weights whose field pattern is shown in Fig. 4.3.

transmit field pattern the main beam provides a level of angular discrimination. In other words, the majority of the energy received by the array will come from the sector illuminated by the main beam. Although the LFP-FDA transmits average power in all directions equally, the signal's variation in azimuth angle should provide angular discrimination.

A measure of angular discrimination can be determined by evaluating the difference between the transmit field at two different angles. The distance, or size of the difference, between two signals $s_1(t)$ and $s_2(t)$ is defined as [36]

$$\|s_1 - s_2\|^2 = \int_{-\infty}^{\infty} [s_1(t) - s_2(t)] [s_1(t) - s_2(t)]^* dt, \quad (4.23)$$

which is equivalent to the integrated, square of the difference [46]

$$\begin{aligned}
\|s_1 - s_2\|^2 &= \int_{-\infty}^{\infty} |s_1(t) - s_2(t)|^2 dt \\
&= \int_{-\infty}^{\infty} |s_1(t)|^2 dt + \int_{-\infty}^{\infty} |s_2(t)|^2 dt \\
&\quad - 2\text{Re} \left[\int_{-\infty}^{\infty} s_1(t) s_2^*(t) dt \right], \tag{4.24}
\end{aligned}$$

where $\text{Re}[\cdot]$ is the real part of a complex number. The first two integrals represents the energy, E_1 and E_2 , of $s_1(t)$ and $s_2(t)$, respectively, and last integral represents the inner product between the two signals. To maximize the difference between the two signals it is desirable for the last integral to be as small as possible; or, defining

$$d(s_1, s_2) \triangleq \text{Re} \left[\int_{-\infty}^{\infty} s_1(t) s_2^*(t) dt \right], \tag{4.25}$$

the maximum difference between the two signals occurs when $d(s_1, s_2)$ is minimized.

Let $s_1(t)$ be the signal at $\bar{\mathbf{r}}_0$ expressed in terms of r_0 and the sine of the azimuth angle u

$$\begin{aligned}
s_1(t) &= s(t, \bar{\mathbf{r}}_0) \\
&= s(t, r_0, u), \tag{4.26}
\end{aligned}$$

and $s_2(t)$ is the same transmit signal, at the same range, but offset in the angular parameter by Δu

$$s_2(t) = s(t, r_0, u + \Delta u). \tag{4.27}$$

Substituting Eq. (4.26) and Eq. (4.27) into Eq. (4.24) results in

$$\begin{aligned}
d(s_1, s_2)(\Delta u) = \text{Re} \left\{ \int_{t=\tau_0}^{\tau_0+MT_c+(N-1)T_p} \sum_{p=0}^{P-1} \sum_{p'=0}^{P-1} \sum_{b=0}^{B-1} \sum_{b'=0}^{B-1} \sum_{m=0}^{M-1} \sum_{n=0}^{N-1} \tilde{a}_{p,b,m,n} \tilde{a}_{p',b',m,n}^* \right. \\
\times \hat{b}(t - \tau_0 - mT_c - nT_p) \hat{b}^*(t - \tau_0 - mT_c - nT_p) \exp[j\omega_0(t - \tau_0 + \Delta\tau_p)] \\
\times \exp[j\Delta\omega_b(t - \tau_0 + \Delta\tau_p - mT_c - nT_p)] \exp[-j\omega_0(t - \tau_0 + \Delta\tau_{p'})] \\
\times \exp[-j\Delta\omega_{b'}(t - \tau_0 + \Delta\tau_{p'} - mT_c - nT_p)] \left. dt \right\}. \quad (4.28)
\end{aligned}$$

The delays $\Delta\tau_p$ and $\Delta\tau_{p'}$ are related to the angle through

$$\begin{aligned}
\Delta\tau_p &= \frac{d_p}{c_0} u_0 \\
\Delta\tau_{p'} &= \frac{d_{p'}}{c_0} (u_0 + \Delta u), \quad (4.29)
\end{aligned}$$

and the remaining signal parameters are common between $s_1(t)$ and $s_2(t)$.

After simplifying Eq. (4.28) (see Appendix A) the difference term is

$$\begin{aligned}
d(s_1, s_2)(\Delta u) = \text{Re} \left\{ T_c \sum_{p=0}^{P-1} \sum_{p'=0}^{P-1} \sum_{b=0}^{B-1} \sum_{b'=0}^{B-1} \sum_{m=0}^{M-1} \sum_{n=0}^{N-1} \tilde{a}_{p,b,m,n} \tilde{a}_{p',b',m,n}^* \right. \\
\times \exp[j\omega_0(\Delta\tau_p - \Delta\tau_{p'})] \exp[j(\Delta\omega_b\Delta\tau_p - \Delta\omega_{b'}\Delta\tau_{p'})] \\
\times \exp \left[j(\Delta\omega_b - \Delta\omega_{b'}) \frac{T_c}{2} \right] \text{sinc} \left[(\Delta\omega_b - \Delta\omega_{b'}) \frac{T_c}{2} \right] \left. \right\}. \quad (4.30)
\end{aligned}$$

Finally, evaluating Eq. (4.30) for the LFP-FDA configuration results in

$$d(s_1, s_2)(\Delta u) = T_c \sum_{p=0}^{P-1} \cos \left[(k_0 + p\Delta k) \Delta d_{y,t} \Delta u \left(p - \frac{P-1}{2} \right) \right]. \quad (4.31)$$

The minimum of Eq. (4.31) corresponds to the maximum difference in the signal between two angles.

Plots of Eq. (4.23) and Eq. (4.25) for the CFA discussed in Section 2.3 with

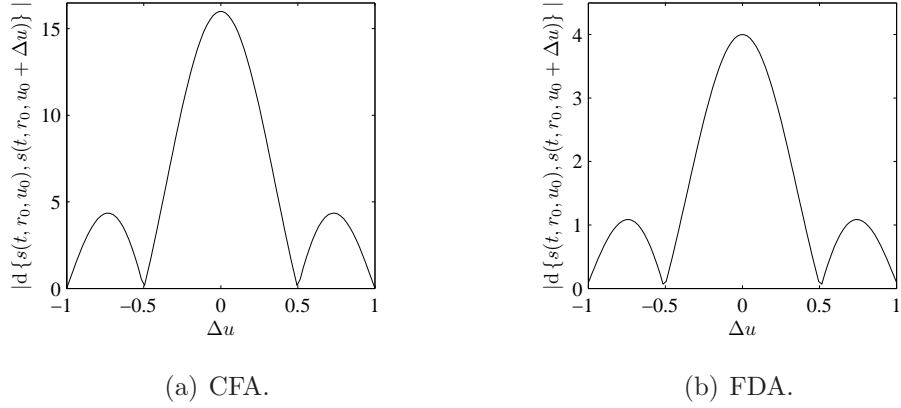


Figure 4.6. Signal difference comparison: CFA and LFP-FDA, $u_0 = 0$. Comparison of the difference function, $d(s_1, s_2)(\Delta u)$, for the signals $u_0 = 0$ and $u_1 = u_0 + \Delta u$ for the CFA and LFP-FDA. The CFA was steered to $u_s = 0$ and $d(s_1, s_2)(\Delta u)$ was evaluated using the parameters in Table 2.1 with $T_c = 2.5\text{ns}$ and the LFP-FDA was evaluated using the parameters in Table 2.3.

parameters in Table 2.1 are shown in Fig. 6(a) and Fig. 7(a). The plot of Eq. (4.25) shown in Fig. 6(a) is consistent with the CFA's array factor, a key relationship found in [46].

The results for the LFP-FDA in Section 2.6 with the parameters listed in Table 2.1 are shown in Fig. 6(b) and Fig. 7(b). The plot shown in Fig. 6(b) for the LFP-FDA is the same as Fig. 6(a) for the CFA except for a scale factor. The significance of the result is important.

When the LFP-FDA illuminates two ideal point targets at $u_0 = 0$ and $\Delta u = 0.5$ with the same range r_0 the LFP-FDA can distinguish between the signals as shown in Fig. 6(b) for the $u_0 = 0$ target and in Fig. 7(b) for the $u_1 = 0.5$ target. The radar receives the same level of power from each ideal target.

Contrast this to the CFA, the CFA will not receive any power from the second target at $u_1 = 0.5$ shown in Fig. 7(a) and so the difference function results in constant zero output. While the LFP-FDA places less power on the targets, the potential ability of an FDA to survey a wide area persistently may be attractive. To cover the

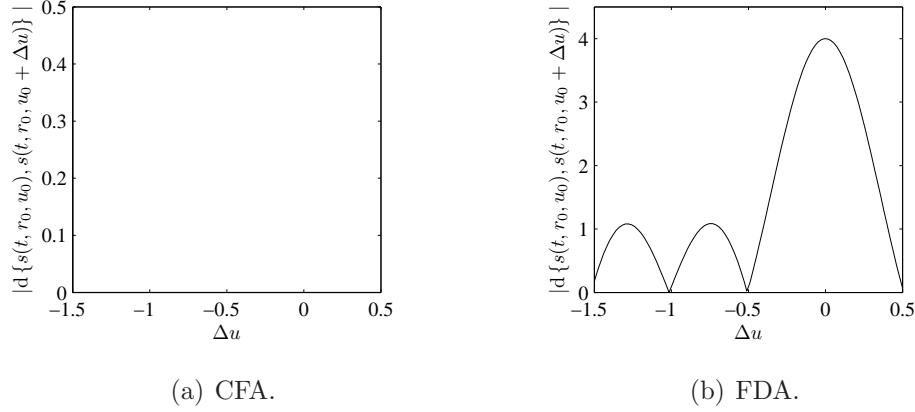


Figure 4.7. Signal difference comparison: CFA and LFP-FDA, $u_0 = 0.5$. Comparison of the difference function, $d(s_1, s_2)(\Delta u)$, for the signals $u_0 = 0.5$ and $u_1 = u_0 + \Delta u$ for the CFA and LFP-FDA. The CFA was steered to $u_s = 0$ and $d(s_1, s_2)(\Delta u)$ was evaluated using the parameters in Table 2.1 with $T_c = 2.5\text{ns}$ the LFP-FDA difference was evaluated using the parameters in Table 2.3.

same area, the CFA would have to be scanned through the azimuth angles and so the net energy on a given target may be similar between configurations for the same dwell time.

4.6 Spectral Analysis

Spectral analysis is useful in a variety of applications where the temporal or spatial signal's complexity prevents analysis. Additionally, certain temporal operations, such as convolution or filtering, are more simply represented in a transform domain where they are efficiently implemented. Analysis of the signal field for a generalized FDA in a transform domain may also be beneficial.

In Section 2.3.4 the relationship between the CFA's array factor and the spatial distribution of the array's elements was summarized. In Appendix C the Fourier transform is summarized, including a brief summary of Fourier optics. In Fourier optics, the far-field diffraction pattern of an aperture illuminated by a monochromatic plane wave is also a Fourier transform relationship (see Appendix C). The relationship

is used to simplify analysis of wave propagation through an optical system and bears many similarities to the CFA Fourier transform methods.

In the generalized FDA spectral analysis, the concepts from the CFA theory and Fourier optics theory are modified and extended to suit transforming the multi-carrier signal's field pattern. The CFA array synthesis transform in Section 2.3.4 cannot be directly applied to FDA because it assumes a narrowband, monochromatic signal. Because of this assumption, the transforms developed in [9] and [47] normalize the frequency. This dilutes the ability to represent a multiple frequency signal using the same transform axis.

The Fourier optics representation is insightful, however, the analysis concerns the projection of the diffraction pattern onto a flat imaging plane also using a monochromatic assumption. In the transform, the angular deviation from the optical axis corresponding to a particular point on the plane has a corresponding spatial frequency. Hence, when the azimuth angle is 90° the spatial frequency on the imaging plane is infinite. In radar, if the field is evaluated around a circle it doesn't make sense to consider infinite spatial frequencies; even though u is considered to be infinite, only the region $u \in [-1, 1]$ corresponds to real angles.

With the aforementioned considerations the following Fourier transform is proposed

$$F(\omega, \bar{y}) = \int_{-\infty}^{\infty} \int_{-\infty}^{\infty} f(t, u) \exp[-j(\omega t + 2\pi \bar{y} u)] dt du, \quad (4.32)$$

and

$$f(t, u) = \frac{1}{2\pi} \int_{-\infty}^{\infty} \int_{-\infty}^{\infty} F(\omega, \bar{y}) \exp[j(\omega t + 2\pi \bar{y} u)] d\omega d\bar{y}, \quad (4.33)$$

where \bar{y} corresponds to $\bar{y} = \hat{y}/\lambda$ which is the \hat{y} -axis normalized by the wavelength.

The sign convention in u and \bar{y} is consistent with the interpretation offered in [27]. Section 1.4 in Appendix A discusses the transform and its interpretation in more detail.

For the far-field amplitude distribution analysis, the transform will be assessed using the DFT and we are primarily interested in the transform's magnitude spectrum. To provide consistent results between the theoretical transform and the calculated transform, the transmit signal definition needs a minor modification. To restrict the pattern to the visible region the pulse function (also a window function) is modified so that

$$\hat{b}(t, u) = \begin{cases} 1, & 0 \leq t \leq T_c, -1 \leq u \leq 1 \\ 0, & \text{otherwise.} \end{cases} \quad (4.34)$$

Using the result from Appendix A and the Fourier transform's time-shifting property, the transform of Eq. (4.15) using the modified window function can be shown to be a sum of weighted sinc functions

$$\begin{aligned} S(\omega, \bar{y}) = & 2T_c \sum_{p=0}^{P-1} \sum_{n=0}^{N-1} \sum_{m=0}^{M-1} \sum_{b=0}^{B-1} \tilde{a}_{p,n,m,b} \exp \left[-j(\omega - \omega_b) \frac{T_c}{2} \right] \\ & \times \exp \{ -j\omega [\tau_0 + (m-1)T_c + (n-1)T_p] \} \\ & \times \text{sinc} \left[(\omega - \omega_b) \frac{T_c}{2} \right] \text{sinc} \left(2\pi\bar{y} - \omega_b \frac{d_p}{c_0} \right). \end{aligned} \quad (4.35)$$

The details for the numerical calculation of the transform using the DFT and the associated Nyquist sampling is discussed in Appendix A.

Figure 4.8 shows the transmit signal fields and their spectra calculated for the CFA, LFP-FDA and OFDM transmit signals. The transmit signals are the same as those used in Fig. 2.16, Chapter II where the shear relationship between the CFA, LFP-FDA and OFDM were observed. Considering the spectral plots, the shear ap-

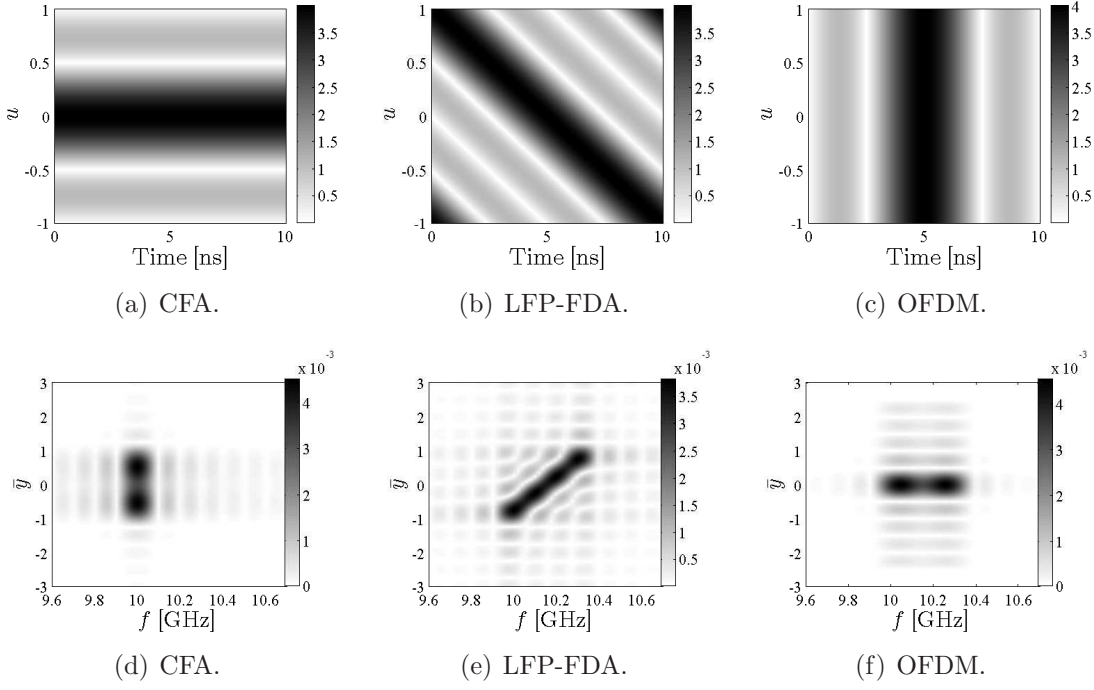


Figure 4.8. Signal field pattern and spectra comparison: CFA, LFP-FDA and OFDM. While the OFDM and CFA signal fields seem to be related through a 90° rotation on the $f - \bar{y}$ plane, the LFP-FDA signal's spectrum appears to be a horizontally sheared version of the CFA signal's spectrum or a vertically sheared version of the OFDM signal's spectrum. The shear directions are opposite compared to the signals' field plots.

pears to be applied in orthogonal directions compared to the signal field plots. Now, the LFP-FDA signal's spectrum is a horizontally sheared version of the CFA signal's spectrum and a vertically sheared version of the OFDM signal's spectrum.

4.7 Experimental Field Model Validation

A simplified block diagram of the circuit used to measure the signal field is shown in Fig. 4.9. A more comprehensive explanation of the circuit and the experiment is provided in Appendix B. Equation (4.15) could not be validated using the circuit because the circuit produces a Double Sideband - Suppressed Carrier (DSB-SC) signal whereas Eq. (4.15) represents a Single Sideband - Suppressed Carrier (SSB-SC) signal.

The difference between a DSB-SC signal and a SSB-SC signal is a filtering opera-

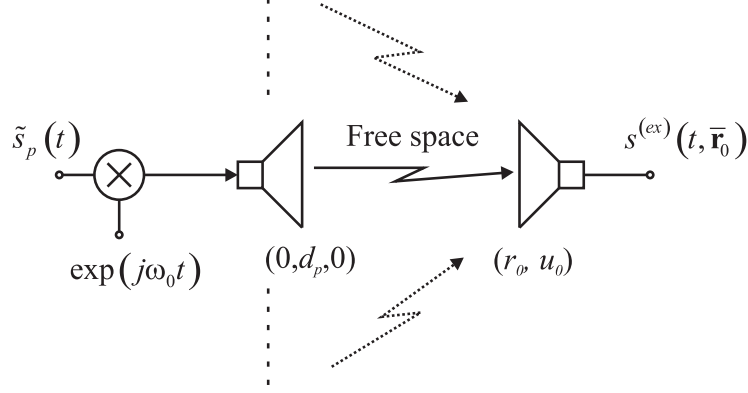


Figure 4.9. Experimental field measurement configuration: simplified diagram.

tion following the product modulator which was not included in the original circuit. The filter selects either the upper or lower sideband of the DSB-SC signal as described in [26]. Because the objective here is more concerned with the angular aspect of the model for frequency and waveform diverse arrays the model was modified to represent the circuit.

The signal model can be modified to agree with the circuit by using only the real part of the baseband signal

$$s^{(ex)}(t, \bar{\mathbf{r}}_0) = \sum_{p=0}^{P-1} \sum_{b=0}^{B-1} \exp[j\omega_0(t - \tau_0 + \Delta\tau_p)] \operatorname{Re} \left\{ \tilde{a}_{p,b} \hat{b}(t - \tau_0) \right. \\ \left. \times \exp[j\Delta\omega_b(t - \tau_0 + \Delta\tau_p)] \exp[j\pi\vartheta_{p,b}(t - \tau_0)^2] \right\}, \quad (4.36)$$

where superscript (*ex*) denotes that the model represents the experimental circuit. Note that the experiments used a single temporal chip so Eq. (4.7) is expressed without *m* or *n* to reduce the notation.

The common experimental parameters used for the experiment are listed in Table 4.1. The primary differences between these parameters and those used to simulate the LFP-FDA (listed in Table 2.3) are the number of transmitters and the signal duration. The number of transmitters is halved while the bandwidth and sub-carrier

Table 4.1. Signal measurement parameters: single-chip signals.

Parameter	Value
Transmitters P	2
Antenna Separation $\Delta d_{\dot{g},t}$	5.5cm
Frequency f_0	$\approx 9.8\text{GHz}$
Bandwidth BW_s	800MHz
Sub-carriers B	4
Sub-carrier separation Δf	200MHz
Chips M	1
Pulses N	100
Chip duration T_c	5ns

separation are doubled. It would have been desirable to use experimental parameters that more closely matched the examples used throughout this study; however, there was insufficient equipment to achieve this.

In the experiments described in Appendix B combinations of twelve different single tone waveform diverse signals, 144 combinations in total, were transmitted from the two transmit antennas. The waveform parameters are listed in Tables B.6, B.7 and B.8 in Appendix B and the set includes single tone, multi-tone and chirp signals. The signal resulting from each signal combination was measured around the circumference of a 1.1m range ring at 21 evenly sampled points in $u \in [-0.4, 0.4]$. The transmitter separation was approximately $2\lambda_0$ resulting in aliasing, while a differential delay in the transmit paths resulted in the $u = 0$ point shifting to $u = 0.12$.

Plots were generated for the 144 combinations using both measured data and data simulated using Eq. (4.7). Figure 4.10 shows comparative plots between the measured and simulated result for one of the combinations between two multi-tone signals. The

two signals used in the main body here are called the *OFDM1* and *OFDM4* signals, each of which contains two sub-carriers and between them they span the entire signal bandwidth. The *OFDM4* signal was transmitted from element $p = 0$ and has signal parameters

$$\tilde{\Upsilon}_{0,b}^{OFDM4} = \begin{cases} (1, \pi, 0), & p = 0, b = 1 \\ (1, \pi/2, 0), & p = 0, b = 3 \\ (0, 0, 0), & \text{otherwise,} \end{cases} \quad (4.37)$$

and the *OFDM1* signal was transmitted from $p = 1$ with parameters

$$\tilde{\Upsilon}_{1,b}^{OFDM1} = \begin{cases} (1, 0, 0), & p = 1, b = 0 \\ (1, 0, 0), & p = 1, b = 2 \\ (0, 0, 0), & \text{otherwise.} \end{cases} \quad (4.38)$$

The normalized signal fields are shown in Fig. 4.10 for the measured and simulated data. The fields were normalized because, providing the main difference between the two is a scaling factor, then the comparison provides some support toward validating the simulation model. Comparing the two results shows that the data simulated using is in fair agreement (i.e. fields are similar through the center portion of the plot) with the data measured in the experiment validating Eq. (4.7). Unfortunately, this only provides weak support to validate the SSB-SC signal model in Eq. (4.15).

4.8 Chapter Summary

A generalized FDA signal model was introduced and a model of the signal's behavior in the radar's far-field was considered. In addition to generalizing the existing LFP-FDA signal model, three traditional analytic techniques were applied to the

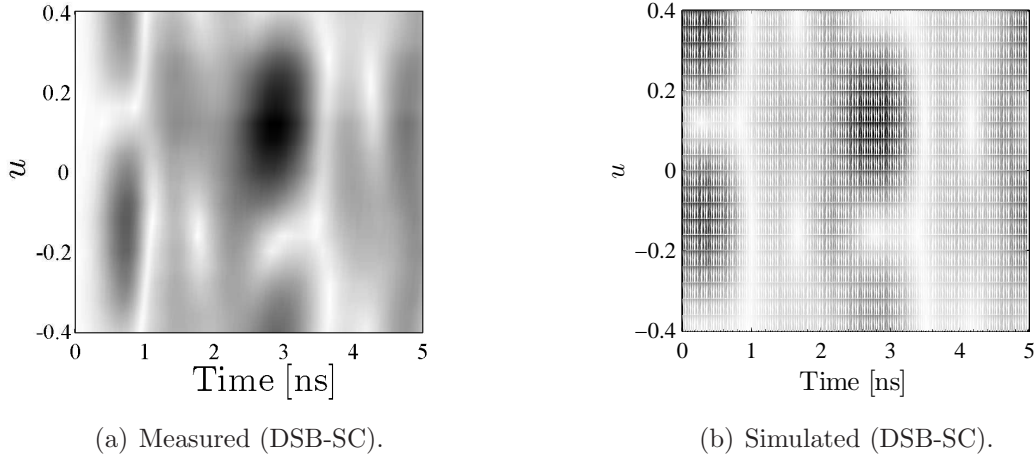
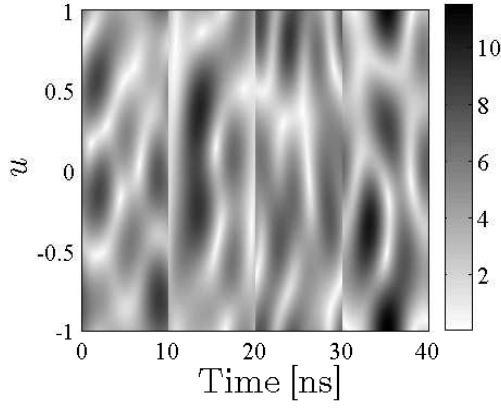


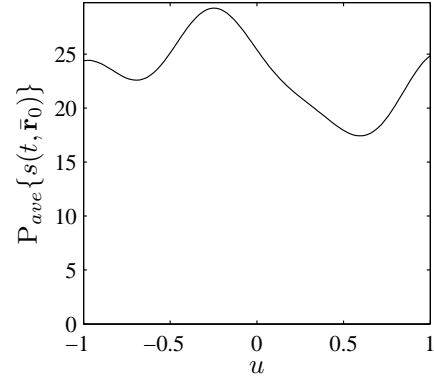
Figure 4.10. Comparison of measured (DSB-SC) and simulated (DSB-SC) field data: *OFDM4* and *OFDM1*. The *OFDM4* signal was transmitted from element $p = 0$ and the *OFDM1* signal was transmitted from the $p = 1$ element. When the DSB-SC version of the transmit signal model is used to simulate data the resulting field pattern is in fair agreement to the measured data.

challenge of analyzing an FDA's transmit signal performance. Specifically the methods extended to FDA analysis were the signal field's average power; the difference in the transmitted signal between two different angles; and a Fourier transform method that relates the signal field's spatial and spectral parameters. The analytic techniques applied to the FDA signal's field may be used in future research for design and optimization, but for the remainder of the study they will provide signal characterization for comparative purposes.

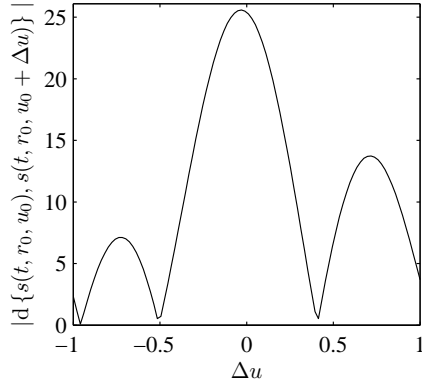
Figure 4.11 shows the signal characteristics for the randomly weighted FDA's whose signal field was introduced in Fig. 4.3. The average power was proposed as a means to compare the signal field's transmit power along different azimuth angles and the calculated average transmit power for the random FDA is shown in Fig. 11(b). Next, the difference between signals at different angles was used both as a pseudo-beamwidth and a measure of angular resolution in the transmit signal. For the CFA this measure corresponds to the array factor and despite the relatively constant power in azimuth angle the LFP-FDA has a similar difference function. A plot of the



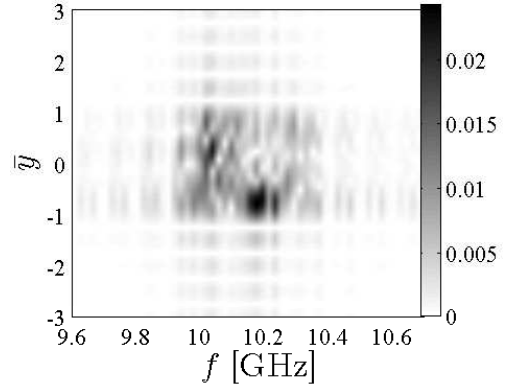
(a) Signal field plot.



(b) Signal field average power.



(c) $d(s_1, s_2)(\Delta u)$ for $u_0 = 0$.



(d) Signal field's spectrum.

Figure 4.11. Transmit signal characteristics: randomly weighted FDA. Signal field pattern plot, average power calculation, signal difference calculation and spectral analysis for a generalized FDA signal with $P = B = 4$, $M = 2$ and $N = 1$ where $\tilde{a}_{p,n,m,b}$ are circularly Gaussian random variables.

difference function for the randomly weighted FDA is shown in Fig. 11(c).

A Fourier transform pair converting the signal field plotted in (t, u) to a spectrum as a function of $\omega - \bar{y}$ was proposed. Because the bandwidths and array spacing are the same between the CFA, LFP-FDA and the random FDA the different spectra have the majority of energy occupying the same region in the $\omega - \bar{y}$ plane. It is possible that, depending on receiver processing, they will perform similarly in terms of angular measurement accuracy. Finally, limited measurements were performed

to validate the signal model; however, the circuit did not reflect the signal model. Modifying the signal model to reflect the DSB-SC circuit showed that the modified signal model reasonably predicts the circuit function.

V. Received Signal and Analysis

5.1 Chapter Overview

The first part of the chapter considers the generalized FDA signal collected by a receiver array. The signal is first modeled using relativistic Doppler scaling and after making a series of approximations the model simplifies to a piece-wise approximation to the Doppler scaled signal. Then, generalized receiver processing is applied to the received signal model and the associated ambiguity function is defined. Finally, measured data is used to support the the signal model's validity.

5.2 Geometry

A diagram of the receiving array's geometry is shown in Fig. 5.1. The receiver array geometry was explained in Section 2.3.1, Chapter II, but will be recapped here for convenience. The array is geometrically centered about the origin with elements extending along the $\hat{\mathbf{y}}$ -axis. The q th element's displacement is

$$\bar{\mathbf{d}}_q = \hat{\mathbf{y}} d_q \quad (5.1)$$

and if the array is configured as a ULA with equal inter-element spacing $\Delta d_{\hat{\mathbf{y}},r}$ the displacement is more specifically

$$\bar{\mathbf{d}}_q = \hat{\mathbf{y}} \left(q - \frac{Q-1}{2} \right) \Delta d_{\hat{\mathbf{y}},r}. \quad (5.2)$$

The signal transmitted from the P -element transmit array reflects from a target with parameters $\Xi_t = (\bar{\mathbf{r}}_{t,0}, \bar{\mathbf{v}}_t)$ where $\bar{\mathbf{r}}_{t,0}$ is the target's displacement at $t = 0$ and $\bar{\mathbf{v}}_t$ is the target's velocity. The target's position is $\bar{\mathbf{r}}_t(t) = \bar{\mathbf{r}}_{t,0} + \bar{\mathbf{v}}_t t$ but will be expressed without the temporal dependance for convenience. The distance from the array's

phase center to the target is r_t , the target's azimuth angle is θ_t and elevation angle is ψ_t . The target's range from the radar will be time-varying when the target's velocity relative to the phase center v_t is not equal to zero. Note the relative velocity is not the target's speed $|\bar{\mathbf{v}}_t|$ because $\bar{\mathbf{v}}_t$ can be in an arbitrary direction, but the relative velocity is the target range's rate of change $v_t = \frac{d}{dt}|\bar{\mathbf{r}}_t(t)|$ which lies along the radar's LOS.

The target's displacement from the q th array element is

$$\bar{\mathbf{r}}_q = \bar{\mathbf{r}}_t - \bar{\mathbf{d}}_q. \quad (5.3)$$

Employing the far-field approximation the distance between the q th element and the target is

$$|\bar{\mathbf{r}}_q| \simeq r_t - \bar{\mathbf{d}}_q \cdot \hat{\boldsymbol{\kappa}}_t, \quad (5.4)$$

where $\hat{\boldsymbol{\kappa}}_t$ is the unit vector in the direction of $\bar{\mathbf{r}}_t$. When the array is aligned along the $\hat{\mathbf{y}}$ -axis the $\bar{\mathbf{d}}_q \cdot \hat{\boldsymbol{\kappa}}_t$ term simplifies to $d_q \sin \theta_t = d_q u_t$ for any target displacement vector in the $\hat{\mathbf{x}}\text{-}\hat{\mathbf{y}}$ plane. The linear array does not have the capacity to determine a target's location in elevation so it suffices to assume all targets are located in the $\hat{\mathbf{x}}\text{-}\hat{\mathbf{y}}$ plane.

The propagation delay from the target to the q th array element is

$$\begin{aligned} \tau_q &= \frac{r_t - d_q u_t}{c_0} \\ &= \tau_t - \Delta\tau_q, \end{aligned} \quad (5.5)$$

where $\Delta\tau_q$ is the differential propagation delay from the array's phase center to the q th element.

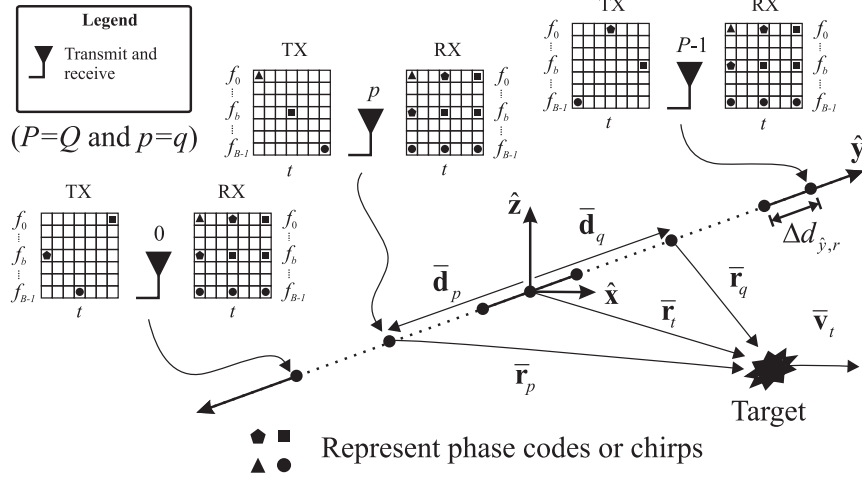


Figure 5.1. Generalized FDA transmitter-receiver.

The path length from the p th transmit element to the q th receive element is

$$\begin{aligned}
 |\bar{\mathbf{r}}_p| + |\bar{\mathbf{r}}_q| &= |\bar{\mathbf{r}}_t - \bar{\mathbf{d}}_p| + |\bar{\mathbf{r}}_t - \bar{\mathbf{d}}_q| \\
 &\approx 2r_t - (d_p + d_q)u_t
 \end{aligned} \tag{5.6}$$

with a bistatic propagation delay

$$\tau_q + \tau_p \approx 2\tau_t - \Delta\tau_p - \Delta\tau_q. \tag{5.7}$$

Only a small fraction of the transmitted energy is reflected from the target and collected by a receiver element. This is due to a number of factors such as the wave propagation scaling which is proportional to r_t^{-2} ; the target's Radar Cross Section (RCS); the transmit and receiver element's aperture functions and aperture gains; and the atmospheric losses. These losses are predicted by the radar range equation which will be simplified to a single multiplicative constant $K_{p,q}$ to describe the loss between bistatic array elements p and q .

5.3 Received Signal

If the transmit signal is reflected from a target with parameters Ξ_t back to the q th receiver element the signal collected is

$$\begin{aligned}
r_q(t, \Xi_t) = & n_q(t) + \sum_{p=0}^{P-1} \sum_{b=0}^{B-1} \sum_{m=0}^{M-1} \sum_{n=0}^{N-1} K_{q,p} \tilde{a}_{p,b,m,n} \sqrt{\alpha_{q,p}} \\
& \times \hat{b}[\alpha_{q,p}(t - \tau_p - \tau_q - mT_c - nT_p)] \exp[j\omega_0 \alpha_{q,p}(t - \tau_p - \tau_q)] \\
& \times \exp[j\Delta\omega_b \alpha_{q,p}(t - \tau_p - \tau_q - mT_c - nT_p)]
\end{aligned} \tag{5.8}$$

where $n_q(t)$ is the receiver's thermal noise and $\alpha_{q,p}$ is the bistatic Doppler scale factor resulting from the target's relative velocity given by Eq. (2.61). For notational convenience the target-related quantities τ_p , τ_q , $K_{q,p}$ and $\alpha_{q,p}$ are expressed without their functional dependence on Ξ_t .

For radar systems $v_t \ll c_0$ and it is assumed that both the target and the radar are static while the signal propagates. However, the target's relative velocity causes relativistic Doppler scaling described in Section 2.4, Chapter II. For a bistatic propagation path the Doppler scale factor is $\alpha_{q,p} = 1 + \frac{\nu_{q,p,b}}{\omega_b}$ [40] where

$$\nu_{q,p,b}(t) = -\frac{2\pi}{\lambda_b} \left[\frac{d}{dt} (|\bar{\mathbf{r}}_p(t)| + |\bar{\mathbf{r}}_q(t)|) \right]. \tag{5.9}$$

In the physics literature ν denotes frequency in Hertz, but here it will have the same units as ω of radians per second. Given that the narrowband, array approximation is valid for the FDA, and the target is not accelerating, the Doppler is approximately independent of p and q in which case the frequency shift simplifies to

$$\begin{aligned}
\nu_b & \approx -\frac{2\pi}{\lambda_b} \left\{ 2 \frac{d}{dt} |\bar{\mathbf{r}}_t(t)| \right\} \\
& \approx -\frac{4\pi v_t}{\lambda_b}.
\end{aligned} \tag{5.10}$$

Next, the narrowband, array approximations are applied to Eq. (5.8). The Doppler scale factor, which is independent of the bistatic path, can be expressed as $\alpha \approx \alpha_{q,p}$ for all pairs (p, q) and the definition for the monostatic Doppler scaling, α , in Eq. (2.61) can be substituted in Eq. (5.8). For an array, the amplitude scaling terms $K_{q,p}$ are also independent of bistatic path and are approximated by $K_{tx,rx} \approx K_{p,q}$ for all pairs (p, q) and the propagation delay $\tau_p + \tau_q$ is approximated using Eq. (5.7).

Following the substitutions Eq. (5.8) the received signal becomes

$$r_q^{(w)}(t, \Xi_t) = n_q(t) + K_{tx,rx} s_q^{(w)}(t, \Xi_t). \quad (5.11)$$

where

$$\begin{aligned} s_q^{(w)}(t, \Xi_t) = & \sqrt{\alpha} \sum_{p=0}^{P-1} \sum_{b=0}^{B-1} \sum_{m=0}^{M-1} \sum_{n=0}^{N-1} \tilde{a}_{p,b,m,n} \hat{b} [\alpha(t - 2\tau_t - mT_c - nT_p)] \\ & \times \exp [j\Delta\omega_b \alpha(t - 2\tau_t + \Delta\tau_p + \Delta\tau_q - mT_c - nT_p)] \\ & \times \exp [j\omega_0 \alpha(t - 2\tau_t + \Delta\tau_p + \Delta\tau_q)]. \end{aligned} \quad (5.12)$$

This form of signal model is the wideband approximation to the Doppler scaled signal and will be referred to as the wideband model for brevity. Superscript (w) will distinguish the wideband model from the other models that will be considered.

Including the Doppler scaling factor α in the signal model makes analysis difficult. Section 2.4 in Chapter II showed that the scaled signal can be approximated using a single frequency shift providing the time-bandwidth product satisfies the constraints in Eq. (2.62). Recalling that the FDA signal, while composed of narrowband signals, is potentially a wideband signal and that simplification to the signal model warrants careful consideration. Two potential simplifications to the wideband model are considered next.

5.4 Doppler Approximation Comparison

What will be termed the intermediate approximation to the Doppler scaling (or intermediate model for brevity) has appeared in the literature for signal models that use multi-carrier signals with widely spaced sub-carriers. The intermediate model is a piece-wise approximation to the Doppler scaling evaluated at each of the sub-carrier frequencies using Eq. (5.10). This approximation has been used in LFP-FDA STAP research [7] and fluctuating target detection using FD-MIMO [50]. The assumption used by the authors is that the sub-carriers are clearly separable in the receiver such that they can be filtered and processed independent of other sub-carriers.

When the sub-carriers are separable, the intermediate Doppler model is a logical extension to the monostatic case and does not require verification. However, in the general case where the signals potentially overlap, and are not separable, the model needs to be evaluated. Other work involving multi-carrier radar signals use either the standard narrowband approximation when the signal time-bandwidth product is small [33] or the wideband model when the time-bandwidth product is large [38].

The intermediate Doppler approximation first makes the narrowband approximation to the signal's pulse envelope

$$\sqrt{\alpha}\hat{b}[\alpha(t - 2\tau_t + \Delta\tau_p + \Delta\tau_q)] \approx \hat{b}(t - 2\tau_t) \quad (5.13)$$

which simply states that the compressive scaling and the propagation time across the array are negligible. Then substituting $\alpha = 1 + \frac{\nu_b}{\omega_b}$ into Eq. (5.12) the received signal at the q th receiver is

$$r_q^{(i)}(t, \Xi_t) = n_q(t) + K_{tx,rx} s_q^{(i)}(t, \Xi_t), \quad (5.14)$$

where the superscript (i) denotes the intermediate model and where

$$\begin{aligned}
s_q^{(i)}(t, \Xi_t) &= \sum_{p=0}^{P-1} \sum_{b=0}^{B-1} \sum_{m=0}^{M-1} \sum_{n=0}^{N-1} \tilde{a}_{p,b,m,n} \hat{b}[(t - 2\tau_t - mT_c - nT_p)] \\
&\times \exp[j(\Delta\omega_b + \Delta\nu_b)(t - 2\tau_t + \Delta\tau_p + \Delta\tau_q - mT_c - nT_p)] \\
&\times \exp[j(\omega_0 + \nu_0)(t - 2\tau_t + \Delta\tau_p + \Delta\tau_q)].
\end{aligned} \tag{5.15}$$

Without the compressive scaling term Eq. (5.15) simplifies the analysis; however, sub-carrier specific Doppler terms $\Delta\nu_b$ prevent further simplification. This motivates the narrowband approximation to the Doppler scaling.

Under some conditions it may be possible to use the narrowband approximation to the wideband model such as that used in [40]. Neglecting the $\Delta\nu_b$ terms in Eq. (5.15) the narrowband Doppler model is

$$r_q^{(n)}(t, \Xi_t) = n_q(t) + K_{tx,rx} s_q^{(n)}(t, \Xi_t), \tag{5.16}$$

where the superscript (n) distinguishes the narrowband model and

$$\begin{aligned}
s_q^{(n)}(t, \Xi_t) &= \sum_{n=0}^{N-1} \sum_{m=0}^{M-1} \sum_{p=0}^{P-1} \sum_{b=0}^{B-1} \tilde{a}_{n,m,p,b} \hat{b}[(t - 2\tau_t - mT_c - nT_p)] \\
&\times \exp[j\Delta\omega_b(t - 2\tau_t + \Delta\tau_p + \Delta\tau_q - mT_c - nT_p)] \\
&\times \exp[j(\omega_0 + \nu_0)(t - 2\tau_t + \Delta\tau_p + \Delta\tau_q)].
\end{aligned} \tag{5.17}$$

For small relative target velocities the three Doppler models should be consistent around $\alpha = 0$. However, as the signal's time-bandwidth product increases the region of consistency should diminish.

Next, the models are compared using a LFP-FDA signal by calculating the difference between the signals over a range of B , and α . The $n_q(t)$, $K_{tx,rx}$ terms are neglected from the received signal equations and the results are simulated for a target

located at a fixed r_t and with $u_t = 0$. The comparison used the LFP-FDA configuration with a fixed bandwidth $BW_s = 1\text{GHz}$ transmitted at a frequency $f_0 = 1\text{GHz}$. The signals are normalized such that

$$\bar{s}(t) = \frac{1}{\sqrt{E}}s(t), \quad (5.18)$$

where the energy for the LFP-FDA signal with $|\tilde{a}_{p,b,m,m}| = 1$ is

$$E = T_c B. \quad (5.19)$$

The normalization is important because the difference function is an energy calculation. The signal duration T_c increases with B for a fixed bandwidth and the energy, which is proportional to both parameters, increases accordingly. The normalization provides a consistent comparison as B is varied.

With the functional dependence on B and α made explicit, the difference between the normalized wideband model and the intermediate model is

$$\Delta^{(i)}(B, \alpha) = \|\bar{s}_q^{(w)}(\cdot, B, \alpha) - \bar{s}_q^{(i)}(\cdot, B, \alpha)\|^2. \quad (5.20)$$

The difference for the narrowband model is similarly defined with $\Delta^{(n)}(B, \alpha)$.

Figures 2(a) through 2(c) show examples of signals received by single element receiver array, for different values of α , from a transmit array transmitting a single pulse with $P = B = 4$ for the wideband, intermediate and narrowband models respectively. The signals predicted using the intermediate model shown in 2(b) closely resemble the signals predicted by the wideband model in terms of compressive scaling for all α , but the narrowband model remains relatively unchanged over α .

Figure 2(d) shows contours of the difference functions for $\Delta^{(i)}(B, \alpha) = 0.001$ and

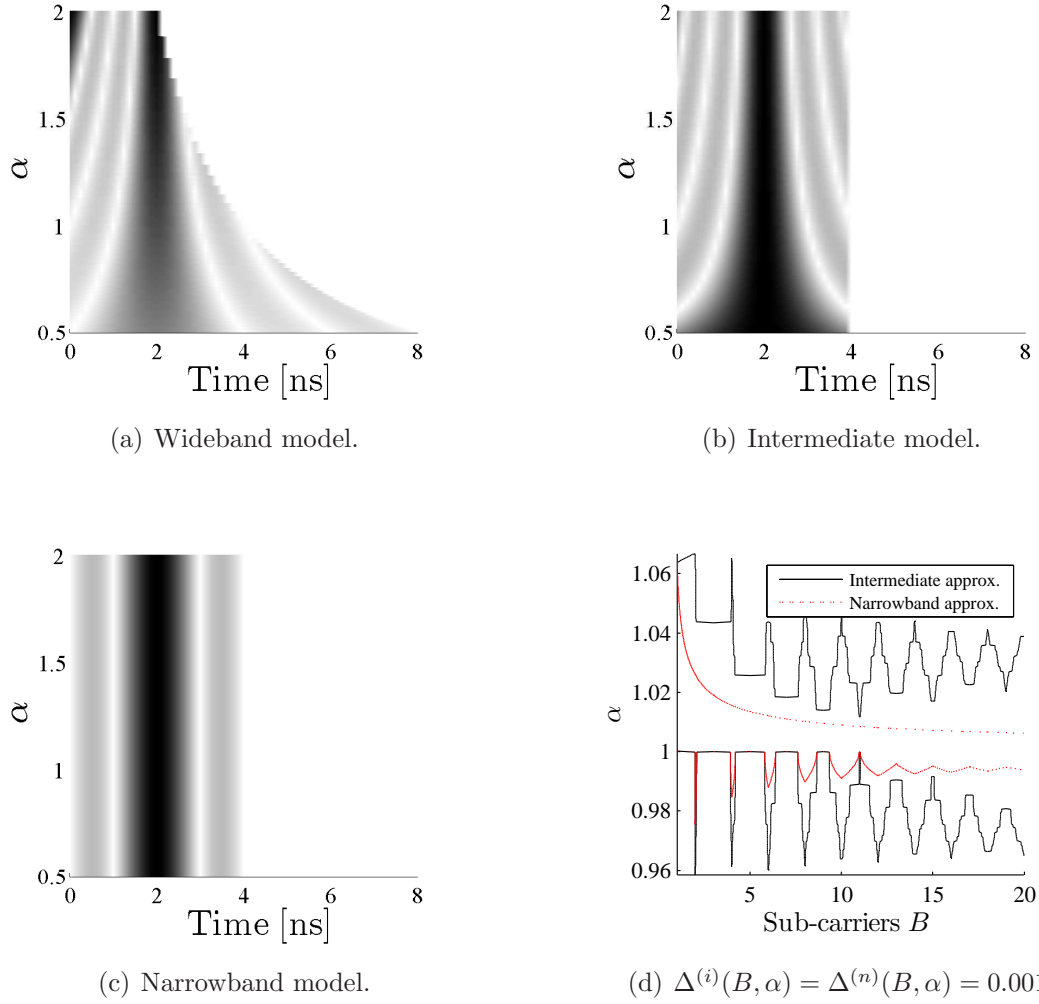


Figure 5.2. Doppler Model Comparison. Comparison between the wideband (Fig. 2(a)), intermediate ((Fig. 2(b))) and narrowband (Fig. 2(c)) Doppler models for a LFP-FDA signal evaluated at $\theta = 0$ with $f_0 = 1\text{GHz}$ and $\text{BW}_s = 1\text{GHz}$. Contours for $\Delta^{(i)}(B, \alpha) = \Delta^{(n)}(B, \alpha) = 0.001$ are shown in Fig. 2(d) for a range of sub-carriers and relative velocities.

$\Delta^{(n)}(B, \alpha) = 0.001$, recognizing that the function is only evaluated for integer values of B . For all values of α and B shown plotted in Fig. 2(d) the intermediate model is a closer approximation to the wideband model. It is also interesting to note that signals using even values of B provide closer approximations to the wideband model than odd values; however, the cause of the relationship is uncertain.

The comparison is limited because it only considers a relatively simple signal configuration along $u = 0$ and so the impact of the Doppler scaling on the angle de-

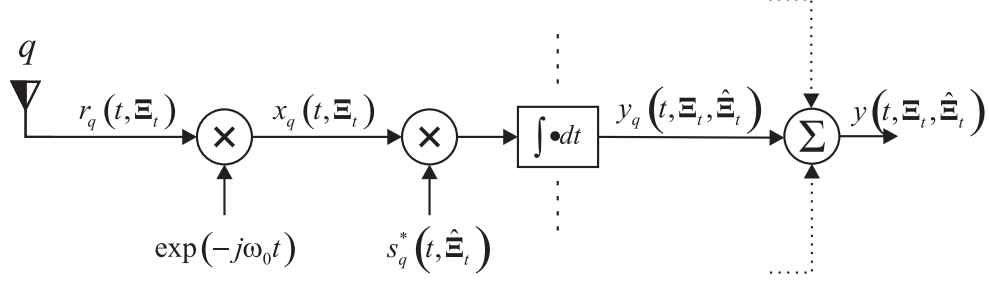


Figure 5.3. FDA receiver processor block diagram.

pendent terms is neglected. A more rigorous treatment could be considered in future to establish more general bounds for the validity of the narrowband and intermediate models. Despite the limitation, the comparison should be adequate to justify using the intermediate model when the signal has overlapping sub-carriers. However, the comparison is not sufficient to establish suitable bounds to use the narrowband model. As a result the intermediate model will be used exclusively and the (i) superscript will be removed from Eq. (5.15) for the remainder of the study.

5.5 Receiver Processing

A schematic of the general receiver processor considered next is shown in Fig. 5.3 in which the first step in the receiver chain is to quadrature demodulate the received signal. This is modeled as $x_q(t, \Xi_t) = r_q(t, \Xi_t) \exp(-j\omega_0 t)$ resulting in

$$\begin{aligned}
 x_q(t, \Xi_t) = & \tilde{n}_q(t) + K_{tx,rx} \sum_{p=0}^{P-1} \sum_{b=0}^{B-1} \sum_{m=0}^{M-1} \sum_{n=0}^{N-1} \tilde{a}_{p,b,m,n} \hat{b}(t - 2\tau_0 - mT_c - nT_p) \\
 & \times \exp[j(\Delta\omega_b + \nu_b)t] \exp[-j(\omega_b + \nu_b)2\tau_0] \exp[j(\omega_b + \nu_b)(\Delta\tau_p + \Delta\tau_q)] \\
 & \times \exp[-j(\Delta\omega_b + \Delta\nu_b)(mT_c + nT_p)], \tag{5.21}
 \end{aligned}$$

where $\tilde{n}_q(t)$ is now circular Gaussian noise. The received signal can be decomposed into several key components: a range component, an angle-dependent component and a velocity- or Doppler-dependant component. The notation can be simplified by first

substituting the basis signal

$$s_b(t) = \hat{b}(t) \exp(j\Delta\omega_b t), \quad (5.22)$$

into Eq. (5.21). Next, the component due to the target's angle relative to the p th transmitter, evaluated at the b th frequency, is

$$\tilde{w}_{p,b}(\Xi_t) = \exp[j(\omega_b + \nu_b)\Delta\tau_p], \quad (5.23)$$

and similarly the component due to the target location relative to the q th receiver, evaluated at the b th frequency, is

$$w_{q,b}(\Xi_t) = \exp[j(\omega_b + \nu_b)\Delta\tau_q]. \quad (5.24)$$

Substituting $s_b(t)$, $\tilde{w}_{p,b}(\Xi_t)$ and $w_{q,b}(\Xi_t)$ into Eq. (5.21) the q th demodulated signal is

$$x_q(t, \Xi_t) = \tilde{n}_q(t) + K_{tx,rx} s_q(t, \Xi_t) \quad (5.25)$$

where $s_q(t, \Xi_t)$ is noise-free, unscaled version of received signal

$$\begin{aligned} s_q(t, \Xi_t) = & \exp(-j\omega_0 2\tau_0) \sum_{p=0}^{P-1} \sum_{b=0}^{B-1} \sum_{m=0}^{M-1} \sum_{n=0}^{N-1} \tilde{a}_{p,b,m,n} s_b(t - 2\tau_0 - mT_c - nT_p) \\ & \times \tilde{w}_{p,b}(\Xi_t) \tilde{w}_{q,b}(\Xi_t) \exp[j\nu_b(t - 2\tau_0)] \exp[-j\Delta\nu_b(mT_c + nT_p)] \end{aligned} \quad (5.26)$$

Following IQ demodulation, a set of Q baseband signals are available to the receiver processor from which it can estimate the target's reflectivity, position and relative velocity. Conceptually, the receiver tests the similarity between the set of Q received signals to a set of ideal signals that would be produced by a target with

parameters $\hat{\Xi}_t = (\hat{r}_t, \hat{u}_t, \hat{v}_t)$. This is mathematically equivalent to forming a set of *PNMB* filters at each of the Q receivers, each matched to one of the transmit signal components $\tilde{a}_{p,b,m,n} s_b(t)$ and to the target parameters under test $\hat{\Xi}_t$. Finally, the outputs from the Q matched filter banks are summed.

The test for a target response in the set of received signals is a sum of inner product integrals

$$\begin{aligned} y(t, \Xi_t, \hat{\Xi}_t) &= \sum_{q=0}^{Q-1} \int_{-\infty}^{\infty} x_q(t, \Xi_t) \hat{s}_q^*(t, \hat{\Xi}_t) dt \\ &= \sum_{q=0}^{Q-1} y_q(t, \Xi_t, \hat{\Xi}_t). \end{aligned} \quad (5.27)$$

The output from the q th element's receiver is

$$y_q(t, \Xi_t, \hat{\Xi}_t) = \tilde{n}_{mf,q}(t) + K_{tx,rx} \int_{-\infty}^{\infty} s_q(t, \Xi_t) s_q^*(t, \hat{\Xi}_t) dt, \quad (5.28)$$

where $\tilde{n}_{mf,q}(t)$ is the total noise contribution after the noise terms from the individual matched filters are combined. The integral term can be decomposed into a finite sum between the individual signal components and the matched filters in the filter bank

$$\begin{aligned} \int_{-\infty}^{\infty} s_q(t, \Xi_t) s_q^*(t, \hat{\Xi}_t) dt &= \int_{-\infty}^{\infty} \left\{ \exp(-j\omega_0 2\tau_0) \sum_{p=0}^{P-1} \sum_{b=0}^{B-1} \sum_{m=0}^{M-1} \sum_{n=0}^{N-1} \tilde{a}_{p,b,m,n} \right. \\ &\quad \times \tilde{w}_{p,b}(\Xi_t) \tilde{w}_{q,b}(\Xi_t) s_b(t - 2\tau_0 - mT_c - nT_p) \\ &\quad \times \exp[j\nu_b(t - 2\tau_0 - mT_c - nT_p)] \Big\} \\ &\quad \times \left\{ \exp(j\omega_0 2\hat{\tau}_0) \sum_{p'=0}^{P-1} \sum_{b'=0}^{B-1} \sum_{m'=0}^{M-1} \sum_{n'=0}^{N-1} \tilde{a}_{p',b',m',n'}^* \right. \\ &\quad \times \tilde{w}_{p',b'}^*(\hat{\Xi}_t) \tilde{w}_{q,b'}^*(\hat{\Xi}_t) s_b^*(t - 2\hat{\tau}_0 - m'T_c - n'T_p) \\ &\quad \times \exp[-j\hat{\nu}_{b'}(t - 2\hat{\tau}_0 - m'T_c - n'T_p)] \Big\} dt. \end{aligned} \quad (5.29)$$

After expanding the product and bringing the integral inside the summation, the result can be expressed as

$$\begin{aligned}
\int_{-\infty}^{\infty} s_q(t, \Xi_t) s_q^*(t, \hat{\Xi}_t) dt &= \exp [j\omega_0(2\hat{\tau}_0 - 2\tau_0)] \\
&\times \sum_{p=0}^{P-1} \sum_{p'=0}^{P-1} \sum_{b=0}^{B-1} \sum_{b'=0}^{B-1} \sum_{m=0}^{M-1} \sum_{m'=0}^{M-1} \sum_{n=0}^{N-1} \sum_{n'=0}^{N-1} \tilde{a}_{p,b,m,n} \tilde{a}_{p',b',m',n'}^* \\
&\times \tilde{w}_{p,b}(\Xi_t) \tilde{w}_{p',b'}^*(\hat{\Xi}_t) \tilde{w}_{q,b}(\Xi_t) \tilde{w}_{q,b'}^*(\hat{\Xi}_t) \\
&\times \int_{-\infty}^{\infty} s_b(t - 2\tau_0 - mT_c - nT_p) s_{b'}^*(t - 2\hat{\tau}_0 - m'T_c - n'T_p) \\
&\times \exp [j\nu_b(t - 2\tau_0 - mT_c - nT_p)] \\
&\times \exp [-j\hat{\nu}_{b'}(t - 2\hat{\tau}_0 - m'T_c - n'T_p)] dt. \tag{5.30}
\end{aligned}$$

Inside the integral the following substitutions can be made

$$\begin{aligned}
t' &= t - 2\tau_0 - mT_c - nT_p \\
t &= t' + 2\tau_0 + mT_c + nT_p, \\
dt' &= dt \tag{5.31}
\end{aligned}$$

and

$$t - 2\hat{\tau}_0 - m'T_c - n'T_p = t' - \Delta\tau - (m' - m)T_c - (n' - n)T_p, \tag{5.32}$$

where $\Delta\tau = 2\hat{\tau}_0 - 2\tau_0$. Positive values of $\Delta\tau$ correspond to the filter estimating a

greater target range. Following the substitutions the result is

$$\begin{aligned}
\int_{-\infty}^{\infty} s_q(t, \Xi_t) s_q^*(t, \hat{\Xi}_t) dt &= \exp(j\omega_0 \Delta\tau) \\
&\times \sum_{n=0}^{N-1} \sum_{m=0}^{M-1} \sum_{p=0}^{P-1} \sum_{b=0}^{B-1} \sum_{n'=0}^{N-1} \sum_{m'=0}^{M-1} \sum_{p'=0}^{P-1} \sum_{b'=0}^{B-1} \tilde{a}_{n,m,p,b} \tilde{a}_{n',m',p',b'}^* \\
&\times w_{p,b}(\Xi_t) w_{p',b'}^*(\hat{\Xi}_t) w_{q,b}(\Xi_t) w_{q,b'}^*(\hat{\Xi}_t) \\
&\times \int_{-\infty}^{\infty} s_b(t') s_{b'}^*[t' - \Delta\tau - (m' - m)T_c - (n' - n)T_p] \exp(j\nu_b t') \\
&\times \exp\{-j\hat{\nu}_{b'}[t' - \Delta\tau - (m' - m)T_c - (n' - n)T_p]\} dt' \quad (5.33)
\end{aligned}$$

Equation (5.33) shows the q th receiver's output is a weighted sum of correlations between Doppler shifted basis signals $s_b(t)$. For $v_t = 0$ the set of integral terms are the matched filter outputs with a peak in their respective outputs when the relative delay of the matched filter is

$$\Delta\tau = -[(m' - m)T_c + (n' - n)T_p]. \quad (5.34)$$

The receiver's AF is considered next.

5.6 Ambiguity Function

When using realistic signals, with finite bandwidths, that are interfaced to the environment through finite apertures (or arrays), the output of the receiver due to a point target will not produce an impulse-like response (i.e. an output only when the receiver is exactly matched to the target parameters). This means that the processor cannot know with 100% certainty the target's relative location, velocity and size. The AF characterizes the accuracy of the radar receiver's measurements. The AF is extended to the generalized FDA framework from the contemporary MIMO AF

work reported in Chapter II and will be used as a tool to evaluate the measurement performance of an FDA configuration.

The receiver is matched to the estimated target parameters which can equivalently be expressed as a difference between estimate and actual parameters are $\hat{\Xi}_t - \Xi_t = (\Delta r, \Delta u, \Delta v_t)$. Noting that the convolution integral in Eq. (5.33) is a time-frequency correlation function, the following function is defined

$$\chi_{(b',m',n')}^{(b,m,n)}(\Delta\tau, v_t) \triangleq \int_{-\infty}^{\infty} s_b(t) s_{b'}^* [t - \Delta\tau - (m' - m)T_c - (n' - n)T_p] \times \exp(j\nu_b t) dt. \quad (5.35)$$

Taking the magnitude of Eq. (5.35), and normalizing the result to have a maximum amplitude of one, would provide a cross-ambiguity function between $s_b(t)$ and $s_{b'}^*(t)$. The physical interpretation of the equation is that the matched filter is looking for a stationary target, $\hat{v}_t = 0$, at variable ranges $\hat{r}_t = r_t + \Delta r$. However, the target is at a fixed location r_t but with variable relative velocities v_t resulting in Doppler frequency mismatches $\nu_b = -2k_b v_t$. The range mismatch results in a delay mismatch $\Delta\tau = \frac{2\Delta r}{c_0}$. Note that using the narrowband, array approximation the cross-correlation function in Eq. (5.35) is independent of angle parameter mismatches.

The collection of $\chi_{(b',m',n')}^{(b,m,n)}(\Delta\tau, v_t)$ form a set of basis correlation functions from which the system's overall ambiguity function is constructed by summing shifted copies of the function that are weighted with a complex value. Including the angle parameter mismatch, the total FDA ambiguity function can be formed as

$$|\chi(\Delta\tau, v_t, u_t, \Delta u)| = \frac{1}{E_{tot}} \left| \sum_{q=0}^{Q-1} \sum_{n=0}^{N-1} \sum_{m=0}^{M-1} \sum_{p=0}^{P-1} \sum_{b=0}^{B-1} \sum_{n'=0}^{N-1} \sum_{m'=0}^{M-1} \sum_{p'=0}^{P-1} \sum_{b'=0}^{B-1} \tilde{a}_{n,m,p,b} \tilde{a}_{n',m',p',b'}^* \right. \\ \left. \times w_{p,b}(\Xi) w_{p',b'}^*(\hat{\Xi}) w_{q,b}(\Xi) w_{q,b'}^*(\hat{\Xi}) \chi_{(b',m',n')}^{(b,m,n)}(\Delta\tau, v_t) \right|, \quad (5.36)$$

where the total signal energy

$$E_{tot} = \int_{-\infty}^{\infty} s_q(t, \Xi_0) s_q^*(t, \Xi_0) dt, \quad (5.37)$$

is the maximum output possible from the system which occurs when $\Xi_0 = (0, 0, 0)$.

When the AF is plotted the delay and Doppler axes will be normalized such that

$$\Delta\bar{\tau} = \Delta\tau \text{BW}_s, \quad (5.38)$$

and

$$\bar{\nu} = \frac{\nu_0}{\text{BW}_s}. \quad (5.39)$$

The angle axis will not be normalized because, for most of the comparisons that follow, L_p and P will be constants. Furthermore, it will be assumed that the signal is received by a single element at the origin so that the AF measures the key features of the transmit waveform.

Figure 5.4 shows plots of the principal AF planes for the LFP-FDA configuration with parameters in Table 2.3 for when the processor searches for a signal from a target at $u_t = 0$. The resulting AF is similar to the plots of CFA's principal AF planes shown in Fig. 2.9. The most notable difference is that the delay-angle plane, shown in Fig. 4(b), reveals that the LFP-FDA has clear coupling between delay and angle. The explanation for this is straightforward considering the LFP-FDA's signal field pattern shown in Fig. 15(b). The signal along any u is a delayed or advanced replica of the signal at $u = 0$ and so the receiver has difficulty distinguishing between a signal from $u = 0$ and a time shifted signal arriving from $u \neq 0$.

The mainlobe width along the delay axis, δ_τ , is the same as the CFA's width

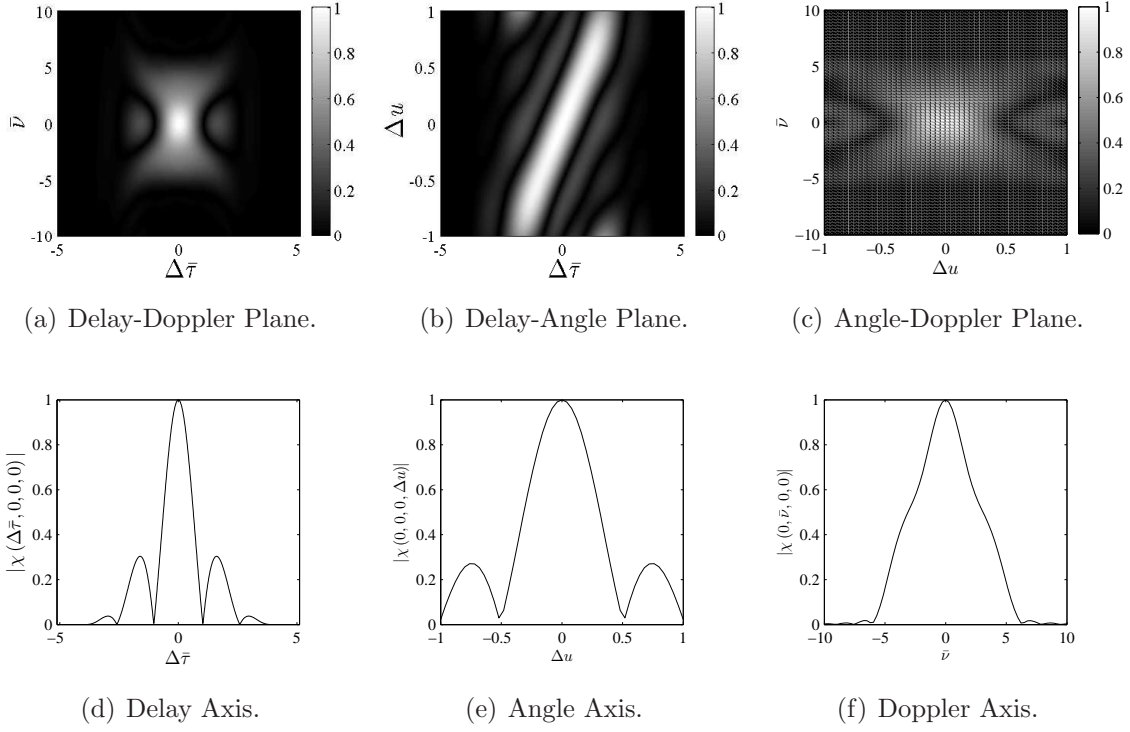


Figure 5.4. AF Principal Planes and Axes: LFP-FDA.

shown in Fig. 2.9, except the the LFP-FDA has sidelobes with Peak Sidelobe Level (PSL) along the delay axis of $\text{PSL}_\tau = 0.3$. The LFP-FDA and CFA AF's have similar responses along the angle axis with $\delta_u = 0.5$ and $\text{PSL}_u = 0.27$. The LFP-FDA's performance along the angle axis is significant because the LFP-FDA transmits average signal power evenly in u whereas the CFA's average signal power is shaped by the array factor. However, the FDA has similar accuracy at measuring a target's location in u .

Comparing the CFA's delay-Doppler plane to the LFP-FDA's angle-Doppler plane, the LFP-FDA's angle-Doppler plane seems to be a mapping from the CFA's delay-Doppler plane. The CFA's Doppler axis seems to map to the LFP-FDA's angle axis and the CFA's delay axis seems to map to the LFP-FDA's Doppler axis. The response along the Doppler-axis is $\delta_\nu = 1$ for both but the CFA has $\text{PSL}_\nu = 0.22$ whereas the LFP-FDA has $\text{PSL}_\nu = 0.02$.

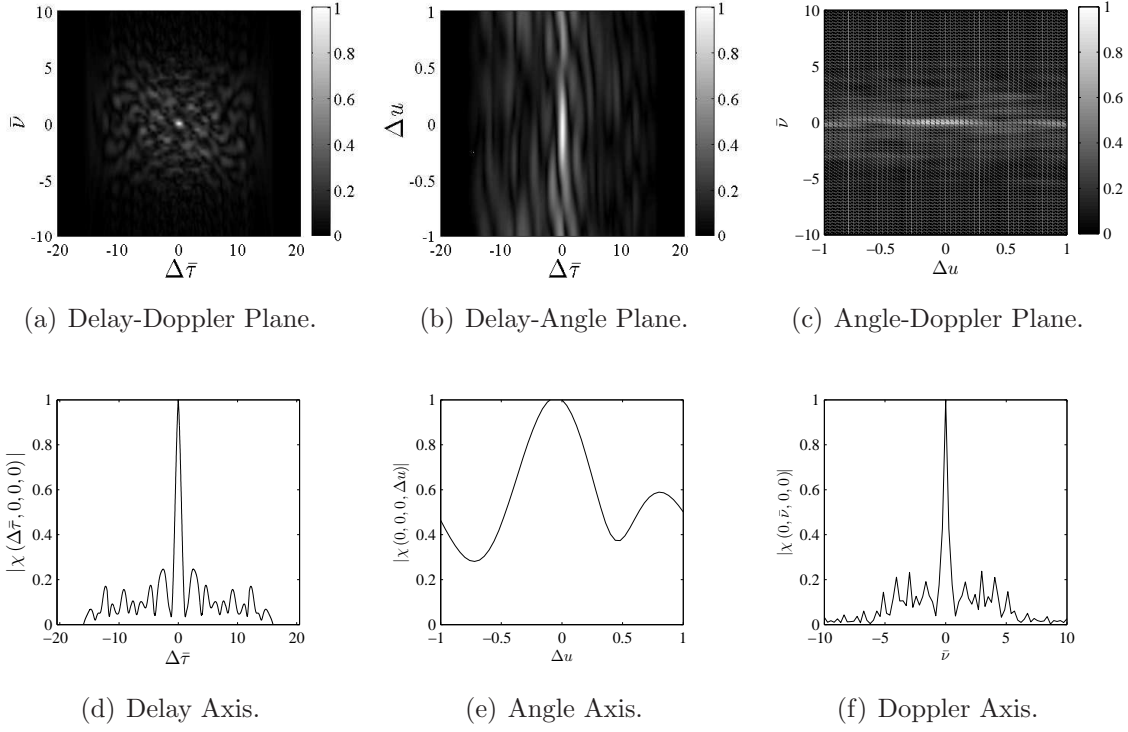


Figure 5.5. AF Principal Planes and Axes: Random-weighted FDA.

In contrast, consider the principal AF planes shown in Fig. 5.5 for the randomly weighted FDA with transmit signal characteristics plotted in Fig. 4.11, Chapter IV. The transmit signal field shown in Fig. 11(a) has no appreciable range-angle coupling compared to the LFP-FDA and as a result there is no appreciable mainlobe coupling evident in the delay-angle plane in Fig. 5(c). In fact the AF does not have a null in along the angle axis which means its resolution will be poor. The mainlobe widths along the delay and Doppler axes are quite narrow with $\delta_{\tau} = 1.2$ and $\delta_{\nu} = 0.81$. Accounting for the difference in normalization to [33], the average sidelobe level along the delay and Doppler axes seems to agree with the OFDM result that the average sidelobe level is approximately $\frac{1}{M}$. With such poor performance along the angle axis the waveform would be of little use in an array.

5.7 Received Signal Model Validation

An experimental, two-channel array configuration was used to validate the receiver's output which is predicted by Eq. (5.27). A simplified diagram for the experimental circuit is shown in Fig. 5.6 and specific details regarding the experiment are provided in Appendix B. Recalling that the circuit produces a DSB-SC modulated signal, the model for the received signal is modified to

$$r_q^{(ex)}(t, \Xi_t) = n_q(t) + \sum_{i=0}^{I-1} K_{tx,rx,i} s_q^{(ex)}(t, \Xi_{t,i}), \quad (5.40)$$

where superscript (ex) distinguishes that the received signal model represents the experimental circuit, the number of targets is $I = 2$ and

$$\begin{aligned} s_q^{(ex)}(t, \Xi_{t,i}) = & \sum_{p=0}^{P-1} \sum_{b=0}^{B-1} \exp [j(\omega_0 + \nu_{0,i})(t - 2\tau_{t,i} + \Delta\tau_{p,i} + \Delta\tau_{q,i})] \\ & \times \text{Re} \left\{ \tilde{a}_{p,b} \hat{b} [(t - 2\tau_t)] \right. \\ & \times \exp [j(\Delta\omega_b + \Delta\nu_{b,i})(t - 2\tau_{t,i} + \Delta\tau_{p,i} + \Delta\tau_{q,i})] \\ & \left. \times \exp [j\pi\vartheta_{p,b} (t - 2\tau_{t,i} + \Delta\tau_{p,i} + \Delta\tau_{q,i})^2] \right\}. \end{aligned} \quad (5.41)$$

The parameters specific to the i th target have i added to the subscript. The signal parameters for the experimental configuration were presented in Section 4.7, Chapter IV. Expressing the target parameter as $\Xi_{t,i} = (r_{t,i}, u_{t,i}, v_{t,i})$ the targets have the parameters $\Xi_{t,0} = (110\text{cm}, 0.39, 0)$ and $\Xi_{t,1} = (110\text{cm}, 0.12, 0)$ and physically are square, metal plates. In the simulation they are modeled as ideal point targets.

Equation (5.41) was used to simulate the received signal using the signal parameters in Section 4.7, in Chapter IV. The simulated and measured signals from the two channel array were processed using Eq. (5.27). The normalized processor output for both the measured and simulated data are shown in Fig. 5.7 and the two results

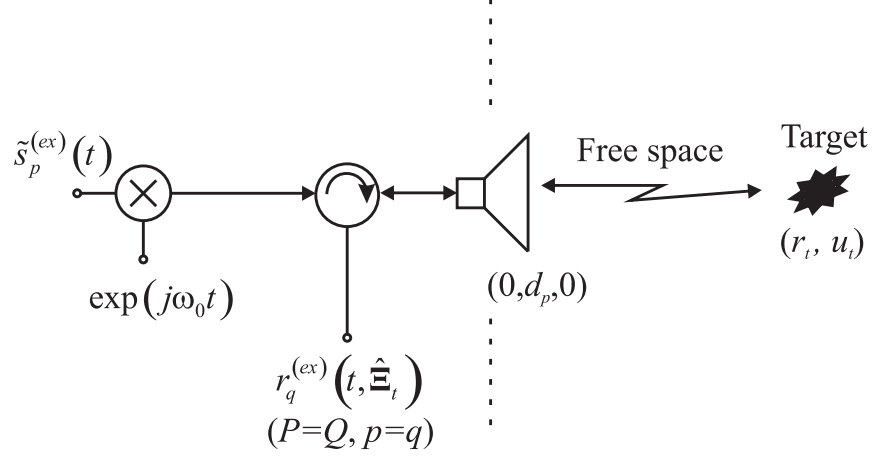


Figure 5.6. Target measurement configuration: simplified diagram.

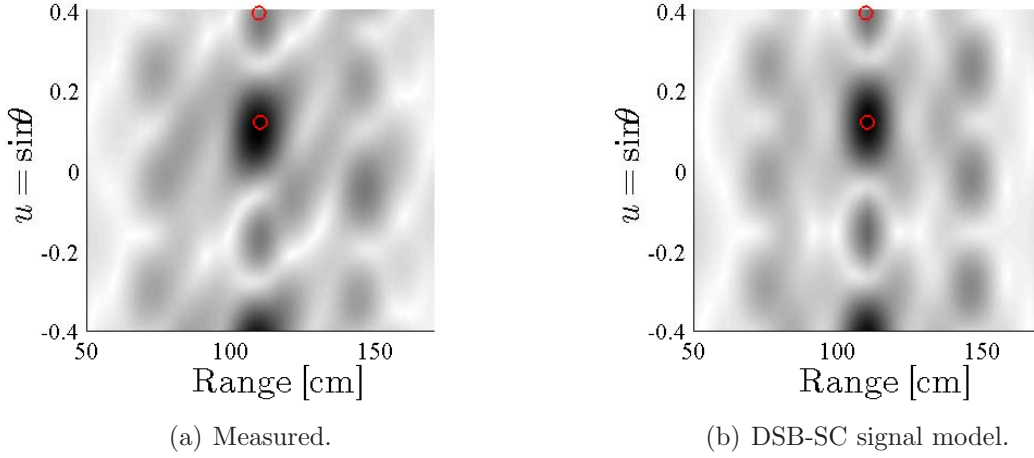


Figure 5.7. Comparison of measured (DSB-SC) and simulated (DSC-SC) received signal data: *OFDM₄* and *OFDM₁*. Reconstructed range-azimuth angle plot using measured and simulated received signal data for targets at $u_1 = 0.49$ and $u_2 = 0.12$ (indicated by the circles). The *OFDM₄* signal is transmitted from $p = 0$ and the *OFDM₁* signal is transmitted from $p = 1$. The signal is received by both antennas. The reconstructed plots show that the modified signal model approximately predicts the measured data within a scale constant.

are in fair agreement (i.e. moderate similarity between the two plots). The difference between the two plots can be attributed to non-ideal waveforms produced by the circuit and mismatches in signal timing and antenna alignments.

While the experiment only verifies a DSB-SC version of the signal model using stationary targets, the experiment shows that signal modeling can accurately repre-

sent a waveform diverse radar system using two transmitters. This provides limited support for validating that the SSB-SC model for generalized FDA signals correctly predicts the response of a real SSB-SC FDA system.

5.8 Chapter Summary

A model was developed for the signal received by a Q -element array due to the signal transmitted by a P -element array that reflected from an ideal point target in the radar's far-field. A narrowband and an intermediate approximation to the wide-band Doppler model were compared and the intermediate approximation was seen to provide more accurate results as the signal's time-bandwidth product increases. The comparison was not exhaustive and could be considered from a more comprehensive analytic perspective, particularly if the narrowband model is used. A matched filter receiver was then adapted from a generalized model of an arbitrary MIMO receiver model, along with the receiver's AF. The AF reveals the receiver's ability to measure target parameters for a given FDA signal configuration. The AF will be a useful tool in the design and analysis of future FDA configurations. The AF for the LFP-FDA and a randomly weighted FDA showed similar angular measuring performance as a CFA. Finally, a DSB-SC signal model was validated using measured data. The validation provides limited support to validate the SSB-SC signal model developed in Chapters IV and V.

VI. FDA Design Examples

6.1 Chapter Overview

The first section of the chapter uses the analytic and numerical methods developed in the previous sections to study the impact of changing key FDA's parameters using the LFP-FDA. The LFP-FDA is only a simple, special case of the waveform diverse model that was developed in prior chapters, but variations of the LFP-FDA are used here because the signal's properties have been well documented in related research. Optimization is not applied to the array design so several obvious parameter choices are investigated. Two methods of combining a LFP-FDA signal and its spatial complement are considered, because in the FDA-SAR application study a similar method was found to improve cross-range resolution. The chapter is concluded by demonstrating how the signal model can be used to study a generalized waveform diverse configuration, but also to highlight the significance of optimization for future FDA-related research. A summary listing of the configurations, their AF mainlobe widths and sidelobe levels is found in Table 6.2 at the end of this chapter.

6.2 LFP-FDA Examples

The LFP-FDA is used as the baseline case in the following experiments from which the parameters will be varied. For ease of reference the LFP-FDA simulation parameters for the base simulation parameters are repeated in Table 6.1. Recall that the LFP-FDA has the following signal parameters

$$\tilde{\Upsilon}_{p,b,m,n} = \begin{cases} (1, \pi \Delta f_b T_c, 0), & p = b \\ (0, 0, 0), & \text{otherwise.} \end{cases} \quad (6.1)$$

Table 6.1. Comparison simulation parameters.

Parameter	Value
Transmitters P	4
Receivers Q	1
Sub-carriers B	4
Frequency f_0	10GHz
Bandwidth BW_s	400MHz
Sub-carrier separation Δf	100MHz
Transmitter spacing $\Delta d_{\hat{y},t}$	$\lambda_{min}/2$
Receiver spacing $\Delta d_{\hat{y},r}$	$\lambda_{min}/2$
Chips M	1
Pulses N	1
Chip duration T_c	10ns

The set of principal AF planes for the LFP-FDA were shown in Fig. 5.4, Chapter V and the CFA's AF principal planes were shown in Fig. 2.9, Chapter II. The mainlobe widths and the PSLs for the CFA and LFP-FDA are listed as "CFA" and "FDA_{base}^{LFP}" respectively in Table 6.2.

The CFA and the LFP-FDA signals were found to have similar mainlobe widths and dissimilar PSLs along the delay and Doppler axes. Considering the LFP-FDA's range-angle coupling it was expected that the width of the LFP-FDA's mainlobe along the Δu axis would be slightly narrower than the CFA's, but it isn't. The lack of improvement may be a result of processing the CFA signal using the processor described in Chapter V instead of the phased-array processor. However, given that the two signals span the same region in $\omega - \bar{y}$ their AF mainlobes have similar widths. The LFP-FDA will be used in the comparisons that follow and the result of increasing

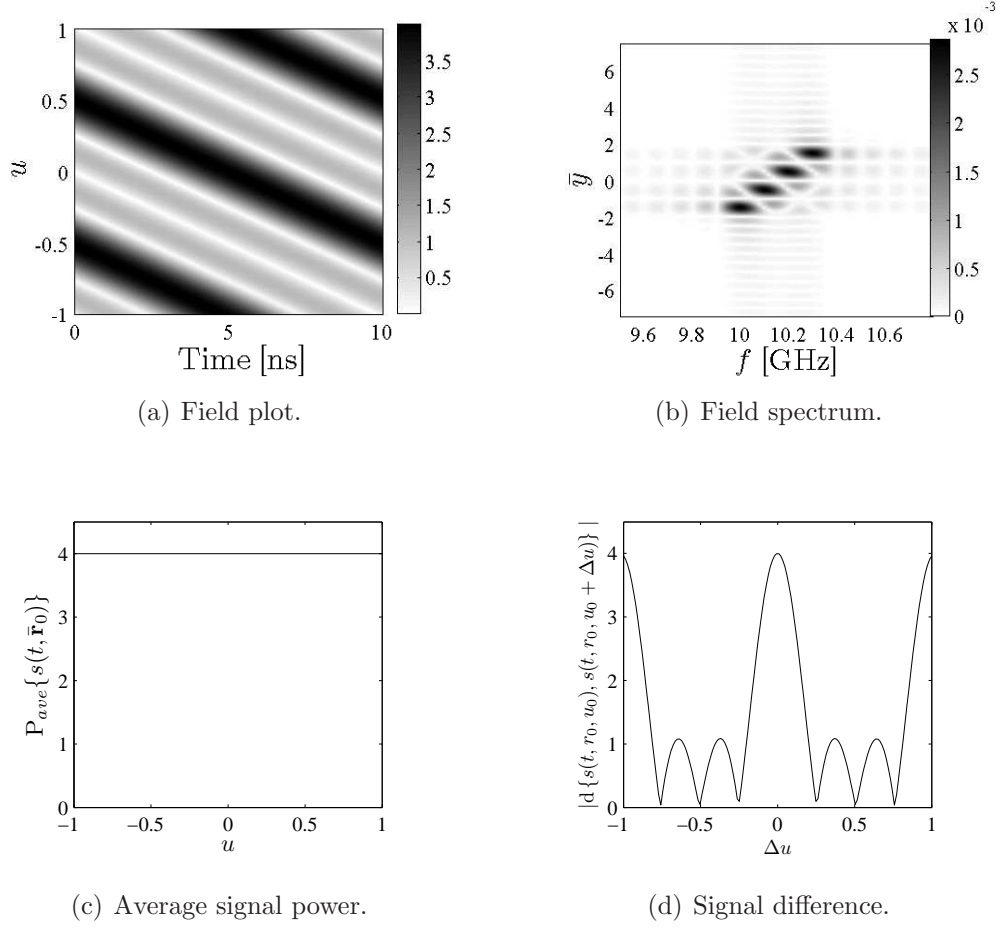


Figure 6.1. Transmit signal characteristics: LFP-FDA, $\Delta_{\hat{y},t} = \lambda_{min}$.

the transmit array's inter-element spacing is considered next.

6.2.1 Transmit Array Inter-element Spacing

Using frequency diversity is thought to reduce or eliminate grating lobes [50] which implies that the array's inter-element spacing does not need to satisfy the $\Delta_{\hat{y},t} = \lambda_{min}/2$ constraint discussed in Chapter II. If that is true then, for the same system complexity and weight, $\Delta_{\hat{y},t}$ can be increased arbitrarily to improve accuracy of the radar's DOA measurement (providing the narrowband, array assumptions are not violated).

The simulation parameters in Table 6.1 are held constant except for the transmit

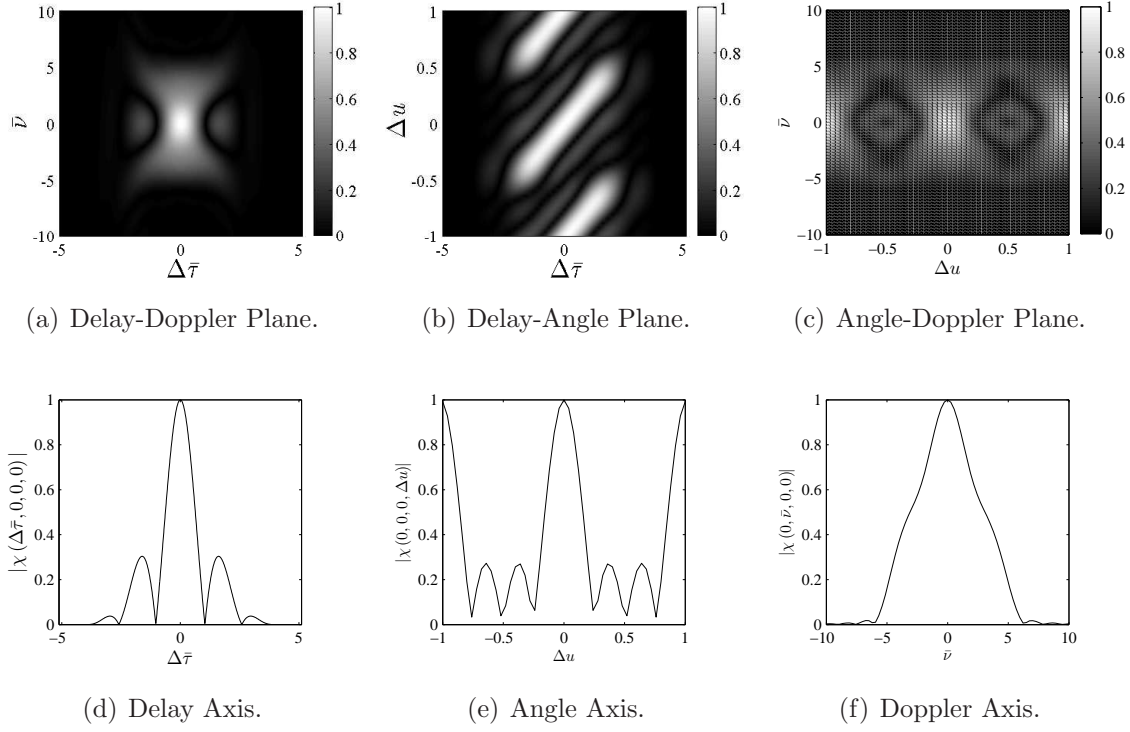


Figure 6.2. AF Principal Planes and Axes: LFP-FDA, $\Delta_{\hat{y},t} = \lambda_{min}$.

array's inter-element spacing which is now increased to $\Delta d_{\hat{y},t} = \lambda_{min}$. The transmit signal's characteristics are shown in Fig. 6.1.

It was shown in Chapter II that if the same frequency is transmitted across the array $\Delta d_{\hat{y},t} = \lambda_{min}$ spacing results in grating lobes, but for the LFP-FDA the average signal power remains constant in u shown in Fig. 1(c). Increasing the spacing amounts to expanding the \bar{y} -axis, resulting in a compression of the u axis, compared to the base configuration. This is seen in both the signal field pattern and the signal difference plots by comparing Fig. 1(a) to Fig. 2.14, Chapter II.

The AF's principal planes are shown in Fig. 6.2 and the results for the mainlobe widths and PSLs are listed under the entry “FDA $_{\Delta_{\hat{y},t}=\lambda_{min}/2}^{LFP}$ ” in Table 6.2. The delay-Doppler plane shown in Fig. 2(a) appears to be relatively unchanged compared to the original configuration; however, the amount of range-angle coupling in Fig. 2(b) has now increased resulting in δ_u reducing by a factor of two shown in Fig. 2(e). The

trade-off is that there is a sidelobe at $u = \pm 1$ because the $u = 0$ transmit signal repeats at $u = \pm 1$. While this is not a grating lobe in terms of the signal's average power it results in ambiguity. If an array was used to process the received signal, instead of a single element, it may be able to attenuate the ambiguous lobes.

In summary, given that the standard matched filter receiver is used to process the entire waveform (as opposed to filtering and processing sub-carrier signals separately) that the inter-element spacing should be maintained at $\Delta d_{\hat{y},t} = \lambda_{min}/2$. Stated differently, the size of δ_u is fundamentally limited by the aperture size and ambiguities will result when the aperture is not adequately sampled.

6.2.2 Sub-Carrier Separation

Next, the case of increasing the sub-carrier separation is considered. It may be desirable to span the same bandwidth using fewer sub-carriers, or to separate the sub-carrier signals and process them separately such as a combined STAP and SAR multi-mission scenario. To maintain the same bandwidth, Δf is increased by increasing the signal duration to $T_c = 20\text{ns}$ such that $\Delta f'_b = (2T_c)^{-1} = 50\text{MHz}$. For the signal parameters in Table 6.1, this results in eight orthogonal sub-carriers spanning BW_s . Only 4 sub-carriers are chosen such that the b th frequency is $f_b = b2\Delta f'_b$ which selects the same sub-carrier frequencies used in the previous comparisons.

The signal field pattern is shown in Fig. 3(a) where it can be seen that the pattern repeats temporally after $t = 10\text{ns}$. Referring to Fig. 3(b), it can be seen that the sub-carriers are clearly separated and span the same region in $f - \bar{y}$, while Fig. 3(c) and Fig. 3(d) show that the average power and signal difference appear unchanged compared to the original LFP-FDA signal.

The impact of increasing the sub-carrier separation is seen in the AF plots shown in Fig. 6.4 and the AF mainlobe's parameters are listed in Table 6.2 under the entry

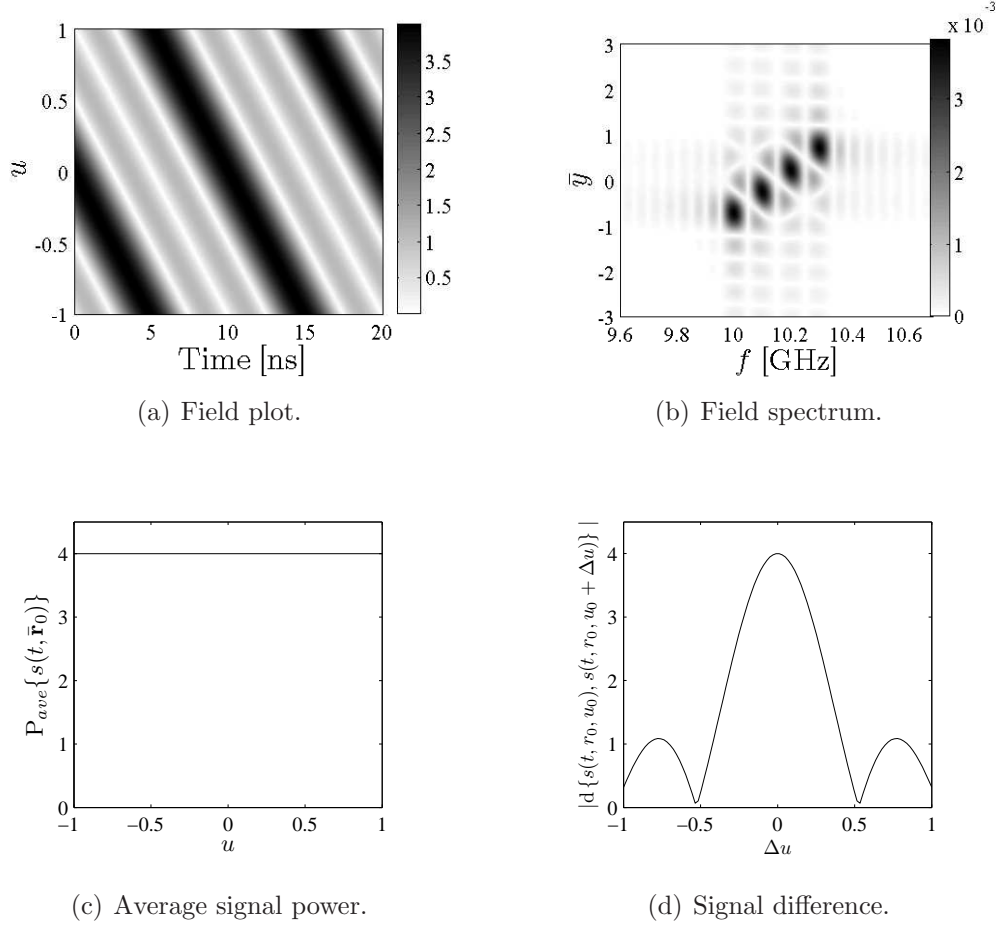


Figure 6.3. Transmit Signal Characteristics: LFP-FDA, $B = 8$.

“FDA $_{B=8}^{\text{LFP}}$ ”. The AF’s δ_τ and δ_ν are significantly reduced, but at the expense of increased PSLs. The configuration does not improve δ_u compared to the original configuration. Based on the signal’s AF plots, the signal should be filtered to separate the different sub-carrier components and each sub-carrier signal processed separately but this is not considered here. This configuration would be inadequate for SAR imaging.

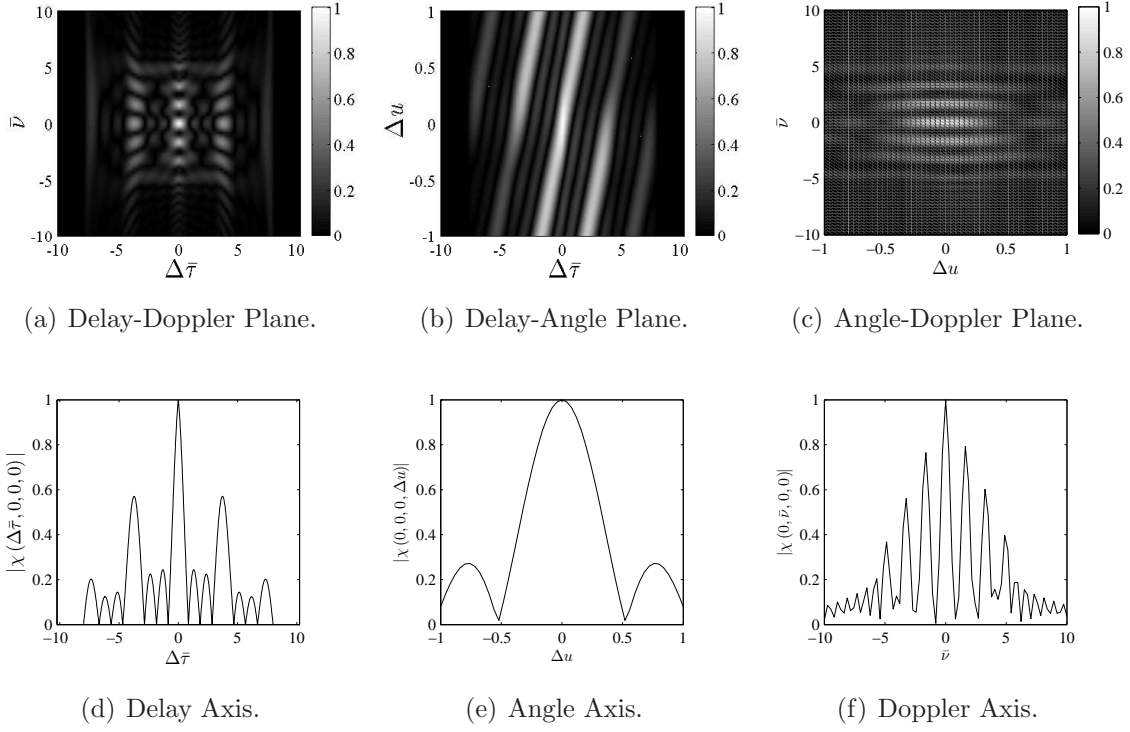


Figure 6.4. AF Principal Planes and Axes: LFP-FDA, $B = 8$.

6.2.3 Chirped Waveforms

It is straightforward to apply LFM signals to the sub-carriers, and the signal parameters are given by

$$\tilde{\Upsilon}_{p,b,m,n} = \begin{cases} (1, \pi \Delta f_b T_c, \vartheta_0), & p = b \\ (0, 0, 0), & \text{otherwise,} \end{cases} \quad (6.2)$$

where $\vartheta_0 = 100\text{MHz}/10\text{ns}$. The chirp rate ensures the entire bandwidth is covered without overlap. The transmit signal characteristics are identical to the base configuration and are not repeated here.

The signal's AF is shown in Fig. 6.5 and its mainlobe widths and PSLs are listed under the entry “FDA_{LFM}^{LFP}” in Table 6.2. The primary difference to the base configuration is that there is now shearing evident in the delay-Doppler plane caused by the

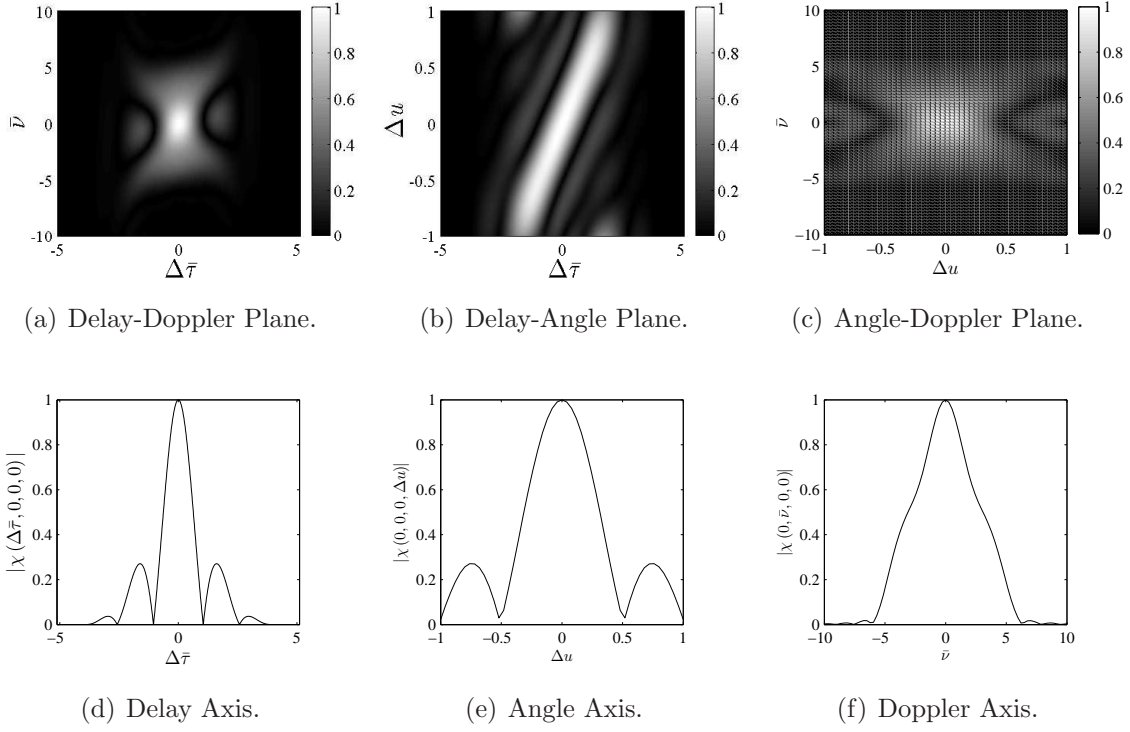


Figure 6.5. AF Principal Planes and Axes: LFP-FDA, LFM.

LFM component. However, applying chirps to the sub-carriers does not significantly reduce either δ_τ or δ_ν as it might for the monostatic case.

6.2.4 Phase Coding with $M = 4$

Next, the base LFP-FDA is extended to transmit four sets of spectral chips sequentially in time (i.e. $M = 4$). The first example uses the same Barker bi-phase code, $(1, 1, 1, -1)$, applied to each of the sub-carriers. The signal's AF is shown in Fig. 6.6 and its mainlobe widths and PSLs are listed in Table 6.2 under the entry “FDA_{Barker}^{LFP}”.

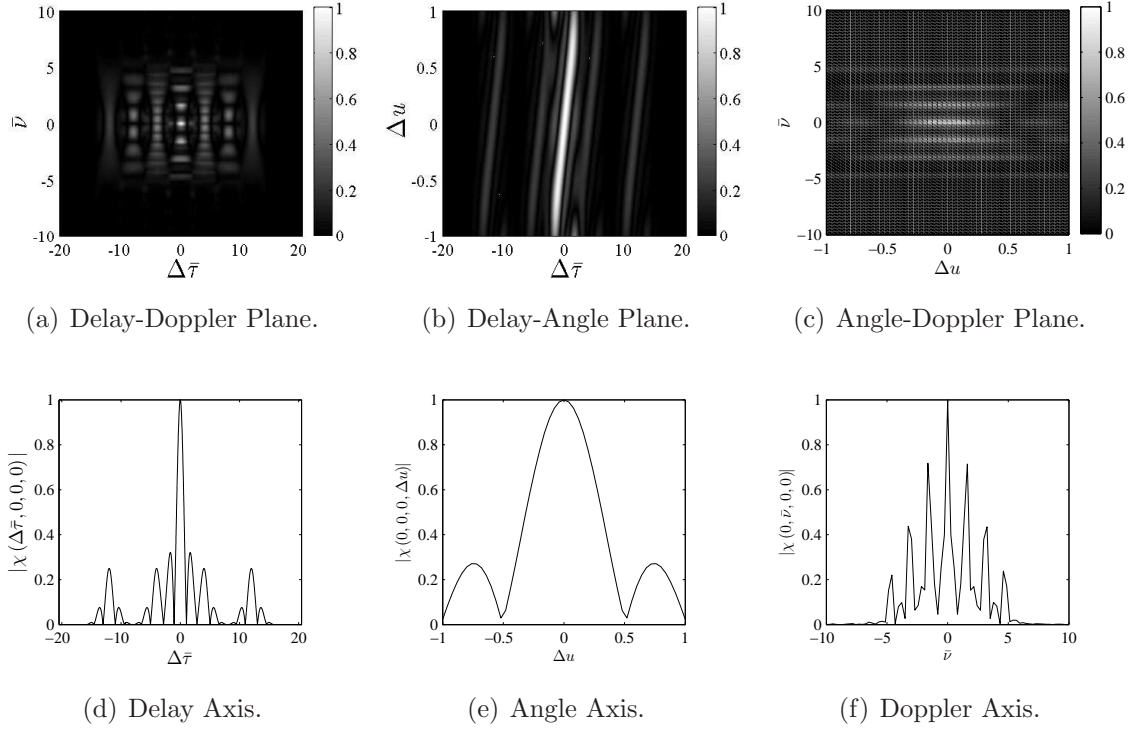


Figure 6.6. AF Principal Planes and Axes: LFP-FDA, $M = 4$ Barker code.

The signal parameters used to generate the signal are described by

$$\tilde{\Upsilon}_{p,b,m,0} = \begin{cases} (1, b\pi, 0), & m = \{0, 1, 2\} \ p = b \\ (1, b\pi + \pi, 0), & m = 3, \ p = b \\ (0, 0, 0), & \text{otherwise,} \end{cases} \quad (6.3)$$

where the $b\pi$ term shifts the transmit waveform's peak to the center of the pulse when the sub-carriers are orthogonal.

The AF's PSL along the delay axis is close to $\max\{\text{PSL}_\tau\} = \frac{1}{M}$ which is a result of using the Barker phase codes; however, its PSL along the Doppler axis is extraordinarily high. The cause of the large spikes seen in Fig. 6(f) is that all sub-carriers transmit the same coded signal. When the signal is Doppler shifted such that the signal's Doppler shifted sub-carrier frequencies match the filter sub-carrier frequen-

cies, the Doppler shifted signal passes through the filter bank with significant energy. Because the scenario uses $B = 4$ there are three significant sidelobes either side of the mainlobe in Fig. 6(f).

The next multi-chip signal coding considered is a set of orthogonal, bi-phase Hadamard codes. This code may be useful to reduce the sub-carrier cross-coupling when the signal is Doppler shifted. Denoting the p th set of codes using

$$\Phi^{(p)} = [\varphi_0^{(p)}, \dots, \varphi_m^{(p)}, \dots, \varphi_{M-1}^{(p)}]$$

the set of signal parameters are

$$\tilde{\Upsilon}_{p,b,m,0} = \begin{cases} \left(1, b\pi + \varphi_m^{(p)}, 0\right), & p = b, \forall m \\ (0, 0, 0), & \text{otherwise,} \end{cases} \quad (6.4)$$

and the set of Hadamard codes for $P = M = 4$ are

$$\begin{aligned} \Phi^{(0)} &= [1, 1, 1, 1] \\ \Phi^{(1)} &= [1, -1, 1, -1] \\ \Phi^{(2)} &= [1, -1, -1, 1] \\ \Phi^{(3)} &= [1, 1, -1, -1]. \end{aligned} \quad (6.5)$$

Fig. 6.7 shows the AF plots for the Hadamard phase coded signal and the key AF parameters are listed under the entry “FDA_{Hadamard}^{LFP}” in Table 6.2. In contrast to the Barker phase coded signal the Hadamard phase coded significantly reduces the Doppler sidelobes which is shown in Fig. 7(f). In both the delay and angle dimensions the phase coded signals have similar performance.

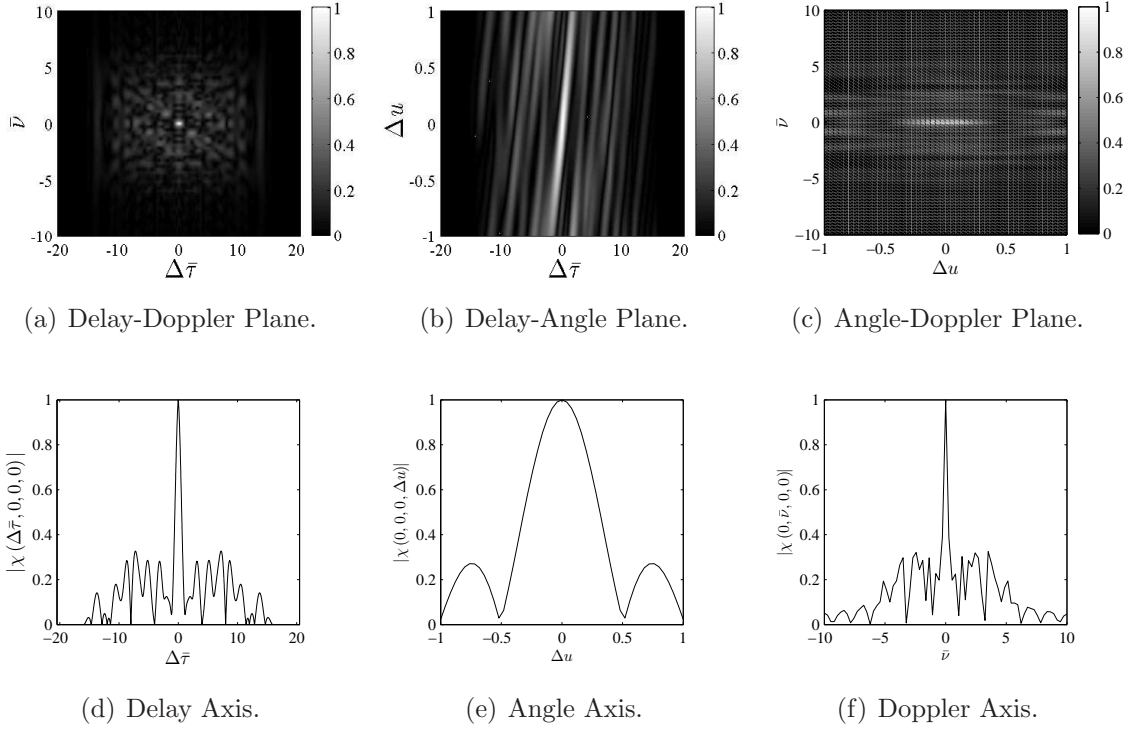


Figure 6.7. AF Principal Planes and Axes: LFP-FDA, $M = 4$ Hadamard code.

6.2.5 Combining a Signal and Its Complement

It was found in a FDA-SAR application study that cross-range resolution could be improved by reversing the order of frequency progression along the array half way through the collection [16]. This divided the synthetic aperture into two sub-apertures and for any signal collected in one aperture there is a corresponding signal in the other aperture, but with the order of frequency progression reversed. The SAR application used the transmit signal's spatial characteristics to modify the synthetic aperture collection locations forming a wider aperture which improved the reconstructed image's cross-range resolution.

The comparison described here considers that a range-angle plot of a point target is analogous to a polar coordinate PSF. The polar coordinate PSF should be closely related to the SAR imaging PSF. The SAR PSF is typically defined in the range

and cross-range dimensions, which is a cartesian coordinate system, but a small angle approximation to the polar PSF can be made for angles close to $u = 0$. Therefore, a method improving the AF over the $\Delta\tau - \Delta u$ plane should also improve the system's PSF and be beneficial in SAR imaging.

For a given transmit signal configuration, its complement is described mathematically by reversing the transmitter indexing. Denoting the complementary signal by superscript (c) the complement's p'' th transmit signal is

$$\begin{aligned} s_{p''}^{(c)}(t) = & \sum_{b=0}^{B-1} \sum_{m=0}^{M-1} \sum_{n=0}^{N-1} \tilde{a}_{p'',b,m,n} \hat{b}(t - mT_c - nT_p) \\ & \times \exp(j\omega_0 t) \exp[j\Delta\omega_b(t - mT_c - nT_p)] \\ & \times \exp[j\pi\vartheta_{p'',b,m,n}(t - mT_c - nT_p)^2], \end{aligned} \quad (6.6)$$

where the signal's index p is related to the complement's index p'' through

$$p'' = (P - 1) - p. \quad (6.7)$$

The transmitted far-field signal, the received signal and the AF relating to the complement are all distinguished by adding a superscript (c) .

Physically, the signal is produced using $N = 2$ in the signal model and reversing the $n = 0$ signal's allocation across the array for the $n = 1$ pulse. For the LFP-FDA with signal parameters in Eq. (6.1) transmitted in the $n = 0$ pulse, the $n = 1$ pulse parameters are specified by

$$\tilde{\Upsilon}_{p,b,0,1} = \begin{cases} (1, \pi\Delta f_b T_c, 0), & b = (P - 1) - p \\ (0, 0, 0), & \text{otherwise.} \end{cases} \quad (6.8)$$

In terms of the AF, a sequence of two pulses results in major lobes at delays of

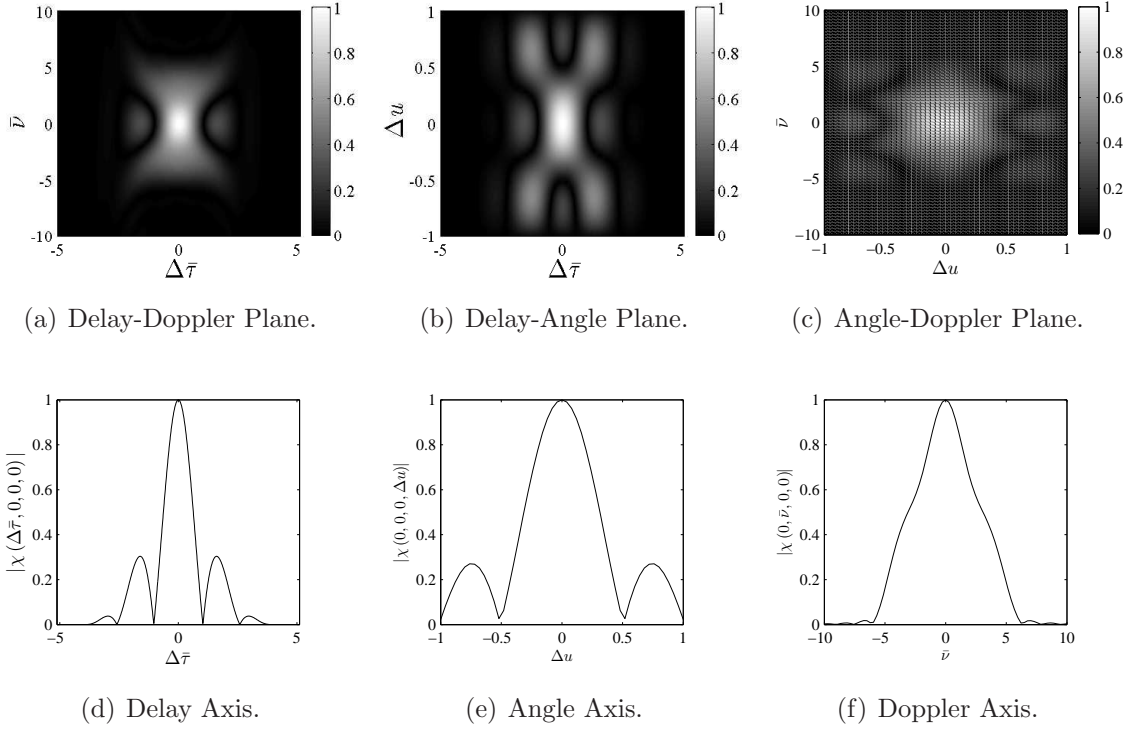


Figure 6.8. AF Principal Planes and Axes: LFP-FDA, $|\chi^{(+)}(\Delta\tau, v_t, u_t, \Delta u)|$.

$\Delta\tau = \pm T_p$; however, these only arise from multiple-time-around returns with sufficient energy to be detected above the receiver noise. Assuming that T_p has been designed to minimize these returns it is sufficient to consider the AF on the interval $\Delta\tau = \pm MT_c$. For clarity the signal and its complement transmitted in succession are considered two separate signals that are added separately. The first method considered, adds the processed signal to its processed complement and the resulting AF is denoted by the superscript (+). Assuming the signal and its complement are processed separately by the receiver, and the outputs are added, the resulting ambiguity function is

$$|\chi^{(+)}(\Delta\tau, v_t, u_t, \Delta u)| = \frac{1}{2}|\chi(\Delta\tau, v_t, u_t, \Delta u) + \chi^{(c)}(\Delta\tau, v_t, u_t, \Delta u)|. \quad (6.9)$$

The principal planes of $|\chi^{(+)}(\Delta\tau, v_t, u_t, \Delta u)|$ are shown in Fig. 6.8 and the AF's

key parameters are listed under the entry “ $\text{FDA}_{\text{Comp. (+)}}^{\text{LFP}}$ ” in Table 6.2. Adding the spatial complement to the original seems to negate the range-angle coupling to create a symmetric pattern in the delay-angle plane shown in Fig. 8(a). The resulting AF has similar performance to the base configuration and does not improve measurement accuracy.

Qualitatively, the result may not significantly improve a SAR image when a single receiver element is used to match filter the received signals; or when the original SAR collection locations are used. It was found in the measured data, that when the method is combined with an array of receiver elements that the quality of a range angle image showing two targets can be improved, but not the measurement accuracy (see Appendix B for the example using measured data).

While experimenting with the signal and its complement, a non-linear method of combining the signals was found to offer improvements to the AF’s delay-angle plot compared to the additive method. Fig. 6.9 shows the principal AF planes for the non-linear combination

$$|\chi^{(\times)}(\Delta\tau, v_t, u_t, \Delta u)| = |\chi(\Delta\tau, v_t, u_t, \Delta u) [\chi^{(c)}(\Delta\tau, v_t, u_t, \Delta u)]|, \quad (6.10)$$

and the AF’s parameters are listed under the entry “ $\text{FDA}_{\text{Comp. (+)}}^{\text{LFP}}$ ” in Table 6.2. The following attempts to justify why it was considered that this combination might improve imaging performance.

Following receiver processing there are cross-terms $\tilde{w}_{p,b}(u)\tilde{w}_{p',b'}^*(\hat{u})$ in the summation of correlation functions in Eq. (5.36). Expressing this spatial term using the harmonic functions, and assuming $v_t = 0$, the cross term is

$$\tilde{w}_{p,b}(u)\tilde{w}_{p',b'}^*(\hat{u}) = \exp[j(\omega_b d_p u - \omega_{b'} d_{p'} \hat{u})]. \quad (6.11)$$

However, for the LFP-FDA, indices p and b are equal and the equation can also be expressed as

$$\tilde{w}_p(u)\tilde{w}_{p'}^*(\hat{u}) = \exp[j(\omega_p d_p u - \omega_{p'} d_{p'} \hat{u})]. \quad (6.12)$$

If the array elements and sub-carriers are equally spaced it simplifies further. When the spatial complement is transmitted, it will have similar terms $\tilde{w}_{p''}(u)\tilde{w}_{p'''}^*(\hat{u})$ related through Eq. (6.7) (p''' is the filter's index). In terms of the original indexing, these terms should be proportional to

$$\tilde{w}_{p''}(u)\tilde{w}_{p'''}^*(\hat{u}) = \exp[-j(\omega_p d_p u - \omega_{p'} d_{p'} \hat{u})], \quad (6.13)$$

because the array is electrically reflected about the \hat{x} -axis. Stating the concept differently, for a target at an angle u_t with a mismatched filter at $u_t + \Delta u$ the original configuration maps the targets to those locations. The spatial complement's transmit signal field and AF is a reflection about the $u = 0$ line compared to the original configuration. This makes it appear that the original configuration was used, but the target is now imaged at $-u_t$ and the filter is mismatched to $-u_t - \Delta u$. During the processing the u_t and $-u_t$ terms are compensated, but not the mismatch contributions Δu and $-\Delta u$.

Providing the above description is accurate, when the signal and its spatial complement are added (such as in the first method) the two exponential terms resulting from the signal and its complement become sinusoids as predicted by Euler's formula. In the multiplicative method, when the signal and its complement are multiplied the exponents' arguments add and the term becomes equal to one.

The algebra has not been evaluated for the entire set of cross-terms resulting from multiplying the signal and its complement to determine exactly why the AF

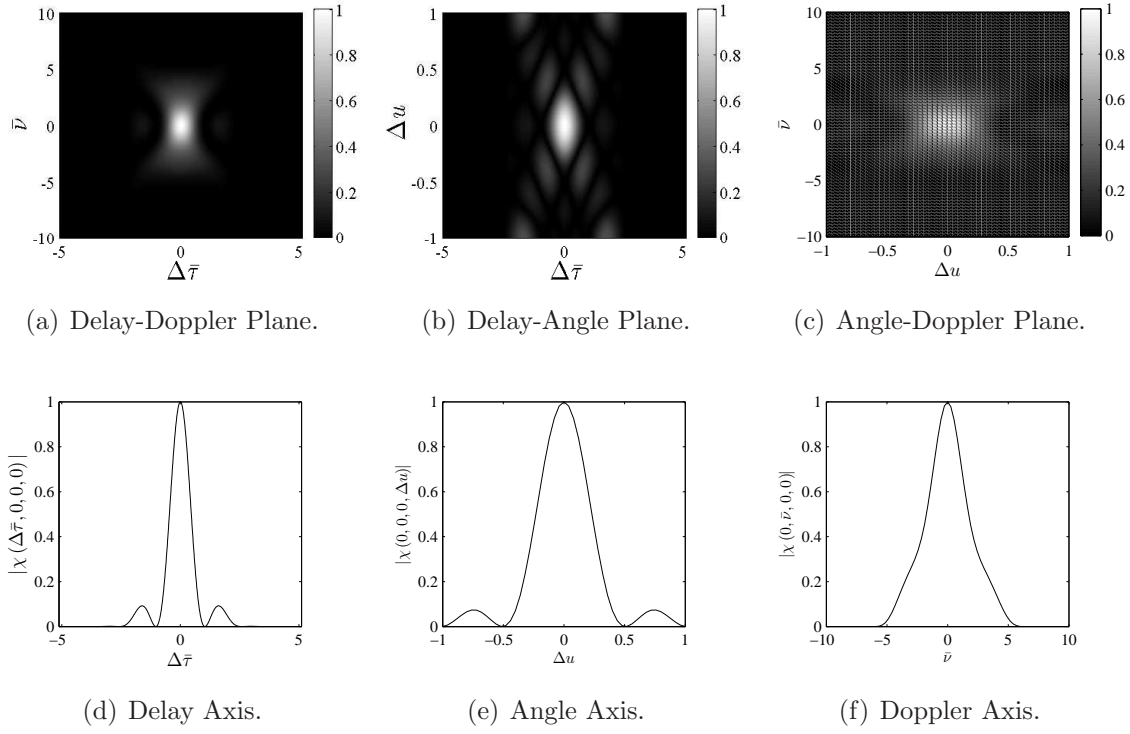


Figure 6.9. AF Principal Planes and Axes: LFP-FDA, $|\chi^{(\times)}(\Delta\tau, v_t, u_t, \Delta u)|$.

plots shown in Fig. 6.9 indicate significant improvements to the resulting delay-angle plot. Without performing further analysis on the method it is difficult to predict how the method performs in a noise-limited system, but the method may be useful in a clutter-limited scenario such as SAR imaging or GMTI and warrants further investigation.

6.3 Waveform Diverse Array

Initially, it was considered that if the transmit signal configuration is highly irregular that the receiver should be able to measure a target's parameters more accurately because there is less coupling between the parameters. One example of coupling that should be minimized by an irregular signal is the delay-angle coupling of the LFP-FDA's signal and another is the classic delay-Doppler coupling of a LFM signal. In the

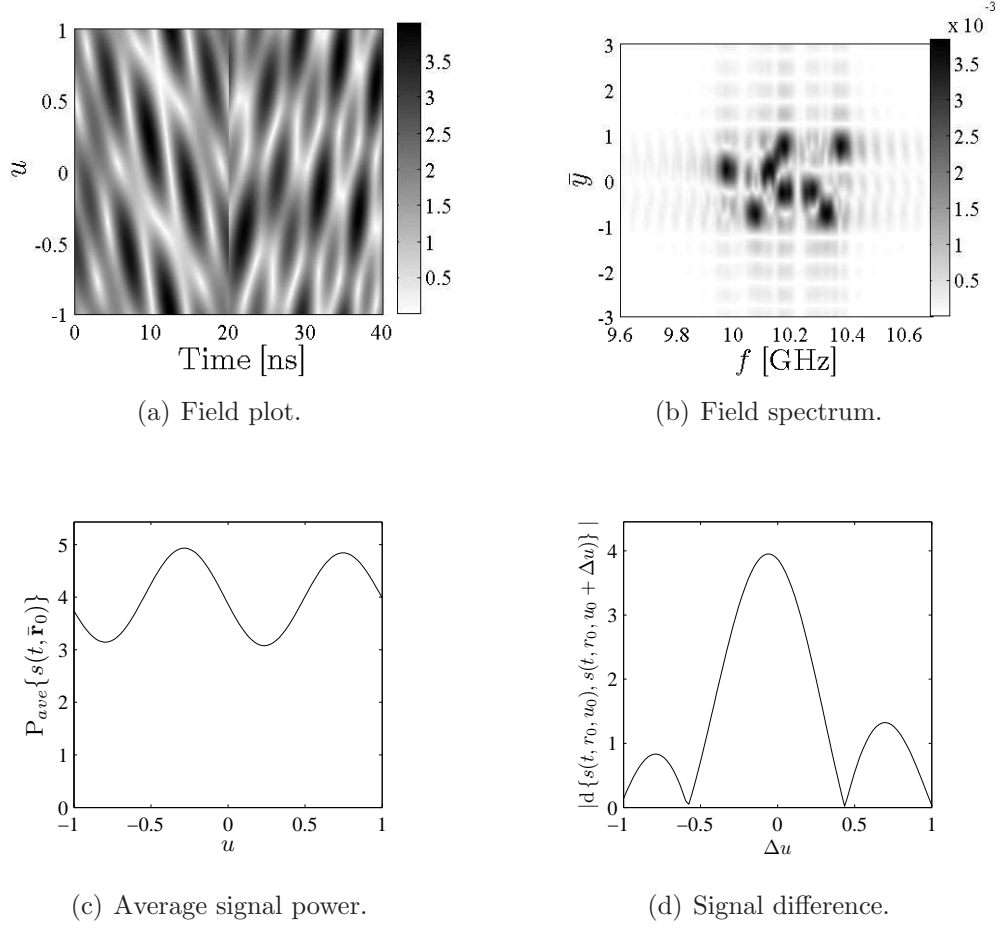


Figure 6.10. Transmit signal characteristics: waveform diverse signal.

final experiment, a generalized FDA is designed to include temporal-spectral-spatial coding, phase coding across the sub-carriers and chirp diversity.

The signal design begins with the parameters in Table 6.1. The chip duration is increased to $T_c = 20\text{ns}$ which doubles the number of sub-carriers spanning BW_s to $B = 8$. The number of transmit elements is maintained at $P = 4$; however, to use all eight sub-carriers such that each sub-carrier is transmitted only once the number of chips is increased to $M = 2$. The total signal duration is then $T_s = 40\text{ns}$ which results in the time-bandwidth product increasing by a factor of four compared to the original LFP-FDA configuration.

Next an eight sequence Costas code is used to code the sub-carriers over transmit

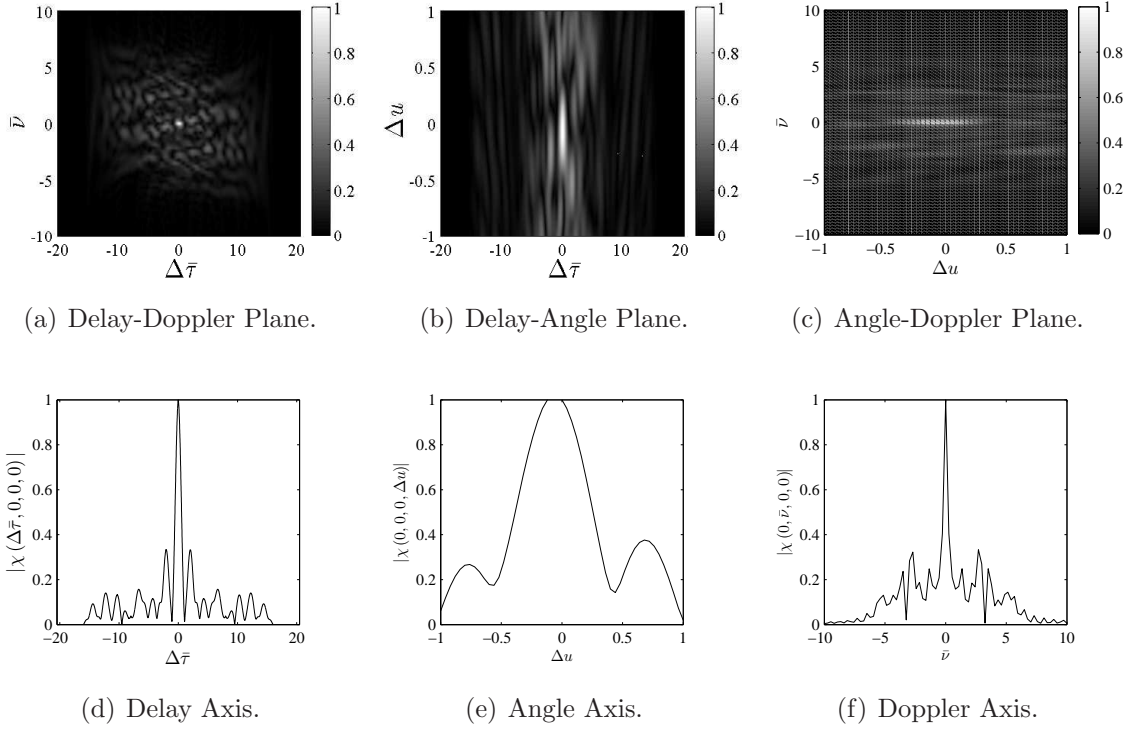


Figure 6.11. AF Principal Planes and Axes: Waveform Diverse Configuration.

elements both spatially and temporally. The sequence is divided into two equal-length sub-codes and each sub-code is used to assign a frequency with index b to a transmit element index p over the two temporal chips. The phases are coded using a derivative of the Newman phase coding presented in Chapter II where the chip on the b th sub-carrier has an initial phase $\varphi_{p,b,m,n} = b^2/B$. Finally, chirps are added to each of the sub-carriers. The chirp rates have equal magnitude $|\vartheta_{p,b,m,n}| = \Delta f/T_c$ and the chirp directions for each of the spatial-temporal chips at each chip index m is determined using a Hadamard sequence.

For the first temporal chip index $m = 0$ the signal parameters for the first set of

signals is

$$\tilde{\Upsilon}_{p,b,0,0} = \begin{cases} (1, \pi/8, \vartheta_0), & p = 0, b = 1 \\ (1, 25\pi/8, -\vartheta_0), & p = 1, b = 5 \\ (1, \pi/2, \vartheta_0), & p = 2, b = 2 \\ (1, 49\pi/8, -\vartheta_0), & p = 3, b = 7 \\ (0, 0, 0), & \text{otherwise.} \end{cases} \quad (6.14)$$

For the second chip with index $m = 1$, the set of signal parameters is

$$\tilde{\Upsilon}_{p,b,1,0} = \begin{cases} (1, 36\pi/8, \vartheta_0), & p = 0, b = 6 \\ (1, 16\pi/8, -\vartheta_0), & p = 1, b = 4 \\ (1, 0, -\vartheta_0), & p = 2, b = 0 \\ (1, 99\pi/8, +\vartheta_0), & p = 3, b = 3 \\ (0, 0, 0), & \text{otherwise.} \end{cases} \quad (6.15)$$

Fig. 6.10 shows the transmit signal's characteristics. The signal configuration is constrained to the same region in $\omega - \bar{y}$ as the LFP-FDA which is shown in Fig. 10(b). The average power is no longer constant over u but has what appears to be a sinusoidal variation with an average value of approximately four. The variation in the average power is due to the chirp diversity applied to the signal. The signal difference function does not appear to be appreciably different to the LFP-FDA base case considered earlier.

Next, consider the AF's principal planes and axes shown in Fig. 6.11. Each of the planes show the function produces a well constrained mainlobe with an irregular sidelobe pattern everywhere. The plots of the AF's principal planes are also strikingly

similar in appearance to the AF principal planes for the randomly weighted FDA shown in Fig. 5.5.

Finally, examining the principal AF axes shown in Fig. 6.11 reveals that, despite the waveform diversity, the width of the mainlobe along the delay and angle axes is fundamentally limited by the array's size and the signal bandwidth; however, the mainlobe width along the Doppler axis shows significant reduction. The AF's mainlobe is shifted along the Δu -axis which is most likely a result of the varying average transmit signal power over u .

In summary, the experiment serves to demonstrate the model's flexibility but seems to disprove that the signal can be made arbitrarily random to improve measurement accuracy in the delay or angular dimensions. Additionally, it seems that a signal's measurement accuracy in angle and range, using a single set of received signals, is fundamentally limited by the aperture size and signal bandwidth. Finally, this example shows that further work is required in the area of FDA signal design and optimization.

6.4 Chapter Summary

The result of varying the LFP-FDA configuration's parameters was explored in this chapter. The experiments using simulated data showed that the FDA's range and angle measurement accuracies are fundamentally constrained by the bandwidth and aperture size respectively. It was seen that increasing the transmit element spacing did not produce grating lobes in terms of average signal power but did result in ambiguities. Covering the bandwidth using a sparse set of sub-carriers resulted in a poor ambiguity function along the principal AF planes; however, a receiver based on clearly separable sub-carriers would process each sub-carrier separately. A chirped LFP-FDA configuration was studied along with two phase-coded configurations based

Table 6.2. Summary of Results.

Configuration.	δ_τ	δ_ν	δ_u	PSL $_\tau$	PSL $_\nu$	PSL $_u$
CFA	1	6.22	0.5	0	0.22	0.27
FDA $_{\text{base}}^{\text{LFP}}$	1	6.22	0.5	0.3	0.02	0.27
FDA $_{\Delta_{\hat{y},t}=\lambda_{\min}/2}^{\text{LFP}}$	1	6.22	0.25	0.3	0.02	1
FDA $_{B=8}^{\text{LFP}}$	0.86	0.81	0.5	0.56	0.79	0.27
FDA $_{LFM}^{\text{LFP}}$	1.05	6.22	0.5	0.27	0.02	0.27
FDA $_{\text{Barker}}^{\text{LFP}}$	1.04	0.81	0.5	0.32	0.71	0.27
FDA $_{\text{Hadamard}}^{\text{LFP}}$	1.12	1.08	0.5	0.33	0.33	0.27
FDA $_{\text{Comp. (+)}}^{\text{LFP}}$	1.02	6.22	0.5	0.3	0.02	0.27
FDA $_{\text{Comp. (x)}}^{\text{LFP}}$	1.04	5.68	0.5	0.09	0	0.07
FDA $^{\text{WD}}$	1.07	0.81	0.5	0.33	0.32	0.37

on a Barker and a Hadamard code. None of the configurations improved the range and angle measurement accuracy, but the phase-coded signals did improve the Doppler measurement accuracy.

Then, the concept of adding a processed FDA signal and its spatial complement to improve the PSF was examined. The additive method was seen to improve measurement accuracy by reducing ambiguities. A multiplicative method to combine the signal and its complement was shown to improve performance over the delay-angle plane even further. Finally, the FDA signal model was used to simulated the performance of a spatially, spectrally and temporally coded signal with chirp diversity. The purposely randomized signal had similar performance to the randomly weighted FDA presented in earlier chapters. This result certainly encourages using optimization to design the FDA signal opposed to randomly selecting signal parameters.

VII. Conclusions

7.1 Research Summary

The research aimed to determine whether the FDA is fundamentally more accurate at measuring a target's position than existing radar technologies. CFA theory was introduced in Chapter II and forms the basis for comparisons. Spectral perspectives relating an array and its far-field pattern were reviewed in relation to CFA design and Fourier optics (Appendix C). Both the traditional and the more recent MIMO ambiguity functions were presented as a base from which to develop an FDA ambiguity function. OFDM was reviewed showing the signal model shares many similarities to the FDA and CFA models. Finally, recent research using the LFP-FDA framework was reviewed providing a primer for the theoretical development to follow. A SAR application study was reviewed showing how FDA could potentially improve traditional radar applications.

The results of the experiments performed using simulated data are tempered by the ideal assumptions underlying the signal model and the simulations. These assumptions were discussed in Chapter III. First, the target measurement accuracy is examined from an ideal signal perspective exclusive of any deleterious effects. This needs to be combined in future with sufficient consideration of at least thermal noise and its impact on parameter estimation. All of the radar equation parameters were modeled without frequency-dependance; it is expected that the FDA model permits a piece-wise approximation to a parameter's spectral response but that was not considered. One of the future challenges will be incorporating these parameters into the signal model efficiently without overly complicating the resulting model.

To provide support for the conclusions, a generic frequency and waveform diverse transmit signal model was developed. Using the model, key transmit signal field

characteristics were evaluated such as the signal's average power over azimuth angle and the difference between the signal at two different angles. A Fourier transform was developed for the transmit signal field that relates the temporal and spatial signal field to the signal's temporal frequency spectrum and the array's size and element locations. Measured data was used to validate the field predicted by the theoretical model using a DSB-SC transmit signal model. Once the analytic framework was established to characterize the transmit signal, a model for the general FDA received signal was addressed.

The model for the received frequency and waveform diverse signal model was developed by making approximations to the definition of a Doppler scaled received signal. The accuracy of the Doppler approximation compared to the Doppler scaled signal model was evaluated for the signal's temporal component showing that the intermediate approximation to the Doppler scaled signal was more accurate as a signal's time-bandwidth-product increases. A generic matched filter receiver was used to process the demodulated signal given a set of estimated target parameters. The processing method was validated using experimental data and data simulated using the DSB-SC version of the received signal. The receiver's AF was specified which measures the receiver's response to an ideal point target over a mismatches in the estimated target range, angle and relative velocity. Both the AF and the transmit signal characterization was used to examine a range of FDA configurations.

The field characterization methods and the AF were used to evaluate several basic FDA configurations. The LFP-FDA was compared to an equivalent CFA in terms of array size and signal bandwidth. The LFP-FDA has similar performance measurement accuracy in terms of measuring the point target's position and performed slightly better at measuring the target's relative velocity. Two experiments were then conducted using the LFP-FDA to investigate whether the LFP-FDA can be used to

improve performance by increasing inter-element spacing and by under-sampling the signal's bandwidth.

The LFP-FDA transmitter's inter-element spacing was increased and the AF's mainlobe showed a corresponding reduction in width along the angular dimension, but ambiguous sidelobes were resulted. Next, the LFP-FDA sub-carrier separation was increased while maintaining the same number of sub-carriers causing the bandwidth to be under-sampled. This resulted in significant sidelobes in the delay and Doppler dimensions rendering the signal useless for radar applications using the proposed receiver. A chirped and two phased-coded LFP-FDA configurations were examined showing only improvements in the AF's mainlobe width along the Doppler axis. Combined, these experiments showed that the LFP-FDA obeys the usual array and bandwidth sampling relationships. Using standard processing the LFP-FDA does not inherently improve target measurement accuracy compared to CFAs.

The measurement performance of a diversified signal was investigated by creating a signal that exploits the complete range of diversity allowed by the signal model. The resulting AF was similar in appearance to the AF to the randomly weighted FDA's AF. The waveform diverse configuration only improved Doppler measurement accuracy compared to the base configuration. Increasing the waveform diversity for a single pulse from the FDA using the proposed receiver did not improve the configuration's angle or range measurement accuracy.

Finally, a method to improve a configuration's range-angle plot by combining a signal and its spatial complement was investigated. It was found that by adding a FDA signal and its spatial complement, formed by reversing the signal allocation across the array, the sidelobes in a range-angle plot of a point target are significantly diminished. When the signal and its spatial complement were multiplied the sidelobes of the range-angle plot were diminished further and the mainlobe width decreased.

The mathematical bases for either of these methods have not been examined but it is suspected that the methods correct phase errors resulting from the matched filter processing cross-terms.

7.2 Suggestions for Future Research

Section 7.1 summarized the limitations of the research. The model of the generalized FDA system, while partially validated using measured data, assumes ideal radar hardware interacting with an ideal target in an ideal environment. The suggestions for future research include waveform optimization, receiver design and optimal array processing, high fidelity simulation, consideration of both planar and distributed geometry, and an FDA-based joint radar-communication system.

7.2.1 Waveform Optimization

The general FDA model has more degrees of freedom than many models used in the current literature with a large cost in terms of complexity and analyticity. Optimization of the transmit signal and array geometry are required to further understand how the signal parameters impact the radar performance. The AF may provide a useful optimization metric.

The AF was shown to be a combination of smaller correlation functions, each of which produces a peak output at a very precise location in the delay-Doppler plane. Although, the locations were not specifically studied, it was observed that all the delay-Doppler correlation functions used to build the ambiguity function have the same functional form which is the rectangular pulse's ambiguity function for non-chirped signals. However, when the two signals' sub-carrier frequencies differ, the correlation function is shifted along the Doppler axis by an amount directly proportional to the frequency difference. The shifted *basis* correlation function, for lack of a

better term, is then weighted using a spatially dependent complex weight. The entire set of shifted and weighted basis correlation functions are added together resulting in the ambiguity function.

Using knowledge of the AF's primary sidelobe locations, predicted by the peaks of the shifted basis correlation functions, an optimization algorithm could be designed to minimize the AF function at those locations. To set-up the optimization problem the algorithm's goal would be to find configurations that minimize peak sidelobe levels at the primary locations throughout the AF's volume by varying element-spacing, phase and amplitude coding, and sub-carrier frequency separation. The mainlobe volume and orientation is determined by the optimization constraints including total bandwidth, number of sub-carriers, number of transmit and receive elements, number of discrete phases, maximum chirp rate and the maximum transmit signal amplitude.

Following a number of constrained optimization scenarios the other techniques introduced in this study could be used to determine the relation between an optimized solution and the signal configuration. This may yield a set of design guides for approaching waveform diverse design.

7.2.2 Receiver Design and Optimal Array Processing

The receiver design used in this study is perhaps the most computationally expensive receiver that could be used. There are likely to be further simplifying assumptions that can be applied to the model in order to reduce the number of computations required to process the received signals. For example, the complex spatial weights applied in the model depended on the base frequency as well as the sub-carrier frequency. Perhaps the sub-carrier frequency dependence can be relaxed without introducing significant error. Relaxing the weight's sub-carrier dependence would allow the spatial weight to be factored from the summation and applied once to the entire signal.

Second, once a suitable and efficient FDA receiver has been established, the receiver's target detection and estimation performance should be evaluated in noise and clutter. A number of optimal processing techniques exist in the literature for narrowband, monochromatic signals such as those used in STAP to spatially and spectrally process the set of signals received by an array. Currently, apart from the FDA-STAP application, existing optimal methods to process the FDA signal have not been studied. Future research should first evaluate existing optimal array processing techniques, and if they are found to be inadequate for a generalized FDA new methods should be developed.

7.2.3 High Fidelity Simulation

Except for the FDA-STAP application study in [7], most of the FDA-related simulations have used ideal point target assumptions without consideration of the real environment. The FDA-STAP was able to model a more realistic scenario because the sub-carriers were widely separated and could be filtered and processed individually. This simplifies the data model because cross-correlation terms between sub-carriers are neglected and the data is treated as a collection of monostatic radar signals.

Until representative systems are built, and data from the system are available, a realistic simulation model is the only way to begin to evaluate processing algorithms designed to exploit the FDA's diverse nature. The first step is to develop a vector simulation data model that efficiently represents a set of received baseband samples while maintaining the essence of the signal's dimensionality. Once the simulation model is developed the result of other FDA design efforts can be evaluated using typical remote sensing scenarios.

7.2.4 Planar and Distributed Aperture Geometries

The linear array geometry was exclusively used in the research primarily because it allows the relationship between the temporal, spatial and spectral aspects of the FDA to be clearly visualized. The signal model has been developed cognisant that resolution in both azimuth and elevation is required in modern applications. As a result the geometric model has not been simplified in this study and the set of array element location vectors can be used to describe any configuration with a volume about the array's phase center. It is possible that because of frequency diversity an FDA with constant element spacing may not be the ideal configuration. Optimal FDA geometric configurations could be the subject of future research and design efforts.

7.2.5 Joint Radar and Communications Waveforms

A key characteristic of the FDA is its spatially varying signal field pattern. Consider taking a message signal and phase coding it onto the FDA's sub-carriers and transmitting the signal to a receiver at $u = 0$ some distance away. As the wave propagates along this LOS the phase relationship between sub-carriers is maintained; however, along a different u the relative phases between components change - modifying the phase of the sub-carriers relative to each other. The amount of phase variation depends on which sub-carrier the information is transmitted on, and how far from the array center it is.

A cooperative communication receiver with knowledge of where it is with respect to the transmitter and how the sub-carriers are assigned across the array elements would be able to correctly account for the phases and decode the message. However, a unfriendly receiver would find it more difficult. The radar has full knowledge of the transmit signal configuration and can use the returns to perform its remote sensing function. Such a system could be used in future remote layered sensing applications

to both send information between sensors and perform remote sensing simultaneously while providing an additional layer of communication security.

Appendix A. Derivations

1.1 Far-field Approximation

The far-field approximation is often made to simplify analysis of a propagating wave's far-field pattern. In addition to the far-field assumptions that follow, it is also important to recognize the a prime assumption is that the wave interacts with point targets. When the target is distributed the consequence of the point target assumption needs to be reevaluated.

Consider the signal transmitted by the p th element of the array in Section 2.3.2. The signal at an arbitrary point $\bar{\mathbf{r}}_0$ is proportional to

$$\begin{aligned} s_p(t, \bar{\mathbf{r}}_0) &= s_p(t - \tau_p) \\ &= \tilde{a}_p \hat{b}(t - \tau_p) \exp [j\omega_0 (t - \tau_p)] \end{aligned} \quad (\text{A.1})$$

where τ_p is the propagation delay

$$\begin{aligned} \tau_p &= \frac{|\bar{\mathbf{r}}_p|}{c_0} \\ &= \frac{|\bar{\mathbf{r}}_0 - \bar{\mathbf{d}}_p|}{c_0} \\ &= \frac{r_0}{c_0} \sqrt{1 - \frac{2y_0 d_p}{r_0^2} + \frac{d_p^2}{r_0^2}}. \end{aligned} \quad (\text{A.2})$$

If Eq. (A.2) is substituted into Eq. (A.1) the resulting expression is complicated by the square root term. The far-field approximation is useful to simplify Eq. (A.2) when the following conditions are met

$$r_0 > 10L_p, \quad \{\text{Amplitude Condition}\}, \quad (\text{A.3})$$

and

$$r_0 > \frac{2L_p^2}{\lambda_0}, \quad \{\text{Phase Condition}\}. \quad (\text{A.4})$$

Equations (A.3) and (A.4) are commonly known as the far-field conditions and relate the far-field range r_0 , the largest array dimension L_p and the wavelength λ_0 .

The truncated Taylor series expansion

$$\sqrt{1+x} \approx 1 + \frac{x}{2}, \quad \text{for } |x| \ll 1, \quad (\text{A.5})$$

is used to simplify Eq. (A.2), and is valid providing

$$\frac{d_p^2}{r_0} \approx 0 \quad (\text{A.6})$$

$$\frac{2y_0 d_p}{r_0^2} \ll 1. \quad (\text{A.7})$$

Both of these simplifying conditions are met when Equations (A.3) and (A.4) are satisfied.

Applying the simplification, the delay becomes

$$\begin{aligned} \tau_p &= \frac{1}{c_0} \sqrt{x_0^2 + z_0^2 + y_0^2 - 2y_0 d_p + d_p^2} \\ &\approx \frac{r_0}{c_0} - \frac{d_p \sin \theta_0}{c_0} \\ &\approx \frac{|\bar{\mathbf{r}}_0| - \bar{\mathbf{d}}_p \cdot \hat{\boldsymbol{\kappa}}}{c_0}. \end{aligned} \quad (\text{A.8})$$

Applying the narrowband approximation and the far-field approximation to Eq. (A.1) results in

$$s_p(t, \bar{\mathbf{r}}_0) = \tilde{a}_p \hat{b}(t - \tau_0) \exp \left(j\omega_0 t - j\frac{\omega_0 r_0}{c_0} + j\frac{\omega_0 \bar{\mathbf{d}}_p \cdot \hat{\boldsymbol{\kappa}}}{c_0} \right). \quad (\text{A.9})$$

This approximation is often invoked to simplify analysis of the far-field pattern of propagating waves. It simplifies the spherical problem to one in which the signal is separable in range and angle.

1.2 Average Transmit Power

The average power of a signal $s(t, \bar{\mathbf{r}}_0)$ with duration T is defined as

$$P_{ave}\{s(t, \bar{\mathbf{r}}_0)\} \triangleq \frac{1}{T} \int_{\tau_0}^{\tau_0+T} s(t, \bar{\mathbf{r}}_0) s^*(t, \bar{\mathbf{r}}_0) dt. \quad (\text{A.10})$$

Consider the p th transmit signal presented in Chapter IV, Eq. (4.3)

$$\begin{aligned} s_p(t) = & \exp(j\omega_0 t) \sum_{b=0}^{B-1} \sum_{m=0}^{M-1} \sum_{n=0}^{N-1} \tilde{a}_{p,b,m,n} s_b(t - mT_c - nT_p) \\ & \times \exp(j\omega_0 t) \sum_{n=0}^{N-1} \sum_{m=0}^{M-1} \sum_{b=0}^{B-1} \tilde{a}_{p,b,m,n} \hat{b}(t - mT_c - nT_p) \\ & \times \exp[j\Delta\omega_b(t - mT_c - nT_p)]. \end{aligned} \quad (\text{A.11})$$

The total signal at a far-field point $\bar{\mathbf{r}}_0$ is collected by a receiving aperture the resulting electrical signal is proportional to

$$s(t, \bar{\mathbf{r}}_0) = \sum_{p=0}^{P-1} K_p s_p(t - \tau_p), \quad (\text{A.12})$$

where K_p is scales the signal amplitude predicted by the Friis transmission equation. If the elements are in an array configuration with identical transmit elements, and approximately constant gain over the transmit bandwidth, the K_p term can be factored from the summation term in which case it will be expressed as $K_{tx} \approx K_p$. Applying

both the narrowband signal and the far-field approximations, the signal is

$$s(t, \bar{\mathbf{r}}_0) = K_{tx} \sum_{p=0}^{P-1} s_p(t - \tau_0 + \Delta\tau_p). \quad (\text{A.13})$$

Substituting Eq. (A.13) into Eq. (A.10) gives the signal power collected aperture in the far-field. Following the substitution the signal's average power is proportional to

$$P_{ave}\{s(t, \bar{\mathbf{r}}_0)\} = \frac{K_{tx}^2}{T} \int_{\tau_0}^{\tau_0+T} \sum_{p=0}^{P-1} s_p(t - \tau_0 + \Delta\tau_p) \sum_{p'=0}^{P-1} s_{p'}^*(t - \tau_0 + \Delta\tau_{p'}) dt. \quad (\text{A.14})$$

The signal duration is specified as T to be generic, however, this represents the power averaged over the entire CPI. The signal may represent multiple pulses, with multiple chips, modulated on multiple sub-carriers. It will be more useful to calculate the average power over the portion of signal that is transmitting opposed to averaging the power over the entire CPI.

The resulting substitution can be formulated as

$$\begin{aligned} P_{ave}\{s(t, \bar{\mathbf{r}}_0)\} &= \frac{K_{tx}^2}{MNT_c} \int_{\tau_0}^{\tau_0+MT_c+(N-1)T_p} \sum_{p=0}^{P-1} \sum_{p'=0}^{P-1} \sum_{b=0}^{B-1} \sum_{b'=0}^{B-1} \sum_{m=0}^{M-1} \sum_{n=0}^{N-1} \tilde{a}_{p,b,m,n} \tilde{a}_{p',b',m,n}^* \\ &\quad \times \hat{b}(t - \tau_0 - mT_c - nT_p) \hat{b}^*(t - \tau_0 - mT_c - nT_p) \\ &\quad \times \exp[j\omega_0(t - \tau_0 + \Delta\tau_p)] \exp[-j\omega_0(t - \tau_0 + \Delta\tau_{p'})] \\ &\quad \times \exp[j\Delta\omega_b(t - \tau_0 + \Delta\tau_p)] \exp[-j\Delta\omega_{b'}(t - \tau_0 + \Delta\tau_{p'})] dt. \end{aligned} \quad (\text{A.15})$$

Setting $\tau_0 = 0$, interchanging the order of the integral and the summation, and

simplifying the terms, Eq. (A.15) becomes

$$\begin{aligned}
P_{ave}\{s(t, \bar{\mathbf{r}}_0)\} &= \frac{K_{tx}^2}{MNT_c} \sum_{p=0}^{P-1} \sum_{p'=0}^{P-1} \sum_{b=0}^{B-1} \sum_{b'=0}^{B-1} \sum_{m=0}^{M-1} \sum_{n=0}^{N-1} \tilde{a}_{p,b,m,n} \tilde{a}_{p',b',m,n}^* \\
&\times \exp[j\omega_0(\Delta\tau_p - \Delta\tau_{p'})] \exp[j(\Delta\omega_b\Delta\tau_p - \Delta\omega_{b'}\Delta\tau_{p'})] \\
&\times \exp[-j(\Delta\omega_b - \Delta\omega_{b'})(mT_c + nT_p)] \\
&\times \int_{mT_c+nT_p}^{(m+1)T_c+nT_p} \exp[j(\Delta\omega_b - \Delta\omega_{b'})t] dt. \tag{A.16}
\end{aligned}$$

Finally, after evaluating the integral and simplifying the result, Eq. (A.16) is

$$\begin{aligned}
P_{ave}\{s(t, \bar{\mathbf{r}}_0)\} &= \frac{K_{tx}^2}{MN} \sum_{p=0}^{P-1} \sum_{p'=0}^{P-1} \sum_{b=0}^{B-1} \sum_{b'=0}^{B-1} \sum_{m=0}^{M-1} \sum_{n=0}^{N-1} \tilde{a}_{p,b,m,n} \tilde{a}_{p',b',m,n}^* \exp[j(\omega_b\Delta\tau_p - \omega_{b'}\Delta\tau_{p'})] \\
&\times \exp[j(\Delta\omega_b - \Delta\omega_{b'})\frac{T_c}{2}] \text{sinc}[(\Delta\omega_b - \Delta\omega_{b'})\frac{T_c}{2}], \tag{A.17}
\end{aligned}$$

where the un-normalized sinc function is used and is defined as

$$\text{sinc}(x) \triangleq \frac{\sin x}{x}. \tag{A.18}$$

Next, consider the case of the LFP-FDA discussed in Chapter II. The frequencies are orthogonal with $\Delta f = T_c^{-1}$ and $\Delta f_p = p\Delta f$, the signal transmits a single pulse so that $M = N = 1$, the number of sub-carriers is equal to the number of elements so that $B = P$, and an element transmits a single frequency such that the weights are

$$\tilde{a}_{p,b,m,n} = \begin{cases} \exp(-j\Delta\omega_b T_c/2), & \text{for } b = p \\ 0, & \text{otherwise.} \end{cases} \tag{A.19}$$

It follows that Eq. (A.17) simplifies to

$$\begin{aligned} P_{ave}\{s(t, \bar{\mathbf{r}}_0)\} &= K_{tx}^2 \sum_{p=0}^{P-1} \sum_{p'=0}^{P-1} \exp [j(\omega_p \Delta \tau_p - \omega_{p'} \Delta \tau_{p'})] \\ &\quad \text{sinc} \left[(\Delta \omega_p - \Delta \omega_{p'}) \frac{T_c}{2} \right]. \end{aligned} \quad (\text{A.20})$$

For orthogonal frequencies the argument of the sinc function is

$$(\Delta \omega_p - \Delta \omega_{p'}) \frac{T_c}{2} = \pi(p - p'), \quad (\text{A.21})$$

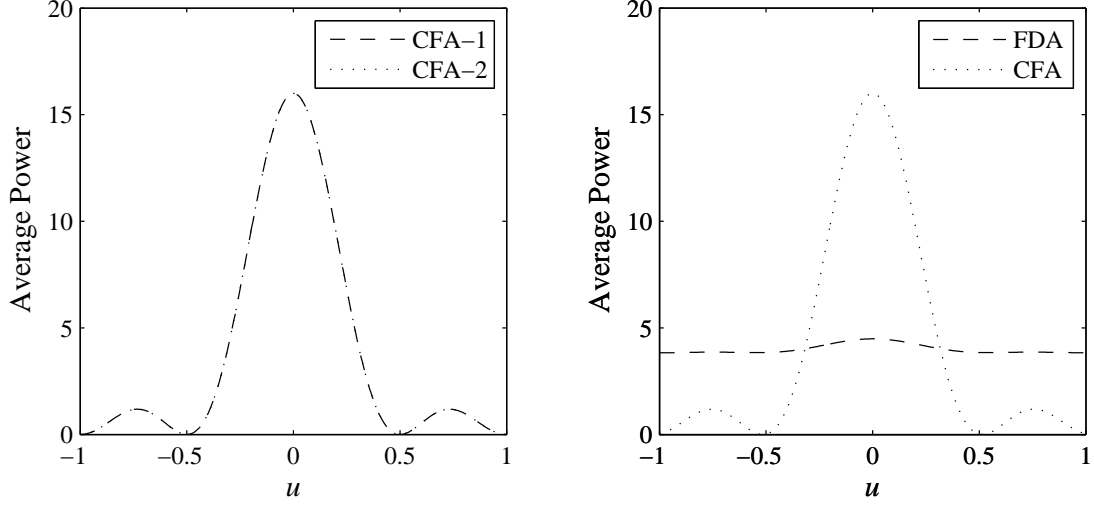
and

$$\text{sinc} [\pi(p - p')] = \begin{cases} 1, & \text{for } p = p' \\ 0, & \text{otherwise.} \end{cases} \quad (\text{A.22})$$

Finally, the average power received in the far-field due to a LFP-FDA transmit signal is proportional to

$$P_{ave}\{s(t, \bar{\mathbf{r}}_0)\} = K_{tx}^2 P. \quad (\text{A.23})$$

A plot of Eq. A.20 compared to Eq. 2.48 is shown in Fig. 1(b) for the parameters in Table 2.3. With no frequency progression the two equations match exactly as shown in Fig. 1(b). When the LFP-FDA parameters are used the average power is shown to be approximately constant $\forall u$. In any development that follows it will be assumed that the transmission amplitude scaling is normalized so that $K_p = 1$ unless it is important to the discussion.



(a) Verification of the CFA's average power calculated using Eq. A.17 (CFA-1) compared to Eq. 2.48 (CFA-2) for $P = 4$.

(b) Comparing the FDA average power, using the values in Table 2.3 shows that the FDA power pattern is approximately isotropic.

Figure A.1. Average Transmit Power Comparison: CFA and FDA.

1.3 Signal Difference

The distance between two signals $s_1(t)$ and $s_2(t)$ is defined as [36]

$$\|s_1 - s_2\|^2 = \int_{-\infty}^{\infty} [s_1(t) - s_2(t)] [s_1(t) - s_2(t)]^* dt, \quad (\text{A.24})$$

which is equivalent to the integrated, square of the difference [46]

$$\begin{aligned} \|s_1 - s_2\|^2 &= \int_{-\infty}^{\infty} |s_1(t) - s_2(t)|^2 dt \\ &= \int_{-\infty}^{\infty} |s_1(t)|^2 dt + \int_{-\infty}^{\infty} |s_2(t)|^2 dt \\ &\quad - 2\text{Re} \left[\int_{-\infty}^{\infty} s_1(t) s_2^*(t) dt \right], \end{aligned} \quad (\text{A.25})$$

where $\text{Re}[\cdot]$ is the real part of a complex number. The first two integrals represent the energy, E_1 and E_2 , of signals $s_1(t)$ and $s_2(t)$ respectively. To maximize the difference between the two signals it is desirable for the last integral to be as small as possible;

or, defining

$$d(s_1, s_2) \triangleq \text{Re} \left[\int_{-\infty}^{\infty} s_1(t) s_2^*(t) dt \right], \quad (\text{A.26})$$

the maximum difference between the two signals is when $d(s_1, s_2)$ is minimum.

The transmit FDA waveform's difference between two angles can be maximized over a number of different parameters, including sub-carrier separation, element locations, and phase coding. The term $d(s_1, s_2)$ was used in [46] to determine the angular resolution for CFA signals.

Let $s_1(t)$ be the signal at $\bar{\mathbf{r}}_0$ expressed in terms of r_0 and u_0

$$\begin{aligned} s_1(t) &= s(t, \bar{\mathbf{r}}_0) \\ &= s(t, r_0, u_0), \end{aligned} \quad (\text{A.27})$$

and $s_2(t)$ is a signal at the same range but offset in the angular parameter

$$s_2(t) = s(t, r_0, u_0 + \Delta u). \quad (\text{A.28})$$

Substituting equations (A.27) and Eq. (A.28) into Eq. (A.25) yields

$$\begin{aligned} d(s_1, s_2)(\Delta u) &= \text{Re} \left\{ \int_{\tau_0}^{\tau_0 + MT_c + (N-1)T_p} \sum_{p=0}^{P-1} \sum_{p'=0}^{P-1} \sum_{b=0}^{B-1} \sum_{b'=0}^{B-1} \sum_{m=0}^{M-1} \sum_{n=0}^{N-1} \tilde{a}_{p,b,m,n} \tilde{a}_{p',b',m,n}^* \right. \\ &\quad \times \hat{b}(t - \tau_0 - mT_c - nT_p) \hat{b}^*(t - \tau_0 - mT_c - nT_p) \exp[j\omega_0(t - \tau_0 + \Delta\tau_p)] \\ &\quad \times \exp[j\Delta\omega_b(t - \tau_0 + \Delta\tau_p - mT_c - nT_p)] \exp[-j\omega_0(t - \tau_0 + \Delta\tau_{p'})] \\ &\quad \left. \times \exp[-j\Delta\omega_{b'}(t - \tau_0 + \Delta\tau_{p'} - mT_c - nT_p)] dt \right\}. \end{aligned} \quad (\text{A.29})$$

The delays $\Delta\tau_p$ and $\Delta\tau_{p'}$ are related to the transmit angles such that

$$\begin{aligned}\Delta\tau_p &= \frac{d_p}{c_0} u_0 \\ \Delta\tau_{p'} &= \frac{d_{p'}}{c_0} (u_0 + \Delta u).\end{aligned}\tag{A.30}$$

The remaining signal parameters are common between $s_1(t)$ and $s_2(t)$.

Similar to the development of the transmit power, set $\tau_0 = 0$, use the definition of $\hat{b}(t)$ from Chapter II, take the integral inside the summation, substitute $t' = t - \tau_0 - mT_c - nT_p$, and rearrange the terms, Eq. (A.29) becomes

$$\begin{aligned}d(s_1, s_2)(\Delta u) &= \text{Re} \left\{ \sum_{p=0}^{P-1} \sum_{p'=0}^{P-1} \sum_{b=0}^{B-1} \sum_{b'=0}^{B-1} \sum_{m=0}^{M-1} \sum_{n=0}^{N-1} \tilde{a}_{p,b,m,n} \tilde{a}_{p',b',m,n}^* \right. \\ &\quad \times \int_0^{T_c} \exp[j\omega_0(t' + \Delta\tau_p + mT_c + nT_p)] \exp[j\Delta\omega_b(t' + \Delta\tau_p)] \\ &\quad \times \exp[-j\omega_0(t' + \Delta\tau_{p'} + mT_c + nT_p)] \\ &\quad \left. \times \exp[-j\Delta\omega_{b'}(t' + \Delta\tau_{p'})] dt' \right\}.\end{aligned}\tag{A.31}$$

Simplifying the expression further, Eq. (A.31) becomes

$$\begin{aligned}d(s_1, s_2)(\Delta u) &= \text{Re} \left\{ \sum_{p=0}^{P-1} \sum_{p'=0}^{P-1} \sum_{b=0}^{B-1} \sum_{b'=0}^{B-1} \sum_{m=0}^{M-1} \sum_{n=0}^{N-1} \tilde{a}_{p,b,m,n} \tilde{a}_{p',b',m,n}^* \right. \\ &\quad \times \exp[j\omega_0(\Delta\tau_p - \Delta\tau_{p'})] \exp[j(\Delta\omega_b \Delta\tau_p - \Delta\omega_{b'} \Delta\tau_{p'})] \\ &\quad \left. \times \int_0^{T_c} \exp[j(\Delta\omega_b - \Delta\omega_{b'})t'] dt' \right\}.\end{aligned}\tag{A.32}$$

Finally, after evaluating the integral the expression becomes

$$\begin{aligned} d(s_1, s_2)(\Delta u) = \text{Re} \left\{ T_c \sum_{p=0}^{P-1} \sum_{p'=0}^{P-1} \sum_{b=0}^{B-1} \sum_{b'=0}^{B-1} \sum_{m=0}^{M-1} \sum_{n=0}^{N-1} \tilde{a}_{p,b,m,n} \tilde{a}_{p',b',m,n}^* \right. \\ \times \exp [j\omega_0(\Delta\tau_p - \Delta\tau_{p'})] \exp [j(\Delta\omega_b\Delta\tau_p - \Delta\omega_{b'}\Delta\tau_{p'})] \\ \left. \times \exp \left[j(\Delta\omega_b - \Delta\omega_{b'}) \frac{T_c}{2} \right] \text{sinc} \left[(\Delta\omega_b - \Delta\omega_{b'}) \frac{T_c}{2} \right] \right\}. \quad (\text{A.33}) \end{aligned}$$

Equation (A.33) is similar to the expression for the average power in Eq. (A.17). Similar to the average power development in Section 1.2, it is also of interest to examine the difference between the signal at two different angles when the configuration is a LFP-FDA. For the LFP-FDA, the waveform difference between two angles can be simplified to

$$d(s_1, s_2)(\Delta u) = T_c \sum_{p=0}^{P-1} \cos \left[(k_0 + p\Delta k) \Delta d_{\hat{y},t} \Delta u \left(p - \frac{P-1}{2} \right) \right]. \quad (\text{A.34})$$

Equation A.34 is quadratic in p so it can only be approximately simplified into a form based on the Dirichlet kernel as was done in [16]. Because the approximation would only be valid for small angles the approach is not taken here. If required, the expression will be evaluated numerically.

1.4 Spectral Analysis Development

Consider a single pulse of the transmit field at some far-field range r_0 expressed as a function of time and parameter u . The signal field represents the signal received by and infinite number of receivers placed on an arc around the transmitter at the range r_0 and assuming $K_{tx} = 1$ the model of the signal field is

$$s(t - \tau_0, u) = \sum_{p=0}^{P-1} \sum_{b=0}^{B-1} \tilde{a}_{p,b} \hat{b}(t - \tau_0) \exp \left[j\omega_b \left(t - \tau_0 + \frac{d_p u}{c_0} \right) \right] \quad (\text{A.35})$$

where d_p is the displacement to the p th transmitter along the \hat{y} -axis. The term signal field is used to distinguish the concept discussed here from the radiated electromagnetic field produced by the array. However, it should be recognized that the two are weakly related.

It was shown in Chapter II that, for a fixed frequency, the inverse transform of the array factor in ξ results on the complex weights applied over the ULA. However, ξ is a scaled version of u and so it should also be possible to take the transform with respect to u . It does not matter whether the transform is viewed as a forward or inverse transform [9; 27]. It will help to define the transform so that the results are somewhat intuitive and correspond with the underlying principles.

Also in Chapter II, the signal field patterns for different configurations were shown plotted on both the (\hat{x}, \hat{y}) plane as well as the $t - u$ plane. The $t - u$ plane will be called the signal plane because it does not correspond exactly to the waveform's spatial distribution. For example, the most appropriate transform of the spatial distribution should involve the Hankel transform because the signal field is polar (in the (\hat{x}, \hat{y}) plane) and separable in azimuth and range (when the far-field conditions are satisfied). However, the Hankel transform becomes more difficult once elements are shifted in cartesian coordinates because the circular symmetry is broken.

The problem is complicated when pulsed signals, modulated by multiple sub-carriers are transmitted from the array. The result from both Fourier optics and CFA theory is that the field pattern around azimuth angle is proportional to the Fourier transform of the aperture assessed at a fixed frequency. If the impinging waveform has multiple frequency components then the field pattern should be assessed at each frequency component. However, in optics, the electric field is of less interest than the intensity so the range-dependent field is relatively inconsequential and is neglected from the calculations.

To encompass the ideas presented in the CFA theory in Chapter II and the Fourier optics theory in Appendix C the following Fourier transform pair is proposed to analyze the signal field $f(t, u)$

$$F(\omega, \bar{y}) = \int_{-\infty}^{\infty} \int_{-\infty}^{\infty} f(t, u) \exp[-j(\omega t + 2\pi \bar{y} u)] dt du, \quad (\text{A.36})$$

and

$$f(t, u) = \frac{1}{2\pi} \int_{-\infty}^{\infty} \int_{-\infty}^{\infty} F(\omega, \bar{y}) \exp[j(\omega t + 2\pi \bar{y} u)] d\omega d\bar{y}, \quad (\text{A.37})$$

where \bar{y} is a scaled version of the y axis. To help explain the interpretation of the field and its transform an example may help. Consider a monochromatic signal with frequency ω_b transmitted from an element displaced from the phase reference by d_p

$$s(t - \tau_0, u) = \exp \left[j\omega_b(t - \tau_0) + \omega_b \frac{d_p}{c_0} u \right]. \quad (\text{A.38})$$

The signal is expressed without a pulse shaping function such that its extent is infinite in both dimensions and if the time offset is not important the signal is

$$s(t, u) = \tilde{a} \exp \left(j\omega_b t + j\omega_b \frac{d_p}{c_0} u \right), \quad (\text{A.39})$$

Evaluating the signal using the transform yields

$$S(\omega, \bar{y}) = 4\tilde{a}\pi^2 \delta(\omega - \omega_b) \delta(2\pi \bar{y} - \omega_b \frac{d_p}{c_0}). \quad (\text{A.40})$$

To interpret the transform, the first impulse corresponds to the usual Fourier transform of the infinite complex exponential function. The second impulse function approximately corresponds to the amount of displacement, in wavelengths, from the

phase reference because the impulse is located at $\bar{y} = d_p/\lambda_b$. If the distance d_p is held constant, but the frequency is halved, the impulse's location will also halve because the wavelength doubles. The impulse's location in the \bar{y} dimension is frequency dependent and varies linearly with ω .

The transform of an infinite wave in both dimensions is a useful theoretical model to illustrate the concept but has limited applicability to radar signal analysis. An approximately bandlimited and range/space limited function is required to determine appropriate sampling rates of the continuous function to use in the DFT algorithm. To aid in the development, the original transmit signal model is considered but the pulse shaping function is modified such that

$$\hat{b}(t, u) = \begin{cases} 1, & 0 \leq t \leq T_c, -1 \leq u \leq 1 \\ 0, & \text{otherwise.} \end{cases} \quad (\text{A.41})$$

The change is relatively minor and limits the extent of the signal in u to the visible region. Considering a single pulse with a single temporal chip, the signal's field is

$$s(t - \tau_0, u) = \sum_{b=0}^{B-1} \sum_{p=0}^{P-1} \tilde{a}_{b,p} \hat{b}(t - \tau_0, u) \exp \left[j\omega_b \left(t - \tau_0 + \frac{d_p}{c_0} u \right) \right]. \quad (\text{A.42})$$

Taking the transform of the signal's field yields

$$\begin{aligned}
S(\omega, \bar{y}) &= \int_{-\infty}^{\infty} \int_{-\infty}^{\infty} \left\{ \sum_{p=0}^{P-1} \sum_{b=0}^{B-1} \tilde{a}_{p,b} \hat{b}(t - \tau_0, u) \exp \left[j\omega_b \left(t - \tau_0 + \frac{d_p}{c_0} u \right) \right] \right\} \\
&\quad \times \exp [-j(\omega t + 2\pi \bar{y} u)] dt du \\
&= \sum_{p=0}^{P-1} \sum_{b=0}^{B-1} \tilde{a}_{p,b} \int_{-1}^1 \int_{\tau_0}^{\tau_0 + T_c} \exp \left[j\omega_b \left(t - \tau_0 + \frac{d_p}{c_0} u \right) \right] \\
&\quad \times \exp [-j(\omega t + 2\pi \bar{y} u)] dt du \\
&= \sum_{p=0}^{P-1} \sum_{b=0}^{B-1} \tilde{a}_{p,b} \exp (-j\omega_b \tau_0) \int_{-1}^1 \int_{\tau_0}^{\tau_0 + T_c} \exp [-j(\omega - \omega_b) t] \\
&\quad \times \exp \left[-j \left(2\pi \bar{y} - \omega_b \frac{d_p}{c_0} \right) u \right] dt du. \tag{A.43}
\end{aligned}$$

Evaluating the integrals the transform of the limited signal field is

$$\begin{aligned}
S(\omega, \bar{y}) &= 2T_c \sum_{b=0}^{B-1} \sum_{p=0}^{P-1} \tilde{a}_{b,p} \exp (-j\omega \tau_0) \exp \left[-j(\omega - \omega_b) \frac{T_c}{2} \right] \\
&\quad \text{sinc} \left[(\omega - \omega_b) \frac{T_c}{2} \right] \text{sinc} \left(2\pi \bar{y} - \omega_b \frac{d_p}{c_0} \right). \tag{A.44}
\end{aligned}$$

Before progressing to the DFT version of the transform, it is necessary to consider sampling in the two dimensions to primarily reduce the impact of aliasing. The temporal dimension can be sampled in at a frequency that satisfies the usual Nyquist sampling criteria. If the signal has a maximum frequency $f_{max} = \omega_{max}/2\pi$ and a baseband bandwidth $\text{BW}_c = T_c^{-1}$ then the temporal sampling must satisfy $\underline{f}_{s,t} \geq 2(f_{max} + \text{BW}_c)$ with a sample interval $\underline{T}_s = \bar{f}_{s,t}^{-1}$. The underlined variables denote the Nyquist rate sample frequencies and intervals.

Next, an understanding of the signal in the u dimension is required to determine a satisfactory sample frequency that satisfies the Nyquist sampling criteria in u . An element's displacement from the origin d_p results in a modulation in the u dimension

with a frequency proportional to $k_b d_p$. Considering the total extent the array has an overall dimension L_p . If the maximum frequency is transmitted across the array the maximum “modulation” in the u dimension is proportional to $2\pi f_{max} L_p / 2c_0$. The sample frequency in the u dimension must then satisfy $\underline{f}_{s,u} \geq f_{max} L_p / c_0$ with an associated maximum sample interval $\underline{U}_s = \underline{f}_{s,u}^{-1}$.

The signal field can be represented as a discrete set of sample points. If scaled sampling frequencies $f_{s,t} = \beta_t \underline{f}_{s,t}$ and $f_{s,u} = \beta_u \underline{f}_{s,u}$ are used for visualization, then the corresponding sample intervals are $T_s = \underline{T}_s / \beta_t$ and $U_s = \underline{U}_s / \beta_u$. β_t and β_u are termed oversampling ratios. Let n_t represent the sample index for the temporal signal and n_u represent the sample index for the u dimension, with a total number of samples in each dimension of \underline{N}_t and \underline{N}_u . Considering a single chip duration, the number of samples is $\underline{N}_t = T_c / T_s$ and the number of samples in u is $\underline{N}_u = 2 / U_s$. Evaluating \underline{N}_t and \underline{N}_u results in

$$\underline{N}_t = 2\beta_t(T_c f_{max} + 1) \quad (\text{A.45})$$

$$\underline{N}_u = \frac{2\beta_u L_p}{\lambda_{min}}, \quad (\text{A.46})$$

where $\lambda_{min} = c_0 / f_{max}$. The sampling in u depends primarily on the array’s length compared to the smallest wavelength. If the array has P elements spaced equally with $\Delta d_{y,p} = \lambda_{min} / 2$, then $\underline{N}_u = P$ which is consistent with the result from the CFA theory presented in Chapter II. The transform may also be evaluated using sequence lengths $N_t \geq \underline{N}_t$ and $N_u \geq \underline{N}_u$ by zero-padding the sequences.

The signal field can be recast in terms of discrete coordinates by sampling the continuous function

$$s[n_t, n_u] = s(n_t T_s, n_u U_s - 1), \quad 0 \leq n_t \leq N_t - 1, \quad 0 \leq n_u \leq N_u - 1, \quad (\text{A.47})$$

with a total of $N_t N_u$ samples and neglecting the offset τ_0 . The shifting of the u dimension from $u \in [-1, 1]$ to $u \in [0, 2]$, results in a linear phase shift applied with respect to \bar{y} . However, this is neglected here because it is only the magnitude spectrum that is of interest. Using the standard DFT in two dimensions, the signal field's DFT is proportional to

$$S[m_\omega, m_{\bar{y}}] = \sum_{n_u=0}^{N_u-1} \left[\sum_{n_t=0}^{N_t-1} s[n_t, n_u] \exp \left(-j \frac{2\pi n_t m_\omega}{N_t} \right) \right] \exp \left(-j \frac{2\pi n_u m_{\bar{y}}}{N_u} \right). \quad (\text{A.48})$$

Appendix B. Experimental Configuration

2.1 Overview

Compared to traditional radar system configurations, waveform diverse radar systems have been shown to offer theoretical improvements in many areas. Practical demonstration of the theoretical improvements is slow to materialize. This may be due to several factors such as security sensitivity, implementation cost, and limited test facilities. In terms of demonstration there are several stages to mature a technology, including: experimental breadboard systems; representative systems; field tests using a prototype system; and operational tests using a production system. For airborne radar, the costs involved in the later demonstration stages are considerable. Combined with the number of design options available in waveform diversity, it is especially important to do more breadboard testing early. The demonstration system developed here provides a means to perform experimental research using a breadboard approach.

The purpose of this section is to explain the experimental configuration used to support the research. The configuration provides a flexible method to perform limited, ad-hoc, close-proximity radar data collections using the Tektronix radar measurement suite in the Radar Instrumentation Laboratory (RAIL) located at the Air Force Institute of Technology (AFIT). The philosophy driving the work is to develop a radar-equivalent breadboard system that can be simply and inexpensively configured to test a broad range of current and future radar options. The system was built through trial-and-error over several months to evolve into the current form. The system's instruments, components, configuration and functional performance are described next.

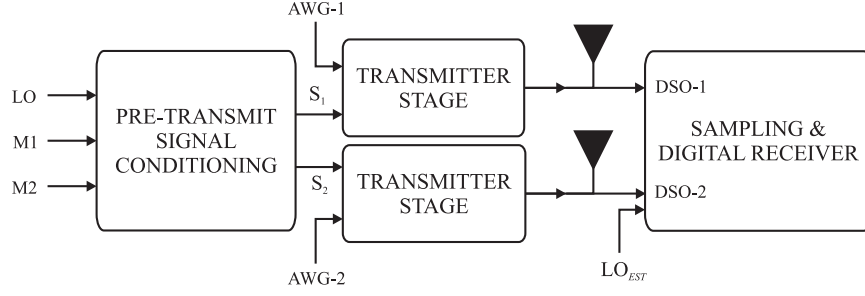


Figure B.1. Experimental configuration block diagram.

2.2 System Block Diagram

The system comprises two matched channels, each of which is capable of transmitting an arbitrary waveform. The waveforms are transmitted using pyramidal horn antennas and the combined waveforms reflect from a target. The target returns are collected by the same antennas and the waveforms are sampled directly at X-band using a high speed digital oscilloscope. The demodulation, IQ sampling and receiver processing are performed digitally.

Figure B.1 is a block diagram of the system. The first block conditions the signal to increase the ratio between the amplitude of the pulse envelope and the local oscillator (LO) leakage. It was found that without a microwave switch to range-gate the signal, excessive out-of-pulse LO leaks throughout the circuit obscuring small targets; this circuit approximates a switch.

The transmitter stage mixes the preconditioned LO rectangular pulse with a signal created using an arbitrary waveform generator. A wide range of signals can be generated and the instrument's ability is discussed in Section 2.3.2. The modulated signals are transmitted using two pyramidal horn antennas described in Section 2.4.4.

Finally, the transmit signal and the reflected signal are sampled and stored using the oscilloscope and all receiver functionality is implemented digitally. The motivation, benefits and limitations of the approach are discussed in Section 2.4.5.

2.3 Primary Instruments

The Tektronix radar suite provides a comprehensive set of tools to generate and measure RF signals. The suite consists of the TDS6123C digital storage oscilloscope (DSO), the AWG7102B arbitrary waveform generator (AWG), and the RSA6114A real-time spectrum analyzer (RSA). All instruments can be controlled remotely through the IEEE-488 General Purpose Interface Bus (GPIB) using custom software created in MATLAB, C++, Visual Basic or Lab-View. In particular the MATLAB programming was used in this application and software is based on the set of Tektronix Virtual Instrument Software Architecture (VISA) commands where the communications with the instruments is controlled through MATLAB's instrument control toolbox.

Each instrument has a proprietary, dedicated processor that performs the instrument's main function. Each instrument also has a general purpose processor that runs Windows XP. Information can be moved from the proprietary processor to the general purpose processor through the in-built GPIB interface. Inter-instrument communications can be achieved either through the external local area network (LAN) or a GPIB network. For these experiments a LAN was used to connect the devices.

A valuable instrument feature is the built-in self-diagnostics and calibration routines that run each time the instrument is powered up. The self-diagnostics and calibrations can also be performed at any time through the menu options. Additionally, the Tektronix service representatives periodically upgrade the instrument's firmware as new versions are released. These features provide a high level of confidence in the instrument's functional status, and hence, confidence in either the generated signal or the signal measurements. Next, the specifications of each instrument is summarized together with their advanced features and operational subtleties.

2.3.1 Oscilloscope

The TDS6124C DSO has an analog bandwidth of 12GHz with a maximum sample rate of 40GSa/s giving a sample interval of 25ps. The instrument is equipped with a variety of advanced features such as complex triggering, adjusting individual channel delays, correcting channel bias, and the FastFrame option. The FastFrame option permits the capture of contiguous waveforms providing the PRI is greater than approximately 250ns, the time it takes to rearm the trigger. Once the data is captured, it is possible to programmatically retrieve the data from the DSO into MATLAB and store it for post-processing.

There are several practical issues to be mindful of. First, the quantization noise is usually specified in terms of quantization levels over the entire span of the scope's vertical axis. However, the captured waves have significantly less amplitude than the scope's span and quantization noise has more impact than amplifier thermal noise. Second, because of this DSO's are not the usual choice for waveform analysis with the RSA being preferred. In this application, we use very short pulse widths and the RSA's IF bandwidth is too small for these signals. In addition, the RSA only has a single capture channel.

To overcome the primary issue of quantization noise we use the FastFrame capture mode to capture contiguous waveforms which facilitates waveform averaging. A 1-ns baseband pulse is sampled 40 times by the DSO which is a relatively high oversampling ratio. The RF waveform at 10GHz has an oversampling ration of 2 times the Nyquist rate. However, to operate using the 40GSa/s rate it is necessary to use one of channel 1 or 2 and one of channel 3 or 4 (two channels total). For example, using both channels 1 and 2 will automatically reduce the sample rate to 20GSa/s.

2.3.2 Arbitrary Waveform Generator

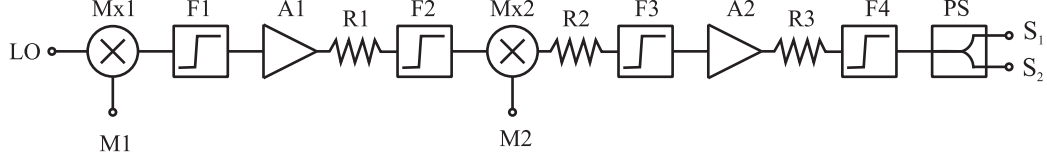
The AWG7002B is capable of producing waveforms on two channels at 10GSa/s in addition to two digital marker outputs per channel. Each standard output also has a complementary output. The instrument is also capable of operating at 20GSa/s in interleave mode using a single channel; however, the marker outputs are disabled in this mode. There are also four DC outputs that could be used to control a voltage controlled oscillator for example. Every function of the AWG can be controlled programmatically and the experiment's software was designed to set the initial configuration, and during the data collection, cycle through the list of designed waveforms. This proved to be a highly efficient method to test a large number of different waveforms for the same antenna and target configuration.

2.3.3 Real-time Spectrum Analyzer

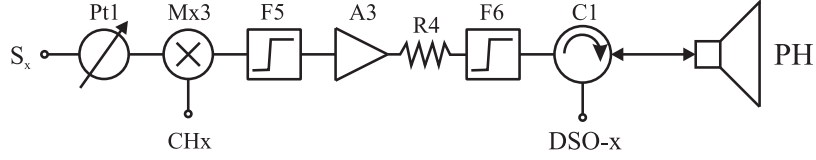
The RSA6114A is capable of capturing waveforms up to 14GHz and an IF bandwidth of 110MHz. In these experiments the RSA use is limited to measuring the LO's frequency. The RSA has a variety of programs for analyzing different waveforms that may be useful in future work; however, the Spectrum application was used exclusively for these experiments. Features of the Spectrum application can be controlled programmatically such as setting and changing the RSA's center frequency and finding the peak value's frequency. Advanced RSA features were not explored or used in this study.

2.4 Circuit Configuration

The circuit implemented for the experiments was built using discrete 50Ω RF components from a variety of suppliers. The advantage of using discrete components is that the circuit can be quickly modified to change the circuit's characteristics. The



(a) Transmit signal preconditioning circuit.



(b) Mixer stage.

Figure B.2. Experimental circuit diagram.

disadvantages are that the components are more expensive than either their plug-in or surface mount counterparts, it is difficult to match impedances to minimize reflections, and circuits with high component counts have a large footprint.

The circuit can be separated into two main functions shown in Fig. B.2. The first function in Fig. 2(a) preconditions the signal that will be mixed with the desired transmit signal. This stage was designed and implemented after working with very small targets. In broad terms the circuit approximates a switch and was necessary because although the mixer and circulator reduces the amount of LO signal that leaks through the the receiver the remaining LO signal obscures small targets.

The second function is a standard product modulator circuit or mixer stage. The preconditioned LO signal is multiplied by a signal produced by the AWG, which is then filtered and amplified. The filter F6 following the amplifier reduces the DC bias introduced by the amplifier before the signal is transmitted by a pyramidal horn antenna PH. If the components were available, an additional amplifier would be used prior to sampling to increase the target signal; however, using the amplifiers was more beneficial in the preconditioning circuit.

The diagram in Fig. B.3 illustrates the connections between the various compo-

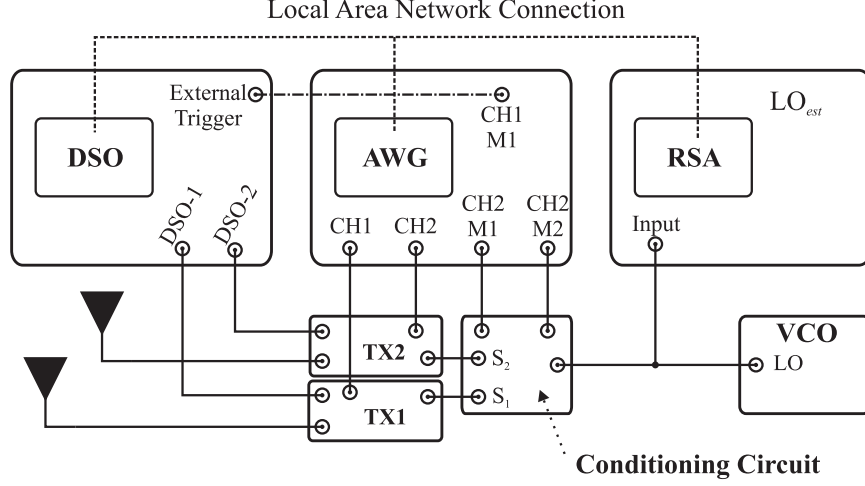


Figure B.3. Instrument connection diagram.

nents and instruments. The DSO is triggered by using one of the output signals from the AWG and due to a lack of connectors the RSA was left free-running. The AWG was configured to repeat waveforms with a PRF of 1MHz. Using such a high PRF should ensure that the LO's frequency should not change significantly over the collection duration and this is important for the digital receiver. One of the advanced RSA features is that like the DSO, it can also operate using the FastFrame feature to capture waveforms at specific intervals. This feature could be useful in future work to measure the LO frequency corresponding to each pulse.

2.4.1 Component List

The circuit presented was finalized after testing many different configurations. One of the challenges was to build a system capable of supporting a variety of waveform diverse measurements using an assortment of inexpensive components. The list of components used in the experiment is in Table B.1. The components are supplied by either MiniCircuits (MC), Narda (ND), LabVolt (LV) or Marki Microwave (MM).

While individually the components are considered inexpensive, the total cost of the design is several thousand dollars. Apart from the DSO, RSA and AWG, the

Table B.1. Circuit components.

Ref.	Description
A1, A3	Amp (MC): ZX60-14014L-S+
A2	Amp (MC) MH-183-S+
PH	Pyramidal Horn (LV): 2" 9535-00
C1	Circulator (ND): 4925
F1, F4	HPF (MC): VHF-8400
F2, F3	HPF (MC): BLK-18-S+
F5, F6	HPF (MC): VHF-6010
Mx1, Mx2	Mixer (MM): M10212MA
Mx3	Mixer (MM): M10412HA
PS	Power Splitter (MC): ZX10-2-126-S+
Pt1	Phase T rimmer (ND): 4572B
R1, R2, R3, R4	Attenuator (MC): 1dB

most expensive components are the amplifiers, circulators and the antennas. Adding additional channels would cost approximately one thousand dollars per channel inclusive of the mixer hardware, antenna and cabling. For each additional pair of channels an additional DSO and AWG would be required using this design. An alternate may be to demodulate the signal to baseband and sample the in-phase and quadrature channels; however, the additional equipment required may also be rather costly.

2.4.2 Pre-conditioning Circuit

The preconditioning circuit in Fig. 2(a) multiplies the LO supplied by the LabVolt radar transmitter with the marker outputs from the AWG (M1 and M2). The markers output a rectangular pulse equal to the width of the transmit waveform. The circuit

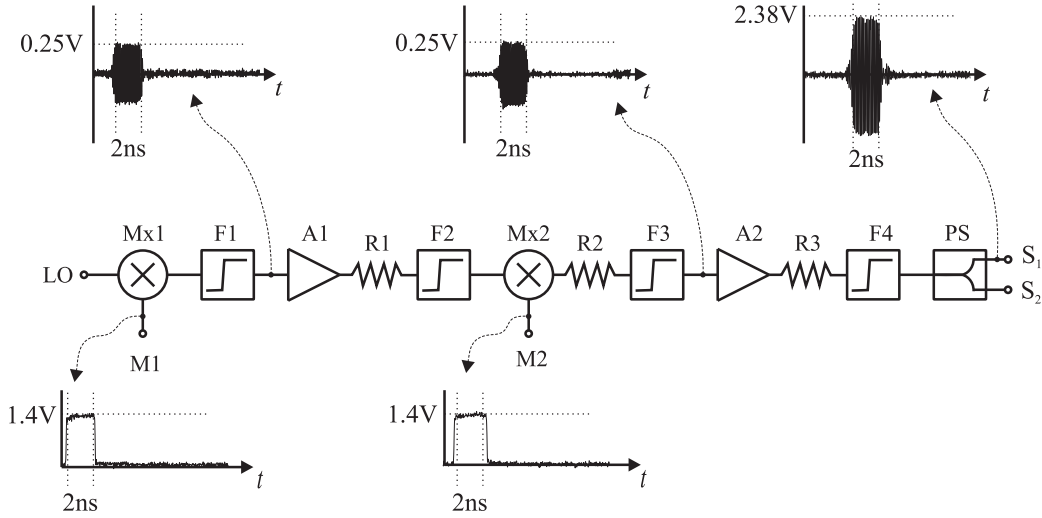


Figure B.4. Pre condition circuit and signals.

approximates a switch by reducing the out-of-pulse LO signal that can leak through the circuit to reach the DSO.

An RF switch capable of switching with adequate speed was available and would have been preferable to the preconditioning circuit in terms of component count. However, the additional equipment to run the switch such as a -5VDC power supply and a pulse amplifier (to control the switch using TTL levels) were not available.

2.4.3 Transmitter Stage

The preconditioned signal is split into two channels each of which is multiplied by an AWG generated waveform, amplified and transmitted through the circulator to the two inch horn antenna. This is shown in Fig. 2(b). A target return is collected by the horn antenna, passes through the circulator and is sampled by the DSO.

The phase trimmer was included to provide some compensation of the phase imbalance between channels. It was found that the phase trimmers did not provide the ability to adequately compensate path length differences between channels.

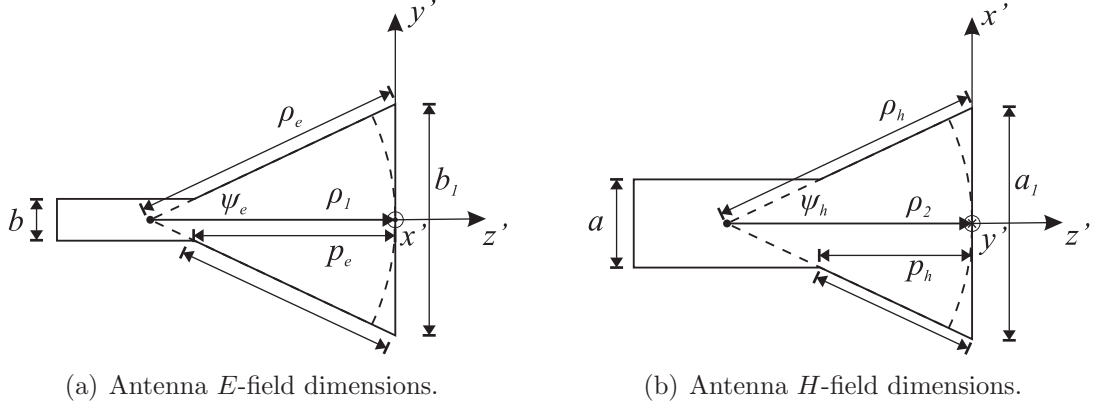


Figure B.5. Antenna dimensions. Antenna dimensions for the two-inch pyramidal horn [9].

Table B.2. Antenna dimensions.

E-Param.	Value	H-Param.	Value
b	10mm	a	22.8mm
b_1	49.8mm	a_1	48.3mm
ρ_e	63.3mm	ρ_h	90.4mm
ρ_l	58.2mm	ρ_2	87.0mm
p_e	63.3mm	p_h	46.0mm
ψ_e	23.2°	ψ_h	15.5°

2.4.4 Antenna Characteristics

The experiment uses two LabVolt, 2-inch pyramidal horn antennas. The dimension of the horn antennas used to analyze the antennas are illustrated in Fig. B.5 and the dimensions of the horn antennas, using a single set of measurements, are listed in Table B.2. An uncalibrated, low-cost, micrometer with a resolution of 0.1mm was used to measure the antenna dimensions.

The primary frequency used in the experiments is $f_0 = 9.8\text{GHz}$ and for this frequency the normalized antenna pattern $\frac{1}{G_0}|G(u, \lambda_0)|$ is shown in Fig. B.6 where G_0

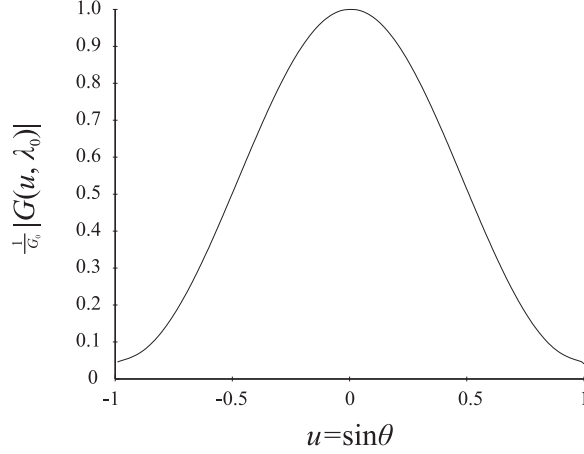


Figure B.6. Pyramidal horn beam pattern. Pyramidal horn beam pattern evaluated at $f_0 = 9.8\text{GHz}$.

is the directive gain along the pattern's mainbeam. The directive gain at $f_0 = 9.8\text{GHz}$ is $G_0 \approx 5$ and the HPBW is approximately 42° . The actual field pattern was not measured.

2.4.5 Receiver Processing

The most important step in the receiver processing is accurately estimating the initial phase prior to digital demodulation. In an analog Receiver Front End (RFE) the incoming waveform is quadrature demodulated and each of the in-phase and quadrature channels are amplified using a low noise amplifier (LNA). There is a fixed time delay between the incoming signal and the LO used for demodulating the signal that doesn't vary significantly between successive pulses in a CPI. The fixed time delay allows coherent pulse addition because the phase between the LO and the received waveforms for a fixed target will be constant.

Figure B.7 shows a representative waveform record. The waveform record com-

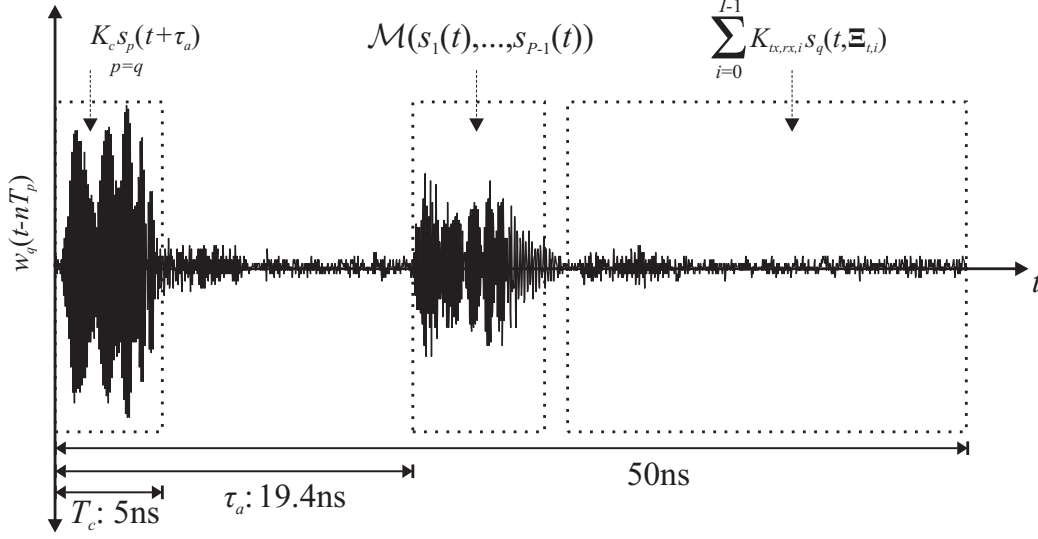


Figure B.7. Waveform record. A waveform record that has been sampled and stored by the oscilloscope.

prises a number of terms and a high-level description may be satisfied by

$$\begin{aligned}
 w_q(t - nT_p) = & K_c s_p(t + \tau_a) + \mathcal{M}(s_1(t), \dots, s_p(t)) \\
 & + \sum_{i=0}^I K_i r_q(t, \bar{\mathbf{r}}_i) + \tilde{n}(t)
 \end{aligned} \tag{B.1}$$

where the first term is a version of the transmit signal that passes directly through the circulator and is scaled by K_c ; the second term represents the mutual coupling and the transmit signal reflecting from the antenna feed; the third term represents a set of discernible targets under a discrete target model and K_i is the range equation scaling; and the final term represents both the LO leakage, the thermal and quantization noise.

The digital receiver, with block diagram shown in Fig. B.8, used for the experiments is most likely not optimal, but it produces acceptable results. The receiver processing is performed using discrete samples but is represented here in terms of continuous-time functions for notational convenience. The first step in the digital receiver processing is Hilbert transforming the signal to create an analytic version (complex valued). The second step involves filtering and demodulating the analytic

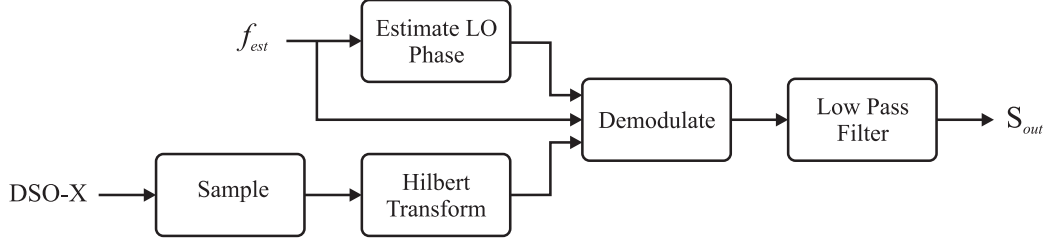


Figure B.8. Digital receiver processing block diagram.

signal. So that the signals add constructively following demodulation, it is important that the initial phase of LO is estimated for each waveform record so that the set of recorded waveforms can be added coherently or Doppler processed.

To estimate the LO's initial phase, $\hat{\phi}_0$, the portion of the waveform record containing $K_c s_p(t + \tau_a)$ is windowed using $\hat{b}_\phi(t)$ to remove the remaining terms. Then using the LO's estimated frequency \hat{f}_0 , measured using the RSA, the initial phase is estimated by

$$\hat{\phi}_{n,0} = \angle \left\{ \int_{-\infty}^{\infty} \exp(-j2\pi\hat{f}_0 t) \hat{b}_\phi(t) w_q(t - nT_p) dt \right\}, \quad (\text{B.2})$$

where $\angle\{\cdot\}$ is the angle of a complex number. The window function's delay and duration can be chosen to select any portion of the waveform record depending on the transmit signal characteristics and the section of waveform record that produces consistent results.

After the phase has been estimated for each waveform record in the set, each record is demodulated to baseband and then filtered using a low-pass filter. Both the low-pass and high-pass filters are implemented using sixth order, Parks-McLelland Finite Impulse Response (FIR) filters. Finally, the portion of the waveform record containing the term relating to target responses can be processed further by matched filtering using the approach discussed in Chapter V.

2.5 Results

Two classes of experiments were performed in order to test the signal model developed in this research. The first series of experiments evaluated the signal field represented by Eq. (4.15). It was found that for a binary phase coded signal operating at a single frequency the model and the measured signal field were in good agreement.

In this section, *good agreement* will mean that the location and shape of both the pattern's peaks and it's nulls are very similar between the two plots. *Fair agreement* will mean that either the peak's or the null's locations and shapes are similar, but not both. *Poor agreement* will mean there is some resemblance between the two field patterns, but less than either good or fair agreement. Finally, *no agreement* will mean there appears to be no similarity between the two plots.

When signals with either multiple sub-carriers or a chirped waveform were used in the circuit, the model and measured signal field did not agree. Modifying the signal model to represent the circuit resulted in good agreement in all cases; however, modifying the circuit to represent the signal model produced results ranging from poor agreement to fair agreement depending on the signal combination's underlying characteristics. With the available equipment the circuit could not be made to accurately mirror the theoretical model.

The second series of measurements was aimed at testing the receiver processing developed in Appendix A. The experiment measured the signal reflected from two targets on the target table and the returns were processed using the method developed in Chapter V. This was compared to a simulation model and there was good agreement between the measured and the simulated results.

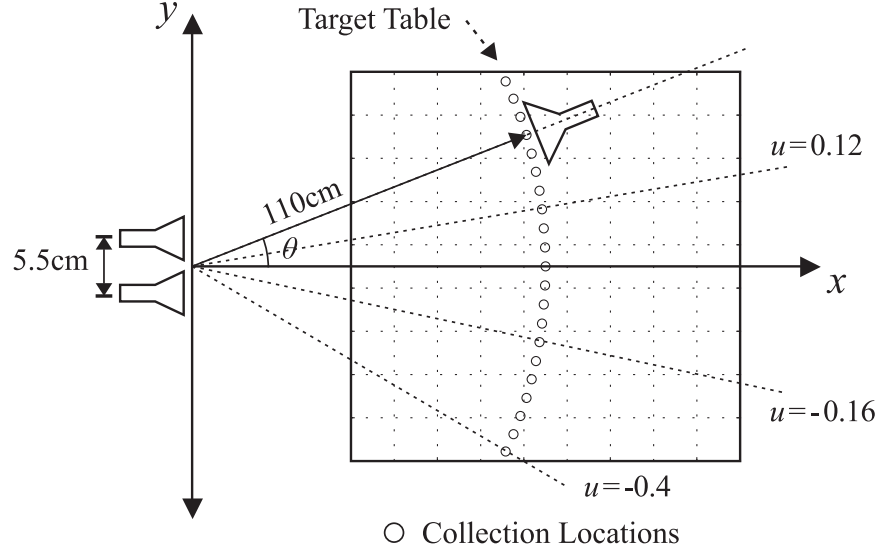


Figure B.9. Field sampling configuration.

2.5.1 Field Measurements

The configuration for the field measurements is shown in Fig. B.9. A standard gain horn was used to collect the transmit signal at each collection location around the circumference of a circle with radius $r = 1.1m$ centered at the transmitter. The set of collection locations represent 21 samples uniformly spaced in $u \in [-0.4, 0.4]$, corresponding to non-uniformly space azimuth angles $\theta \in [-25^\circ, 25^\circ]$. The transmit antennas are separated by $\Delta_{\hat{y},t} = 5.5cm$ and by Eq. (2.11) the far-field condition is satisfied because $r > 0.8m$ (given that $L_p \approx 11cm$).

2.5.1.1 Single frequency, Binary Phase-coded Signals

The first signal field measurements used a set of binary phase-coded transmit signals with common parameters listed in Table B.3 and signal-unique parameters in Table B.4. There are two classes of signals in the set; the first class comprises the four-chip, mutually orthogonal Hadamard sequences and the second class comprises the two, four-chip Barker sequences. Each chip has duration $T_c = 500ps$ with a total signal duration $2ns$.

Table B.3. Signal measurement parameters: binary, phase coded signals.

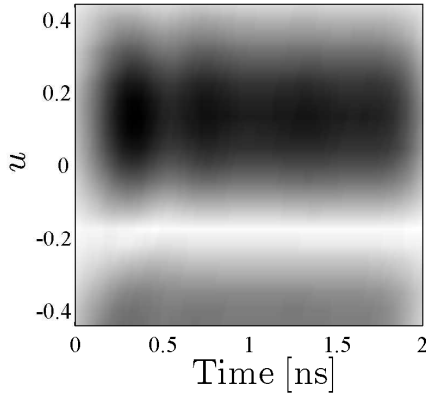
Parameter	Value
Transmitters P	2
Antenna Separation $\Delta d_{\hat{y},t}$	5.5cm
Frequency f_0	$\approx 9.8\text{GHz}$
Bandwidth BW_s	2GHz
Sub-carriers B	1
Chips M	4
Pulses N	100
Chip duration T_c	500ps
AWG Sample frequency $f_{s,AWG}$	10GSa/s
Scope sample frequency $f_{s,TDS}$	40GSa/s

The result shown in Fig. B.10 compares the measured signal field to the theoretical result for the *Hadamard1* transmitted from both antennas. The signal is classed as one of the Hadamard sequences but it is also the same as a CFA signal with duration $2ns$. The measured signal field in Fig. 10(a) shows the mainbeam is focussed at $u = 0.12$ with the first null at $u = -0.2$. The theoretical signal field Fig. 10(b) was adjusted so that it focusses the mainbeam along $u = 0.12$ and the field is multiplied by the normalized, theoretical antenna pattern $\frac{1}{G_0}|G(u, \lambda_0)|$. The mainbeam in the theoretical pattern, due to the array factor, is narrower than the measured result; however, the distribution of the signal's amplitude between the two field plots are in good agreement.

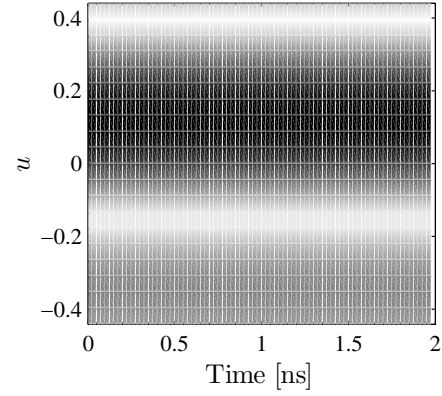
All possible combinations of transmitting the set of signals from the two antennas was tested and compared to the theoretical model. Two comparative results from the experiment are shown in Figures B.11 and B.12. In Fig. B.11, the *Barker2* signal was

Table B.4. Signal parameters: binary, phase coded signals.

Signal	Label	Parameter and Value
$s_{b1}(t)$	<i>Hadamard 1</i>	$\tilde{a}_{p,b,m,n} = \begin{cases} \{1, 1, 1, 1\}_{m=0}^{m=3} \\ 0, & \text{else} \end{cases}$
$s_{b2}(t)$	<i>Hadamard 2</i>	$\tilde{a}_{p,b,m,n} = \begin{cases} \{1, -1, 1, -1\}_{m=0}^{m=3} \\ 0, & \text{else} \end{cases}$
$s_{b3}(t)$	<i>Hadamard 3</i>	$\tilde{a}_{p,b,m,n} = \begin{cases} \{1, 1, -1, -1\}_{m=0}^{m=3} \\ 0, & \text{else} \end{cases}$
$s_{b4}(t)$	<i>Hadamard 4</i>	$\tilde{a}_{p,b,m,n} = \begin{cases} \{1, -1, -1, 1\}_{m=0}^{m=3} \\ 0, & \text{else} \end{cases}$
$s_{b5}(t)$	<i>Barker 1</i>	$\tilde{a}_{p,b,m,n} = \begin{cases} \{1, 1, 1, -1\}_{m=0}^{m=3} \\ 0, & \text{else} \end{cases}$
$s_{b6}(t)$	<i>Barker 2</i>	$\tilde{a}_{p,b,m,n} = \begin{cases} \{1, 1, -1, 1\}_{m=0}^{m=3} \\ 0, & \text{else} \end{cases}$



(a) Measured signal field.



(b) Theoretical signal field.

Figure B.10. Comparison of measured and simulated data: CFA Signal. The signal transmitted from both antennas are *Hadamard1* signals specified in Tables B.3 and B.4.

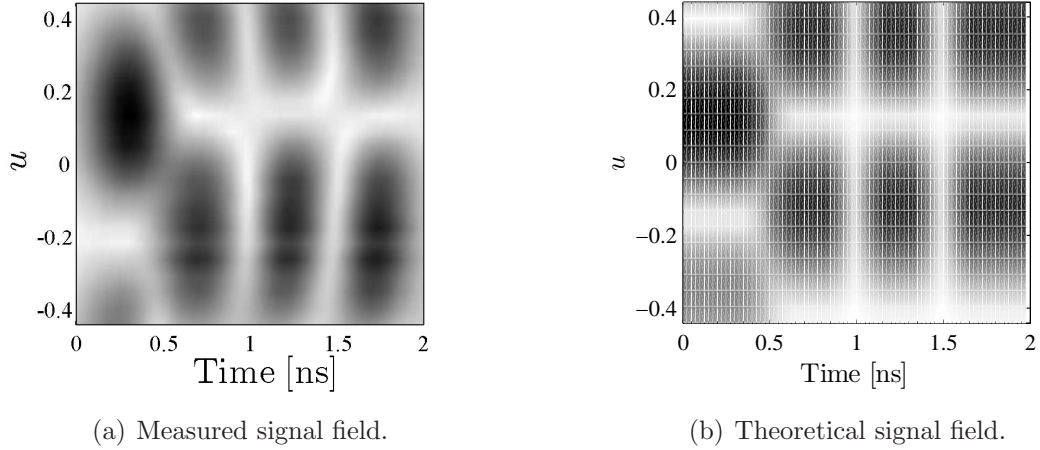


Figure B.11. Comparison of measured (DSB-SC) and simulated (SSB-SC) data: *Barker2* and *Hadamard2* Signals. The signal transmitted from $p = 0$ is the *Barker2* signal and from $p = 1$ is the *Hadamard2* signal. The signals are specified in Tables B.3 and B.4.

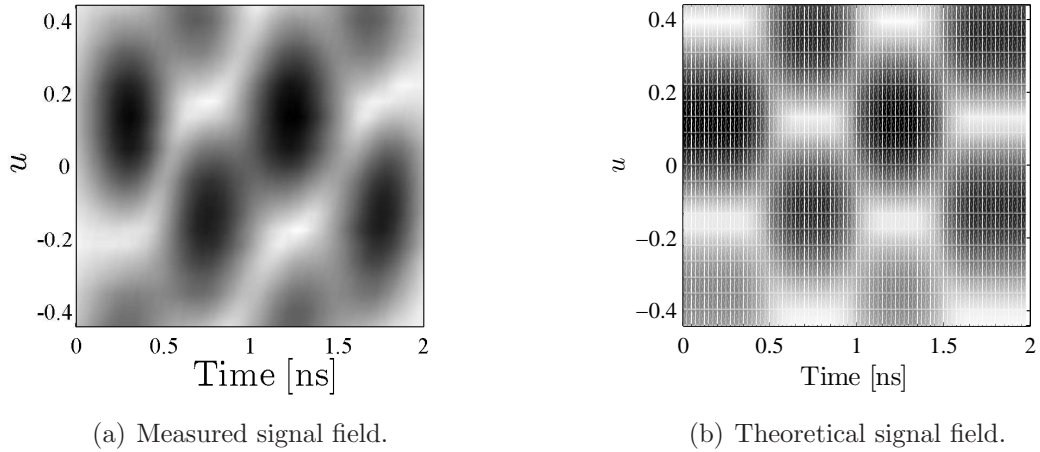


Figure B.12. Comparison of measured and simulated data: *Hadamard2* and *Hadamard1*. The signal transmitted from $p = 0$ is the *Hadamard2* signal and from $p = 1$ is the *Hadamard1* signal. The signals are specified in Tables B.3 and B.4.

transmitted element $p = 0$ and the *Hadamard2* signal was transmitted from element $p = 1$. In Fig. B.12 the *Hadamard2* signal was transmitted from element $p = 0$ and the *Hadamard1* was transmitted from element $p = 1$.

The results show that for those combinations, the theoretical signal field distribution generated using Eq. (4.15) with the parameters in Tables B.3 and B.4 was in

Table B.5. Signal measurement parameters: single-chip signals.

Parameter	Value
Transmitters P	2
Antenna Separation $\Delta d_{g,t}$	5.5cm
Frequency f_0	$\approx 9.8\text{GHz}$
Bandwidth BW_s	800MHz
Sub-carriers B	4
Sub-carrier separation Δf	200MHz
Chips M	1
Pulses N	100
Chip duration T_c	5ns
AWG Sample frequency $f_{s,AWG}$	10GSa/s
Scope sample frequency $f_{s,TDS}$	40GSa/s

good agreement with the signal field measured using the experimental circuit. An exhaustive presentation of each unique combination of transmit signals, both in this section and the subsequent sections, would require a large page count. The results of all combinations were plotted and compared; and for the binary, phase-coded signals in Table B.4 the measured results were in good agreement with the simulated results.

2.5.1.2 Multiple Frequency Signals: OFDM and LFM

Next, sets of frequency diverse signals were tested using the experimental configuration. The common experimental parameters between the three sets of signals are listed in Table B.5. The first set of signals with parameters in Table B.6 are single chip, single frequency, orthogonal signals such as those that may be used in a LFP-FDA.

Table B.6. Signal parameters: single chip, single frequency signals.

Signal	Label	Parameter and Value
$s_{s1}(t)$	<i>0-Hz</i>	$\tilde{a}_{p,b,m,n} = \begin{cases} 1, & b = 0 \\ 0, & \text{else} \end{cases}$
$s_{s2}(t)$	<i>200-MHz</i>	$\tilde{a}_{p,b,m,n} = \begin{cases} 1, & b = 1 \\ 0, & \text{else} \end{cases}$
$s_{s3}(t)$	<i>400-MHz</i>	$\tilde{a}_{p,b,m,n} = \begin{cases} 1, & b = 2 \\ 0, & \text{else} \end{cases}$
$s_{s4}(t)$	<i>600-MHz</i>	$\tilde{a}_{p,b,m,n} = \begin{cases} 1, & b = 3 \\ 0, & \text{else} \end{cases}$

Table B.7. Signal parameters: single chip, OFDM signals.

Signal	Label	Parameter and Value
$s_{m1}(t)$	<i>OFDM1</i>	$\tilde{a}_{p,b,m,n} = \begin{cases} e^{-j\pi\Delta f_b T_c}, & b = \{0, 2\} \\ 0, & \text{else} \end{cases}$
$s_{m2}(t)$	<i>OFDM2</i>	$\tilde{a}_{p,b,m,n} = \begin{cases} e^{-j\pi\Delta f_b T_c}, & b = \{1, 3\} \\ 0, & \text{else} \end{cases}$
$s_{m3}(t)$	<i>OFDM3</i>	$\tilde{a}_{p,b,m,n} = \begin{cases} e^{-j\pi\Delta f_b T_c}, & b = 0 \\ e^{-j\pi\Delta f_b T_c + \pi/2}, & b = 3 \\ 0, & \text{else} \end{cases}$
$s_{m4}(t)$	<i>OFDM4</i>	$\tilde{a}_{p,b,m,n} = \begin{cases} e^{-j\pi\Delta f_b T_c}, & b = 1 \\ e^{-j\pi\Delta f_b T_c + 3\pi/2}, & b = 3 \\ 0, & \text{else} \end{cases}$

The second set are different OFDM signals, using two frequency chips per temporal chip, created using the same orthogonal frequency tones used in the set of single tones.

Table B.8. Signal parameters: single chip, LFM signals.

Signal	Label	Parameter and Value
$s_{c1}(t)$	<i>LFM1</i>	$\vartheta_{p,b,m,n} = 1.6 \times 10^{17}$ $\tilde{a}_{p,b,m,n} = \begin{cases} 1, & b = 0 \\ 0, & \text{else} \end{cases}$
$s_{c2}(t)$	<i>LFM2</i>	$\vartheta_{p,b,m,n} = 1.6 \times 10^{17}$ $\tilde{a}_{p,b,m,n} = \begin{cases} 1, & b = 2 \\ 0, & \text{else} \end{cases}$
$s_{c3}(t)$	<i>LFM3</i>	$\vartheta_{p,b,m,n} = -1.6 \times 10^{17}$ $\tilde{a}_{p,b,m,n} = \begin{cases} 1, & b = 0 \\ 0, & \text{else} \end{cases}$
$s_{c4}(t)$	<i>LFM4</i>	$\vartheta_{p,b,m,n} = -1.6 \times 10^{17}$ $\tilde{a}_{p,b,m,n} = \begin{cases} 1, & b = 2 \\ 0, & \text{else} \end{cases}$

The parameters for the OFDM signal set are listed in Table B.7.

Finally, a set of LFM signals was created with the parameters in Table B.8. Each LFM signal has a chirp rate ϑ such that the chirp spans 400MHz in 5ns with either a positive or negative chirp rate. Between them the signals can span a 800MHz bandwidth with two sub-bands 0-400MHz and 400-800MHz.

The motivation for choosing the particular set of signals was to examine waveforms that may be of future interest to studies of FDA or waveform diverse array configurations. The results in the following sections evaluate the theoretical model used to describe these types of signals in a waveform diverse array radar system.

Consider the signal field results in Fig. B.13. The field is generated by transmitting

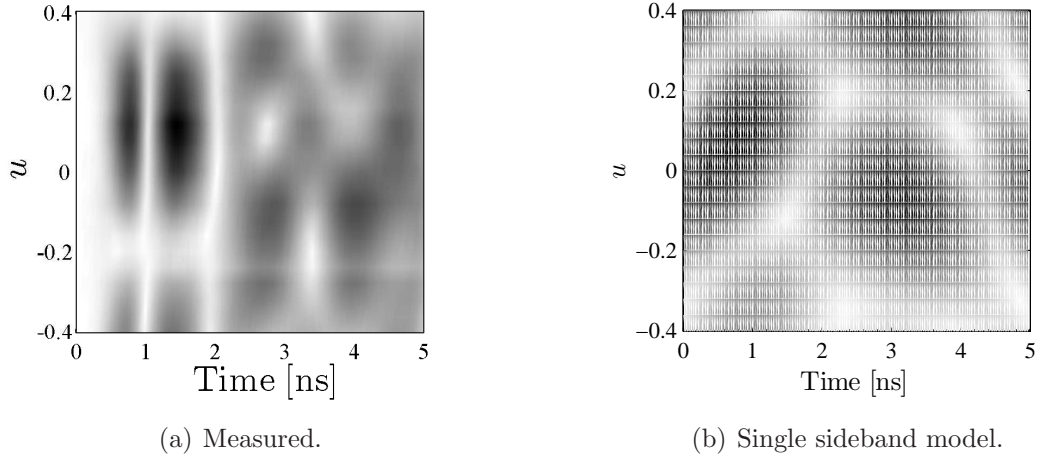


Figure B.13. Comparison of measured (DSB-SC) and simulated (SSB-SC) data: *OFDM4* and *LFM3*. Comparison of frequency diverse signal field patterns with no agreement. Transmit signal $p = 0$ is the *OFDM4* signal and transmit signal $p = 1$ is the *LFM3* signal.

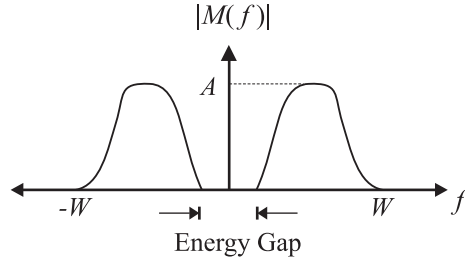


Figure B.14. Illustration of a baseband signal spectrum.

the *OFDM4* signal from element $p = 0$ and the the *LFM3* signal from element $p = 1$ and it is clear that the model and the measured results do not agree. The reason is that the signal model in Eq. (4.15) represents SSB-SC modulation while the experimental circuit in Fig. B.2 represents DSB-SC modulation [26].

To highlight the difference, consider the spectrum of signal $m(t)$ shown in Fig. B.14. The two-sided spectrum at baseband is typical of a real valued signal with the positive portion of the spectrum reflected about the origin. If $m(t)$ is product modulated by a real carrier $\cos(2\pi f_0 t)$ the result is a DSB-SC signal with spectrum in Fig. 15(a).

The lack of agreement in Fig. B.13 is because the model used in this study (in

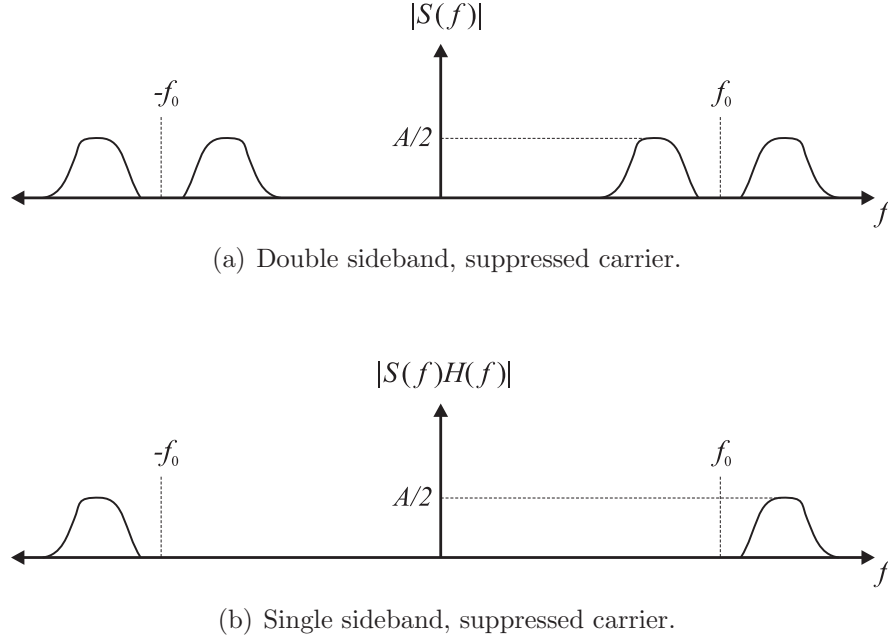


Figure B.15. Illustration of the spectra for DSB-SC and SSB-SC signals.

Eq. (4.15)) represents SSB-SC signals. A SSB-SC spectrum for $m(t)$ is shown in Fig. 15(b) for the case where the upper sideband is retained. The SSB-SC can be represented by filtering the signal with a high pass filter $H(f)$ resulting in $H(f)[\frac{1}{2}M(f + f_0) + \frac{1}{2}M(f - f_0)]$. Practically, the SSB-SC signal can be generated by passing a DSB-SC signal through either a high-pass or low-pass filter with response $H(f)$ depending on whether the upper or lower sideband is retained. This method is most effective when the baseband signal's spectrum has an energy gap shown in Fig. B.14. Without the energy gap, the resulting signal will contain vestiges of the discarded sideband [26].

The first, and simplest, method to seek agreement between the model's signal field and the measured signal field is to modify the signal model. In this case the baseband

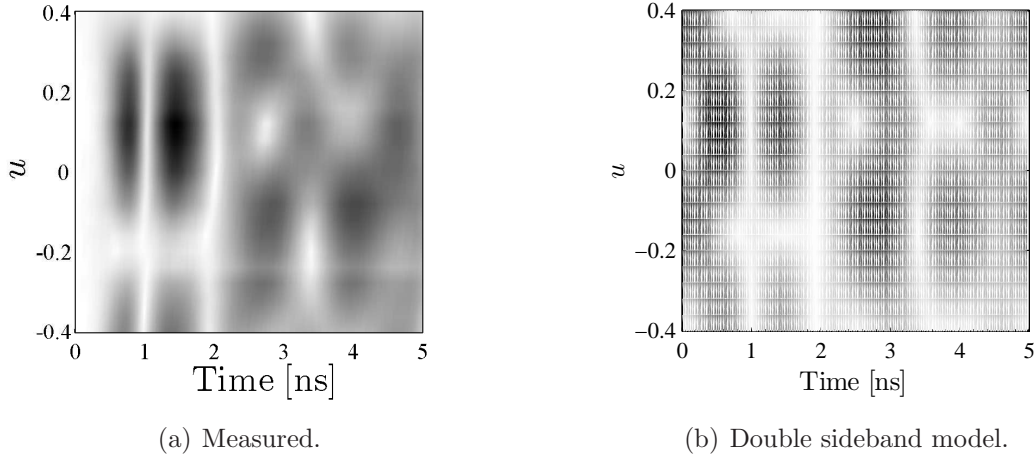


Figure B.16. Comparison of Measured (DSB-SC) and Simulated (DSB-SC) Data: *OFDM4* and *LFM3*. Transmit signal $p = 0$ is the *OFDM4* signal and transmit signal $p = 1$ is the *LFM3* signal. The field plots show fair agreement.

signal is represented as a real signal and the model is described by Eq. (B.3).

$$\begin{aligned}
 s(t, \bar{\mathbf{r}}_0) = & \sum_{p=0}^{P-1} \sum_{n=0}^{N-1} \sum_{m=0}^{M-1} \sum_{b=0}^{B-1} \exp[j\omega_0(t - \tau_0 + \Delta\tau_p)] \\
 & \times \text{Re} \left\{ \tilde{a}_{p,n,m,b} \hat{b}(t - \tau_0 - mT_c - nT_p) \right. \\
 & \left. \exp[j\Delta\omega_b(t - \tau_0 + \Delta\tau_p - mT_c - nT_p)] \right\}. \quad (\text{B.3})
 \end{aligned}$$

The result of using the modified signal model, is shown in Fig. B.16. There is fair agreement between the simulated and the measured results. Examining the entire collection of processed signals revealed that all measured and simulated signal fields are either in good or fair agreement using the DSB-SC modulation signal model.

The second method to seek agreement was to modify the circuit. Filters F1 and F6 were interchanged so that the output of the mixer stage is filtered by a filter with a higher cut-off frequency; a nominal 3dB cut-off of 9GHz. The *LFM1* signal shown in Fig. 17(a) was observed while the LO's frequency was reduced until the amplitude modulation was suppressed, and the signal appeared as shown in Fig. 17(b). This

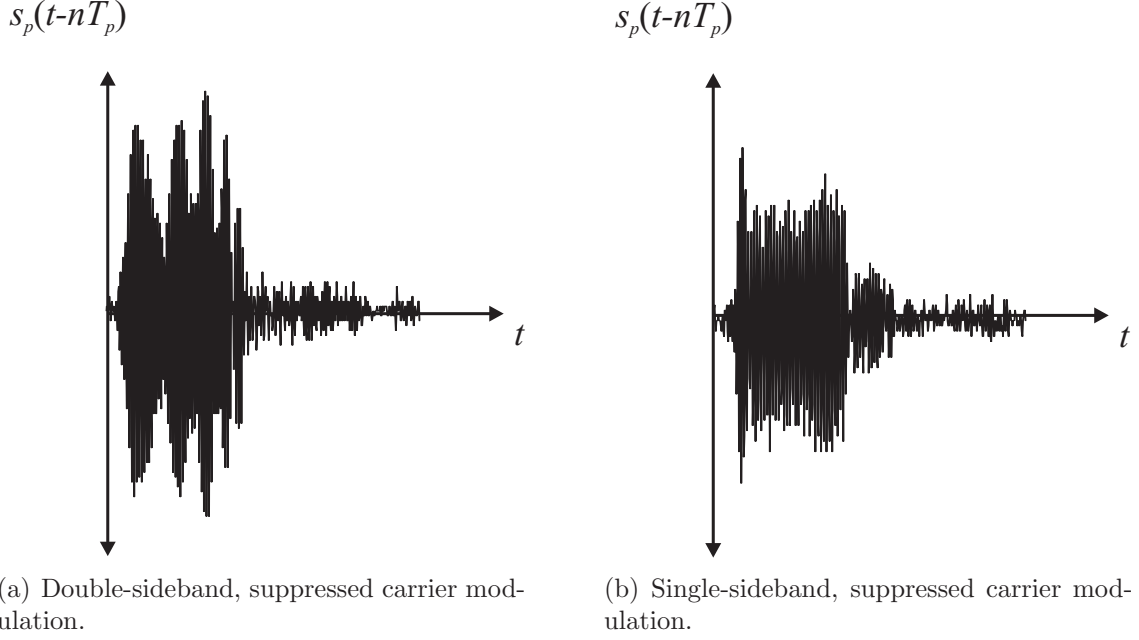


Figure B.17. DSB-SC and SSB-SC comparison: LFM signal. Comparison of DSB-SC and SSB-SC modulation of the *LFM1* signal.

particular waveform was chosen because it begins at 0Hz and spans 400MHz and it does not have the energy gap shown in Fig. B.14. The LO frequency that achieved this level of amplitude modulation suppression was approximately 8.4GHz, coinciding with F1's 20dB attenuation point. The resulting approximate, SSB-SC modulated, *LFM1* signal has a relatively flat envelope with an associated reduction in peak amplitude.

The result of modifying the circuit produced mixed results over the set of all signal combinations and a typical example is shown in Fig. B.18. In most combinations, there was poor agreement between the simulated signal field using Eq. (4.15) and the measured result. However, there was no agreement between some combinations due to the sideband vestiges and the lack of an energy gap in the baseband signal.

In future work, agreement between the measured and simulated results could be improved either by ensuring each signal is designed with a sufficiently wide energy gap or by acquiring high-pass filters with steeper roll-off to further minimize vestiges of the lower sideband. Taking advantage of the AWG's capabilities the signal design

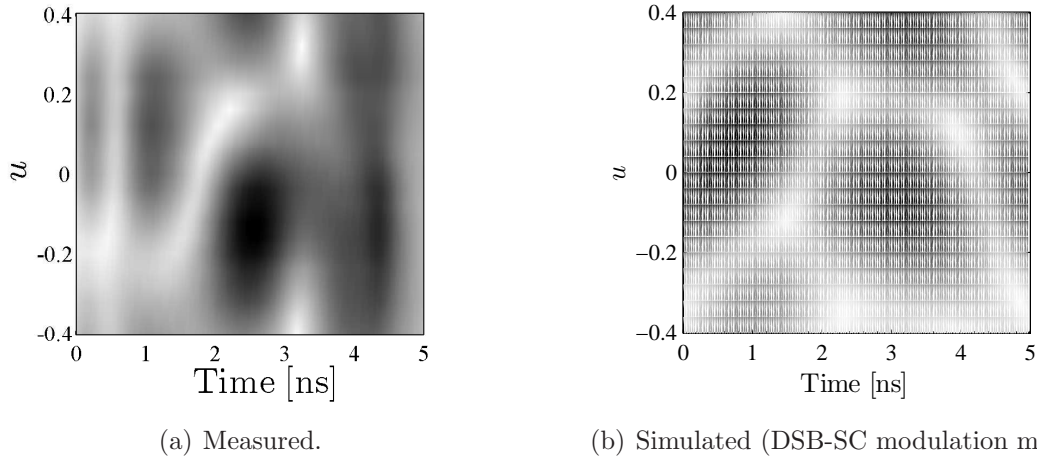


Figure B.18. Comparison of Measured (SSB-SC) and Simulated (SSB-SC) Data: *OFDM4* and *LFM3*. Transmit signal $p = 0$ is the *OFDM4* signal and transmit signal $p = 1$ is the *LFM3* signal. The field plots show poor agreement.

option would be the least expensive option.

2.5.2 Target Measurements and Receiver Processing

The experimental configuration shown in Fig. B.19 was used to compare the theoretical and measured received signals due to two targets placed on the target table. Two four-inch, square, metal plates were used as targets; the location of one target was fixed and the location of the second target was varied. Data for several different azimuth angles was collected, but because of aliasing the results varied across the collection sets. The data set used to illustrate the following examples were from one of the target configurations least degraded by aliasing. The primary aim of the experiment was to verify that the signal model and processing methods developed in Chapter V could be applied to the measured data.

The RF circuit was configured to the DSB-SC modulation circuit because the amplitude of the reflected signal using the approximate SSB-SC modulation circuit resulted in poor SNR. However, the baseband signal was processed using the single sideband matched filter consistent with the theoretical model. The simulated target

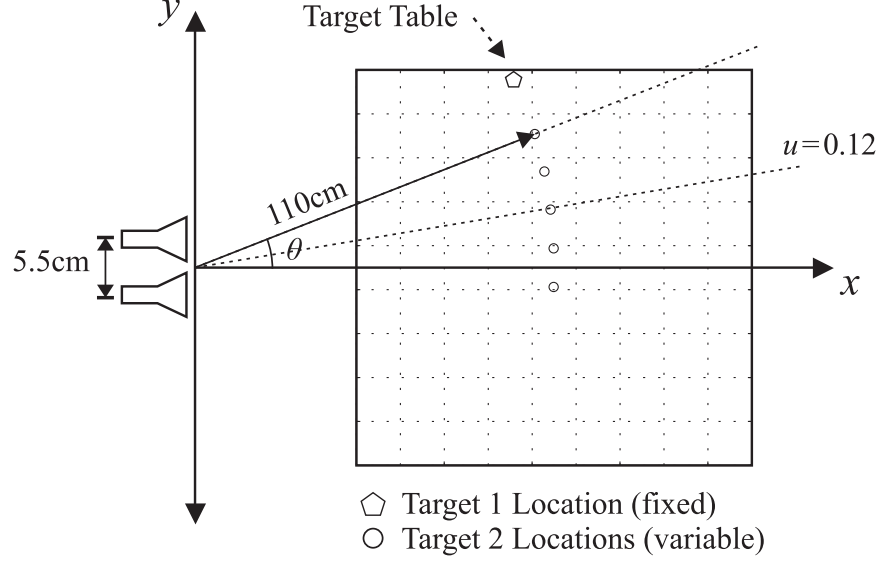


Figure B.19. Target measurement configuration.

returns were constructed using the double sideband model with relative amplitudes determined by the theoretical antenna pattern. For all combinations the theoretical results were in good agreement with the measured results.

Figure B.20 shows the result when the LFM_4 signal was transmitted from both antenna. The resulting range-azimuth plot is consistent with the CFA result clearly showing Target 2, but because Target 1 is located at an array factor null, there is no apparent reflection from Target 1. The peak-to-first-null width in range is approximately 24cm and in u is approximately 0.2. The pattern in u is dominated by the array factor and because the antenna separation is greater than half a wavelength the pattern repeats with an ambiguous peak at $u = -0.4$.

Figures B.21 and B.22 show the result when two different signals are transmitted from each antenna. In Fig. B.21 the range-azimuth plots are shown for the $OFDM_4$ signal transmitted from channel 1 and the LFM_1 signal transmitted from channel 2. Between the two signals the total bandwidth spanned is approximately 600MHz and the OFDM and LFM signals overlap at 200MHz. Associated with the increased signal bandwidth there is a corresponding reduction in the mainlobe's peak-to-first-null in

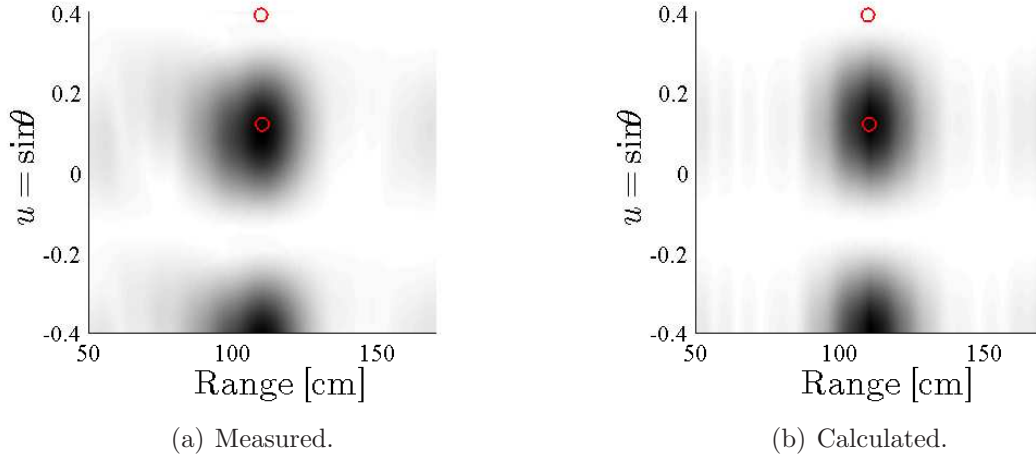


Figure B.20. Comparison of measured (DSB-SC) and simulated (DSB-SC) data: *LFM4* with targets. Range-azimuth plot comparison of the matched filter output due to two targets at $u_0 = 0.39$ and $u_1 = 0.12$. Both $p = 0$ and $p = 1$ transmitted the *LFM4* signal and the response is similar to the CFA result. The target locations are marked by circles.

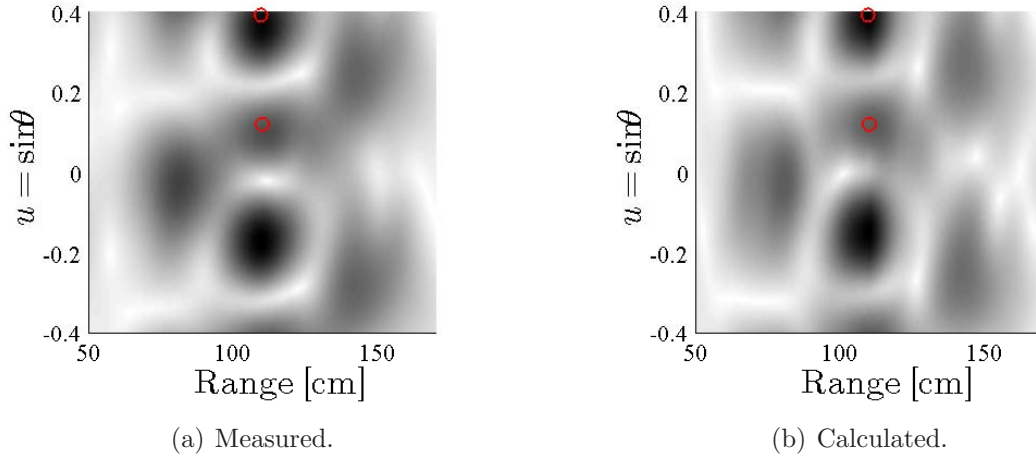


Figure B.21. Comparison of measured (DSB-SC) and simulated (DSB-SC) data: *OFDM4* and *LFM1* with targets. Range-azimuth plot comparison of the matched filter output due to two targets at $u_1 = 0.39$ and $u_2 = 0.12$. Element $p = 0$ transmitted the *OFDM4* signal and $p = 1$ transmitted the *LFM1* signal. The target locations are marked by circles.

range but there is also an increase in the sidelobe levels. The return due to Target 2 is small compared to Target 1's return, most likely because of the sidelobe interaction between Target 1's mainlobe and its alias at $u \approx -0.2$.

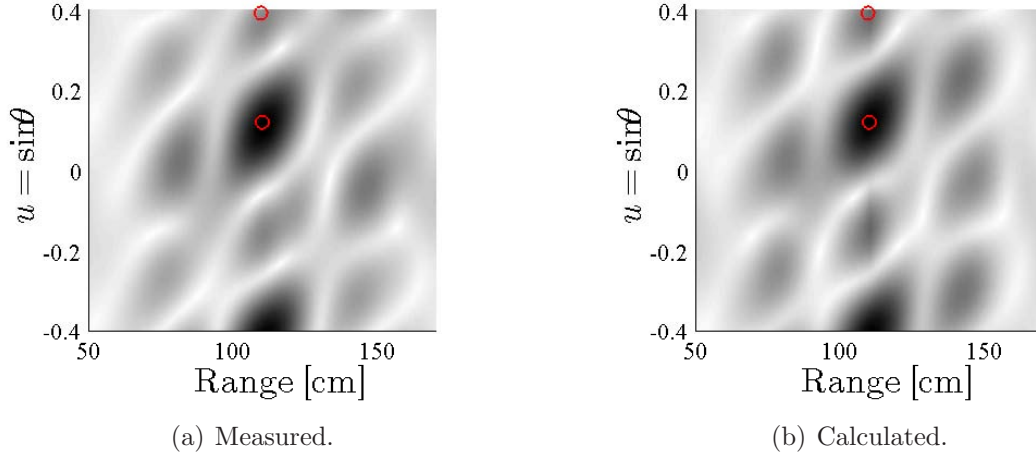


Figure B.22. Comparison of measured (DSB-SC) and simulated (DSB-SC) data: *OFDM4* and *OFDM1* with targets. Range-azimuth plot comparison of the matched filter output due to two targets at $u_0 = 0.39$ and $u_1 = 0.12$. Channel $p = 0$ transmitted the *OFDM4* signal and channel $p = 1$ transmitted the *OFDM1* signal. The target locations are marked by circles.

In Fig. B.22 the range-azimuth plots are shown for the *OFDM4* signal transmitted from channel 1 and the *OFDM1* signal transmitted from channel 2. Between the two signals the total bandwidth spanned is approximately 800MHz. In contrast to the previous configuration, the return due to Target 1 is small compared to Target 2's return. An interesting feature of the matched filter output is the delay-angle coupling observed in the plot. Switching the order that the signals are transmitted (i.e. the configuration's complement) switches the direction of the coupling.

The final plot in Fig. B.23 shows range-azimuth plot created by adding the normalized, complex plots from the two previous configurations, as well as their complements. The idea of a signal's complement is if for the first transmission signal one is sent from channel one and signal two from channel two, the next transmission will send signal two over channel one and signal one from channel two. In the resulting range-azimuth plot, the two target responses, and their aliases, are clearly discernible in both range and azimuth. The sidelobe level is relatively small, fringe the mainlobes, and do not appear to exhibit range-angle coupling observed in B.22.

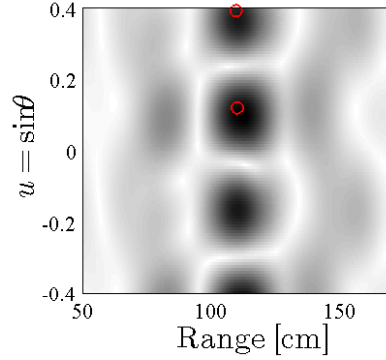


Figure B.23. Measured data: adding two signals and their complements. Range-azimuth plot generated using two complementary sets of signals. The image is formed using the same configurations used for Figures B.22 and B.21, and their complements. The target locations are marked by circles.

The mainlobe due to Target 2 has a peak-to-first-null width of 17.4cm in range and 0.125 in u which compares to 18.75cm and 0.3 for a CFA with equivalent spacing and signal bandwidth. Qualitatively, the target responses in Fig. B.23 appear clearer than either Fig. B.20 or Fig. B.21.

Increasing the plot quality by combining waveform diverse signals is certainly possible and seems to improve the radar's performance. In Figures B.20 through B.22 only a single target could be distinguished from the background noise, clutter and sidelobes. Although the azimuth resolution in Fig. B.23 is not very high due to $P = Q = 2$, and there is aliasing in the range-angle plot, Fig. B.23 shows that a two transmitter configuration can be used to provide reasonable imaging of two targets by using waveform diversity.

2.6 Summary

In this appendix the experimental configuration used to verify the signal model was explained. The RF circuit was constructed using relatively low-cost components, that are easily reconfigured, and provide a rapid prototyping method to build and explore basic radar system performance. The RAIL instruments were utilized to a

relatively advanced level to automate data collection allowing large amounts of data to be collected efficiently.

The RF circuit used a product modulator configuration and it was shown that the single sideband radar signal model did not accurately model the signal field produced by the circuit when frequency diversity was considered; however, a double sideband model accurately predicted the circuit's performance for a broad range of transmit signal configurations. The result of changing the circuit to approximate a single sideband modulation model was less promising. To find agreement between the signal model and the modified circuit, the set of transmit signals need to be designed with an energy gap so that the remaining sideband is not distorted.

The second set of experiments verified the process used to digitally demodulate and match filter the sampled signals collected by the DSO. The result of processing the measured data was compared to the simulation model and the two results were in good agreement for the range of signals used in this appendix. Furthermore, limited waveform diversity was used to improve the quality of the range-azimuth plot by combining the plots of two different signal configurations and their complements. When a variety of different signals were integrated an improved range-azimuth plot was produced and the two targets were clearly visible.

Appendix C. Fourier Transforms: Properties, Transform Pairs and Application to Optics

The purpose of this appendix is to provide a background of basic Fourier transform theory, both from the contemporary temporal and temporal frequency perspective of signal processing and from the spatial perspective found in Fourier optics.

3.1 One Dimension Fourier Transforms

Two situations that may require analysis using the one dimension Fourier transform are temporal frequency analysis and analysis of waves propagating in a single direction.

3.1.1 Temporal Signals

The material in this section is drawn from [21]. The temporal Fourier transform is well established in a variety of applications and will only be presented here. Given a function of time $f(t)$ its Fourier transform is

$$\begin{aligned} F(\omega) &= \mathcal{F}\{f(t)\} \\ &= \int_{-\infty}^{\infty} f(t) \exp(-j\omega t) dt, \end{aligned} \tag{C.1}$$

and given the Fourier transform $F(\omega)$, the original signal can be recovered by applying the inverse transform

$$\begin{aligned} f(t) &= \mathcal{F}^{-1}\{F(\omega)\} \\ &= \frac{1}{2\pi} \int_{-\infty}^{\infty} F(\omega) \exp(j\omega t) d\omega. \end{aligned} \tag{C.2}$$

The existence of the Fourier transform generally requires satisfaction of the Dirichlet conditions that the signal is absolutely integrable

$$\int_{-\infty}^{\infty} |f(t)| dt < \infty, \quad (\text{C.3})$$

and $f(t)$ has a finite number of maxima, minima and discontinuities in a finite interval.

The conditions include all useful energy signals, that is, signals that satisfy

$$\int_{-\infty}^{\infty} |f(t)|^2 dt < \infty. \quad (\text{C.4})$$

Some signals do not satisfy these conditions, they have infinite energy. Impulse functions are allowed in the Fourier integral enabling some non-finite energy signals to be represented such as the step function. If the infinite energy signals have finite power, i.e. a power signal, then it satisfies

$$\lim_{T \rightarrow \infty} \int_{-T/2}^{T/2} |f(t)|^2 dt < \infty. \quad (\text{C.5})$$

The Fourier transform properties are listed in Table C.1 and the common transform pairs are listed in Table C.2.

3.1.2 Spatial Signals

The spatial Fourier transform in one dimension is analogous to the temporal Fourier transform with a substitution of a spatial variable for time and an angular spatial frequency for the angular temporal frequency. The material in this section is drawn from [27]; in which the integral transforms are defined with a subtle difference.

Table C.1. Table of one-dimensional, time-frequency FT properties [21].

	Property	Relation
1.	Transform	$s(t) \leftrightarrow S(\omega)$
2.	Linearity	$a_1 s_1(t) + a_2 s_2(t) \leftrightarrow a_1 S_1(\omega) + a_2 S_2(\omega)$
3.	Symmetry	$s(\omega) \leftrightarrow \frac{1}{2\pi} S(t)$
4.	Scaling	$s(at) \leftrightarrow \frac{1}{ a } S\left(\frac{\omega}{a}\right)$
5.	Delay	$s(t - t_0) \leftrightarrow e^{-j\omega t_0} S(\omega)$
6.	Modulation	$e^{j\omega_0 t} s(t) \leftrightarrow S(\omega - \omega_0)$
7.	Convolution	$s_1(t) \star s_2(t) \leftrightarrow S_1(\omega) S_2(\omega)$
8.	Multiplication	$s_1(t) s_2(t) \leftrightarrow \frac{1}{2\pi} S_1(\omega) \star S_2(\omega)$
9.	Reversal	$s(-t) \leftrightarrow S(-\omega)$
10a.	Differentiation	$\frac{d^n}{dt^n} s(t) \leftrightarrow (j\omega)^n S(\omega)$
10b.	Differentiation	$\frac{d}{d\omega} S(\omega) \leftrightarrow -jt s(t)$

Table C.2. Table of one-dimensional, time-frequency FT pairs [21].

	$s(t)$	$S(\omega)$
1.	$k\delta(t)$	k
2.	k	$2\pi k\delta(\omega)$
3.	$u(t)$	$\pi\delta(\omega) + \frac{1}{j\omega}$
4.	$\cos(\omega_0 t)$	$\pi[\delta(\omega - \omega_0) + \delta(\omega + \omega_0)]$
5.	$\sin(\omega_0 t)$	$\pi[\delta(\omega - \omega_0) - \delta(\omega + \omega_0)]$
6.	$e^{j\omega_0 t}$	$2\pi\delta(\omega - \omega_0)$
7.	$\text{rect}(t)$	$\text{sinc}\left(\frac{\omega}{2}\right)$

Given $f(x)$, a function of spatial variable x , its Fourier transform is

$$\begin{aligned} F(k) &= \mathcal{F}\{f(x)\} \\ &= \int_{-\infty}^{\infty} f(x) \exp(jkx) dx, \end{aligned} \tag{C.6}$$

and given the Fourier transform $F(\omega)$, the original signal can be recovered by applying the inverse transform

$$\begin{aligned} f(x) &= \mathcal{F}^{-1}\{F(k)\} \\ &= \frac{1}{2\pi} \int_{-\infty}^{\infty} F(k) \exp(-jkx) dk. \end{aligned} \tag{C.7}$$

Comparing equations (C.6) and (C.7) to equations (C.1) and (C.2) shows that the sign of the exponential basis functions are reversed between the two sets. The difference is commented on in [27] and the two representations are equivalent. The signs in the spatial transform is consistent with (C.1) and (C.2) in another leading optics text [24]. The reason why the two may differ may be that in [27] the propagating wave is defined as

$$s(t, \bar{\mathbf{r}}_0) = \exp[j(\omega t - \bar{\mathbf{k}} \cdot \bar{\mathbf{r}}_0)] \tag{C.8}$$

whereas [24] defines the propagating wave as

$$s(t, \bar{\mathbf{r}}_0) = \exp[j(\bar{\mathbf{k}} \cdot \bar{\mathbf{r}}_0 - \omega t)], \tag{C.9}$$

which is the more traditional Fourier optics approach [27]. By the reversal property it can be shown that two representations are equivalent, but Eq. (C.8) is most often adopted in electrical engineering and Eq. (C.9) in the physics literature.

3.1.3 Amplitude and Phase Spectra

The Fourier transform of either the temporal or spatial signal is generally a complex-valued function

$$F(\omega) = A(\omega) + jB(\omega), \quad (\text{C.10})$$

where $A(\omega)$ and $B(\omega)$ are both real-valued functions. The spectrum can also be expressed as a function of amplitude and phase

$$F(\omega) = |F(\omega)| \exp [j\phi(\omega)]. \quad (\text{C.11})$$

The amplitude spectrum is

$$|F(\omega)| = \sqrt{A^2(\omega) + B^2(\omega)}, \quad (\text{C.12})$$

and the phase spectrum is

$$\phi(\omega) = \tan^{-1} \frac{B(\omega)}{A(\omega)}. \quad (\text{C.13})$$

The amplitude and phase spectra are useful when discussing different applications.

3.1.4 Discrete Fourier Transform

The Discrete Fourier Transform is an important transform that arises in digital computation of the Fourier transform from a sampled continuous signal. The DFT pair relating a sequence of signal samples $f[n]$ to a sequence of frequency samples

$F[k]$ is

$$F[k] = \sum_{n=0}^{N-1} f[n] W_N^{kn} \quad (\text{C.14})$$

and

$$f[n] = \sum_{k=0}^{N-1} F[k] W_N^{-kn} \quad (\text{C.15})$$

where

$$f[n] = f(t)|_{t=nT_s}$$

$$F[k] = F(\omega)|_{\omega=k\Delta\omega}$$

$$W_N = \exp(-j2\pi/N)$$

$$T_s = f_s^{-1}$$

$$\Delta\omega = \frac{2\pi}{NT_s},$$

f_s is the sample frequency, T_s is the sample interval, and $\Delta\omega$ is the interval between frequencies corresponding to the interval between spectral samples k .

There are a number of subtleties when using the DFT such as aliasing, periodicity in the signal and its spectrum, and the result of the periodicity on the convolution operation. These issues are discussed in Oppenheim, however, the DFT and its computationally efficient FFT form are prevalent in processing real signals.

3.2 Two Dimension Fourier Transform

A comprehensive source of background on two- and three-dimensional Fourier transforms is found in Fourier optics. While the application is slightly different, the subject relates electromagnetic wave propagation and its Fourier transform. The

primary references for the material are [27] and [24].

Table C.3. Table of two-dimensional, rectangular, spatial FT properties [24].

	Property	Relation
1.	Transform	$s(x, y) \leftrightarrow S(k_x, k_y)$
2.	Linearity	$a_1 s_1(x, y) + a_2 s_2(x, y) \leftrightarrow a_1 S_1(k_x, k_y) + a_2 S_2(k_x, k_y)$
3.	Scaling	$s(ax, by) \leftrightarrow \frac{1}{ ab } S\left(\frac{k_x}{a}, \frac{k_y}{b}\right)$
4.	Shift	$s(x - x_0, y - y_0) \leftrightarrow e^{-j(ak_x + bk_y)} S(k_x, k_y)$
4.	Multiplication	$s_1(x, y) s_2(x, y) \leftrightarrow S_1(k_x, k_y) \star S_2(k_x, k_y)$
5.	Convolution	$s_1(x, y) \star s_2(x, y) \leftrightarrow S_1(k_x, k_y) S_2(k_x, k_y)$

3.2.1 Transform in Rectangular Coordinates

Given $f(x, y)$, a function of spatial variables x and y , if its Fourier transform exists, the function and its transform are related by the transform pairs

$$\begin{aligned}
 F(k_x, k_y) &= \mathcal{F}\{f(x, y)\} \\
 &= \int \int_{-\infty}^{\infty} f(x, y) \exp[j(k_x x + k_y y)] \, dx dy,
 \end{aligned} \tag{C.16}$$

and

$$\begin{aligned}
 f(x, y) &= \mathcal{F}^{-1}\{F(k_x, k_y)\} \\
 &= \frac{1}{(2\pi)^2} \int \int_{-\infty}^{\infty} F(k_x, k_y) \exp[-j(k_x x + k_y y)] \, dk_x dk_y.
 \end{aligned} \tag{C.17}$$

The two dimension transform properties are listed in Table C.3.

3.2.2 Transform in Polar Coordinates

The Fourier transform of a function separable in polar coordinates can be represented as an infinite sum of Hankel transforms [24]. A polar function $f(r, \theta)$ separable in range r and azimuth angle θ can be expressed as $f(r, \theta) = f_R(r)f_\Theta(\theta)$. Its transform to a polar Fourier domain with coordinates ρ and ϕ is

$$\mathcal{F}\{f(r, \theta)\} = \sum_{k=-\infty}^{\infty} c_k (-j)^k \exp(jk\phi) \mathcal{H}_k\{f_R(r)\}, \quad (\text{C.18})$$

where

$$c_k = \frac{1}{2\pi} \int_0^{2\pi} f_\Theta(\theta) \exp(-jk\theta) d\theta, \quad (\text{C.19})$$

and $\mathcal{H}_k\{\cdot\}$ is the Hankel transform operator of order k , defined by

$$\mathcal{H}_k\{f_R(r)\} = 2\pi \int_0^{\infty} r f_R(r) J_k(2\pi r \rho) dr. \quad (\text{C.20})$$

The function $J_k(\cdot)$ is the k th-order Bessel function of the first kind.

For a circularly symmetric function $f(r, \theta) = f_R(r)$ the Fourier-Bessel function is a simpler transform

$$F(\rho, \phi) = F(\rho) = 2\pi \int_0^{\infty} r f_R(r) J_0(2\pi r \rho) dr. \quad (\text{C.21})$$

A key result is that, given a circularly symmetric function, there is no difference between the forward and inverse transform [24].

In the radar problem, the wave is typically treated as a spherical propagating wavefront. In the far-field, the wavefront is approximately separable in angle and range and the transforms in this section may seem a natural choice. However, both

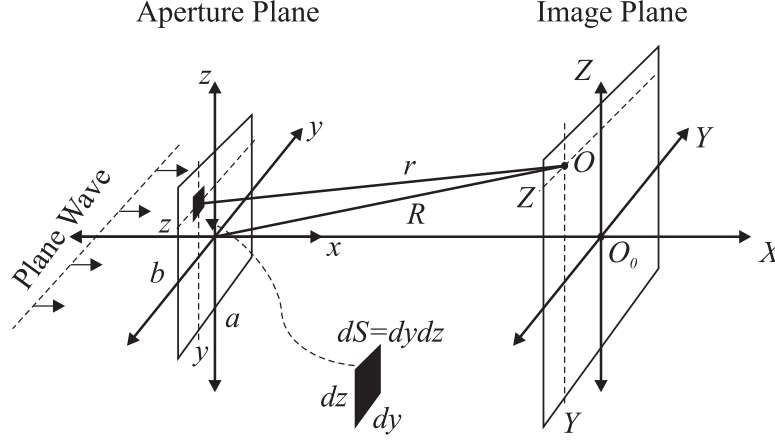


Figure C.1. Rectangular aperture geometry [27].

transforms are derived from the rectangular Fourier transform and have limited applicability once the higher dimensions are considered in the array problem.

3.3 Fourier Optics

Two dimensional Fourier transform theory is popular in optics to model plane wave, electromagnetic wave propagation through optical systems. The theory does not directly relate to the radar problem, however, there are several useful analogies. The primary results stem from the study of Fraunhofer (or far-field) diffraction patterns resulting from plane waves propagating through an optical system.

First, a brief background is provided on diffraction analysis using analytic geometry. Consider the system in Fig. C.1, a plane wave propagates with its wavevector aligned to the x axis and passes through an rectangular aperture on the $y - z$ plane centered about the origin. According to the Huygens-Fresnel principle a differential area $dS = dydz$ can be considered as being covered with secondary point sources [27]. Because dS is much smaller than a wavelength the contributions of the point sources at a point on the plane, containing P , add constructively. In other words, dS is a source of a secondary spherical wave.

If the source strength per unit area is ϵ_A , assumed constant over the aperture, the disturbance at P due to dS is the real or imaginary part of

$$dE = \frac{\epsilon_A}{r} \exp[j(\omega t - kr)]. \quad (\text{C.22})$$

Using the far-field approximation for small angles [27], the distance from dS to P is

$$r = R[1 - (Yy + Zz)/R^2], \quad (\text{C.23})$$

where

$$R = \sqrt{X^2 + Y^2 + Z^2}, \quad (\text{C.24})$$

and the total disturbance arriving at P is

$$E(Y, Z) = \frac{\epsilon_A}{r} \exp[j(\omega t - kr)] \int \int_{\text{Aperture}} \exp[jk(Yy + Zz)/R] dS. \quad (\text{C.25})$$

Substituting

$$\alpha = kaZ/2R \quad (\text{C.26})$$

$$\beta = kbY/2R \quad (\text{C.27})$$

into Eq. (C.25) and evaluating the integral results in the disturbance over the image plane

$$E(Y, Z) = \frac{ab\epsilon_A}{r} \exp[j(\omega t - kr)] \text{sinc}(\alpha) \text{sinc}(\beta). \quad (\text{C.28})$$

There is one primary difference between the optics problem and the radar problem (at least in the forward direction). In optics the transmitted field is assessed over a flat plane at some distance x from the aperture, with only small angular deviations from the imaging axis. In the forward propagation radar problem the field is typically characterized at rings of constant radius with any angle. With the difference in mind, it is interesting to see the results of Fourier transform theory applied to optical system analysis.

3.3.1 Diffraction Pattern and the Fourier Transform

In Eq. (C.29) it was assumed the aperture is illuminated by a constant field ϵ_A . More generally, it can be assumed the aperture illumination is a complex function

$$A(y, z) = A_0(y, z) \exp[\phi(y, z)], \quad (\text{C.29})$$

and also incorporates the multiplicative constants such as the $1/R$ terms and the complex phase $\exp[j(\omega t - kr)]$. Equation (C.25) can then be represented as

$$E(Y, Z) = \int \int_{-\infty}^{\infty} A(y, z) \exp[jk(Yy + Zz)/R] dydz. \quad (\text{C.30})$$

If the differential field at a point P is considered to be due to a plane wave with amplitude determined by $A(y, z)dydz$, with wavevector $\bar{\mathbf{k}}$, and with spatial frequencies

$$k_Y = kY/R = k \sin \theta, \quad (\text{C.31})$$

$$k_Z = kZ/R = k \sin \psi. \quad (\text{C.32})$$

Each point on the image plane corresponds to a spatial frequency [27] and Eq. (C.33) can be expressed as

$$E(k_Y, k_Z) = \iint_{-\infty}^{\infty} A(y, z) \exp[jk(k_Y y + k_Z z)] dy dz. \quad (\text{C.33})$$

The key result in Eq. (C.33) is that the diffraction pattern viewed on an image plane is approximately the Fourier transform of the field distribution across the aperture [27]. Associated with this result is an interesting interpretation of the spatial frequencies and how they relate to a particular point in space.

The result is analogous to the theory used to determine the radar array's weights by taking the inverse transform of a desired array factor. It is also analogous to the Fourier transform method of determining the current distribution of a continuous line source from a desired field distribution [9].

Note that the result here assumes the impinging source is a monochromatic plane wave and as such is consistent with CFA theory. Another useful result from Fourier optics is that for waves consisting of multiple frequency components the resulting field is a superposition of the Fourier transforms assessed at the corresponding frequencies [24].

Additionally, regardless of the illuminating source's frequency, the spatial frequencies k_Y and k_Z have baseband bandwidths centered about the origin $Y = 0$, $Z = 0$. This seems counterintuitive because the spatial frequencies should correspond more closely with the transmit signal frequency. In this case however, the spatial frequency associated with the source frequency is more closely related to the x directed portion, which, in optics, is less relevant because it cannot be measured directly [27].

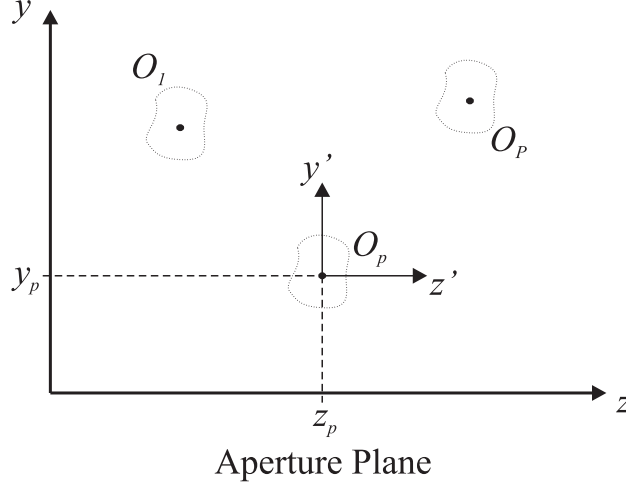


Figure C.2. Optical array geometry [27].

3.3.2 Optical Array Theorem

An optics theorem that is the dual of CFA array theory is the optical array theory. Given the geometry in Fig. C.2, P identical apertures are located in the aperture plane centered on points O_p with coordinates (y_p, z_p) . At each aperture center a local coordinate system (y', z') is defined and a point in the local coordinate system has coordinates $(y_p + y', z_p + z')$ in the reference coordinate system. If each aperture is illuminated identically the diffraction field at some point on the image plane is a superposition of the diffraction field resulting from each sub-aperture; or,

$$\begin{aligned}
 E(Y, Z) &= \sum_{p=0}^{P-1} \int_{-\infty}^{\infty} \int_{-\infty}^{\infty} A_P(y', z') \exp\{jk_0[Y(y_p + y') + Z(z_p + z')]/R\} dy' dz' \\
 &= \int_{-\infty}^{\infty} \int_{-\infty}^{\infty} A_P(y', z') \exp[jk_0(Yy' + Zz')/R] dy' dz' \\
 &\quad \times \sum_{p=0}^{P-1} \exp[jk_0(Yy_p + Zz_p)/R]
 \end{aligned} \tag{C.34}$$

Expressing Eq. (C.34) as a Fourier integral from the previous section results in

$$E(k_Y, k_Z) = \int \int_{-\infty}^{\infty} A_P(y', z') \exp[j(k_Y y' + k_Z z')] dy' dz' \\ \times \sum_{p=0}^{P-1} \exp[j(k_Y y_p + k_Z z_p)]. \quad (\text{C.35})$$

The summation term is the Fourier transform of an array of delta functions

$$A_\delta = \sum_{p=0}^{P-1} \delta(y - y_p) \delta(z - z_p), \quad (\text{C.36})$$

and the transform of the total aperture function is $\mathcal{F}\{A(y, z)\} = \mathcal{F}\{A_P(y, z)\} \mathcal{F}\{A_\delta\}$. This is analogous to the pattern multiplication that was briefly discussed with respect to the CFA theory in Chapter II.

Bibliography

- [1] “IEEE Standard Radar Definitions”. c1–41, 21 2008.
- [2] *Defending Australia in the Asia Pacific Century: Force 2030*. White paper, Australian Department of Defence, May 2009.
- [3] AFRL. “Sensors as Robots (BAA-07-02-IFKA)”. Online, October 2006.
- [4] Antonik, P. *An investigation of a frequency diverse array*. Ph.D. thesis, University College of London, Apr. 2009.
- [5] Antonik, P., M.C. Wicks, H.D. Griffiths, and C.J. Baker. “Frequency diverse array radars”. *Proceedings 2006 IEEE Radar Conference*, 3 pp. April 2006.
- [6] Antonik, P., M.C. Wicks, H.D. Griffiths, and C.J. Baker. “Multi-mission multi-mode waveform diversity”. *Proceedings 2006 IEEE Radar Conference*, 3 pp. April 2006.
- [7] Baizert, P. *Forward-looking radar clutter suppression using frequency diverse radar*. Master’s thesis, Air Force Institute of Technology, Mar. 2006.
- [8] Baizert, P., T.B. Hale, M.A. Temple, and M.C. Wicks. “Forward-looking radar GMTI benefits using a linear frequency diverse array”. *Electronics Letters*, 42(22):1311–1312, October 2006. ISSN 0013-5194.
- [9] Balanis, C.A. *Antenna Theory*. Hoboken, NJ: John Wiley and Sons, 3rd edition, 2005.
- [10] Bryant, M., P. Johnson, B.M. Kent, M. Nowak, and S. Rogers. *Layered Sensing: Principles for AFRL Strategic Technology Development*. Technical report, Air Force Research Laboratory, May 2008.
- [11] Chen, C. and P.P. Vaidyanathan. “Properties of the MIMO radar ambiguity function”. *Proceedings 2008 International Conference on Acoustics, Speech and Signal Processing*, 2309–2312. April 2008. ISSN 1520-6149.
- [12] Colegrove, S.B. “Project Jindalee: from bare bones to operational OTHR”. *Proceedings 2000 IEEE International Radar Conference*, 825–830. 2000.
- [13] Coleman, C. and H. Yardley. “Passive bistatic radar based on target illuminations by digital audio broadcasting”. *IET Radar, Sonar & Navigation*, 2(5):366–375, October 2008. ISSN 1751-8784.
- [14] Daum, F. and J. Huang. “MIMO radar: Snake oil or good idea?” *IEEE Aerospace and Electronic Systems Magazine*, 24(5):8–12, May 2009. ISSN 0885-8985.

- [15] Dooley, S.R. and A.K. Nandi. “Notes on the interpolation of discrete periodic signals using sinc function related approaches”. *IEEE Transactions on Signal Processing*, 48(4):1201–1203, Apr 2000.
- [16] Farooq, J. *Frequency diversity for improving synthetic aperture radar*. Ph.D. thesis, Air Force Institute of Technology, Mar. 2009.
- [17] Farooq, J., M.A. Temple, and M.A. Saville. “Exploiting frequency diverse array processing to improve SAR image resolution”. *Proceedings 2008 IEEE Radar Conference*, 1–5. May 2008. ISSN 1097-5659.
- [18] Fishler, E., A. Haimovich, R. Blum, D. Chizhik, L. Cimini, and R. Valenzuela. “MIMO radar: an idea whose time has come”. *Proceedings 2004 IEEE Radar Conference*, 71–78. April 2004. ISSN 1097-5659.
- [19] Franken, G.E.A., H. Nikookar, and P. van Genderen. “Doppler tolerance of OFDM-coded radar signals”. *Proceedings 2006 European Radar Conference*, 108–111. September 2006.
- [20] Fuhrmann, D.R., P.J. Browning, and M. Rangaswamy. “Ambiguity function analysis for the hybrid MIMO phased-array radar”. *Proceedings 2009 IEEE Radar Conference*, 1–6. May 2009. ISSN 1097-5659.
- [21] Gabel, R.A. and R.A. Roberts. *Signals and linear systems*. New York: John Wiley and Sons, 1987.
- [22] Garmatyuk, D., J. Schuerger, K. Kauffman, and S. Spalding. “Wideband OFDM system for radar and communications”. *Proceedings 2009 IEEE Radar Conference*, 1–6. May 2009.
- [23] van Genderen, P. “Recent advances in waveforms for radar, including those with communication capability”. *Proceedings 2009 European Radar Conference*, 318–325. October 2009.
- [24] Goodman, J.W. *Introduction to Fourier optics*. Greenwood Village, CO: Roberts and Company Publishers, 3rd edition, 2005.
- [25] Hale, T. and M.A. Saville. “EENG 668 Advanced Radar System Analysis Course Notes”, 2009. Course notes for advanced radar system course.
- [26] Haykin, S. *Communication Systems*. New York, NY: John Wiley and Sons, 4th edition, 2001.
- [27] Hecht, E. *Optics*. San Francisco, CA: Addison Wesley, 4th edition, 2002.
- [28] Huang, J., K. Tong, and C.J. Baker. “Frequency diverse array with beam scanning feature”. *Proceedings 2008 IEEE Antennas and Propagation Society International Symposium*, 1–4. July 2008.

- [29] Huang, J., K. Tong, K. Woodbridge, and C.J. Baker. “Frequency diverse array: simulation and design”. *Proceedings 2009 IEEE Radar Conference*, 1–4. May 2009. ISSN 1097-5659.
- [30] Klemm, R. *Principles of Space-Time Adaptive Processing*. London, UK: The Institute of Electrical Engineers, 2nd edition, 2002.
- [31] Lellouch, G., R. Pribic, and P. van Genderen. “Frequency agile stepped OFDM waveform for HRR”. *Proceedings 2009 International Waveform Diversity and Design Conference*, 90–93. February 2009.
- [32] Lellouch, G., R. Pribic, and P. van Genderen. “Merging frequency agile OFDM waveforms and compressive sensing into a novel radar concept”. *Proceedings 2009 European Radar Conference*, 137–140. October 2009.
- [33] Levanon, N. and E. Mozeson. *Radar Signals*. Hoboken, NJ: John Wiley and Sons, 2004.
- [34] Li, J., P. Stoica, and Y. Xie. “On probing signal design for MIMO radar”. *Proceedings Fortieth Asilomar Conference on Signals, Systems and Computers*, 31–35, November 2006. ISSN 1058-6393.
- [35] Massonnet, D. and J. Souyris. *Imaging with synthetic aperture radar*. Boca Raton, FL: CRC Press, 2008.
- [36] Ozaktas, H.M., Z. Zalevsky, and M.A. Kutay. *The fractional fourier transform with applications in optics and signal processing*. West Sussex, England: John Wiley and Sons, 2001.
- [37] Rose, L.J. “Air Force Research Laboratory’s Focused Long Term Challenges”, April 2008. Accessed 15 Sep 2009.
- [38] Ruggiano, M. and P. van Genderen. “Wideband ambiguity function and optimized coded radar signals”. *Proceedings 2007 European Radar Conference*, 142–145. October 2007.
- [39] Sammartino, P.F. and C.J. Baker. “The frequency diverse bistatic system”. *Proceedings 2009 IEEE International Waveform Diversity and Design Conference*, 155–159. February 2009.
- [40] San Antonio, G., D.R. Fuhrmann, and F.C. Robey. “MIMO radar ambiguity functions”. *IEEE Journal of Selected Topics in Signal Processing*, 1(1):167–177, June 2007. ISSN 1932-4553.
- [41] Secmen, M., S. Demir, A. Hizal, and T. Eker. “Frequency diverse array antenna with periodic time modulated pattern in range and angle”. *Proceedings 2007 IEEE Radar Conference*, 427–430. April 2007. ISSN 1097-5659.

- [42] Skolnik, M.I. *Introduction to Radar Systems*. New York, NY: McGraw-Hill Higher Education, 3rd edition, 2001.
- [43] Tigrek, R.F., W. de Heij, and P. van Genderen. “Multi-carrier radar waveform schemes for range and Doppler processing”. *Proceedings 2009 IEEE Radar Conference*, 1–5. May 2009. ISSN 1097-5659.
- [44] United States Air Force. *Air Force Doctrine Document 2-3 Irregular Warfare*, August 2007.
- [45] United States Air Force. *Air Force Doctrine Document 2-9 Intelligence, Surveillance, and Reconnaissance Operations*, July 2007.
- [46] Urkowitz, H., C.A. Hauer, and J.F. Koval. “Generalized resolution in radar systems”. *Proceedings of the IRE*, 50(10):2093–2105, October 1962.
- [47] Van Trees, H.L. *Optimum Array Processing*, volume 4 of *Detection, Estimation, and Modulation Theory*. New York, NY: John Wiley and Sons, 2001.
- [48] Wicks, M.C. “A brief history of waveform diversity”. *Proceedings 2009 IEEE Radar Conference*, 1–6. May 2009.
- [49] Wicks, M.C. and W. Moore. “Distributed and layered sensing”. *Proceedings 2007 IEEE International Waveform Diversity and Design Conference*, 233–239. June 2007.
- [50] Zhang, J.J. and A. Papandreou-Suppappola. “MIMO radar with frequency diversity”. *Proceedings 2009 International Waveform Diversity and Design Conference*, 208–212. February 2009.
- [51] Zhuang, L. and X. Liu. “Application of frequency diversity to suppress grating lobes in coherent MIMO radar with separated subapertures”. *EURASIP Journal on Advances in Signal Processing*, 2009:10, May 2009. ISSN 1053-587X.

Vita

Flight Lieutenant Steven Brady is a member of the Royal Australian Air Force (RAAF). He graduated in July 2003 from Curtin University of Technology, Perth, Western Australia with a Bachelor of Engineering (Electronics and Communications). In October, 2004 he commissioned into the RAAF, completing the Initial Officers' Course in March, 2005 at the Officer Training School, then located at Point Cook, Victoria. Following a brief assignment at the Air Lift System Program Office in Richmond, New South Wales he served for approximately three years at No. 33 Squadron as a maintenance officer, also in Richmond. When No. 33 Squadron's fleet of Boeing 707 air-to-air refuelling aircraft were retired in 2009 he was selected to participate in AFIT's graduate program to gain a Master's degree in electrical engineering. Following completion of the Master's program he returns to the Joint Electronic Warfare Operational Support Unit in Adelaide, South Australia.

REPORT DOCUMENTATION PAGE					Form Approved OMB No. 0704-0188	
<p>The public reporting burden for this collection of information is estimated to average 1 hour per response, including the time for reviewing instructions, searching existing data sources, gathering and maintaining the data needed, and completing and reviewing the collection of information. Send comments regarding this burden estimate or any other aspect of this collection of information, including suggestions for reducing this burden to Department of Defense, Washington Headquarters Services, Directorate for Information Operations and Reports (0704-0188), 1215 Jefferson Davis Highway, Suite 1204, Arlington, VA 22202-4302. Respondents should be aware that notwithstanding any other provision of law, no person shall be subject to any penalty for failing to comply with a collection of information if it does not display a currently valid OMB control number. PLEASE DO NOT RETURN YOUR FORM TO THE ABOVE ADDRESS.</p>						
1. REPORT DATE (DD-MM-YYYY)		2. REPORT TYPE		3. DATES COVERED (From — To)		
25-03-2010		Master's Thesis		Aug 2008 — Mar 2010		
4. TITLE AND SUBTITLE				5a. CONTRACT NUMBER		
Frequency Diverse Array Radar: Signal Characterization and Measurement Accuracy				5b. GRANT NUMBER		
				5c. PROGRAM ELEMENT NUMBER		
				5d. PROJECT NUMBER		
6. AUTHOR(S)				5e. TASK NUMBER		
Steven H.R. Brady, FLTLT, RAAF				5f. WORK UNIT NUMBER		
7. PERFORMING ORGANIZATION NAME(S) AND ADDRESS(ES)				8. PERFORMING ORGANIZATION REPORT NUMBER		
Air Force Institute of Technology Graduate School of Engineering and Management (AFIT/EN) 2950 Hobson Way WPAFB OH 45433-7765				AFIT/GE/ENG/10-04		
9. SPONSORING / MONITORING AGENCY NAME(S) AND ADDRESS(ES)				10. SPONSOR/MONITOR'S ACRONYM(S)		
Air Force Research Laboratory Sensors Directorate (AFRL/RYRR), Mr Tom Lewis 2241 Avionics Circle Wright-Patterson AFB, OH, 45433 937 255 6427 x4347 and thomas.lewis3@wpafb.af.mil				AFRL/RYRR		
				11. SPONSOR/MONITOR'S REPORT NUMBER(S)		
12. DISTRIBUTION / AVAILABILITY STATEMENT						
APPROVED FOR PUBLIC RELEASE; DISTRIBUTION UNLIMITED.						
13. SUPPLEMENTARY NOTES						
14. ABSTRACT						
<p>Radar systems provide an important remote sensing capability, and are crucial to the layered sensing vision; a concept of operation that aims to apply the right number of the right types of sensors, in the right places, at the right times for superior battle space situational awareness. The layered sensing vision poses a range of technical challenges, including radar, that are yet to be addressed. To address the radar-specific design challenges, the research community responded with waveform diversity; a relatively new field of study which aims reduce the cost of remote sensing while improving performance. Early work suggests that the frequency diverse array radar may be able to perform several remote sensing missions simultaneously without sacrificing performance. With few techniques available for modeling and characterizing the frequency diverse array, this research aims to specify, validate and characterize a waveform diverse signal model that can be used to model a variety of traditional and contemporary radar configurations, including frequency diverse array radars. To meet the aim of the research, a generalized radar array signal model is specified. A representative hardware system is built to generate the arbitrary radar signals, then the measured and simulated signals are compared to validate the model. Using the generalized model, expressions for the average transmit signal power, angular resolution, and the ambiguity function are also derived. The range, velocity and direction-of-arrival measurement accuracies for a set of signal configurations are evaluated to determine whether the configuration improves fundamental measurement accuracy.</p>						
15. SUBJECT TERMS						
Radar, Frequency Diverse Array, Waveform Diversity, Ambiguity Function, Spectral Methods.						
16. SECURITY CLASSIFICATION OF:			17. LIMITATION OF ABSTRACT	18. NUMBER OF PAGES	19a. NAME OF RESPONSIBLE PERSON	
a. REPORT	b. ABSTRACT	c. THIS PAGE			Maj M.A. Saville; michael.saville@afit.edu	
U	U	U	U	117	19b. TELEPHONE NUMBER (include area code)	
					(937) 255-3636, x4719	